U N I V E R S I T Y O F S P L I T
FACULTY OF ELECTRICAL ENGINEERING, MECHANICAL ENGINEERING
AND NAVAL ARCHITECTURE

Manigandan Paneer

DEVELOPMENT OF MESHLESS METHOD FOR MULTIPHASE FLOW SIMULATIONS INCLUDING PHASE CHANGE AND FLUID STRUCTURE INTERACTION

DOCTORAL THESIS

Split, 2026.

U N I V E R S I T Y O F S P L I T
FACULTY OF ELECTRICAL ENGINEERING, MECHANICAL ENGINEERING
AND NAVAL ARCHITECTURE

Manigandan Paneer

Development of Meshless Method for Multiphase Flow Simulations including Phase Change and Fluid Structure Interaction

DOCTORAL THESIS

Split, 2026.

The research reported in this thesis was carried out at Mechanical Engineering, University of Split, Faculty of Electrical Engineering, Mechanical Engineering and Naval Architecture.

Supervisor: prof. dr. sc. Damir Sedlar, asst. prof. dr. sc. Josip Basic, FESB, University of Split, Croatia
Disertation number: xxx

BIBLIOGRAPHIC INFORMATION

Keywords: multiphase, variable density, variable viscosity, Lagrangian flow, meshless method, heat transfer, phase change, fluid structure interaction
Scientific area: Technical sciences
Scientific field: Fundamental technical sciences
Scientific branch: Technical mechanics (Mechanics of rigid and deformable bodies)
Institution of PhD completion: University of Split, Faculty of Electrical Engineering, Mechanical Engineering and Naval Architecture
Supervisors of the thesis: prof. dr. sc. Damir Sedlar, asst. prof. dr. sc. Josip Basic
Number of pages: 238
Number of figures: 89
Number of tables: 16
Number of references: 196

Committee for assessment of doctoral dissertation:

1. Xxxx. dr. sc. Xxxx Yyyyy, Institution name and City/Town
2. Xxxx. dr. sc. Xxxx Yyyyy, Institution name and City/Town
3. Xxxx. dr. sc. Xxxx Yyyyy, Institution name and City/Town
4. Xxxx. dr. sc. Xxxx Yyyyy, Institution name and City/Town
5. Xxxx. dr. sc. Xxxx Yyyyy, Institution name and City/Town

Committee for defence of doctoral dissertation:

1. Xxxx. dr. sc. Xxxx Yyyyy, Institution name and City/Town
2. Xxxx. dr. sc. Xxxx Yyyyy, Institution name and City/Town
3. Xxxx. dr. sc. Xxxx Yyyyy, Institution name and City/Town
4. Xxxx. dr. sc. Xxxx Yyyyy, Institution name and City/Town
5. Xxxx. dr. sc. Xxxx Yyyyy, Institution name and City/Town

Dissertation defended on: xx. month. 20xx.

Development of Meshless Method for Multiphase Flow Simulations including Phase Change and Fluid Structure Interaction

Abstract:

The numerical simulation of multiphase flows involving sharp interfaces, phase change, buoyancy effects, and fluid structure interaction (FSI) is widely identified as a major challenge in computational fluid dynamics. Such problems involve large density and viscosity contrasts, moving and deforming boundaries, strong variations in thermophysical properties, and complex interfacial phenomena. This thesis presents the development of an advanced Lagrangian meshless computational framework based on Lagrangian Differencing Dynamics (LDD) for multiphase flows, including phase change and fluid-structure interaction. The central contribution is the development of a weakly coupled FSI solver using a modal superposition approach. Structural dynamics are solved in reduced-order form using precomputed mode shapes and natural frequencies, while loads are obtained directly from the LDD flow solver. The fully Lagrangian–Lagrangian coupling enables direct use of structural surface meshes as fluid boundaries, eliminating conventional mesh-to-mesh mapping procedures. Then, the extension of LDD into a Multiphase Lagrangian Differencing Dynamics (MP-LDD) framework that preserves sharp interfaces without density or viscosity diffusion while maintaining second-order spatial consistency. Interface sharpness is maintained through systematic point-cloud regularization, preventing spurious phase mixing. Surface tension and dynamic contact angle models are incorporated to capture interfacial physics accurately. To model thermally driven multiphase flows, an Implicit Phase-Coupled Energy formulation is developed to ensure stable coupling between temperature evolution and phase-fraction dynamics. A Hierarchical Buoyancy Modelling Framework provides consistent treatment of buoyancy across varying density regimes. Phase change processes are modelled using an enthalpy-based formulation with thermodynamically consistent phase-fraction evaluation and vapour-pressure equilibrium enforcement. Extensive validation using benchmark problems demonstrates accurate resolution of moving interfaces, steep thermal gradients, strong property contrasts, and coupled structural response without numerical diffusion or spurious oscillations. Overall, this work establishes MP-LDD as a unified, robust multiphase meshless framework for thermal-fluid and fluid structure interaction applications.

Keywords:
Meshless method, Mode superposition, FSI, Multiphase flow, Variable density & viscosity, Surface Tension, Dynamic contact angle, Heat transfer, Buoyancy and Phase change

Razvoj bezmrežne metode za simulacije višefaznog toka uključujući promjenu faze i interakciju fluida i strukture

Sažetak:

Numerička simulacija višefaznih tokova s oštrim međupovršinama, promjenom faze, uzgonskim efektima i interakcijom fluida i konstrukcije (FSI) ostaje jedan od najzahtjevnijih izazova u računalnoj dinamici fluida. Takvi problemi uključuju velike razlike u gustoći i viskoznosti, pomične i deformabilne granice, snažne varijacije termofizikalnih svojstava te složene međupovršinske pojave. Ova disertacija predstavlja razvoj naprednog Lagrangeovog bezmrežnog računalnog okvira temeljenog na Lagrangeovoj diferencijalnoj dinamici (LDD) za višefazne tokove, uključujući promjenu faze i interakciju fluida i konstrukcije. Središnji doprinos je razvoj slabo spregnutog FSI rješavača korištenjem pristupa modalne superpozicije. Strukturna dinamika rješava se u obliku reduciranog reda korištenjem unaprijed izračunatih oblika oscilacija i prirodnih frekvencija, dok se opterećenja dobivaju izravno iz LDD rješavača toka. Potpuno Lagrangeovo–Lagrangeovo sprezanje omogućuje izravnu upotrebu površinskih mreža konstrukcije kao granica fluida, eliminirajući uobičajene postupke preslikavanja između mreža. Zatim se LDD proširuje u okvir Višefazne Lagrangeove diferencijalne dinamike (MP-LDD) koji čuva oštrine međupovršina bez difuzije gustoće ili viskoznosti uz zadržavanje prostorne konzistentnosti drugog reda. Oštrina međupovršine održava se sustavnom regularizacijom oblaka točaka, sprječavajući lažno miješanje faza. Modeli površinske napetosti i dinamičkog kontaktnog kuta uključeni su radi točnog opisivanja međupovršinske fizike. Za modeliranje termički pobuđenih višefaznih tokova razvija se implicitna fazno-spregnuta energetska formulacija kojom se osigurava stabilno sprezanje između evolucije temperature i dinamike udjela faze. Hijerarhijski okvir za modeliranje uzgona omogućuje dosljednu obradu uzgona u različitim režimima gustoće. Procesi promjene faze modelirani su entalopijskom formulacijom s termodinamički konzistentnom procjenom udjela faze i enforcing ravnoteže tlaka pare. Opsežna validacija na referentnim problemima pokazuje točno razrješavanje pomičnih međupovršina, strmih toplinskih gradijenata, snažnih razlika u svojstvima te spregnutog strukturnog odziva bez numeričke difuzije ili lažnih oscilacija. Sveukupno, ovim radom MP-LDD se uspostavlja kao jedinstveni, robusni višefazni bezmrežni okvir za primjene u termofluidnoj dinamici i interakciji fluida i konstrukcije.

Ključne riječi:
Bezmrežna metoda, modalna superpozicija, FSI, višefazni tok, promjenjiva gustoća i viskoznost, površinska napetost, dinamički kontaktni kut, prijenos topline, uzgon i promjena faze

Acknowledgments

II would like to express my deepest gratitude to all those who have supported me throughout my doctoral research.First and foremost, I sincerely thank my supervisors, Prof. Dr. Sc. Damir Sedlar and Asst. Prof. Dr. Sc. Josip Bašić, FESB, University of Split, Croatia, for their invaluable guidance, continuous encouragement, and insightful feedback throughout this research. Their expertise and dedication have been instrumental in shaping both this work and my development as a researcher. I would also like to extend my appreciation to the members of my thesis committee for their constructive comments and suggestions, which have significantly improved the quality of this dissertation. I am grateful to my colleagues and friends at FESB, University of Split, Croatia, for providing a stimulating and collaborative research environment. My sincere thanks also go to Engineering Software Steyr GmbH for providing the professional environment, resources, funding, and support that facilitated parts of this research. Special thanks are extended to Dr. Martin Schifko for his support and valuable contributions.Finally, I would like to express my heartfelt gratitude to my family, especially my parents and my spouse, for their unwavering support, patience, and encouragement throughout my doctoral journey. Without their love and motivation, this achievement would not have been possible.This dissertation is dedicated to my parents, Paneer M and Pachyammal P, and to my wife, Kavitha R.

Contents

Abstract iv
Sažetak v
Acknowledgments vii
List of Tables xiii
List of Figures xix

NOMENCLATURE **xxi**

1 INTRODUCTION **1**
1.1 Multiphase flow 1
1.2 Phase change 3
1.3 Fluid Structure Interaction (FSI) 3
1.4 Motivation and Open Challenges 4
1.5 Scope of work and application 5
1.5.1 Research Objectives 5
1.5.2 Hypotheses 6
1.5.3 Scientific Contributions 7
1.5.4 Applications 7
1.6 Thesis Outline 8

2 BACKGROUND AND LITERATURE REVIEW **11**
2.1 Numerical Background 11
2.1.1 Governing Equations 11
2.1.2 Equation based formulation 13
2.1.3 Classification of Multiphase Modeling Techniques 14
2.1.4 Surface Tension 26
2.1.5 Dynamic Contact Angle (DCA) 29
2.1.6 Energy Equation 35
2.1.7 Fluid-Structure Interaction (FSI) 36
2.2 Past Research Overview 38
2.2.1 Literature Review - Lagrangian Differencing Dynamics (LDD) . . . 38
2.2.2 Literature Review - Multiphase 39
2.2.3 Literature Review - Surface Tension and Dynamic Contact Angle . 41

2.2.4 Literature Review - Fluid Structure Interaction (FSI) 44
2.2.5 Literature Review - Heat Transfer and Phase Change 47
2.3 Research Gaps and Implications 50
2.3.1 Identified Gaps 50
2.3.2 Thesis Implications 50

3 LAGRANGIAN DIFFERENCING DYNAMICS 53
3.1 Governing Equations for Incompressible Flow 53
3.1.1 Pressure Velocity Decoupling 53
3.2 Discretization Techniques 54
3.2.1 LDD Approximation 54
3.2.2 Gradient Operator 56
3.2.3 Laplacian Operator 56
3.2.4 Weighting Function 57
3.3 Pressure Poisson Equation Solution 58
3.4 Particle Based Dynamics (PBD) 58
3.5 Boundary Condition 58
3.6 Time Integration 59
3.7 Auto Time Stepping 59
3.8 Summary 60

4 FLUID STRUCTURE INTERACTION WITH MODAL COUPLING 61
4.1 Mode Superposition 61
4.2 Force Transfer from Fluid to Structure 64
4.3 Methodology 65
4.4 Numerical Procedure of the Modal Superposition Method 66
4.4.1 Step 1: Governing Dynamic Equation 66
4.4.2 Step 2: Eigenvalue Problem (Undamped Free Vibration) 67
4.4.3 Step 3: Mass Normalisation and Orthogonality 67
4.4.4 Step 4: Modal Coordinate Transformation 67
4.4.5 Step 5: Substitution into the Governing Equation 68
4.4.6 Step 6: Diagonalisation of Damping via Rayleigh Proportional Damping 68
4.4.7 Step 7: Fully Decoupled SDOF Equations of Motion 68
4.4.8 Step 8: Solution via the Complementary Function and Particular Integral (CFPI) Method 69
4.4.9 Step 9: Recovery of Physical Displacements 70
4.4.10 Summary of the Mode Superposition Method 70

5 MULTIPHASE LDD (MP-LDD) WITH SHARP INTERFACES 71

5.1 Multiphase Extension of LDD . . . 71
5.1.1 Variable Laplacian for MP-LDD . . . 71
5.1.2 Multiphase Pressure Solver . . . 72
5.1.3 Multiphase Velocity Solver . . . 74
5.1.4 A Structured Method for Point Cloud Regularization . . . 75
5.1.5 Split Scheme Solver . . . 80
5.2 Numerical Procedure of the Multiphase LDD (MP-LDD) Formulation . . . 82
5.2.1 Step 1: Variable-Coefficient Laplacian Operator . . . 82
5.2.2 Step 2: Pressure Poisson Equation (PPE) - Continuous Form . . . 82
5.2.3 Step 3: Lagrangian Time-Step Criterion and RHS . . . 83
5.2.4 Step 4: Discrete PPE - Left-Hand Side . . . 83
5.2.5 Step 5: Algebraic Form of the Discrete PPE . . . 84
5.2.6 Step 6: Preconditioned Solver for the PPE . . . 84
5.2.7 Step 7: Boundary Condition for the PPE . . . 85
5.2.8 Step 8: Pressure Acceleration . . . 85
5.2.9 Step 9: Velocity Solver - BDF2 Temporal Discretisation . . . 86
5.2.10 Step 10: Discrete Velocity Equation with Variable Viscosity . . . 87
5.2.11 Step 11: Lagrangian Advection . . . 87
5.2.12 Summary of the MP-LDD . . . 88

6 INTERFACE DYNAMICS MODELLING 89
6.1 Surface Tension . . . 89
6.1.1 Capillary Time-Step Restriction . . . 91
6.2 Numerical Procedure of Surface Tension . . . 91
6.2.1 Step 1: Physical Origin and Continuum Definition . . . 91
6.2.2 Step 2: Converting Surface Force to Volumetric Body Force . . . 92
6.2.3 Step 3: Approximation of the Delta Function . . . 92
6.2.4 Step 4: Density-Based Normal in MP-LDD . . . 92
6.2.5 Step 5: Unit Normal and Curvature . . . 93
6.2.6 Step 6: Dimensional Conversion to Volumetric Force . . . 93
6.2.7 Step 7: Summary of Surface Tension . . . 94
6.3 Dynamic Contact Angle Modeling . . . 94
6.4 Numerical Procedure of Dynamic Contact Angle Modelling . . . 95
6.4.1 Step 1: Physical formulation . . . 95
6.4.2 Step 2: Meniscus Radii from Geometric Constraint . . . 96
6.4.3 Step 3: Static Equilibrium Angle via Curvature-Weighted Interpolation 96
6.4.4 Step 4: Velocity-Dependent Dynamic Correction . . . 96
6.4.5 Step 5: Dynamic Contact Angle Update . . . 97
6.4.6 Step 6: Restoring Force at the Contact Line . . . 97

6.4.7 Step 7: Derivation of the DCA Coefficient . . . 98
6.4.8 Step 8: Integration into the Momentum Equation . . . 98
6.4.9 Step 9: Summary of DCA . . . 98

7 HEAT TRANSFER AND PHASE CHANGE 101
7.1 Enthalpy Based Energy Equation For Phase Change . . . 101
7.2 Implicit Phase-Coupled Energy (IPCE) Formulation . . . 102
7.2.1 Saturation Check via Temperature Criterion . . . 105
7.2.2 Phase Change Workflow . . . 106
7.3 Hierarchical Buoyancy Modelling Framework . . . 107
7.4 Phase Change Solver workflow . . . 110
7.5 Numerical Procedure of the Heat Transfer and Phase Change Formulation . . . 111
7.5.1 Part I: Enthalpy-Based Energy Equation . . . 111
7.5.2 Part II: Implicit Phase-Coupled Energy (IPCE) Formulation . . . 112
7.5.3 Part III: Saturation Check via Antoine Relation . . . 115
7.5.4 Part IV: Hierarchical Buoyancy Modelling Framework (HBMF) . . . 116
7.5.5 Summary of the Heat Transfer and Phase Change . . . 118

8 VALIDATION AND VERIFICATION 121
8.1 Fluid Structure Interaction . . . 121
8.1.1 Testing of the LDD and Modal Solver . . . 121
8.1.2 Deformation of a Cantilever Gate . . . 126
8.1.3 Elastic Baffle in a Sloshing Tank . . . 126
8.1.4 Elastic Beam Subjected to Sloshing Loads in Shallow Oil . . . 130
8.1.5 Impact of a Fluid Column on a Cantilever Beam . . . 133
8.1.6 Water Entry of a Wedge . . . 137
8.1.7 Summary . . . 141
8.2 Multiphase LDD . . . 142
8.2.1 Low Density Ratio Rayleigh-Taylor Perturbation . . . 143
8.2.2 Dam Break Over a Trapezoidal Step . . . 145
8.2.3 Dam Break With a Vertical Obstacle . . . 146
8.2.4 Sloshing in a Harmonically Excited Rectangular Tank . . . 150
8.2.5 Two-Dimensional Sloshing Validation . . . 152
8.2.6 Injection of Oil into Water . . . 154
8.2.7 Summary . . . 156
8.3 Surface Tension and DCA . . . 156
8.3.1 Square Droplet - Non Equilibrium Oscillation . . . 156
8.3.2 Bubble Rising . . . 158
8.3.3 Static Contact Angle on a Square Droplet . . . 161

8.3.4 Effect of Surface Tension and Dynamic Contact Angle on Droplet Spreading . . . 163
8.3.5 Summary . . . 166
8.4 Energy Formulation . . . 167
8.4.1 Heat Conduction . . . 167
8.4.2 Buoyancy Driven Convection in a Square Cavity . . . 169
8.4.3 Stefan Problem - Vaporization . . . 175
8.4.4 Two Dimensional Solidification . . . 178
8.4.5 Film Boiling . . . 183
8.4.6 Summary . . . 187

9 CONCLUSION AND FUTURE WORK 189
9.1 Conclusion . . . 189
9.2 Future Work . . . 190
9.2.1 Further Verification and Conservation Assessment . . . 190
9.2.2 Capillary and Wetting-Scale Validation . . . 191
9.2.3 Fluid–Structure Interaction Enhancements . . . 191
9.2.4 Three-Dimensional and Large-Scale Applications . . . 191
9.2.5 Thermal and Phase-Change Extensions . . . 192
9.2.6 Wetting and Contact-Line Physics . . . 192
9.2.7 Adaptive Resolution and Computational Performance . . . 193

BIBLIOGRAPHY 195

List of Tables

2.1 *Summary of meshless methods.* 24

2.2 *Summary of interface tracking methods for grid-based methods* 27

2.3 *Summary of study on Multiphase methods and literature reviews.* 42

8.1 *Deviation of numerically predicted pressure from the experimentally measured values at the sloshing pressure peaks.* 123

8.2 *First five natural frequencies of the cantilever beam.* 125

8.3 *First Five Vibration Modes of the Elastic Baffle.* 128

8.4 *Deviation of numerically predicted baffle deformation from the reference solution of Sampann.* 130

8.5 *First Five Vibration Modes of the Elastic Baffle.* 131

8.6 *First five natural frequencies of the wedge.* 137

8.7 *Deviation of numerically predicted pressure from the experimental measurements at the first and second sloshing pressure peaks.* 154

8.8 *Fluid parameters used in the bubble rising simulation based on Hysing et al* 159

8.9 *Error norms comparing MP-LDD and analytical solution* 168

8.10 *Grid convergence and error norms comparing MP-LDD with reference solution* 182

8.11 *Antoine equation coefficients for water* 183

8.12 *Particle resolution study for MP-LDD simulation* 183

8.13 *Computational time for 2D film boiling simulations* 187

List of Figures

1.1 *Diversity of flow regimes in gas-liquid systems.* 2

2.1 *Representation of the domain to solve the NS for Multiphase flow. One equation Method (Left), Separate Equation for each phase is called Multi Equation (center), Ghost or sharp interface using ghost particles* 13

2.2 *Multiscale Modeling Framework for Fluid Systems* 15

2.3 *A detailed overview of Multiphase Modelling and Methods* 16

2.4 *Representation of domain with mesh or grid for the mesh-based method* . . 18

2.5 *Representation of the domain with particles or points for the meshless method* 21

2.6 *Interface tracking methods for gird based methods. Phase field: Diffuse (controlled by interface width), VOF: Diffuse (over a few cells), Level set: Sharp, but smeared numerically, Marker and cell: Diffuse using markers and Front tracking: Sharp interface using Lagrangian particle* 25

2.7 *Representation of surface tension on a liquid-air system.* 28

2.8 *Representation of contact angle at the three-phase boundary point* 30

2.9 *Classification of Surface and Wettability nature with respect to contact angle* 31

3.1 *Neighbouring points within a defined compact radius(h).* 55

4.1 *Flowchart of the LDD-based FSI solver illustrating the weakly coupled modal integration procedure.* 66

5.1 *Modeling of boundary/solid points and the pressure at those points.* 74

5.2 *Behaviour of the modified PBD scheme with differing relaxation values under low-density ratio flow conditions.* 77

5.3 *Zoomed view of Figure 5.2 showing the effect of the modified PBD with various relaxation factors.* 78

5.4 *Influence of the relaxation parameter on the modified PBD scheme under high-density ratio flow conditions.* 78

5.5 MP-LDD solver workflow for a single time step. 81

7.1 Schematic representation of the enthalpy–temperature relationship during phase change. The sloped regions correspond to sensible heating in single phases (solid, liquid, or gas), while the horizontal plateaus represent isothermal phase transitions, where enthalpy increases or decreases due to latent heat absorption or release. 103

7.2 Sequential workflow for the phase change numerical solver. 107

7.3 Flowchart of the Hierarchical Buoyancy Modelling Framework (HBMF). The model selection is based on the local temperature deviation ε*. For small deviations, the Boussinesq approximation is applied. For larger deviations, phase-specific density models are used. Viscosity is updated according to phase.* 109

7.4 Flowchart of the MP–LDD solver workflow for coupled flow, heat transfer, surface tension, and phase change simulations. 111

8.1 Cuboidal tank geometry used for the sloshing validation study. 122

8.2 Pressure time history at sensor location P1 obtained from the LDD simulation compared against the experimental measurements. 122

8.3 Cantilever beam configuration experiencing constant tip load, used for verifying the modal superposition implementation. 123

8.4 X-Directional Displacement of the Cantilever Beam : Vibration Mode Shapes 124

8.5 Y-Directional Displacement of the Cantilever Beam : Vibration Mode Shapes. 124

8.6 Validation of the numerically obtained dynamic displacement response against the analytical solution for a cantilever beam subjected to a constant tip load. 125

8.7 Time-varying behaviour of the cantilever gate deformation at $t = 0.08$ *s, 0.16 s, 0.24 s, 0.32 s, and 0.40 s, compared against the reference experimental data.* 127

8.8 Schematic of the sloshing tank featuring a flexible baffle fixed at the base. . 128

8.9 First five mode shapes of the elastic baffle with the undeformed geometry shown as a wireframe reference. 129

8.10 X-displacement at monitoring location D1 predicted by the current numerical solution compared against the reference numerical data. 130

8.11 Tank and elastic beam configuration used for the sloshing validation study in shallow oil. 131

8.12 First five mode shapes of the elastic beam shown relative to the undeformed wireframe geometry. 132

8.13 *X-directional displacement at the beam tip: comparison between the present simulation and experimental and numerical reference solutions.* 133

8.14 *Deformation of the cantilever beam and pressure distribution at successive time instants during the dam-break simulation.* 134

8.15 *X-directional deformation at the mid-section and free tip of the beam over the full simulation duration.* 135

8.16 *Y-directional deformation at the mid-section and free tip of the beam over the full simulation duration.* 135

8.17 *X-directional deformation at the mid-section and free tip of the beam during the initial 1 s of the simulation.* 136

8.18 *Y-directional deformation at the mid-section and free tip of the beam during the initial 1 s of the simulation.* 136

8.19 *Numerical configuration for the wedge water entry study, showing the tank filled to 1.5 m depth with the wedge positioned 0.25 m above the free surface.* 138

8.20 *Surface triangulation of the wedge used for both modal analysis and the LDD-modal coupling simulation.* 138

8.21 *First five mode shapes of the wedge structure shown relative to the undeformed wireframe geometry.* 139

8.22 *Dynamic pressure history at monitoring point PS1 compared against the experimental reference measurements.* 140

8.23 *Dynamic pressure history at monitoring point PP1 compared against the experimental reference measurements.* 140

8.24 *Distribution of structural displacements in the X, Y, and Z coordinate directions and resultant deformation magnitude of the wedge under peak impact conditions.* 141

8.25 *Temporal development of the RT instability interface at dimensionless times $t^* = 1$, 3, and 5, compared against the Level Set results (white dotted line) and SPH results (black dotted line) from the reference study.* 143

8.26 *Point spacing convergence study showing the interface profile at $t^* = 5$ for spacings of 0.0015 m (red), 0.003 m (blue), and 0.006 m (fluorescent blue).* 144

8.27 *Computational domain and initial configuration for the dam-break over a trapezoidal obstacle.* 145

8.28 *Sequential snapshots of the dam-break flow over the trapezoidal obstacle at $t = 2.50$, 3.00, 3.26, 3.54, 3.66, and 3.80 s: experimental observations (left column), MP-LDD simulation (centre column), and single-phase LDD reference solution (right column).* 146

8.29 *Initial configuration for the dam-break with vertical obstruction case, showing the water phase(red) and air region (blue).* 147

8.30 *Temporal sequence of dam-break flow over the vertical obstacle from the MP-LDD simulation compared against the experimental photographic record.* 148

8.31 *Time history of the free surface water level from the MP-LDD simulation compared against the experimental measurements.* 149

8.32 *Time-dependent pressure history at monitoring point P1 from the MP-LDD simulation compared against the experimentally recorded measurements.* . 149

8.33 *Free surface snapshots at* $t = 1.1T$, $1.2T$, $1.3T$, *and* $1.4T$*: experimental observations (left column), MP-LDD simulation (middle column), and single-phase LDD reference solution (right column).* 151

8.34 *Pressure time history at the wall-mounted sensor located 0.1 m above the tank base, comparing the MP-LDD prediction against the experimental pressure data.* 151

8.35 *Temporal evolution of the fluid motion within the two-dimensional sloshing tank at successive normalised time instants* t/T. 153

8.36 *Pressure time history at monitoring point P1 from the MP-LDD simulation (blue), the single-phase LDD simulation (red), and the experimental measurements (black).* 153

8.37 *Computational domain configuration for the oil injection into water study, showing the initial fluid distribution in the two compartments separated by the perforated barrier.* 154

8.38 *Comparison of the oil-water interface development at* $T = 0.2$ *s and* $T = 1.5$ *s between the MP-LDD simulation and the reference numerical study.* . 155

8.39 *Schematic of the Case Setup for Square Ethanol Droplet Oscillation* 157

8.40 *Non-equilibrium oscillation of square droplet at different time step* 158

8.41 *Comparison of bubble shape and position at* $t = 3$ *s obtained using MP-LDD (coloured region) against the benchmark dataset of Hysing et al. (white dots).* 160

8.42 *Quantitative comparison of bubble rising dynamics: centre-of-mass trajectory obtained with MP-LDD (blue solid line) against the reference data of Hysing et al. (red markers).* 160

8.43 *Quantitative comparison of bubble rising dynamics: rising velocity (Right) obtained with MP-LDD (blue solid line) against the reference data of Hysing et al. (red markers).* 161

8.44 *Equilibrium shapes of a square ethanol droplet on a flat solid surface at* $T = 2$ *s for static contact angles of* $\theta_s = 30°$, $60°$, $90°$, $120°$, $150°$, *and* $180°$. 162

8.45 *Droplet profiles at $t = 0.05$ s for the three configurations: ST + No DCA (top), ST + DCA (middle), and No ST + No DCA (bottom).* 164

8.46 *Droplet profiles at $t = 0.10$ s for the three configurations: ST + No DCA (top), ST + DCA (middle), and No ST + No DCA (bottom).* 165

8.47 *Case setup for the 2D heat conduction.* 167

8.48 *Comparison between analytical output (left) and MP-LDD output (right) for temperature distribution.* 168

8.49 *Representation of a square cavity (2D) subjected to thermal gradient boundary conditions used for the buoyancy-driven convection benchmark.* 170

8.50 *Normalized temperature distribution (T^*) at steady state ($t^* = 0.5$).* 171

8.51 *Comparison of MP-LDD simulation and benchmark results: Normalised temperature profile (T^*) along x/L at mid-height ($y/L = 0.5$).* 172

8.52 *Comparison of MP-LDD simulation and benchmark results: Associated L1 and L2 norm errors quantifying deviation from the reference data.* 172

8.53 *Density distribution in the cavity at steady state.* 173

8.54 *Velocity distribution in the cavity at steady state.* 173

8.55 *Visualisation of flow dynamics.* 174

8.56 *Buoyancy-driven motion is reflected in magnitude and direction, with benchmark comparison confirming model accuracy.* 174

8.57 *Case setup of the 2D Stefan problem for the vaporization process.* 175

8.58 *Temperature distribution along the x direction of the MP-LDD result at 300 sec.* 176

8.59 *Density distribution along the x direction of the MP-LDD result at 300 sec.* 176

8.60 *Temporal evolution of the two-phase vapour-liquid boundary position for the 2D Stefan problem at various grid resolutions. Symbols represent the analytical Neumann solution, while lines denote MP-LDD results. The inset highlights the asymptotic convergence of the 0.005 mm mesh at $t = 300$ s. The corresponding L_1 and L_2 error norms (bottom) indicate a $> 97\%$ reduction in numerical error when refining the mesh from 0.01 mm to 0.005 mm.* 177

8.61 *Comparison of temperature distribution along the x-direction obtained from MP-LDD and analytical solution at $t = 300$ s for the resolution of 0.005 mm.* 177

8.62 *Schematic setup of the two-dimensional solidification benchmark problem.* . 179

8.63 *Evolution of density and temperature fields during the solidification process at different time instances.* 180

8.64 Comparison of temperature distribution along the vertical centerline with the results of Uyar et al. 181

8.65 Grid convergence analysis for the 2D Stefan solidification benchmark. . . . 181

8.66 Grid dependence study for the film boiling simulation. The panels show the progression of the vapor bubble boundary (blue line) assessed against the benchmark data by Biswas et al. (red dots) at varying particle spacings: (a) 3×10^{-5} *mm, (b)* 2.5×10^{-5} *mm, and (c)* 2×10^{-5} *mm. Increased resolution demonstrates better convergence with the experimental interface profile.* . . 183

8.67 Density field of a vapor bubble in film boiling at near-critical conditions. The red markers indicate reference points from Biswas et al and blue line show the vapor boundary. The domain shows the formation of the bubble from a sinusoidal interface on a superheated wall at 0.1 sec. 184

8.68 Evolution of density and velocity fields across three stages of phase change $(0.05s, 0.1s\&0.15s)$*. Left column: temperature distribution. Right column: velocity magnitude with streamlines.* 185

NOMENCLATURE

Symbols

D/Dt	Material derivative
$\mathbf{u}$	Velocity
p	Pressure
∇	Vector of partial derivative operator
∇p	Pressure gradient
$\nabla \mathbf{u}$	Velocity gradient
$\nabla \cdot \mathbf{u}$	Velocity divergence
$\nabla^2 \mathbf{u}$	Velocity Laplacian
ρ	Density
ν	Kinematic viscosity
μ	Dynamic viscosity
$\mathbf{g}$	Acceleration due to gravity
$\mathbf{F}_{s+d}$	Surface tension and dynamic contact angle force per unit volume
$\partial/\partial t$	Partial derivative with time
σ	Surface tension coefficient
κ	Curvature of the interface
$\mathbf{n}$	Unit normal vector to the interface
Ω	Domain around the interface
W	Weighting function
$W(\mathbf{r}-\mathbf{r}')$	Smoothing kernel
$\mathbf{r}$	Distance vector of the neighbour point
$\mathbf{r}'$	Distance vector of the center point
∇H	Gradient of Heaviside function
ϕ	Phase indicator
$H(\phi)$	Heaviside function
$\delta(\phi)$	Dirac delta function
θ	Contact angle
γ_{sg}	Solid-gas surface energy
γ_{sl}	Solid-liquid surface tension

γ_{lg}	Liquid-gas surface tension
θ_D	Dynamic contact angle
θ_A	Advancing contact angle
θ_R	Receding contact angle
θ_E	Equilibrium contact angle
θ_{app}	Apparent contact angle
Ca	Capillary number
L	Apparent length
a_1, a_2	Fitted parameters
$\mathbf{u}_0$	Radial velocity
$\mathbf{u}_{cl}$	Contact line velocity
$g(\theta)$	Integral function or g-function
λ	Slip length
M	Mobility parameter
θ_{mda}	Maximum dynamic advancing angle
θ_{mdr}	Maximum dynamic receding angle
k_a	Material dependent contact for advancing
k_r	Material dependent contact for receding
E	Total energy
U	Internal energy
KE	Kinetic energy
PE	Potential energy
D_ν	Viscous dissipation
q	Heat flux
Q	Volumetric heat source
T	Temperature
Γ_w	Wall boundary
Γ_{fs}	Free surface
$\mathbf{U}$	Wall velocity
p_{atm}	Atmospheric pressure
Δr	Point spacing
r_{ij}	Distance between the points i and j
$\mathbf{x_i}$ and $\mathbf{x_j}$	Spatial coordinates of points i and j
ψ_{ij}	Normalized weighting function
$\mathcal{N}_i$	Set of neighboring points of point i
h	Support radius
$\mathbf{B_i}$	Renormalized tensor
$\mathbf{o_i}$	Offset vector
$\otimes$	Outer tensor product

d	spatial dimensionality
$\mathbf{A}$	Sparse coefficient matirx
$\mathbf{p}$	Unknown vector
$\mathbf{b}$	Known vector
$\mathbf{dx_i}$	Displacement increment
δt	Time step
$n+1$	Next time step
n	Current time step
$n-1$	Previous time step
M	Mass-normalized matrix
C	Damping matrix
K	Stiffness matrix
u	Column vector for degrees of freedom
t	Time
$f(t)$	Applied forces over time
ω, ω_n	Natural frequency
Φ	Mass normalized modal vector
ζ	Damping ratio
a_K, a_M	Rayleigh constants
y_t	Displacement at current time step
y_{t-1}	Displacement at previous time step
$\dot{y}_t$	Velocity at current time step
$\dot{y}_{t-1}$	Velocity at previous time step
α_t	Ratio of consecutive time step
P_i	Position of point i
λ	Lagrangian multiplier
ρ_0	Rest density
A	Atwood number
Z_relax	PBD relaxation factor
$\hat{\mathbf{n}}$	Unit interfacial normal
H	Enthalpy
f_p	Phase fraction
c_p	Heat capacity
L	Latent heat
α	Thermal diffusivity
k	Thermal conductivity
p_{sat}	Saturation pressure
T_{sat}	Saturation temperature
ε	Relative temperature deviation

β	Thermal expansion
E_a	Activation energy
R_g	Universal gas constant
S	Sutherland constant
γ	Linear thermal expansion

Abbreviation

FSI	Fluid-Structure Interaction
VOF	Volume of Fluid
SPH	Smoothed Particle Hydrodynamics
GPU	Graphics Processing Unit
LDD	Lagrangian Differencing Dynamics
MP-LDD	Multiphase Lagrangian Differencing Dynamics
HBMF	Hierarchical Buoyancy Modelling Framework
PBD	Particle Based Dynamics
CFD	Computational Fluid Dynamics
PPE	Pressure Poisson Equation
GFM	Ghost Fluid Method
MD	Molecular Dynamics
DPD	Dissipative Particle Dynamics
LBM	Lattice Boltzmann Method
PDE	Partial Differential Equation
FVM	Finite Volume Method
FDM	Finite Difference Method
FEM	Finite Element Method
BEM	Boundary Element Method
IBM	Immersed Boundary Method
MPS	Moving Particle Semi-Implicit
GFDM	Generalized Finite Difference Method
MLS	Moving Least Squares
FPM	Finite Pointset Method
PLIC	Piecewise Linear Interface Calculation
MAC	Marker-and-Cell Method
CSF	Continuum Surface Force
SCSF	Smoothed Continuum Surface Force
SSF	Sharp Surface Force
DCA	Dynamic Contact Angle

MDA	Maximum Dynamic Advancing
MDR	Maximum Dynamic Receeding
NVH	Noise-Vibration-Harshness
CPU	Central Processing Unit
BiCGSTAB	Bi-Conjugate Gradient Stabilized
PLS	Particle Level Set
XFEM	Extended Finite Element Method
EFG	Element-Free Galerkin
PFEM	Particle Finite Element Method
ISPH	Incompressible Smoothed Particle Hydrodynamics
MMPS	Multiphase Moving Particle Semi-Implicit
MMPS-CA	MMPS - Continuous Acceleration
MMPS-HD	MMPS - Harmonic Density
DIM	Diffuse Interface Model
DES	Detached Eddy Simulation
URANS	Unsteady Reynolds-Averaged Navier–Stokes
RANS	Reynolds-Averaged Navier–Stokes
DEM	Discrete Element Method
MLPG	Meshless Local Petrov–Galerkin
RKPM	Reproducing Kernel Particle Method
AB2	Adams Bashforth 2
LCFL	Lagrangian Courant Friedrichs Lewy
DOF	Degree Of Freedom
SDOF	Single Degree Of Freedom
MDOF	Multi Degree Of Freedom
ODE	Ordinary Differential Equation
RBF	Radial Basis Function
RHS	Right Hand Side
LHS	Left Hand Side
PBICGSTAB	Preconditioned Bi-Conjugate Gradient Stabilized
PBF	Position Based Fluids
IPCE	Implicit Phase-Coupled Energy
RT	Rayleigh Taylor
2D	Two Dimensional
3D	Three Dimensional
LNG	Liquefied Natural Gas

1 INTRODUCTION

Multiphysics problems involving multiphase flow, phase change, and Fluid Structure Interaction (FSI) are central to a wide range of naturally occurring processes and engineered technologies. These processes govern the behavior of many industrial systems, including automotive, energy conversion devices, thermal management systems, manufacturing processes, environmental flows, marine, space and biomedical applications. The interaction between multiple phases, thermal effects, and deformable or moving structures results in complex flow behaviour that directly impacts system efficiency, reliability, and safety. As a result, understanding and modelling these coupled phenomena has become an important research topic in computational science and engineering [1, 2].

1.1 Multiphase flow

Multiphase flow involves the simultaneous movement of different phases, such as liquids, gases, and solids, or immiscible fluids within a shared system. This phenomenon is fundamental and has significant implications across various industries and scientific fields. The dynamics of multiphase flows can be observed in many technological applications, including oil and gas extraction, chemical processing, environmental science, nuclear reactor cooling, and biomedical engineering. The behavior of these flows often determines the efficiency, safety, and overall success of the processes involved, making it essential to understand and accurately model their underlying mechanisms. The distinct physical attributes of each phase such as density, viscosity, and compressibility add complexity to multiphase flow modeling, especially as these phases interact with one another at their interfaces. The evolution of these interfaces is influenced by factors like surface tension, buoyancy forces, shear stresses, and other interfacial phenomena. These interactions can result in intricate behaviors, including droplet formation, bubble breakup, and particle aggregation. As a result of these complexities, multiphase flows can exhibit a wide range of behaviors, from stable stratified flows to highly chaotic and turbulent regimes. Therefore, effectively modeling multiphase flows is not only a significant scientific challenge, but it is also crucial for optimizing industrial applications, ensuring environmental safety, and advancing scientific research. The diversity of flow regimes in gas-liquid systems is illustrated in Figure 1.1 , which shows the transition between different flow types as liquid and gas velocities vary. Each regime represents a

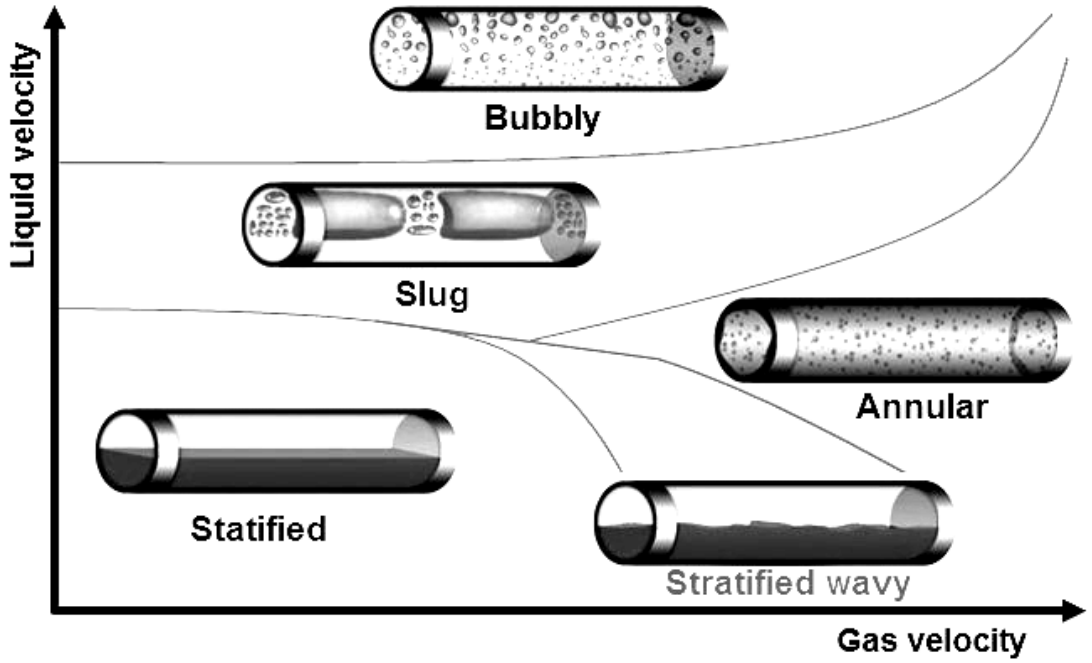

Figure 1.1. Diversity of flow regimes in gas-liquid systems.

unique arrangement and interaction of the phases, highlighting the complexity and richness of multiphase flow behavior.

One of the distinctive challenges in computational modeling of multiphase flows lies in the diverse range of flow regimes that can arise, depending on the relative velocities, properties, and orientations of the phases involved. In gas-liquid flows, for instance, these regimes include bubbly, slug, annular, stratified, and stratified wavy flows, each with distinct characteristics. Bubbly flow features dispersed gas bubbles within a continuous liquid phase, commonly seen in low-velocity gas streams. With an increase in gas velocity, discrete bubbles tend to merge, forming elongated gas pockets interspersed with liquid segments, thereby establishing the slug flow regime. In annular flow, typically observed at higher gas velocities, a thin liquid film surrounds a continuous gas core. Stratified flow is characterized by a separated, layered arrangement of gas and liquid phases, while stratified wavy flow occurs when surface waves form at the interface due to higher relative velocities between the phases. These regimes are not only visually distinctive but also impact pressure drop, flow stability, and heat and mass transfer rates, which are critical factors in engineering design and operation.

1.2 Phase change

Phase change involves the transformation of matter between different thermodynamic states, such as melting, solidification, evaporation, and condensation. These processes are commonly encountered in thermal energy storage, electronic cooling, metal casting, additive manufacturing, refrigeration, and boiling heat transfer applications. Phase change introduces strong coupling between flow dynamics and heat transfer through latent heat effects and moving phase boundaries [3, 4]. The presence of phase change significantly alters the flow behavior by modifying local material properties and energy transport mechanisms. For example, melting and solidification processes influence fluid motion through density variations and thermal gradients, while boiling and condensation involve complex interactions between vapor generation, interface dynamics, and heat transfer. Accurately capturing phase change phenomena is therefore critical for predicting thermal performance, structural integrity, and overall system behavior in many engineering applications [5].

Understanding and accurately modeling phase change is essential for optimizing the performance of thermal systems, such as heat exchangers, refrigeration cycles, power generation systems, and materials processing equipment.The complexity of phase change modeling arises from several factors. First, the interface between phases is inherently unsteady and can undergo rapid morphological changes. Second, the phase transition process is governed by coupled heat and mass transfer mechanisms, which require simultaneous solution of energy and momentum equations. Third, interfacial phenomena such as surface tension, contact angle dynamics, and nucleation play significant roles in determining the phase change behavior. In boiling processes, for example, bubble nucleation, growth, and detachment from heated surfaces are controlled by a delicate balance between thermal driving forces, surface tension effects, and hydrodynamic forces. Similarly, in condensation, the formation and removal of liquid films or droplets on cold surfaces significantly affect heat transfer rates. These interfacial dynamics are further complicated by the presence of non-condensable gases, flow patterns, and surface properties.

1.3 Fluid Structure Interaction (FSI)

Fluid structure interaction describes the mutual coupling between fluid flow and structural motion or deformation. In many practical systems, the fluid exerts forces on solid structures, causing deformation or motion, which in turn modifies the surrounding flow field. This two-way coupling is particularly important in applications involving flexible structures, large deformations, or transient loading, such as sloshing tanks, coating processes, aeroelasticity, biomedical devices, and thermal expansion due to phase change [6]. When fluid–structure interaction occurs in multiphase environments, the problem becomes even more complex as a result of the combined influence of interface motion, phase change, and structural response.

For example, dip coating, icing, and gearbox lubrication involve simultaneous interaction between multiple fluid phases and solid components under dynamic conditions. Understanding FSI in such multiphase systems is essential for predicting load transfer, material wear, coating uniformity, and structural durability [7].

1.4 Motivation and Open Challenges

Multiphase flows, characterized by the simultaneous presence and interaction of multiple fluid or solid phases, are fundamental to numerous engineering and scientific applications, including thermal management systems, energy conversion devices, material processing, icing and melting phenomena, and fluid-structure interaction problems. The accurate numerical simulation of such flows remains challenging due to the presence of moving and deforming interfaces, large contrasts in density and viscosity, interfacial forces such as surface tension, and strong coupling between hydrodynamic, thermal, and structural effects. These complexities motivate continued research into numerical methods that can reliably and accurately capture multiphase dynamics across different physical regimes. Conventional grid based methods, such as the Volume of Fluid (VOF), Level Set, and Front Tracking approaches, have been extensively applied to computational modeling of multiphase flows. While these methods are well established, they often encounter limitations related to numerical diffusion of interfaces, mass conservation errors, spurious currents associated with surface tension modelling, and reduced robustness in the presence of high density and viscosity ratios. Moreover, their application to problems involving large deformations, complex geometries, or moving and deforming boundaries frequently requires sophisticated mesh motion or remeshing techniques, which increase algorithmic complexity and computational cost.

Meshless and particle-based methods provide an alternative framework that avoids explicit mesh connectivity and is therefore well suited for problems involving large interface motion, topological changes, and strong coupling with solid structures. Methods such as Smoothed Particle Hydrodynamics (SPH) and related particle formulations have demonstrated advantages in handling free-surface and multiphase flows. However, these approaches often suffer from numerical instability, pressure noise, excessive dissipation, and difficulties in maintaining sharp and physically consistent interfaces, particularly for flows with large density ratios or strong interfacial forces. The accurate and stable incorporation of surface tension and dynamic contact angle models remains a persistent challenge in this class of methods.

The modeling of phase change further increases the complexity of multiphase simulations. Phase transition processes involve latent heat effects and strong coupling between the energy equation and the phase distribution, leading to stiff source terms and rapidly evolving interfaces. Many existing numerical approaches rely on explicit interface tracking or simplified phase change models, which can compromise numerical stability, conservation prop-

erties, or physical consistency. Achieving a robust and efficient treatment of phase change within a multiphase framework remains an open research problem.

Fluid structure interaction problems introduce additional challenges due to the mutual coupling between fluid motion, interfacial dynamics, and structural deformation. Ensuring stable and accurate momentum and energy transfer across fluid–fluid and fluid–structure interfaces is particularly difficult in the presence of large density contrasts, strong added-mass effects, and evolving contact conditions. A unified formulation capable of handling multiphase flow, phase change, and FSI in a consistent manner is still largely lacking.

In addition to physical and numerical challenges, computational efficiency and scalability are critical considerations for practical applications. High-fidelity multiphase simulations often involve a large number of degrees of freedom and require efficient parallelization strategies to exploit modern high-performance computing architectures, including Graphical Processing Units (GPU). Developing numerical methods that combine robustness, accuracy, and computational efficiency therefore, remains an important open challenge.

In summary, there is a clear need for advanced numerical methodologies that can accurately capture sharp interfaces, handle large density and viscosity ratios, robustly model surface tension, wetting, and phase change phenomena, and consistently couple fluid and structural dynamics, while remaining accurate and computationally efficient. Addressing these challenges forms the primary motivation for the present thesis and underpins the development of the proposed numerical framework.

1.5 Scope of work and application

1.5.1 Research Objectives

While significant progress has been made in numerical methods for multiphase flows, phase change, and FSI individually, challenges remain when these phenomena are coupled or when complex interfacial dynamics are involved:

1. **Multiphase Flow Challenges:** Traditional mesh based methods face difficulties in capturing sharp interfaces, especially in flows with high density ratios. Interface diffusion, spurious currents near interfaces remain ongoing challenges. Additionally, handling complex topological changes such as droplet breakup and coalescence requires sophisticated interface tracking or capturing techniques.

2. **Phase Change Modeling:** Accurate simulation of phase change phenomena requires resolving fine scale interfacial physics while simultaneously solving macroscopic flow and heat transfer. The moving interface, discontinuous material properties, and latent heat effects introduce numerical difficulties. Furthermore, incorporating contact angle dynamics and surface tension models adds additional complexity.

3. **FSI:** Traditional FSI simulations, especially those involving strongly coupled systems, are computationally expensive. The need for repeated mesh generation or complex mapping procedures between fluid and structural domains further increases the computational burden. For problems involving complex geometries or large structural displacements, efficient coupling strategies are essential.

4. **Unified Framework:** There is a need for a unified computational framework that can handle all three phenomena—multiphase flow, phase change, and FSI within a consistent numerical approach. Such a framework would enable the simulation of realistic engineering problems where these phenomena occur simultaneously.

The primary objective of this research is to develop and validate an advanced Lagrangian meshless computational framework capable of simulating complex multiphysics problems involving multiphase flows with sharp interfaces, phase change phenomena, and fluid-structure interactions. Specific objectives include:

1. Implement an efficient weakly coupled FSI solver using modal superposition techniques that leverages the Lagrangian nature of Lagrangian Differencing Dynamics (LDD) to achieve direct coupling without mesh mapping procedures.

2. Extend the LDD method to Multiphase Lagrangian Differencing Dynamics (MP-LDD) to handle multiphase flows with high density and viscosity ratios while maintaining sharp interfaces without numerical diffusion.

3. Develop and implement models for surface tension effects, and dynamic contact angle behaviour in the MP-LDD framework

4. Implementation of Implicit heat formation and Hierarchical Buoyancy Modelling Framework (HBMF) in the MP-LDD framework

5. Develop a phase change module within the MP-LDD framework to simulate boiling, condensation, and melting processes, incorporating interfacial phenomena such as surface tension and dynamic contact angles.

6. Validate each developed capability through comprehensive benchmark cases and, where possible, comparison with experimental data.

7. Demonstrate the applicability of the integrated framework to realistic engineering problems involving coupled multiphysics phenomena.

1.5.2 Hypotheses

H1: The integration of a two-way weakly-coupled modal solver with LDD enables efficient fluid-structure interaction (FSI)

H2: The variable Laplacian with second-order consistency and improved position-based dynamics accurately describes the sharp and precise interface modelling in LDD, resulting in accurate modelling of multiphase.

H3: Enthalpy-based phase change scheme in LDD enables the modeling of condensation and evaporation at the interfaces, including the latent heat during phase transitions

1.5.3 Scientific Contributions

1. The development of the integration method of the weakly coupled modal solver based on the superposition of modes using the Lagrangian Differentiating Dynamics (LDD) method

2. Extending the Lagrangian Differencing Dynamics (LDD) method into a novel Multiphase Lagrangian Differencing Dynamics (MP-LDD) with sharp interfaces and interface dynamics, without density and viscosity diffusion at the interfaces.

3. Development of a robust enthalpy-based phase model that provides accurate phase transitions (melting, solidification, evaporation) while maintaining numerical stability and computational efficiency.

1.5.4 Applications

The MP-LDD framework is designed to address a wide range of industrial, environmental, and scientific applications where multiphase flow and phase interactions are critical. Key applications include:

- **Spray Coating and Paintshop Processes:** Modeling of droplet formation, surface tension effects, dynamic wetting, and dip coating processes to improve uniformity and quality in automotive, aerospace, and electronics manufacturing.

- **Environmental and Underwater Engineering:** Simulation of sediment transport, oil spill dispersion, and multiphase wave interactions for environmental assessment and underwater engineering applications.

- **Droplet Manipulation and Injection Systems:** Simulation of droplet dynamics under surface tension, acoustic, electric, magnetic, and thermocapillary forces for applications in microfluidics, space, and precision fluid delivery systems.

- **Hydrogen Production and Storage:** Simulation of bubble dynamics and phase interfaces in water electrolysis, steam reforming, and hydrogen storage systems to optimize efficiency and ensure safe operation.

- **Gearbox Lubrication and Oil Distribution:** Analysis of oil flow in high-speed rotating gearboxes, including violent multiphase interactions, to optimize lubrication performance and reduce wear.
- **Biofouling and Hydrophobic Surface Design:** Investigation of fluid–solid interactions on hydrophobic and self-cleaning surfaces for marine, medical, and industrial applications to prevent fouling and improve longevity.
- **Additive Manufacturing and Laser Welding:** Modeling of molten metal flow, phase change, and surface tension effects in metal 3D printing, laser bed welding, and thermal processing to optimize manufacturing quality and reduce defects.

By targeting these application areas, the MP-LDD framework demonstrates its versatility and potential to serve as a high-fidelity, computationally efficient tool for advanced multiphase flow modeling across multiple industries and research domains.

1.6 Thesis Outline

This thesis is organized into nine chapters:
Chapter 1 Introduction provides an overview of multiphase flows, phase change phenomena, and fluid-structure interaction, along with the research motivation, objectives, hypotheses, scientific contribution and applications.
Chapter 2: Background and Literature Review presents a comprehensive review of existing numerical methods for multiphase flows, heat transfer and phase change, and fluid-structure interaction. The chapter identifies research gaps and highlights the implications of this work.
Chapter 3: Lagrangian Differencing Dynamics (LDD) Method describes the foundational LDD method, including governing equations, discretization techniques, the pressure Poisson equation formulation, and Position Based Dynamics(PBD) for point-cloud regularization.
Chapter 4: Fluid-Structure Interaction with Modal Coupling describes the development of the weakly coupled FSI solver, including modal superposition theory, the coupling algorithm, and validation through various FSI benchmark problems.
Chapter 5: Multiphase LDD with Sharp Interfaces presents the development of the Multiphase Lagrangian Differencing Dynamics (MP-LDD) method, including the variable coefficient Laplacian operator, density and viscosity treatment and interface handling techniques.
Chapter 6: Interface Dynamics Modeling provides the modelling of surface tension and dynamic contact angle in MP-LDD framework including formualtion and algorithm for interface dynamics.
Chapter 7: Heat Transfer and Phase Change Modeling details the extension of MP-LDD

to incorporate heat transfer, buoyancy and phase change phenomena, including formulation and algorithms for phase transitions.

Chapter 8: Validation and Verification summarizes, validation through benchmark cases for FSI, multiphase, interface dynamics and phase change

Chapter 9: Conclusions and Future Work summarizes the key findings and contributions of this research, discusses limitations, and provides recommendations for future research directions.

2 BACKGROUND AND LITERATURE REVIEW

This section provides a background and comprehensive review of existing numerical methods relevant to this research, covering meshless methods for computational fluid dynamics, multiphase flow modelling techniques, heat transfer and phase change simulation approaches, and fluid-structure interaction methods. The review identifies research gaps and positions the contributions of this thesis within the broader context of computational multiphysics.

2.1 Numerical Background

In computational fluid dynamics (CFD), accurate modelling of multiphase flow is fundamental for engineers and scientists aiming to reliably simulate complex systems. Traditional single-phase models often fall short in capturing the intricate interactions at phase boundaries and the unique phenomena associated with multiphase systems. To effectively simulate multiphase flows, specialized modeling techniques are necessary. These techniques must accommodate the distinct characteristics of each phase, account for interactions between phases, and manage the presence of phase interfaces. Recent research in this field has focused on developing robust, flexible, accurate and computationally efficient multiphase flow models that cater to the diverse needs of various applications, ranging from large-scale industrial processes to microscale biological environments.

2.1.1 Governing Equations

The mathematical model governing incompressible viscous fluid motion is based on the Navier–Stokes equations, which together ensure the conservation of mass and momentum. For an incompressible fluid, these governing equations take the following form:

$$\nabla \cdot \mathbf{u} = 0 \tag{2.1}$$

$$\frac{D\mathbf{u}}{Dt} = -\frac{1}{\rho}\nabla p + \nu\nabla^2\mathbf{u} + \mathbf{g} + \frac{1}{\rho}\mathbf{F}_{s+d} \tag{2.2}$$

where $\mathbf{u}$ denotes the fluid's velocity vector field, ρ is the fluid density, p represents the pressure field, ν is the fluid's kinematic viscosity, $\mathbf{g}$ is the gravitational acceleration vector,

and $\mathbf{F}_{s+d}$ represents the combined effect of surface tension and dynamic contact angle forces per unit volume.

The continuity equation (2.1) is a direct consequence of mass conservation applied to an incompressible medium. It enforces a zero-divergence condition on the velocity field, mathematically asserting that no net volumetric flux can accumulate at any point within the fluid domain, that is, the fluid neither compresses nor expands locally.

The momentum equation (2.2) which originates from Newton's second law applied to a fluid continuum, expressed within the Lagrangian reference frame, where the motion is tracked from the perspective of individual fluid particles rather than fixed spatial points. The left-hand side contains the material derivative operator D/Dt, which captures the total rate of change of velocity experienced by a fluid parcel as it travels through the flow field. This operator decomposes into two physically distinct contributions:

$$\frac{D\mathbf{u}}{Dt} = \underbrace{\frac{\partial \mathbf{u}}{\partial t}}_{\text{local acceleration}} + \underbrace{\mathbf{u}\cdot\nabla\mathbf{u}}_{\text{convective acceleration}} \tag{2.3}$$

The local acceleration term $\partial\mathbf{u}/\partial t$ reflects the temporal change in velocity at a fixed location in the domain, while the convective term $\mathbf{u}\cdot\nabla\mathbf{u}$ accounts for the spatial transport of momentum as fluid particles move from one region to another. Together, these two terms fully describe the inertial response of a fluid particle within the Lagrangian framework.

In equation (2.2)'s right-hand side, four distinct physical mechanisms govern the evolution of the momentum field. The pressure gradient term $-\frac{1}{\rho}\nabla p$ drives fluid motion from regions of elevated pressure toward regions of lower pressure. The viscous diffusion term $\nu\nabla^2\mathbf{u}$ represents the internal resistance to deformation arising from molecular friction within the fluid. The gravitational body force $\mathbf{g}$ acts uniformly throughout the fluid volume. Finally, $\frac{1}{\rho}\mathbf{F}_{s+d}$ incorporates interfacial effects at the free surface, specifically the influence of surface tension and the dynamic contact angle on fluid motion near solid boundaries or phase interfaces.

Pressure and Velocity Solution Procedure

Solving the coupled system of equations (2.1) and (2.2) for an incompressible flow requires the simultaneous determination of both the pressure and velocity fields across the discretized computational domain. Since no explicit time-evolution equation exists for pressure in the incompressible formulation, the pressure field is instead recovered through the Pressure Poisson Equation (PPE), obtained by taking the divergence of equation (2.2) and enforcing the incompressibility constraint:

This elliptic equation links the spatial distribution of pressure to the divergence of the acceleration field, and must be solved at every time step to ensure that the resulting velocity field remains divergence-free in accordance with the continuity constraint (2.1). Once the

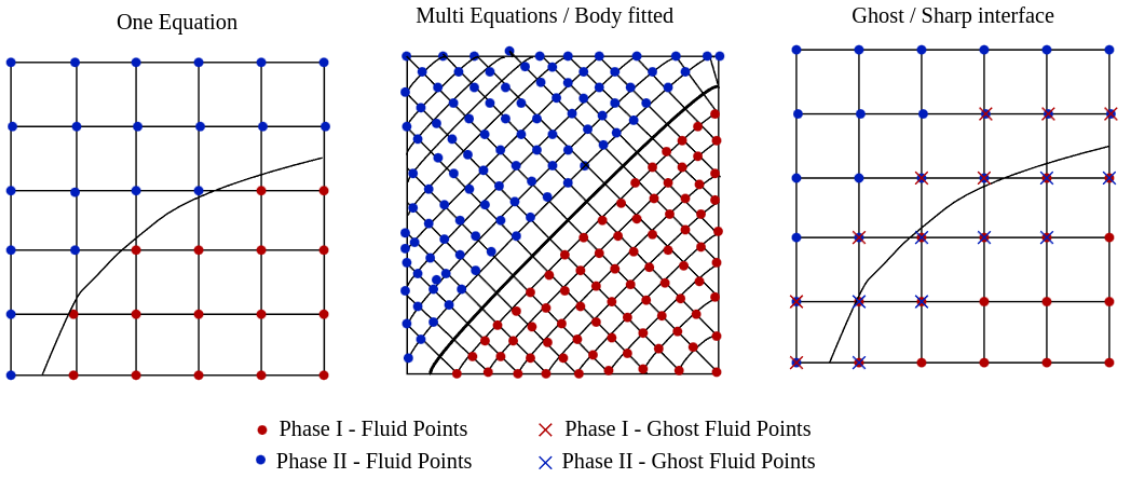

Figure 2.1. Representation of the domain to solve the NS for Multiphase flow. One equation Method (Left), Separate Equation for each phase is called Multi Equation (center), Ghost or sharp interface using ghost particles

pressure field is determined, the velocity field is advanced in time by integrating the full momentum equation 2.2

$$\frac{D\mathbf{u}}{Dt} = -\frac{1}{\rho}\nabla p + \nu\nabla^2\mathbf{u} + \mathbf{g} + \frac{1}{\rho}\mathbf{F}_{s+d} \tag{2.4}$$

This solution procedure forms the computational backbone of incompressible flow solvers and is central to the numerical framework employed in the present work.

2.1.2 Equation based formulation

One Equation Approach

The one equation approach models multiphase flows by treating the entire domain as a single fluid, solving a single set of Navier-Stokes Equations (2.2). The differences in density and viscosity across phases are incorporated through fluid properties that vary spatially, defined as functions of a scalar field (e.g., volume fraction) [8, 9, 10, 11, 12]. Interface effects like surface tension are included by adding terms in the momentum equations to account for interfacial forces. This approach avoids explicitly tracking the interface, making it computationally efficient for complex flows. It can capture the behavior of interfaces in situations where phases do not separate sharply. Diffuse interfaces can arise, leading to a loss of sharpness in representing phase boundaries, especially for high-density ratio flows. Surface tension effects can be challenging to model accurately without a fine grid resolution in gird based methods. However, this can be easily adapted for the Lagrangian methods [13, 14]. Representation of the domain to solve the NS is shown in Figure 2.1.

Multi Equation Approach

For each phase, separate Navier-Stokes Equations (2.2) are solved, and conditions at the interface are applied to maintain continuity between two phases as below:

$$[\mathbf{u}_1 - \mathbf{u}_2] = 0 \quad \text{at the interface.} \tag{2.5}$$

Where,

- $\mathbf{u}_1$ is phase one velocity
- $\mathbf{u}_2$ is phase two velocity

It is best suited for cases where interfaces experience mild deformation. This method captures sharp interfaces precisely, providing high accuracy in phase boundary representation. Interface dynamics, including surface tension and phase changes, can be directly applied with continuity and boundary conditions [15, 16, 17, 18]. In Eulerian-based methods, It is achieved using body grid methods as shown in Figure 2.1.

Ghost Fluid Method or Sharp Interface Methods

Sharp-interface techniques like the Ghost Fluid Method (GFM), represent the interface between phases on a structured grid and use "ghost nodes" to capture discontinuities across the interface in the Eulerian method. These ghost nodes allow the method to interpolate values across the interface, avoiding the need for re-meshing while retaining a sharp interface. In Lagrangian methods, ghost particles are created by projection with respect to interface and compact radius. These methods solve the Navier-Stokes Equations (2.2) separately in each phase but include ghost nodes as shown in Figure 2.1 , across the interface to handle discontinuities with ghost node values enforcing jump conditions [19, 20, 21, 22, 23, 24].

$$\left[\rho \frac{\partial \mathbf{u}}{\partial t}\right]_{\text{across interface}} = -\nabla p + \text{surface tension terms}, \tag{2.6}$$

2.1.3 Classification of Multiphase Modeling Techniques

Multiphase flow modeling encompasses various approaches, each tailored to specific applications and physical phenomena. The classification of these techniques can be broadly categorized into three primary groups: Molecular Modeling, Macroscopic Modeling, and Mesoscopic Modeling. Each category employs different methodologies and computational strategies to capture the complexities of multiphase interactions. Figure 2.2 presents a multiscale approach for modeling fluids across different time and length scales. At the smallest, quantum scale, atomic-level interactions are studied, focusing on electronic configurations. Moving up, the molecular scale models individual molecules and their dynamics, while the

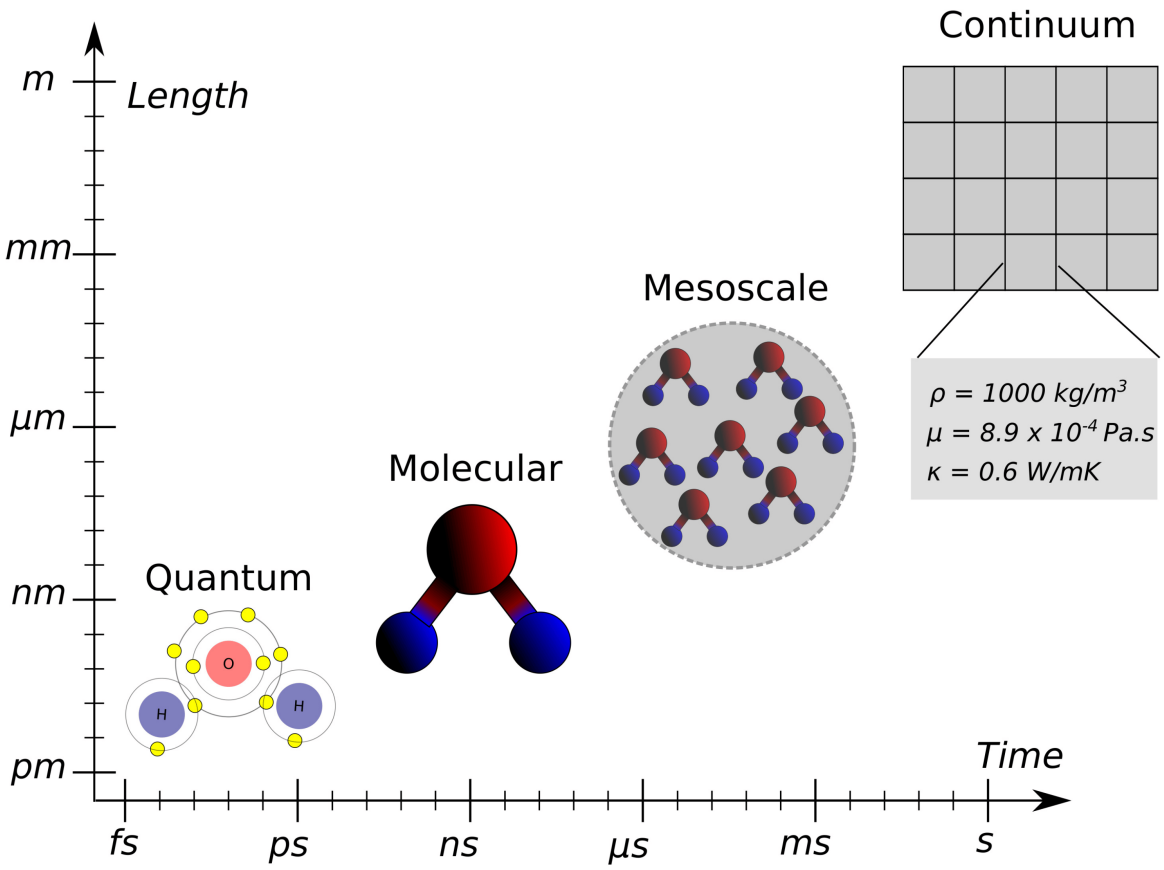

Figure 2.2. Multiscale Modeling Framework for Fluid Systems

mesoscale groups collections of molecules, often using simplified methods to capture collective behavior like diffusion. At the largest, continuum scale, fluid properties are represented as averaged quantities (e.g., density, viscosity, and thermal conductivity), allowing for efficient modeling of large-scale fluid behavior. This framework enables selecting appropriate modeling techniques based on the scale of interest [25]. Complete overview of multiphase modelling is shown in Figure 2.3.

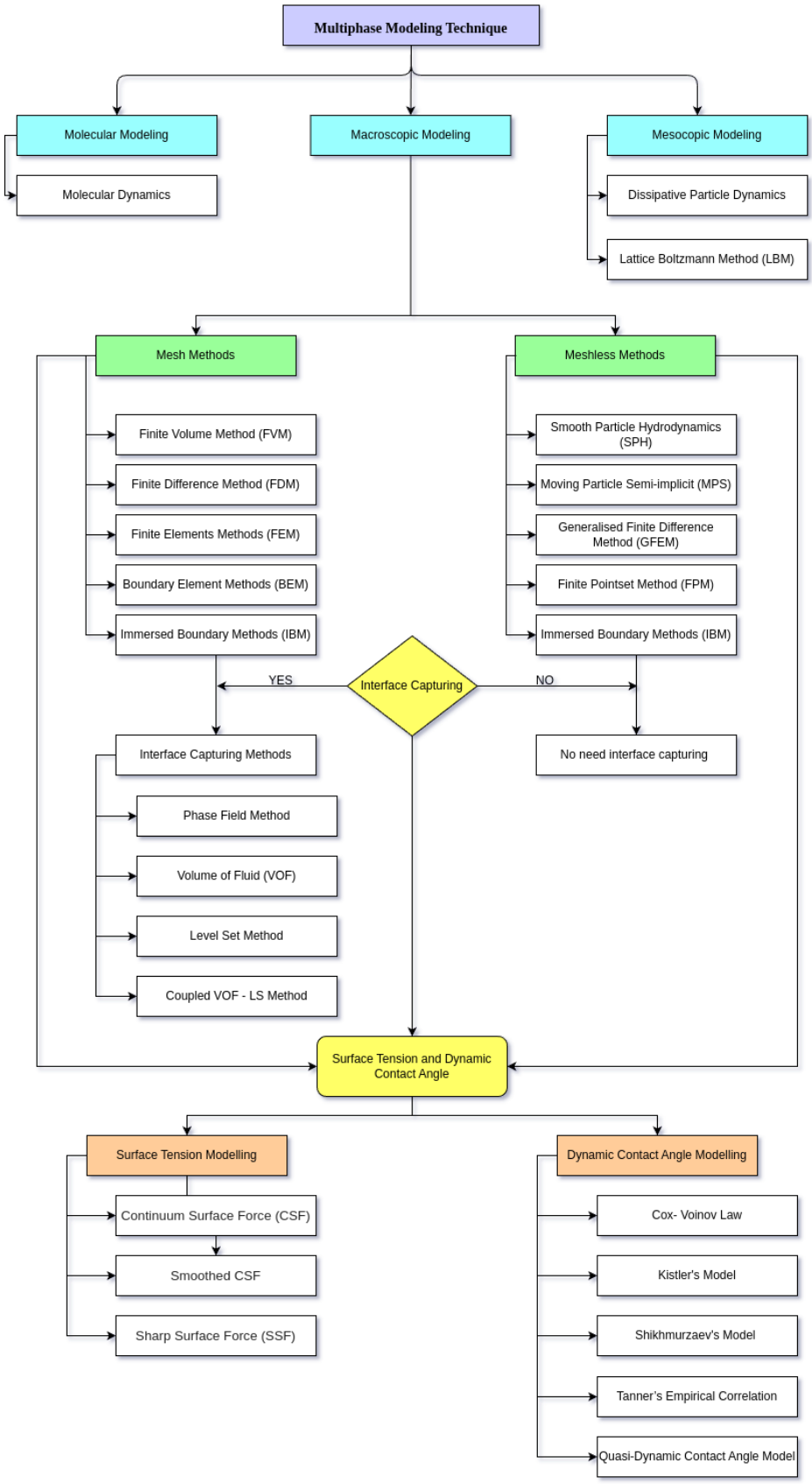

Figure 2.3. A detailed overview of Multiphase Modelling and Methods

Molecular Modeling

Molecular modeling techniques focus on the fundamental interactions between molecules and are particularly useful for understanding phenomena at the nanoscale. This helps in understanding processes like diffusion, wetting, and nanoscale fluid behavior in pores.

Molecular Dynamics (MD): This method simulates the physical movements of atoms and molecules over time, providing insights into the properties of materials and interactions at the molecular level. However, MD is computationally intensive and not suitable for large-scale systems.

Mesoscopic Modeling

Mesoscopic modeling bridges the gap between molecular and macroscopic approaches, capturing essential features of multiphase flows without resorting to molecular details.

Dissipative Particle Dynamics (DPD): It employs a particle-based approach that simulates interactions while embedding key macroscopic properties, enabling complex fluid dynamics without molecular-level resolution. DPD is useful for simulating soft matter and complex fluids. It is commonly applied in polymer science and biological simulations.

Lattice Boltzmann Method (LBM): Mesoscale kinetic theory technique simulating fluid flow while effectively handling complex boundaries and interfaces. Commonly applied in porous media, multiphase flows, and microfluidics.

Macroscopic Modeling

Macroscopic approach, which treats multiphase flows as continuous fields governed by partial differential equations. These models work at scales where continuum assumptions hold, allowing the phases to be treated as continuous, interpenetrating media. Macroscopic models are used extensively in industrial and environmental simulations, where large-scale flows and bulk properties are more important than individual particle interactions. It is widely classified as Mesh methods and Meshless methods.

Mesh Methods: Mesh or Grid based methods are numerical techniques employed to solve Partial Differential Equations (PDEs) by discretizing the continuous space into a grid or mesh of points or cells as shown in Figure 2.4 . This discretization facilitates the approximation of continuous variables at specific locations, transforming the governing equations into a set of algebraic equations that can be solved numerically. By utilizing appropriate numerical schemes, the derivatives in the equations are estimated based on the values of neighboring grid points. These methods are versatile and adaptable, making them suitable for a wide array of applications in fluid dynamics, heat transfer, and structural analysis. Accurate specification of boundary and initial conditions is critical, as these significantly influence the solution. Overall, grid-based methods provide a systematic and efficient approach to analyzing complex physical phenomena across various scientific and engineering fields.

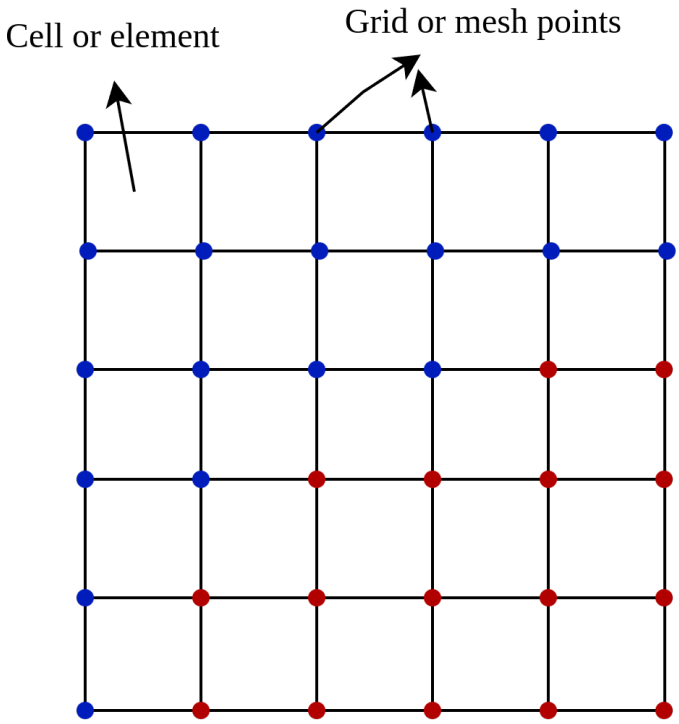

Figure 2.4. Representation of domain with mesh or grid for the mesh-based method

Finite Volume Method (FVM): The Finite Volume Method (FVM) is a robust numerical technique widely used to approximate solutions to partial differential equations, particularly in computational fluid dynamics (CFD) and heat transfer problems. This method divides the spatial domain of interest into small, discrete control volumes, each centered around a grid point. Within each control volume, integral conservation laws are applied for fundamental quantities such as mass, momentum, and energy. This framework ensures that the flux of a conserved quantity across the boundaries of each control volume is balanced, thereby upholding the physical principles of conservation throughout the simulation. In FVM, differential equations are transformed into algebraic equations by integrating over each control volume, simplifying complex partial differential equations that can then be solved iteratively. The adaptability of FVM allows it to manage irregular, non-uniform meshes and boundary conditions, which often arise in real-world applications. Its conservative nature makes it particularly effective for simulating flows with high accuracy across boundaries, even in complex geometries. The combination of flexibility, accuracy, and adherence to conservation principles positions the FVM as a preferred choice in engineering and scientific applications, where precise modeling of fluid flow, thermal transfer, and other transport phenomena is essential.

Finite Difference Method (FDM): The Finite Difference Method (FDM) is a numerical technique utilized to solve differential equations by approximating them with difference

equations. This method is particularly beneficial for analyzing problems in computational fluid dynamics, heat conduction, and other domains governed by partial differential equations. FDM operates by discretizing the continuous domain into a grid, where derivatives are substituted with finite differences, enabling the transformation of differential equations into algebraic equations. In FDM, continuous variables are represented at specific nodal locations, and derivatives there are estimated through are approximated using Taylor series expansions or simple difference formulas. For example, the first derivative can be approximated by the forward or backward difference, while higher-order derivatives may be represented using central differences. This results in a linear system of equations solvable iteratively or directly, contingent on the problem's complexity. One of the primary advantages of FDM is it's straightforward implementation and ease of use, especially for problems defined on structured grids. However, challenges may arise when dealing with complex geometries and irregular domains, where maintaining accuracy can be difficult. Despite these limitations, FDM remains a widely adopted approach due to its effectiveness in addressing time-dependent problems, offering good accuracy for smooth solutions, and providing a clear framework for both steady-state and transient analyses. It's versatility and relative simplicity render it a valuable tool in engineering and scientific research for modeling various physical phenomena.

Finite Element Method (FEM): The Finite Element Method (FEM) is a powerful numerical technique extensively employed in computational fluid dynamics (CFD) for solving complex partial differential equations that characterize fluid flow, heat transfer, and other physical phenomena. Unlike methods that utilize structured grids, FEM divides the computational domain into a mesh of small, simple shapes called elements, which can take various geometries (e.g., triangles or quadrilaterals in two dimensions, or tetrahedra or hexahedra in three dimensions). This flexibility enables FEM to effectively tackle complex geometries and boundary conditions frequently encountered in engineering applications. In FEM, governing differential equations are transformed into a weak formulation through the application of variational principles. Within each element, shape functions are defined to approximate the solution locally. By integrating the governing equations over each element and applying the relevant boundary conditions, a system of algebraic equations is derived. These equations are then assembled into a global system representing the entire computational domain. The solution is obtained using numerical techniques, such as the Newton-Raphson method or iterative solvers, to resolve the resulting system of equations. A significant advantage of FEM in CFD is, it's capability to accurately model complex flow phenomena, including turbulence, phase interactions, and fluid-structure interactions. The method's adaptability to varying mesh densities allows for localized refinement, where a greater number of elements are utilized in regions with high gradients or complexity, thereby enhancing solution accuracy. Moreover, FEM is particularly well-suited for problems involving nonlinear behavior and transient dynamics, making it a popular choice for simulating real-world fluid dynamics

scenarios in fields such as aerospace, automotive, and biomedical engineering. It's robustness, flexibility, and accuracy position the FEM as an essential technique for fluid system evaluation and engineering design.

Boundary Element Method (BEM): The Boundary Element Method (BEM) is a numerical technique employed to solve partial differential equations relevant to various engineering and physical applications, especially in fluid dynamics, heat transfer, and structural analysis. Unlike traditional methods that require full discretization of the entire volume of the domain, BEM focuses on the boundaries of the domain, significantly reducing the problem's dimensionality. This approach proves particularly efficient for problems involving infinite or semi-infinite domains, such as potential flow around objects or heat conduction in semi-infinite media. In BEM, the governing equations are reformulated in terms of boundary integrals, utilizing the boundary conditions of the problem to express the solution. The domain is divided into boundary elements, with the unknowns typically represented by interpolating functions over these boundaries. By applying integral equations derived from the governing differential equations, a system of equations is generated that correlates the unknown boundary values to the known boundary conditions. Solving this system yields the values at the boundaries, from which the solution in the entire domain can be reconstructed. A primary advantage of BEM is its capacity to accurately model problems with complex geometries and boundary conditions without requiring a dense mesh throughout the entire domain. Consequently, this results in fewer degrees of freedom compared to volume-based methods like FEM or FVM, thereby reducing computational cost and time. BEM is particularly effective for steady-state problems and those involving linear differential equations. However, it may be less efficient for nonlinear problems and may necessitate special handling for non-homogeneous boundary conditions.

Immersed Boundary Method (IBM): The Immersed Boundary Method (IBM) is a numerical technique utilized to simulate fluid flow in the presence of complex, moving geometries. This method is particularly advantageous in CFD for scenarios involving fluid-structure interactions, such as biological systems (e.g., blood flow around heart valves or fish swimming) and engineering applications (e.g., flow over airfoils or the motion of flexible structures). In IBM, the fluid domain is typically represented on a fixed Cartesian grid, while the solid boundaries are immersed within this grid. The fundamental concept is to impose the effects of the immersed boundaries on the surrounding fluid flow without conforming the grid to the shape of the object. This is achieved by employing special forcing terms in the Navier-Stokes equations that represent the boundary conditions at the interface between the fluid and the solid. Consequently, the immersed boundaries exert forces on the fluid, which are incorporated into the governing equations, enabling effective interaction between the fluid and the boundaries. A notable advantage of the Immersed Boundary Method is its capability to manage complex geometries and moving interfaces without the computational overhead associated with mesh generation and refinement, common in traditional methods like the

FEM or FVM. In addition, IBM can easily accommodate substantial boundary deformations, making it suitable for simulating flexible structures and dynamic interactions. However, the accuracy of the method can be influenced by the choice of forcing functions and the grid resolution, particularly near the boundaries. Therefore, careful consideration of grid size and numerical scheme is essential to ensure accurate capture of interactions between the fluid and immersed boundaries.

Meshless Methods: Meshless methods represent a class of numerical techniques utilized to solve Partial Differential Equations (PDEs) without relying on a predefined grid or mesh as shown in Figure 2.5 . This allows for greater flexibility in handling complex geometries and dynamic problems. Instead of discretizing the domain, meshless methods utilize a set of scattered points within the computational domain to represent the solution. They approximate the governing equations by constructing local or global shape functions based on the values at neighboring points, enabling the computation of derivatives and integrals directly from the scattered data. This approach is particularly beneficial for problems involving large deformations, moving boundaries, or evolving interfaces, as it mitigates issues related to mesh generation and refinement. Meshless methods are increasingly employed in various fields, including fluid dynamics, structural analysis, and material science, offering a powerful alternative to traditional mesh-based techniques for simulating complex physical phenomena. A detailed summary is provided in Table 2.1.

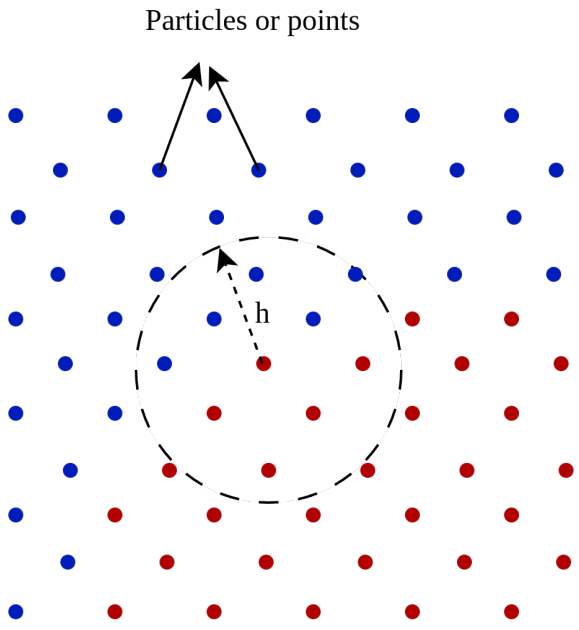

Figure 2.5. Representation of the domain with particles or points for the meshless method

Smoothed Particle Hydrodynamics (SPH): SPH is a meshless, Lagrangian numerical method employed to simulate fluid flows and various continuum mechanics phenomena. Ini-

tially developed for astrophysical applications, SPH has gained prominence in diverse fields such as fluid dynamics, geophysics, and biomechanics due to its capability to effectively handle complex fluid interfaces and free surfaces. In SPH, the fluid is represented by a discrete set of particles, each possessing properties such as mass, position, velocity, and other relevant physical characteristics. The interactions between particles are governed by a kernel function that calculates the influence of neighboring particles. This smoothing approach enables the approximation of continuous fields, including density and pressure, without the necessity of a fixed grid. A primary advantage of SPH lies in its flexibility to manage large deformations, free-surface flows, and complex boundary conditions, rendering it well-suited for simulating phenomena such as fluid fragmentation, mixing, and solid-fluid interactions. Moreover, the absence of a mesh alleviates complications associated with mesh generation and refinement, particularly in dynamic simulations where the fluid domain may undergo significant alterations over time. Nonetheless, SPH is not without challenges, particularly concerning numerical stability. Maintaining accuracy during high-velocity impacts or in scenarios with strong gradients can be problematic. To address these issues and enhance the method's performance, various enhancements have been proposed, including kernel corrections and multi-resolution techniques.

Moving Particle Semi-Implicit (MPS): The MPS method is a numerical approach employed for simulating fluid flows and dynamic phenomena, with particular emphasis on free-surface flows and fluid-structure interactions. As a meshless Lagrangian technique, MPS does not rely on a fixed grid or mesh, providing enhanced flexibility in managing complex geometries and large deformations. In the MPS framework, fluid is represented by a collection of moving particles, each characterized by properties such as mass, position, velocity, and density. The interactions among these particles are computed utilizing a semi-implicit scheme that improves numerical stability. This method integrates explicit and implicit time-stepping techniques to solve the governing equations of fluid motion, allowing for effective management of stability during time integration—particularly beneficial when employing large time steps in dynamic simulations. A notable advantage of MPS is its efficacy in modeling free-surface flows, making it suitable for applications such as dam break simulations, sloshing in tanks, and other scenarios involving fluid motion and interfaces. Furthermore, the method can accommodate complex boundary conditions and moving objects with relative ease, a significant advantage over traditional mesh-based methods. Despite its merits, MPS faces limitations concerning particle distribution and potential numerical instability under certain conditions. Ongoing research seeks to enhance the robustness of the method through optimized particle arrangements and correction schemes aimed at improving accuracy.

Generalized Finite Difference Method (GFDM): GFDM utilizing meshless interpolation combine the advantages of finite difference techniques with the flexibility of meshless approaches for solving partial differential equations. In this framework, traditional finite difference schemes are generalized to accommodate irregular point distributions, allowing for

more accurate derivative approximations without a fixed grid. Meshless interpolation techniques, such as Moving Least Squares (MLS) or radial basis functions, are employed to estimate field variables at non-grid points, enhancing the method's adaptability to complex geometries and boundary conditions. This approach proves particularly beneficial for simulating problems characterized by evolving interfaces or irregular domains, providing a robust and flexible tool applicable across a diverse range of fields, including fluid dynamics, heat transfer, and material science.

Finite Pointset Method (FPM): The FPM is a meshless numerical technique utilized for solving partial differential equations by representing the domain with a discrete set of points. In contrast to traditional mesh-based methods, FPM does not rely on a predefined mesh, allowing for enhanced flexibility in addressing complex geometries and dynamic interfaces. Within the FPM framework, the governing equations are solved by approximating field variables at pointset locations using local polynomial or radial basis function interpolations. The method incorporates a background grid to facilitate derivative integration and enforce boundary conditions. FPM is particularly well-suited for scenarios involving large deformations, fluid-structure interactions, and free-surface flows, establishing it as a valuable tool in engineering and scientific research for simulating intricate physical phenomena without the complications associated with mesh generation and refinement.

Interface Tracking Methods for Grid Based Method

In grid-based methods for multiphase flow simulation, accurately tracking the interface between different phases is essential for capturing interfacial dynamics and phase interactions. The interface represents the boundary where properties like density, viscosity, and surface tension can vary sharply, and its accurate tracking is crucial to avoid artificial mixing and ensure realistic simulations. Several approaches are employed as shown in Figure 2.6 to handle this challenge, each with unique strengths and limitations. A detailed summary is provided in Table 2.2.

Phase-Field Method: The Phase-Field method captures the interface between two fluid phases by representing it as a diffuse transitional zone rather than an infinitely thin boundary. A scalar order parameter, referred to as the phase field, is introduced to characterise this transition, varying continuously from one bulk phase value to the other across the interfacial region. The dynamics of this order parameter are governed by the Cahn-Hilliard equation, which describes the thermodynamic forces driving interface motion and deformation. A key advantage of this diffuse interface representation is its inherent ability to handle complex topological changes such as droplet merging and breakup, without requiring explicit interface reconstruction. However, maintaining a physically representative interface thickness demands sufficient mesh refinement in the interfacial region, which increases the computational cost of the simulation.

Volume of Fluid (VOF) Method: The Volume of Fluid (VOF) method is one of the

Table 2.1. Summary of meshless methods.

Feature	SPH	MPS	GFDM	FPM
Basic Concept	Interpolates physical quantities using smoothing kernels	Solves NS equations with semi-implicit formulations	Approximates derivatives using weighted least squares	Uses Taylor expansions for point cloud data
Domain Rep.	Lagrangian particles	Lagrangian particles	Arbitrary point clouds (no connectivity)	Arbitrary point clouds (no connectivity)
Conservation	Good mass conservation, challenges in momentum and energy	Good mass conservation, handles pressure better than SPH	Conservation depends on weighting functions	Conservation depends on Taylor series accuracy
Boundaries	Requires special techniques (ghost particles, kernel corrections)	Requires special boundary particles	Requires explicit boundary conditions	Handles boundaries with high flexibility
Diffusion	Moderate (depends on kernel and radius)	Low (better pressure calculations)	Depends on weighting schemes	Low (accurate derivative computation)
Accuracy	Moderate, sensitive to kernel choice and particle distribution	Moderate to high	High, flexible accuracy with higher-order derivatives	High, flexible accuracy for well-distributed points
Cost	Moderate to high	Moderate to high	High (matrix assembly for weights)	High (matrix operations for Taylor expansions)
Flexibility	Fully meshless, ideal for free-surface flows	Fully meshless, ideal for incompressible flows	Fully meshless, suitable for arbitrary geometries	Fully meshless, suitable for arbitrary geometries
Applications	Free-surface flows, astrophysics simulations	Incompressible flows, multiphase flows	General CFD, heat transfer, elasticity	General CFD, aeroacoustics, multiphysics
Advantages	Handles large deformations and free surfaces	Stable pressure and incompressible flows	High flexibility and accuracy for arbitrary geometries	High flexibility and accuracy for arbitrary geometries
Disadvantages	Sensitive to particle distribution, kernel choice	High computational cost for large systems	High computational cost, complex weighting schemes	High computational cost, complex setup for Taylor expansions

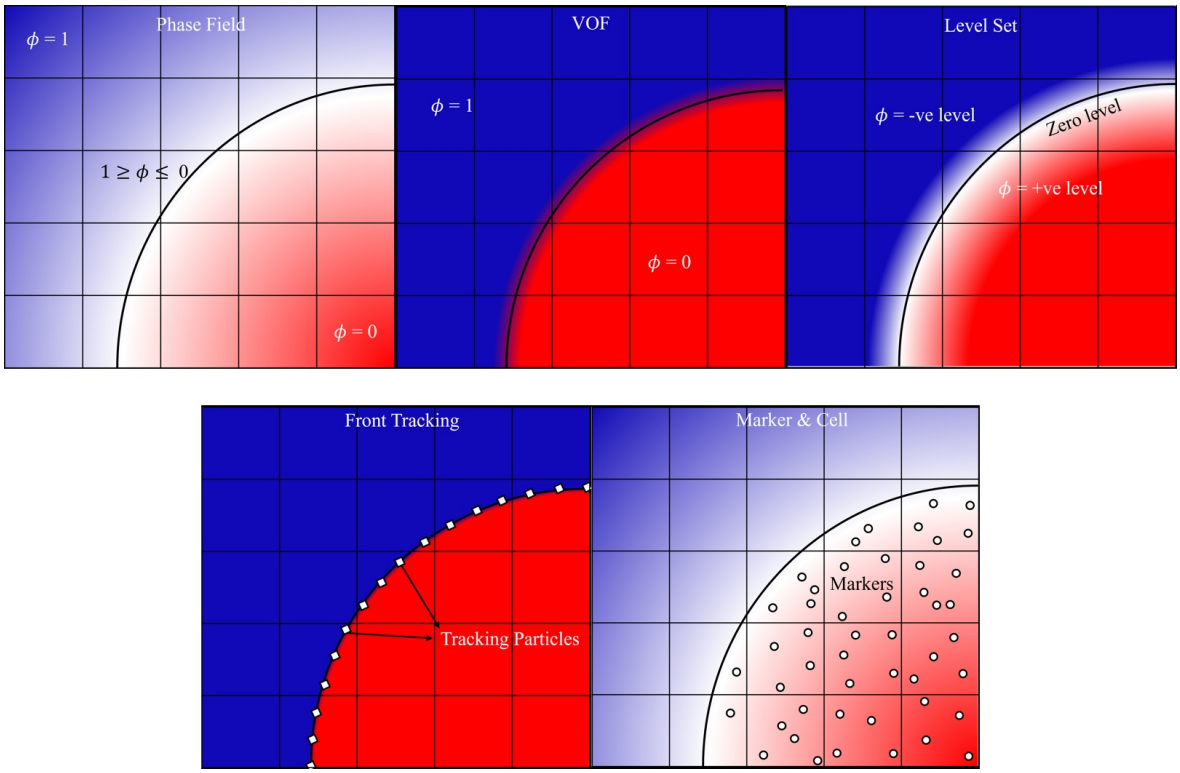

Figure 2.6. Interface tracking methods for gird based methods. Phase field: Diffuse (controlled by interface width), VOF: Diffuse (over a few cells), Level set: Sharp, but smeared numerically, Marker and cell: Diffuse using markers and Front tracking: Sharp interface using Lagrangian particle

most widely adopted interface capturing techniques in grid-based computational fluid dynamics, particularly for multiphase flow simulations involving large interfacial deformations. The method operates by assigning a volume fraction field to each computational cell, representing the proportion of that cell occupied by a given fluid phase. This scalar quantity is bounded between zero and unity, where a value of zero or one indicates a cell fully occupied by a single phase, and intermediate values identify cells containing the interface. To recover a geometrically meaningful representation of the interface from this discontinuous field, reconstruction algorithms such as the Piecewise Linear Interface Calculation (PLIC) are commonly employed to approximate the local interface orientation and position within each interfacial cell. The VOF method inherently conserves mass, making it well suited for simulations involving violent interfacial events such as wave breaking, droplet impact, and jet fragmentation. A recognised limitation, however, is the tendency for numerical diffusion to smear the interface across several cells, particularly in high-resolution computations, which can compromise the sharpness and geometric fidelity of the captured interface.

Level Set Method: The Level Set method provides an implicit framework for interface capturing in multiphase flow simulations, representing the interface through a signed distance function. In this formulation, the magnitude of the function at any point in the domain corresponds to its shortest Euclidean distance to the interface, with the sign convention as-

signing positive values to one fluid phase and negative values to the other. The interface is consequently defined as the zero isocontour of this function, that is, the locus of points where the signed distance equals zero. This implicit representation offers a natural and computationally convenient means of handling complex interfacial geometries and topological transitions, such as interface merging and fragmentation, without requiring explicit tracking or reconstruction. The temporal evolution of the interface is governed by the Level Set transport equation, which advects the signed distance function according to the underlying velocity field. Despite providing a smooth and well-defined interface, the method is susceptible to numerical drift in the signed distance property over successive time steps. To restore this property, periodic reinitialization of the Level Set function is required, a process that can introduce localised errors in the interface position and, in some cases, compromise the overall mass conservation of the simulation.

Front-Tracking Method: Front tracking technique explicitly tracks the interface by using a separate set of markers or an independent mesh, typically represented as a collection of points or segments that define the interface boundary. These markers move along with the fluid velocity and are coupled with the Eulerian grid used for the fluid flow. This method maintains a highly accurate, sharp interface, making it especially useful for simulations involving surface tension and fine-scale interfacial details. However, the front-tracking method is computationally intensive, as it requires managing the interface markers separately and addressing complex topological changes, like breakup and merging events. Despite these challenges, the front-tracking method is often chosen when a precise interface representation is needed for detailed interfacial phenomena.

Marker-and-Cell (MAC) Method: The Marker-and-Cell (MAC) method is an interface tracking technique that employs marker particles to distinguish different fluid regions and locate the interface. These particles are advected with the flow, marking the regions occupied by each phase, which helps in maintaining a sharp interface. The particle information is coupled with a grid-based solver that calculates fluid properties across the domain. The MAC method is mainly applicable for simulating free surface flows and it naturally captures the dynamic interface between the phases. However, it can be computationally demanding since it requires a high density of marker particles near the interface to maintain accuracy, which increases the computational load for high-resolution simulations.

2.1.4 Surface Tension

Surface tension arises where two immiscible phases meet, such as at a water–air boundary, as illustrated in Figure 2.7. It originates from the imbalance of cohesive intermolecular forces experienced by molecules residing at the interface. Unlike bulk molecules, which are uniformly surrounded by neighbouring molecules and experience balanced attractive forces, interfacial molecules lack neighbours on one side, resulting in a net inward pull toward the

Table 2.2. Detailed summary of interface tracking methods for grid-based methods. Phase field: Diffuse (controlled by interface width), VOF: Diffuse (over a few cells), Level set: Sharp, but smeared numerically, Marker and cell: Diffuse using markers and Front tracking: Sharp interface using Lagrangian particle.

Feature	Front Tracking	Marker-and-Cell (MAC)	Phase-Field Method	Volume of Fluid (VOF)	Level Set Method
Interface Representation	Explicit (Lagrangian markers)	Implicit (tracer particles)	Implicit (Cahn-Hilliard equation)	Implicit (volume fraction)	Implicit (distance function)
Interface Sharpness	Sharp, well-maintained	Diffuse	Diffuse (controlled by interface width)	Diffuse (over a few cells)	Sharp, but smeared numerically
Grid Setup	Eulerian + Lagrangian mesh	Eulerian (staggered grid)	Eulerian (uniform grid)	Eulerian (uniform grid)	Eulerian (uniform grid)
Handling of Surface Tension	Accurate	Less accurate	Accurate (surface tension in free energy)	Less accurate (special techniques required)	Accurate (gradient-based)
Numerical Diffusion	Minimal at interface	Higher at interface	Controlled by interface width	Moderate (depends on advection scheme)	Moderate (depends on reinitialization)
Complex Interface Topology	Challenging (merging/splitting)	Challenging	Easy (naturally handled by diffuse interface)	Easy (automatic via volume fractions)	Easy (automatic via level set evolution)
Mass Conservation	Good	Good	Poor (not strictly conserved)	Excellent (strictly conserved)	Poor (not strictly conserved)
Computational Cost	Moderate	Low	High (additional equations)	Moderate	High (additional equations)
Physical Basis	Explicit tracking via markers	Particle-based advection	Thermodynamic free energy	Volume fraction advection	Distance function advection
Applications	Sharp interface flows, high surface tension effects	General incompressible flows	Multiphase flows with diffuse interfaces	Multiphase flows with strict mass conservation	Multiphase flows requiring sharp interfaces

bulk liquid. This force imbalance causes the interface to contract and behave analogously to an elastic film under tension, which acts to reduce the total interfacial area. Surface tension is measured as the force acting per unit length along the interface, with SI units of N/m, and can be connected to the interfacial surface energy as shown below:

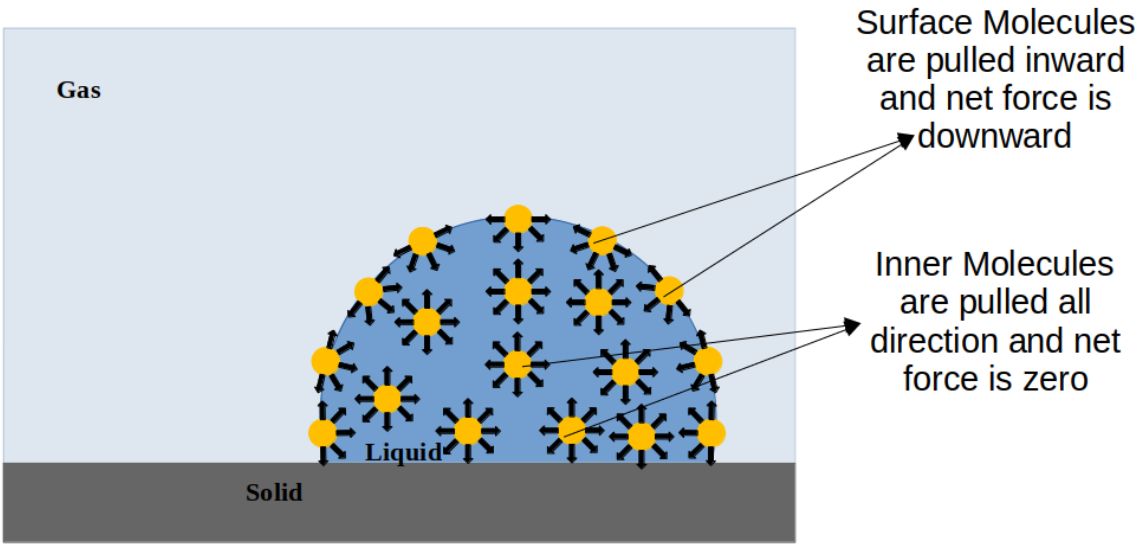

Figure 2.7. Representation of surface tension on a liquid-air system.

$$\text{Surface energy} = \mathbf{F}_s \times \text{Area} \tag{2.7}$$

Surface tension therefore represents the interfacial energy per unit area at the phase boundary. It governs several physically important phenomena in multiphase flows, including droplet formation, capillary wave propagation, and interfacial stability. Several approaches have been developed within the CFD framework to model surface tension forces, the most prominent of which will be outlined in the sections that follow.

Continuum Surface Force (CSF)

The Continuum Surface Force (CSF) method, introduced by Brackbill et al. [26], reformulates surface tension as a volume-distributed force acting on the fluid spread throughout the interfacial region. The surface tension as a body force acting through the volume is expressed as:

$$\mathbf{F}_s = \sigma\kappa\mathbf{n} \tag{2.8}$$

where σ is the surface tension coefficient, $\mathbf{n}$ is the unit normal vector to the interface, and κ is the local interface curvature. The curvature is evaluated from the divergence of the interface unit normal:

$$\kappa = \nabla \cdot \mathbf{n} \tag{2.9}$$

In practice, the normal vector and curvature are typically derived from the gradients of a phase indicator function, such as a level set or phase field variable.

Smoothed Continuum Surface Force (Smoothed CSF)

The Smoothed CSF method extends the standard CSF approach by distributing the surface tension force over a finite region surrounding the interface rather than concentrating it at the interface itself. This is achieved through the application of a smoothing weighting function $W(\mathbf{r})$:

$$\mathbf{F}_s = \int_{\Omega} \sigma \kappa \mathbf{n} W(\mathbf{r} - \mathbf{r}')\, d\mathbf{r}' \tag{2.10}$$

where Ω denotes the domain surrounding the interface, $W(\mathbf{r} - \mathbf{r}')$ is the smoothing weighting function, $\mathbf{r}$ is the position vector of the neighbouring point, and $\mathbf{r}'$ is the position vector of the evaluation point. This smoothed formulation reduces numerical oscillations near the interface and improves overall simulation stability.

Sharp Surface Force (SSF)

The Sharp Surface Force (SSF) method applies surface tension directly at the interface without any smoothing, making it suitable for simulations where a well-defined sharp interface must be preserved. The surface tension force per unit volume is formulated using a Dirac delta function $\delta(\phi)$ to confine the force strictly to the interfacial region:

$$\mathbf{F}_s = \sigma \kappa \delta(\phi) \nabla \phi \tag{2.11}$$

Alternatively, the force can be expressed using a Heaviside function $H(\phi)$ that distinguishes between the two fluid phases:

$$\mathbf{F}_s = \sigma \kappa \nabla H \tag{2.12}$$

2.1.5 Dynamic Contact Angle (DCA)

The contact angle is established at the boundary of three-phases: a liquid, a solid, and a gas that are present in phase that meet simultaneously, as illustrated in Figure 2.8. It serves as a quantitative measure of the wettability of a solid surface by a liquid, reflecting the balance of intermolecular forces acting at the interface. A liquid droplet resting on a solid substrate forms a measurable angle between the liquid-gas interface and the solid surface, the magnitude of which characterises the degree of liquid-solid interaction. This parameter finds

practical relevance in numerous industrial applications, including the formulation of coatings, inks, and adhesives, where the spreading behaviour of a liquid on a substrate directly influences product performance. Based on the magnitude of the contact angle, the interaction

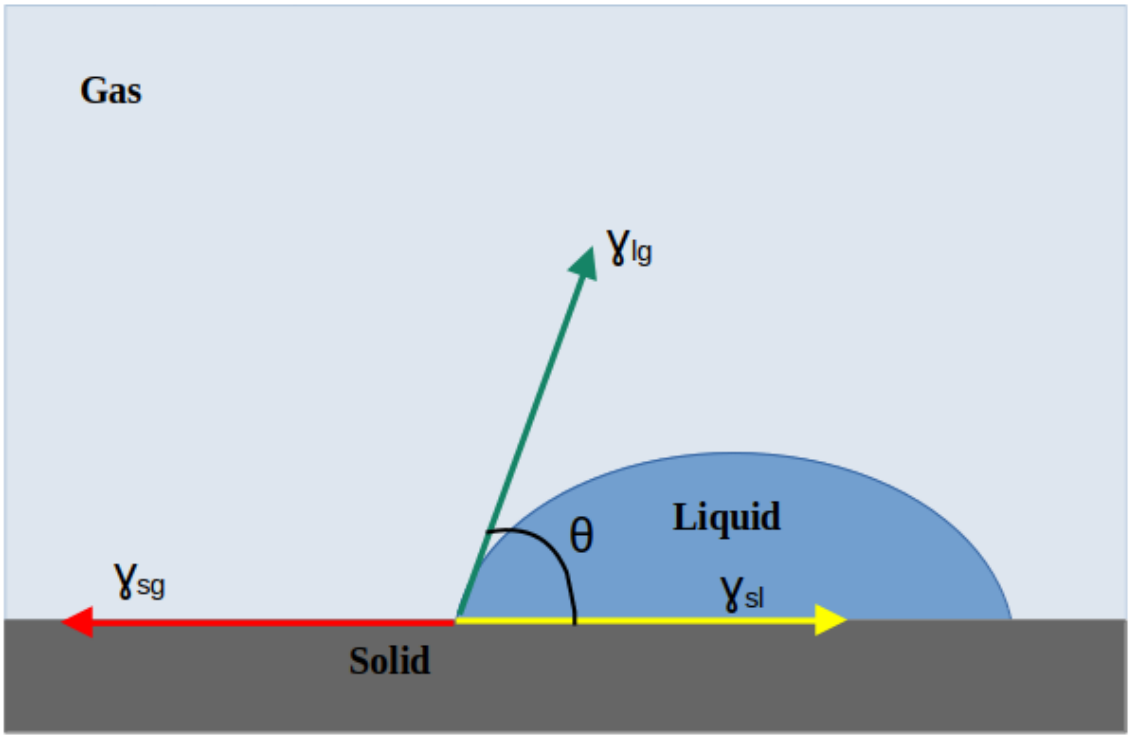

Figure 2.8. Representation of contact angle at the three-phase boundary point

between a liquid and a solid surface can be grouped into two broad categories:

1. **Non-wetting:** The contact angle is close to 180°, meaning the liquid tends to stay in droplet form and does not spread across the surface.

2. **Wetting:** The contact angle is close to 0°, meaning the liquid fully covers the surface, a phenomenon referred to as "perfect" or "complete" wetting.

Wettability varies inversely proportional to the contact angle: as the angle decreases, wettability increases. For most real-world cases, the contact angle lies between 0° and 180°. When $\theta = 90°$, the situation is neither fully wetting nor non wetting. The contact angle less than 90° indicates wetting behavior, while an angle greater than 90° suggests non-wetting behavior. Based on contact angle measurements, surfaces can be classified into the following categories and shown in Figure 2.9:

1. **Hydrophilic:** Contact angle $< 90°$

2. **Hydrophobic:** Contact angle $> 90°$

3. **Superhydrophobic:** Contact angle $> 150°$

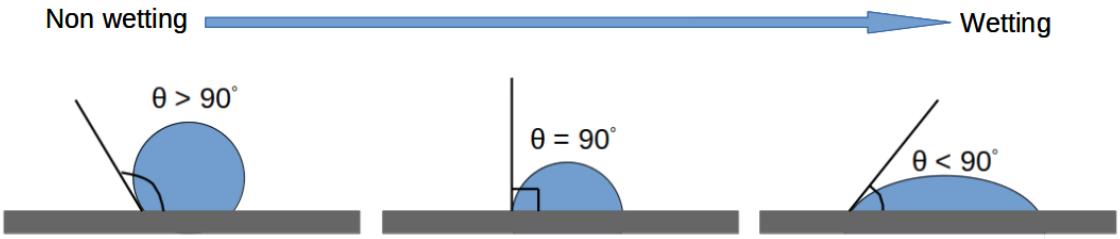

Figure 2.9. Classification of Surface and Wettability nature with respect to contact angle

The magnitude of the contact angle is influenced by the physical characteristics of the materials involved, particularly surface tension. The spherical shape of a droplet is determined not only by the nature of the surface it rests on but also by the liquid's surface tension. Surface tension causes liquids, such as water, to naturally form droplets due to cohesive forces between molecules. Within the bulk of the liquid, these forces are balanced; however, at the surface, molecules experience a net inward force because they are not surrounded equally on all sides. This imbalance creates a higher-energy surface state, driving the liquid to adopt a shape that minimizes surface area—typically a sphere. Liquids with higher surface tension tend to maintain larger contact angles and remain as distinct droplets. In contrast, liquids with lower surface tension exhibit smaller contact angles and spread more readily across solid surfaces. This behavior can be summarized as follows:

1. **Non-wettability:** High surface tension results in a larger contact angle.
2. **Wettability:** Low surface tension results in a small contact angle.

Contact angle theory is rooted in surface tension, as described by the Young-Laplace equation. This equation determines the contact angle by balancing the interfacial energies at the junction of the liquid, solid, and gas phases:

$$\gamma_{sg} = \gamma_{sl} + \gamma_{lg} \cos\theta$$

Where,

- θ represents the contact angle,
- γ_{sg} denotes the solid–gas interfacial energy,
- γ_{sl} is the solid-liquid surface tension and
- γ_{lg} is the liquid-gas surface tension.

The properties of the solid surface play a significant role in determining wettability. When the droplet reaches equilibrium, the forces acting on it are balanced. The contact angle can

then be expressed as:

$$\cos\theta = \frac{\gamma_{sg} - \gamma_{sl}}{\gamma_{lg}}$$

This equation shows how surface energies influence the contact angle:

1. If $\gamma_{sg} < \gamma_{sl}$, then $\cos\theta$ will be negative, resulting in $\theta < 90^\circ$, indicating a wetting condition.

2. If $\gamma_{sg} > \gamma_{sl}$, then $\cos\theta$ will be positive, resulting in $\theta > 90^\circ$, indicating a non-wetting condition.

Various methods have been developed in computational fluid dynamics (CFD) to model the dynamic contact angle. The most common approaches are presented in the sections below.

Kistler's Model

Kistler's model [27] describes the advancing contact angle (θ_A) as a function of the capillary number (Ca) and the equilibrium contact angle (θ_E), utilizing Hoffman's empirical formulation [28]:

$$\theta_A = f_H\left(Ca + f_H^{-1}(\theta_E)\right) \tag{2.13}$$

Where,

- θ_A denotes the advancing contact angle
- Ca represents the capillary number
- θ_E orresponds to the equilibrium contact angle and
- $f_H(x)$ is Hoffman's function

Hoffman's function, $f_H(x)$, is defined as:

$$f_H(x) = \arccos\left(1 - 2\tanh\left(5.16\left(\frac{x}{1+1.31x^{0.99}}\right)^{0.706}\right)\right) \tag{2.14}$$

"This model is widely applied to estimate advancing contact angles but additional considerations are necessary for receding angles, which can be handled by coupling with another model.

Dynamic Receding Contact Angle Model

Nichita et al. [29] extended Tanner's empirical work to formulate a model for receding angles. This model relates the dynamic receding contact angle (θ_D) to the capillary number:

$$\theta_D = \left(\theta_R^3 - 72Ca\right)^{1/3} \tag{2.15}$$

Where, θ_R represents the static receding contact angle. This approach is useful for simulations where receding angle dynamics are significant.

Shikhmurzaev's Model

Shikhmurzaev [30] proposed a model that links the DCA with the contact line velocity ($\mathbf{u}_{cl}$) and phenomenological constants:

$$\cos(\theta_D) = \cos(\theta_A) - \frac{2u(a_1 + a_2\mathbf{u}_0)}{(1-a_2)\left((a_1 + \mathbf{u}_{cl}^2)^{1/2} + \mathbf{u}_{cl}\right)} \tag{2.16}$$

Where, $\mathbf{u_0}$ is radial velocity, a_1, a_2, and other parameters are fitted values specific to the fluid interface being studied. This model provides flexibility for applications involving varied wettability conditions.

Cox's Model

Cox's model [31] calculates both advancing and receding contact angles by incorporating the apparent contact angle (θ_{app}), the capillary number, apparent length (L) and the slip length (λ):

$$\theta_D = g^{-1}\left(g(\theta_{\text{app}}) + Ca\log\left(\frac{L}{\lambda}\right)\right) \tag{2.17}$$

Where, $g(\theta)$ is an integral function given by:

$$g(\theta) = \int_0^{\theta} \frac{x - \sin(x)\cos(x)}{2\sin(x)}\,dx \tag{2.18}$$

This model is particularly advantageous in simulations that require precise representation of slip effects at the contact line.

Quasi-Dynamic Contact Angle Model

The quasi-dynamic model, as discussed by Göhl et al. [32], simplifies the contact angle behavior by setting a constant advancing angle (θ_A) and receding angle (θ_R) depending on

the contact line motion direction:

$$\theta_D = \begin{cases} \theta_A & \text{if advancing} \\ \theta_R & \text{if receding} \end{cases} \tag{2.19}$$

This model is computationally efficient and applicable where experimental data for contact angle hysteresis is available, though it may lack the accuracy of more detailed models.

Yokoi's Model

The dynamic contact angle is modeled as a function of the contact line velocity $\mathbf{u}_{cl}$ and Tanner's law [29], combining capillary-dominated and inertia-dominated regimes[33]:

$$\theta(\mathbf{u}_{cl}) = \begin{cases} \min\left(\theta_E + \left(\frac{\mathrm{Ca}}{k_a}\right)^{1/3}, \theta_{mda}\right), & \text{if } \mathbf{u}_{cl} \geq 0 \quad \text{(Advancing phase)}, \\ \max\left(\theta_E + \left(\frac{\mathrm{Ca}}{k_r}\right)^{1/3}, \theta_{mdr}\right), & \text{if } \mathbf{u}_{cl} < 0 \quad \text{(Receding phase)}, \end{cases} \tag{2.20}$$

Where:

- $\theta(\mathbf{u}_{cl})$: Dynamic contact angle as a function of the contact line velocity $\mathbf{u}_{cl}$.
- Ca: Capillary number, defined as:

  $$\mathrm{Ca} = \frac{\mu \mathbf{u}_{cl}}{\sigma},$$

  Where, μ is the liquid dynamic viscosity, $\mathbf{u}_{cl}$ is the contact line velocity, and σ is the surface tension.
- θ_E: Equilibrium contact angle at zero velocity ($\mathrm{Ca} = 0$).
- θ_{mda}: The upper bound of the dynamic advancing angle.
- θ_{mdr}: The lower bound of the dynamic receding angle.
- k_a, k_r: Material-dependent constants for the advancing and receding phases, respectively.

For the advancing phase ($\mathbf{u}_{cl} \geq 0$), the dynamic contact angle increases with $\mathbf{u}_{cl}$ and is capped at θ_{mda}. For the receding phase ($\mathbf{u}_{cl} < 0$), the dynamic contact angle decreases with $\mathbf{u}_{cl}$ but is limited by θ_{mdr}. This model captures the asymmetric nature between the advancing and receding behavior of contact angles using distinct constants (k_a, k_r) and dynamic limits ($\theta_{mda}, \theta_{mdr}$).

Davis–Hocking Model for Contact-Line Dynamics

The Davis–Hocking model relates the dynamic contact angle θ to the contact-line velocity $\mathbf{u}_{cl}$ via the mobility parameter M. The fundamental equation is:

$$M\Delta\alpha = \mathbf{u}_{cl}, \tag{2.21}$$

Where, $\Delta\alpha = \theta - \theta_E$ represents the deviation of the dynamic contact angle from its equilibrium contact angle θ_E. In systems with contact angle hysteresis, the model expands as [34]:

$$\theta = \begin{cases} \theta_a + \frac{\mathbf{u}_{cl}}{M}, & \text{if } \mathbf{u}_{cl} > 0 \quad \text{(advancing)} \\ \theta_r + \frac{\mathbf{u}_{cl}}{M}, & \text{if } \mathbf{u}_{cl} < 0 \quad \text{(receding)}, \end{cases} \tag{2.22}$$

Where, θ_A and θ_R are the advancing and receding static contact angles, respectively. To ensure the dynamic contact angle remains physical, the following boundary condition is applied:

$$\theta = \max(\min(\theta, 180^\circ), 0^\circ). \tag{2.23}$$

This model captures the linear dependence of the dynamic contact angle on the contact-line velocity, incorporating material properties via the mobility parameter M.

2.1.6 Energy Equation

Energy is a fundamental scalar quantity that is transferred between physical systems through mechanisms such as work and heat transfer. It is governed by the first law of thermodynamics, which dictates that the total energy of an isolated system remains constant, with energy only changing from one form to another [35]. The total energy E of a system comprises three contributions: internal (thermal) energy U, kinetic energy KE, and potential energy PE:

$$E = U + KE + PE. \tag{2.24}$$

In thermal-fluid systems, however, the energy equation is typically formulated in terms of internal energy, as it directly reflects temperature-related variations rather than the full total energy. For a moving fluid, the general conservation equation of internal energy is comprises three contributions: [36]

$$\frac{DU}{Dt} = -\frac{p}{\rho}(\nabla \cdot \mathbf{u}) + D_\nu + \frac{1}{\rho}\nabla \cdot q + Q, \tag{2.25}$$

where the first term on the right-hand side corresponds to pressure work, D_ν denotes viscous dissipation, q is the heat flux, and Q accounts for volumetric heat sources. For incompressible flows, the density is constant and $\nabla \cdot \mathbf{u} = 0$, which eliminates the pressure work contribution. Furthermore, viscous dissipation D_ν can be approximated using the Laplacian of velocity, i.e., $D_\nu \approx \nu \nabla^2 \mathbf{u}$, consistent with the viscous term in the momentum equation for Newtonian fluids [37]. In many low-speed incompressible flow applications, viscous heating is negligible; however, in lubrication flows, polymer melts, or molten metals, its inclusion is essential [38]. Under these assumptions, the energy equation in a Lagrangian framework reduces to

$$\frac{DU}{Dt} = \frac{1}{\rho} \nabla \cdot q + Q, \tag{2.26}$$

with the heat flux is defined according to Fourier's law as $q = k \nabla T$, with k denoting the thermal conductivity and T the local temperature.

$$\frac{DU}{Dt} = \nabla \cdot \left(\frac{k}{\rho} \nabla T \right) + Q. \tag{2.27}$$

2.1.7 Fluid-Structure Interaction (FSI)

Fluid-Structure Interaction (FSI) encompasses various methodologies for simulating the coupled behaviour of multiphase fluids and solid structures, which is critical in numerous engineering and scientific applications. These interactions become particularly complex in multiphase scenarios, where different fluid phases (such as liquid, gas, and particles) exert varying forces and moments on the structure. This complexity can significantly influence the dynamics of the system, affecting factors such as stability, performance, and material integrity. FSI problems involving multiphase flows phenomena are widely encountered across automotive and industrial engineering disciplines (e.g., Noise-Vibration-Harshness (NVH)), chemical engineering (e.g., mixing of different fluids in reactors), environmental engineering (e.g., sediment transport in rivers), and biomedical engineering (e.g., the behavior of blood flow in the presence of air bubbles or emboli). The accurate modeling of these interactions is essential for predicting the behavior of the system under diverse operating conditions. Various methodologies, including fully coupled (monolithic) methods, partitioned methods, weak coupling, and strong coupling, are employed to tackle these challenges, each with its own set of advantages and limitations. As computational resources expand and numerical techniques evolve, the capability to simulate multiphase FSI with greater precision continues to advance, empowering engineers and researchers to develop more effective and resilient systems.

Fully Coupled (Monolithic) Methods

Fully coupled methods solve fluid and structural equations simultaneously within an integrated computational framework, treating the interaction as a single problem. This approach provides high accuracy and robustness by accounting for the complex nonlinear behaviors of both fluid and structure. However, it is computationally intensive and requires sophisticated algorithms, making implementation more challenging.

Partitioned Methods

Partitioned methods divide the FSI problem into independent fluid and structure subproblems, solving each sequentially or iteratively. This flexibility allows for the use of specialized solvers for each component, which can be optimized separately. While this method reduces the initial computational cost and allows for scalability, it may encounter convergence issues and requires careful treatment of the interface to ensure accuracy. Weak and strong coupling can occur within both fully coupled (monolithic) methods and partitioned methods, but they have different implications depending on the context. In partitioned methods, weak coupling implies minimal interaction, while strong coupling means frequent data exchanges. In fully coupled methods, strong coupling is inherent due to simultaneous solving of the fluid and structural equations. Understanding these methodologies allows for better selection in engineering applications involving fluid-structure interactions.

Weak Coupling

Weak coupling features a loose interaction between fluid and structure, where data exchange occurs infrequently, typically at larger time intervals. This approach reduces computational effort and simplifies implementation, making it easier to utilize existing solvers. However, it can lead to inaccuracies in scenarios with strong interactions, as it does not fully account for the fluid's effect on the structure or vice versa.

Strong Coupling

Strong coupling involves a tight interaction with frequent data exchange between fluid and structure solvers, allowing for a more accurate representation of their dynamics. This method enhances accuracy and convergence in highly dynamic systems, but it also significantly increases computational demands and complexity in implementation due to the need for close coordination between solvers.

2.2 Past Research Overview

2.2.1 Literature Review - Lagrangian Differencing Dynamics (LDD)

The theoretical foundation of the Lagrangian Differencing Dynamics (LDD) method was established by Bašić et al. [39], who introduced meshless renormalized Laplacian operators for the solution of boundary value problems. This foundational work laid the groundwork for a novel class of Lagrangian meshless methods capable of simulating free surface flows with high accuracy and computational efficiency. The LDD method distinguishes itself fundamentally from other established meshless approaches in its underlying design philosophy. While conventional meshless methods typically prioritise conservation properties first and subsequently address solution consistency, the LDD method adopts the inverse approach. It begins with a carefully constructed approximation scheme that guarantees second-order consistency in both gradient and Laplacian operators, which in turn permits the use of a comparatively smaller support domain and thereby achieves greater computational efficiency. Beyond its approximation scheme, the LDD method incorporates several additional distinguishing features. A position-based point regularization scheme is employed throughout the solution process, which is unconditionally stable and inherently preserves conservation properties. Boundary treatment within LDD requires only a surface mesh, considerably simplifying the handling of boundary conditions relative to traditional meshless approaches. All governing equations are solved in a fully mesh-free manner, with the implementation fully parallelized on both GPU and CPU architectures, enabling maximum computational throughput and scalability to large-scale problems. The solution procedure within a single time step of the LDD method commences with the Lagrangian advection of computational points, wherein each point is displaced in space according to its instantaneous velocity. The volumetric compressibility issues inherent to Lagrangian advection are addressed through the Particle-Based Dynamics (PBD) technique [40], which iteratively corrects the spatial positions of points by enforcing uniform inter-neighbour distances, thereby maintaining a regular and well-conditioned point distribution throughout the simulation. Following the regularization step, the Pressure Poisson Equation (PPE) is discretized using the renormalized discrete differential operators introduced in [41], and subsequently solved using a preconditioned BiCGSTAB linear solver, as described in [40]. The capabilities of the LDD method were progressively demonstrated and extended through a series of subsequent studies. Bašić et al. [42] applied the LDD framework to sloshing simulations, demonstrating its capability to accurately capture complex free surface dynamics in confined fluid domains. The method was further extended to the prediction of green water loadings, demonstrating its suitability for maritime engineering applications involving wave impact events and hydrodynamic fluid loadings on structures. Subsequent refinements to the incompressible flow formulation broadened the scope of the method to a wider range of fluid flow scenarios [43]. Bašić

et al. [44] investigated the coupling of the LDD method with structural analysis solvers, integrating a meshless non-Newtonian fluid flow solver within a structural mechanics framework, demonstrating the method's versatility in handling fluid-structure interaction problems involving complex rheological behaviour. The application domain of LDD was further diversified by Peng et al. [45], who extended the method to granular flow modelling, expanding its utility beyond conventional fluid simulations to encompass particulate and granular materials. Recent contributions by Paneer et al. [46, 47] have advanced the LDD framework in two important directions: the modelling of elastic structural behaviour and the simulation of fluid-structure interactions, respectively. These developments further consolidate the LDD method as a versatile and high-fidelity computational tool applicable across a broad spectrum of coupled multiphysics problems. Separately, Johannes et al. [48] developed a GPU-accelerated finite difference solver employing a generalised Riemann solver approach for incompressible multiphase flows. This formulation incorporates a dedicated dampening scheme capable of handling high-density ratios, leveraging the LDD Laplacian operator originally introduced in [39], thereby extending the reach of the LDD mathematical framework for multiphase flow solvers.

2.2.2 Literature Review - Multiphase

Multiphase flow dynamics is concerned with the behaviour of immiscible fluid phases separated by a deformable interface, which is subject to complex morphological transformations as the constituent phases evolve. The accurate numerical representation of such interfaces is of paramount importance across a broad spectrum of engineering and scientific disciplines, including industrial process engineering, environmental fluid mechanics, and fluid-structure interaction analysis. Depending on the computational framework adopted, distinctly different strategies are employed to capture interfacial dynamics.

Within Eulerian frameworks, in which the governing equations are discretized on a stationary computational grid, the interface is resolved through specialised tracking or capturing techniques.. The Phase Field method, originally introduced by Cahn and Hilliard [8], represents the interface implicitly through a continuous scalar field variable that transitions smoothly between phase properties across a diffuse interfacial zone. This approach is particularly attractive for modelling phase transitions and interfacial thermodynamics due to its mathematical elegance and ease of implementation. The Volume of Fluid (VOF) method, developed by Hirt and Nichols [9], tracks the interface by defining a fractional volume function within each computational cell, indicating the local proportion of each fluid phase. This method has an effective balance between numerical accuracy and computational expense, rendering it a widely utilised approach in engineering simulations that involve moderately deforming interfaces.The Level Set method, proposed by Osher and Sethian [49], defines the interface implicitly as the zero isocontour of a signed distance function, providing a geomet-

rically smooth and topologically flexible representation of the interface. Sussman et al. [10] subsequently extended the Level Set method to handle two-phase flows with high density ratios and surface tension effects, significantly improving its applicability to air-water type flow configurations. The Front Tracking method of Unverdi and Tryggvason [50] takes an explicit approach, representing the interface through a set of marker points whose positions are tracked directly throughout the simulation, making it well suited to problems involving large interfacial displacements. The Conservative Level Set method [51] combines desirable features of both the VOF and Level Set approaches to simultaneously achieve mass conservation and topological flexibility. In more recent work, Theillard et al. [12] developed a sharp interface formulation for incompressible two-phase flows on adaptive Cartesian grids, wherein capillary forces are embedded directly within the pressure correction step to preserve numerical stability under complex interfacial conditions. Kamran et al. [52] introduced a hybrid formulation combining the Extended Finite Element Method (XFEM) with the Particle Level Set (PLS) method, providing an effective computational strategy for multi-fluid engineering applications.

In contrast, Lagrangian methods intrinsically formulated to follow the trajectories of individual fluid particles or parcels, allowing the interface to be captured naturally without the need for explicit tracking algorithms. Smoothed Particle Hydrodynamics (SPH), independently established by Gingold and Monaghan [53] and Lucy [54], is the most widely adopted Lagrangian method. Within the SPH framework, the fluid domain is discretized into interacting particles that carry physical properties including density, pressure, and velocity, with particle interactions governed by a smoothing kernel function. The method handles large deformations and free surface flows naturally, though numerical instabilities can arise in multiphase configurations involving sharp interfaces and significant density contrasts. The Moving Particle Semi-Implicit (MPS) method [55] addresses some of these stability concerns through semi-implicit time integration, offering improved performance in free surface and multiphase flow simulations. The Element-Free Galerkin (EFG) method [56] solves the governing equations using nodal representations without relying on a fixed computational mesh, providing additional flexibility for problems with large deformations. The Particle Finite Element Method (PFEM) [57] adopts a hybrid approach wherein particles serve as material points and a finite element mesh is regenerated dynamically at each time step, offering versatility at the cost of increased computational overhead.

Considerable research effort has been directed toward overcoming the limitations of these methods in multiphase flow contexts. Within the SPH framework, improvements to kernel functions [58, 59] have enhanced numerical precision and stability in multiphase simulations. Early SPH formulations for flows with density variations [13] have been progressively refined to accommodate particles of non-uniform density, facilitating physically realistic interactions between fluid phases of different properties. These developments have found application in astrophysical simulations involving mixed-density environments [60].

Hu and Adams [61] applied SPH to macroscopic and mesoscopic multiphase flows, effectively addressing density contrast and interfacial dynamics. Grenier et al. [62] introduced a Hamiltonian interface SPH formulation that improved the handling of multi-fluid free surface problems, while Monaghan et al. [63] formulated a stabilized SPH algorithm for immiscible flows capable of managing high-density ratio interfaces. Rezavand et al. [64] proposed an incompressible SPH (ISPH) scheme employing repulsive inter-particle forces to preserve interface sharpness and enhance stability, with subsequent work [65] extending these improvements to violent multiphase flow regimes. Shimizu et al. [66] applied ISPH to oil spill modelling, incorporating turbulence and oil-water mixing effects. Olejnik et al. [67] investigated wetting phenomena within the SPH framework, while Vacondio et al. [68] conducted a comprehensive assessment of outstanding challenges in SPH, particularly regarding computational efficiency and numerical robustness. Zhang et al. [69] subsequently developed a multi-scale SPH framework for fluid-structure multiphase interactions, enabling higher-fidelity computational representations of coupled real-world problems.

Parallel advancements have been made within the MPS framework. Building on the original formulation of Koshizuka and Oka [55], Duan extended MPS into a dedicated multiphase framework termed Multiphase MPS (MMPS), specifically formulated to treat fluids exhibiting pronounced contrasts in viscosity and density. Two stabilization strategies were introduced within this framework: MMPS-HD, based on harmonic density averaging, and MMPS-CA, employing continuous acceleration corrections, both aimed at suppressing interfacial instabilities through modified particle interaction schemes [14]. Validation studies confirmed that MMPS-CA offers superior performance in high-density and high-viscosity ratio configurations.Further enhancements incorporating an improved Laplacian operator with error-free first-order derivatives were subsequently introduced to address residual instabilities in violent multiphase flow scenarios [70]. A detailed summary of the study on multiphase systems is presented, along with relevant literature, as shown in the Table 2.3.

2.2.3 Literature Review - Surface Tension and Dynamic Contact Angle

Surface tension constitutes a critical physical mechanism in multiphase flow simulations, and a variety of numerical methods have been proposed for its effective modelling, each offering distinct advantages depending on the application. The Continuum Surface Force (CSF) method treats surface tension as a body force distributed across the interface, enabling a robust handling of interface dynamics without explicitly tracking the interface position, which makes it well-suited for simulating complex fluid behaviors in large-scale simulations [26]. In contrast, sharp interface methods directly apply the Young-Laplace equation to impose pressure jumps across interfaces, making them particularly suitable for scenarios where precise interface tracking and resolution are required, such as in simulations of droplet dynamics or bubble formation [11]. The Ghost Fluid Method (GFM) applies ghost

Table 2.3. Summary of study on Multiphase methods and literature reviews.

Method	Description
Phase Field Method	Uses a continuous field variable to represent the interface as a diffuse region, allowing a smooth transition between phases [8].
Volume of Fluid (VOF)	Tracks the interface using a fractional volume function, representing the proportion of each fluid in mesh elements [9].
Level Set Method	Uses a signed distance function to implicitly characterize the interface at the zero-level set [49].
Improved Level Set	Enhances the original Level Set method for handling high-density ratios and surface tension effects [10].
Front Tracking	Directly tracks the interface using marker points to explicitly define interface positions [50].
Conservative Level Set	Combines VOF and Level Set methods for improved mass conservation and complex interface dynamics [51].
Sharp Interface Level Set	Integrates modified pressure correction and adaptive grids, incorporating capillary forces into pressure estimation for high stability [12].
XFEM with Particle Level Set	Uses extended finite element with particle level set to simulate multi-fluid flows, handling complex interfaces and boundary interactions [52].
SPH	Particle-based, using smoothing kernels for properties like density and pressure, suited for free-surface flows and astrophysics [53, 54, 58, 59, 13, 60, 61, 62, 63, 64, 65, 66, 67, 68, 69].
Moving Particle Semi-implicit (MPS)	Particle-based method with semi-implicit time stepping, ensuring stable calculations for incompressible flows with complex interfaces [55, 14, 70].
PFEM	Combines particle and finite element approaches, where particles represent material points, used for remeshing and solving governing equations [57].

cells to enforce discontinuities in variables near the interface, enabling an accurate representation of abrupt changes in physical properties such as pressure and velocity. This makes it particularly effective for capturing sharp interface behavior while minimizing numerical errors near boundaries. [71]. Diffuse Interface Models (DIM) represent the interface as a smooth transition between phases, effectively avoiding explicit interface tracking while still capturing interfacial phenomena such as capillary waves and phase separation, making them ideal for systems where the interface is less distinct or more diffusive in nature [72]. The Lattice-Boltzmann Method (LBM) introduces surface tension through modified particle interactions, enabling the simulation of complex geometries and fluid behavior in systems with intricate boundaries, such as porous media or microfluidic devices [73]. Lastly, Smoothed Particle Hydrodynamics (SPH) employs a meshless approach to calculate surface tension forces among particles, excelling in scenarios with significant interface deformation, including free-surface flows. It is also well-suited for large-scale simulations that require adaptive resolution and dynamic interfaces. [74]. Each of these methods has its own set of advantages and trade-offs, making them suitable for different types of multiphase flow problems.

Dynamic contact angle (DCA) models are essential for accurately simulating multiphase flow systems, especially where wetting dynamics are complex and vary with surface interactions and fluid velocities. The first rigorous description of the contact angle was introduced by Young in 1805, who described the static contact angle as the equilibrium state of a droplet on a solid surface, now famously expressed by Young's Equation [75]. However, Young's equation applied only to static, equilibrium conditions, without addressing the concept of dynamic contact angles. Shortly after, Pierre-Simon Laplace extended the understanding of capillary action in 1806 by formulating the Young-Laplace equation, which relates the pressure difference across a curved liquid interface to the surface tension [76]. In the early 20th century, scientists began exploring the contact angle changes as the contact line advances or recedes. Harkins and Jordan (1930) were among the first to show that the contact angle varies during the motion of a liquid over a surface, introducing the concept of contact angle hysteresis, in which the advancing angle exceeds the receding angle [77]. Blake and Haynes (1969) furthered this by studying liquid-liquid displacement kinetics, focusing on how interfacial properties and dynamic contact angles impact fluid movement in capillaries [78]. A major theoretical breakthrough occurred with Joanny and de Gennes (1984), who proposed a model for the dynamic contact line. It was demonstrated that the contact angle is governed not only by surface tension, but also by the velocity of the moving contact line, with increasing velocities leading to greater deviations from the equilibrium contact angle [79]. Charles Extrand and Alan Shapiro (1995) further advanced the understanding of dynamic wetting by systematically studying contact angle hysteresis. They observed that when a liquid advances across a surface, it encounters greater resistance due to surface roughness or chemical heterogeneity, leading to a larger contact angle. Conversely, during receding, the contact angle is smaller [80]. Another important theoretical advancement came with the Cox-Voinov

law (1976), which relates the dynamic contact angle to the velocity of the moving contact line through a logarithmic correction term, particularly useful for low-speed wetting scenarios such as in coating flows [81]. Cox extended the model to calculate both advancing and receding dynamic contact angles by accounting for the capillary number and apparent contact angle, including physical slip length, thereby improving the representation of viscous forces and surface interactions [31]. Tanner's empirical correlation (1979) laid one of the early foundations for describing receding contact angles based on the capillary number, influencing subsequent models dealing with contact line dynamics in multiphase flow [29]. Kistler's Model (1993), leveraging Hoffman's empirical function [28], relates the dynamic contact angle to the capillary number and static contact angle, widely applied for advancing angles. Adaptations of this model also allow for the prediction of receding angles [27]. Shikhmurzaev's Model (1997) links the dynamic contact angle to the contact line velocity and phenomenological constants, offering versatility for complex fluid behaviors on surfaces with varying wettabilities [82]. The Dynamic Receding Contact Angle Model (2010), introduced by Nichita et al., extended Kistler's model to provide a cubic-root function-based approach for receding contact angles, combining Kistler's model with Tanner's correlation to describe receding behavior in multiphase flow [83]. Yokoi et al. (2009) proposed a model for dynamic contact angles that describes the angle as a function of contact line velocity, incorporating capillary and inertia-dominated regimes. Their model uses Tanner's law for low velocities and applies maximum/minimum dynamic angles for high velocities, ensuring asymmetry between advancing and receding phases for more accurate droplet behavior predictions [33]. The Quasi-Dynamic Contact Angle Model (2015) simplifies the modeling process by employing fixed advancing and receding angles based on experimental data. While less computationally demanding, its accuracy relies heavily on the availability of detailed experimental data [84]. Snoeijer and Andreotti (2013) introduced the concept of contact line friction, a molecular-scale interaction that resists the motion of the contact line, providing a more refined understanding of dynamic wetting by linking microscopic molecular forces to macroscopic observations [85]. Ludwicki et al. (2022) investigated whether the contact-line mobility parameter, which describes the relationship between the dynamic contact angle and contact-line velocity, is a material parameter, using both experimental and numerical approaches to study binary sessile drop coalescence on various surfaces [34]. These models and developments have greatly enhanced our understanding of dynamic wetting behavior in multiphase flow and continue to be integral in improving the accuracy of simulations in various industrial and scientific applications.

2.2.4 Literature Review - Fluid Structure Interaction (FSI)

Fluid-Structure Interaction (FSI) represents a physically fundamental and technically demanding class of problems in which the dynamics of a fluid medium and a deformable or

rigid structure are mutually coupled, each continuously influencing the behaviour of the other. The practical relevance of FSI spans a broad spectrum of engineering domains. Notable examples include the interaction between hydrodynamic wave loads and coastal vegetation in wetland environments, and the mechanical interaction between ocean waves and sea ice in Arctic regions, both of which carry significant implications for coastal flood mitigation and the understanding of extreme environmental conditions [86], [87]. In offshore and maritime engineering, FSI analysis is integral to the structural design and performance optimisation of offshore installations, wind turbines, and naval vessels [88], where accurate prediction of fluid-induced loads is essential to ensuring structural integrity and operational reliability. Incorporating FSI analysis at early design stages allows potential structural vulnerabilities to be identified and resolved before manufacturing, thereby avoiding costly modifications during production or service [89]. FSI is equally important in the hydrodynamic performance assessment of marine propellers, as demonstrated in recent studies [90], [91]. In such systems, structural damping governs the dissipation of vibrational energy within each oscillation cycle and plays a determining role in resonance phenomena, directly influencing vibration amplitudes and the temporal evolution of dynamic responses. While damping effects are often negligible in lightly damped systems operating away from resonance, they become the dominant mechanism near resonant frequencies, where the excitation energy is primarily balanced by dissipation rather than inertial or stiffness forces [92].

Despite its broad relevance, the numerical simulation of FSI problems presents considerable challenges, requiring carefully considered assumptions in both the fluid and structural modelling components. In the majority of CFD simulations, elastic deformation of structural boundaries is neglected for simplicity [40], while structural analyses conventionally assume uniform pressure conditions at both interior and exterior boundaries. Paik et al. [93] addressed this limitation by developing a coupled framework that integrates CFD solvers with both rigid and elastic ship hull models for the computation of structural loads under hydrodynamic excitation. Both one-way and two-way coupling strategies were implemented and compared. In the one-way coupling approach, hydrodynamic forces computed by the CFD solver are transferred to the structural model for load analysis, but the resulting structural deformations are not communicated back to the fluid solver. The two-way coupling approach, by contrast, incorporates structural deformations as updated boundary conditions within the CFD solution, enabling a fully bidirectional exchange of information between the two solvers. A URANS/DES overset solver combined with the modal superposition method was employed in this framework, with a gluing interpolation technique used to transfer forces and displacements between non-conforming CFD and structural meshes [93].

Extensive methodological developments have been undertaken to manage the complexities inherent in both one-way and two-way fluid–structure interaction (FSI) coupling. The fully coupled monolithic strategy solves fluid and structural governing equations simultaneously within a unified computational framework [94, 95], offers the highest degree of

physical consistency but introduces significant computational challenges. In particular, conventional CFD solvers are formulated within an Eulerian reference frame, whereas structural mechanics solvers typically adopt a Lagrangian description of motion. This fundamental kinematic incompatibility introduces a stiffness mismatch between the fluid and structural subsystems, rendering the monolithic approach computationally prohibitive for large-scale or complex configurations [96]. Partitioned methods have consequently gained widespread adoption as a more practical alternative, solving the fluid and structural subproblems independently on separate meshes using dedicated solvers [97]. These methods require robust interface communication protocols to transfer forces from the fluid to the structure mesh and return structural displacements to the fluid solver. Mesh-based partitioned solvers additionally require careful management of fluid mesh nodes adjacent to moving boundaries to prevent mesh entanglement or excessive distortion [98], [99]. Recent applications of partitioned approaches include the coupling of thin-walled girder theory with potential flow formulations [44, 100], and the integration of modal structural solvers with RANS-VOF solvers and Boundary Integral Equation Methods [101]. The Solid4Foam library, implemented within the OpenFOAM framework, represents another established tool for partitioned FSI analysis [102, 103].

Meshless partitioned methods offer particular advantages in FSI scenarios involving free surfaces, violent and highly transient flow conditions, geometrically complex configurations, and large structural deformations [104]. By eliminating the requirement for mesh regeneration following structural deformation, these methods provide a naturally adaptive framework for simulating coupled fluid-structure problems. Within this class of methods, FSI is commonly realised by coupling Smoothed Particle Hydrodynamics (SPH) with structural solvers based on the Finite Element Method (FEM) [105, 106, 107] or the Discrete Element Method (DEM) [108, 109, 110] to compute structural deformation under fluid loading. The transfer of physical quantities between the fluid and structural solvers remains non-trivial, requiring careful treatment of the interfacial energy balance [111]. Although the computation of structural deformation within this meshless framework incurs considerable computational cost, it generally remains more efficient than the equivalent monolithic formulation.

The Mode Superposition method has attracted growing interest in recent years as a computationally efficient and robust approach for resolving structural deformation within FSI frameworks. Debrabandere et al. (2012) introduced a reduced-order modeling approach for fluid–structure interaction (FSI) simulations, in which structural dynamics are described using modal analysis within a reduced-order framework. The resulting modal equations are directly integrated into the computational fluid dynamics (CFD) solver through a complementary function and particular solution formulation. This approach has demonstrated good agreement with benchmark cases and highlights its effectiveness for efficient aeroelastic analysis of deformable structures within turbomachinery systems [112]. Sun et al. (2019) coupled the Moving Particle Semi-Implicit (MPS) method with modal superposition to sim-

ulate violent hydroelastic phenomena [113], while Corrado et al. (2020) validated a two-way CFD-FEM coupling framework against the HIRENASD aeroelastic benchmark case [114]. Modal superposition is valued for its conceptual simplicity and computational efficiency, though its accuracy degrades in the presence of large structural deformations, as the underlying assumptions of linear behaviour and modal orthogonality are violated under conditions of significant geometric or material nonlinearity. Within its range of validity, however, the method remains an effective and well-established tool for the dynamic analysis of structures subjected to time-varying fluid loads [112, 113, 114].

Weak coupling strategies in FSI offer practical advantages in terms of implementation simplicity and suitability for transient loading scenarios. However, they are subject to inherent limitations, most notably numerical stability constraints that necessitate the use of short time increments, that can significantly reduce computational efficiency for extensive simulations where the fluid and solid subsystems may operate optimally at different temporal resolutions. The modal superposition approach partially mitigates this constraint by adding minimal computational overhead to the structural solution step, allowing the structural time integration to be aligned more closely with the time step requirements of the flow solver [115], [112], [100].

2.2.5 Literature Review - Heat Transfer and Phase Change

Heat transfer, coupled with buoyancy and phase change phenomena such as melting, solidification, evaporation, and condensation, plays a critical role in diverse engineering applications and natural systems. Examples include incorporating phase-change heat storage mechanisms, additive manufacturing, cryogenic cooling technologies, and large-scale processes such as climate and geophysical modelling [116, 117]. The accurate representation of these processes requires resolving the strong coupling between thermal transport, phase transition kinetics, and multiphase flow behavior across evolving interfaces. However, the inherent nonlinearity of phase change, together with sharp thermal and density gradients at the interface, poses long-standing challenges for numerical formulation and computational analysis. In conventional Eulerian frameworks, heat transfer and phase change are typically modeled within mesh-based discretization schemes such as the Finite Volume Method (FVM) and Finite Element Method (FEM). To capture the evolution of the phase boundary, these approaches often employ interface-capturing techniques such as the Level Set and Volume of Fluid (VOF) methods [8, 9, 49, 10]. In the presence of phase transition, additional energy-based formulations are introduced to account for latent heat effects. One of the most widely used approaches is the enthalpy–porosity method, introduced by Brent et al. [118], which reformulates the energy equation in terms of enthalpy and models the partially melted or solidified region as a porous structure featuring spatially varying porosity. Another common approach, the effective heat capacity method [3], implicitly accounts

for latent heat by altering the specific heat capacity within the phase change temperature interval, allowing for continuous temperature evolution during the phase transition process. Classical Stefan problem [119] provides a more explicit representation of the phase boundary as a moving interface, with its velocity determined by the local heat flux and latent heat balance. However, implementing such sharp interface tracking in Eulerian grids is numerically demanding, particularly for complex interface topologies and high-density ratios. To address these challenges, hybrid formulations have been proposed that couple Level Set or Front Tracking methods with phase change models. For instance, Son and Dhir [120] developed a Level Set-based framework to simulate film boiling and bubble growth dynamics, while Juric and Tryggvason [121] incorporated heat transfer and phase transition into a Front Tracking scheme to model melting and solidification processes. More recent advances, such as those by Tanguy et al. [122], have focused on sharp-interface formulations that explicitly impose the discontinuity in thermal and heat flow continuity through the interface, improving the accuracy of interfacial energy transfer and curvature-driven effects. Despite these advancements, Eulerian-based approaches remain limited when applied to problems involving large interface deformations, topological transitions, and complex geometries. Grid distortion, numerical diffusion, and mass loss near the interface can compromise the fidelity of simulations, especially in cases involving strong coupling between momentum, energy, and phase change fields. These limitations have prompted the advancement of meshless Lagrangian methods, that inherently avoid grid dependency and can naturally capture large deformations and complex interfacial dynamics. By modeling the fluid region using distinct particles, these methods enable direct tracking of phase evolution, local heat transfer, and latent energy transport, offering a promising framework for simulating multiphase systems with strong thermodynamic and interfacial coupling.

Among meshless approaches, several prominent methods have been developed for multiphase flow and phase transition simulations. Smoothed Particle Hydrodynamics (SPH) [53, 54] and the Moving Particle Semi-Implicit (MPS) method [55] are widely employed for free-surface flows and phase change modelling. Other notable meshless frameworks include the Element-Free Galerkin (EFG) method [56], Meshless Local Petrov–Galerkin (MLPG) method [123], Reproducing Kernel Particle Method (RKPM) [124], and Meshless Finite Difference (MFD) or Generalized Finite Difference (GFD) methods. These approaches approximate spatial derivatives using scattered nodes rather than structured grids, making them well-suited for problems involving complex geometries, moving interfaces, and large deformations. Classical phase change formulations in meshless contexts include enthalpy-based methods [125], collocation-based schemes for liquid–vapor transitions [126], and hybrid SPH–FEM or SPH–Lattice Boltzmann (LBM) approaches for solidification and melting [127, 128].

The Generalized Finite Difference Method (GFDM), introduced by Perrone and Kao [129], has undergone significant advances, including stability enhancements on irreg-

ular grids [130], radial basis function extensions for solid mechanics [131], and consistent formulations for conservation laws [132, 133]. More recently, GFDM has been employed for time-dependent heat transfer in spatially tailored materials [134], inverse thermal source problems [135], and coupled nonlinear convection–diffusion systems [136], demonstrating its versatility for complex heat transfer applications.

In meshless formulations, buoyancy forces are introduced as a volume force within the momentum equation. The most common approach is the Boussinesq approximation, where density fluctuations are disregarded everywhere except within the gravitational term , resulting in a buoyancy source term proportional to the local temperature deviation. This yields a buoyancy source term of the form, which has been widely applied in natural convection studies using Meshless Local Petrov-Galerkin Simulation (MLPG) and Moving Least Square (MLS) based methods [123, 137]. For cases involving large temperature gradients, the variable-density formulation is preferred, where density is treated as a temperature-dependent property and directly coupled into the momentum equations [138]. This approach has also been adopted in RBF-based meshless methods and SPH variants for simulating buoyancy-driven turbulent flows, such as continuous casting. In both cases, buoyancy is strongly coupled with the energy equation, ensuring interaction between thermal and flow fields. Classical phase change formulations, such as enthalpy-based methods [125], meshfree collocation schemes for liquid–vapor transitions [126], and hybrid approaches for solidification [127], have addressed key aspects of latent heat treatment and interface capturing. Nonetheless, the coupling of temperature evolution, buoyancy effects, and multiphase interactions within a single meshless framework has yet to be fully achieved. This gap limits the predictive capability of numerical models in scenarios involving strong property contrasts, steep thermal gradients, and vapor–liquid equilibrium. Despite these advancements, accurately modeling phase change coupled with buoyancy-driven flows remains a challenging task in meshless formulations. This approach has been widely applied in natural convection studies using MLPG and Moving Least Squares (MLS)-based methods [123, 137]. However, in cases involving large temperature gradients or strong phase transitions, a variable-density formulation becomes necessary, where density is treated as a temperature-dependent property and directly coupled with the momentum equations [138].

2.3 Research Gaps and Implications

The literature review reveals several critical gaps that motivate the developments in this thesis:

2.3.1 Identified Gaps

Fluid-Structure Interaction: Efficient Lagrangian-Lagrangian coupling strategies are underexplored. Modal superposition methods, despite proven efficiency in mesh-based FSI, remain largely uncombined with meshless fluid solvers, missing opportunities for direct force transfer without mesh mapping.

Lagrangian Multiphase Methods: Existing SPH and MPS approaches face a fundamental trade-off between interface sharpness and numerical stability. Repulsive force methods introduce non-physical forces, while color function approaches suffer interface smearing at high density ratios (>100:1). Standard formulations lose second-order consistency at discontinuous property fields, and particle regularization techniques do not account for phase-specific material properties.

Phase Change and Interfacial Physics: Meshless methods lack robust frameworks for energy-conserving phase change with moving interfaces. Surface tension models adapted from Eulerian methods (e.g., CSF) face challenges in curvature computation on irregular particle distributions. Dynamic contact angle models accounting for velocity and temperature dependence are rarely implemented in particle methods.

Buoyancy-Driven Thermal Flows: Lagrangian methods struggle to maintain hydrostatic balance in stratified fluids, leading to spurious velocities in natural convection problems. When coupled with phase change, the multi-scale density variations from thermal gradients and compositional differences require systematic treatment currently absent from existing approaches.

Unified Multiphysics Framework: No existing Lagrangian method simultaneously provides sharp multiphase interfaces, coupled heat transfer and phase change, accurate interfacial phenomena modeling, buoyancy effects, and efficient FSI—all within a consistent second-order accurate scheme.

2.3.2 Thesis Implications

This implication addresses these gaps through the following advancements:

1. **Modal FSI with direct Lagrangian coupling**, enabling efficient weakly coupled simulations through direct particle-to-modal force transfer in LDD

2. **Multiphase LDD (MP-LDD)** with variable coefficient Laplacian operator maintaining second-order consistency across discontinuous property fields, and Atwood

number-based particle regularization for sharp interfaces at density ratios as high as 1000:1.

3. **Surface tension and dynamic contact angle models** adapted for MP-LDD.

4. **Energy-conserving phase change module** with implicit thermal heat formulation, and integrated treatment of latent heat effects.

5. **Hierarchical Buoyancy Modeling Framework (HBMF)** achieving machine-precision hydrostatic balance and multi-scale density treatment for thermal and compositional variations.

6. **Comprehensive validation** through 25+ benchmark cases spanning multiphase flows, phase change, capillary flows, natural convection, and FSI, with demonstrations of coupled multiphysics capabilities.

These developments establish a unified computational framework for complex multiphysics problems involving simultaneous multiphase flow, heat transfer, phase change, interfacial effects, and structural interaction.

3 LAGRANGIAN DIFFERENCING DYNAMICS

This chapter introduces the foundational Lagrangian Differencing Dynamics (LDD) method that serves as the basis for all developments in this thesis. As a meshless Lagrangian framework, LDD is designed for simulating incompressible fluid flows, characterized by its unique discretization scheme that ensures second-order consistency for spatial derivatives.

3.1 Governing Equations for Incompressible Flow

Within the LDD framework, the incompressible Navier-Stokes equations are solved in strong form through a Lagrangian formulation, grounded in the Generalised Finite Difference Method (GFDM). The governing system for incompressible flow comprises two key relations: the continuity equation (2.1) and the momentum equation (2.2) for LDD framework:

$$\nabla \cdot \mathbf{u} = 0 \quad \text{in } \Omega \cup \Gamma_w \cup \Gamma_{fs} \tag{3.1}$$

$$\frac{D\mathbf{u}}{Dt} = -\frac{1}{\rho}\nabla p + \nu \nabla^2 \mathbf{u} + \mathbf{g} \quad \text{in } \Omega \tag{3.2}$$

where Ω denotes the fluid domain, Γ_w represents wall boundaries, and Γ_{fs} denotes free surfaces. Boundary conditions include:

$$\mathbf{u} = \mathbf{U} \quad \text{on } \Gamma_w \tag{3.3}$$

$$p = p_{atm} \quad \text{on } \Gamma_{fs} \tag{3.4}$$

where $\mathbf{U}$ denotes the prescribed wall velocity and p_{atm} refers to the atmospheric pressure.

3.1.1 Pressure Velocity Decoupling

To separate the pressure and velocity fields, the LDD method makes use of a projection-based approach. The resulting Pressure Poisson Equation (PPE) is obtained by applying the divergence operator to the momentum equation and subsequently imposing the incompressibility condition:

$$\nabla^2 p = -\rho \nabla \cdot \frac{D\mathbf{u}}{Dt} \quad \text{in } \Omega \tag{3.5}$$

with boundary conditions:

$$\mathbf{n} \cdot \nabla p = \rho \mathbf{n} \cdot \left[-\frac{D\mathbf{u}}{Dt} + \mathbf{g} + \nu \nabla^2 \mathbf{u} \right] \quad \text{on } \Gamma_w \tag{3.6}$$

$$p = p_{atm} \quad \text{on } \Gamma_{fs} \tag{3.7}$$

here $\mathbf{n}$ represents the unit normal vector directed outward from the boundary surface.

3.2 Discretization Techniques

The LDD method discretizes the problem domain through a collection of Lagrangian particles (points) that advect with the local fluid motion. Each particle i located at position $\mathbf{r}_i$ carries physical quantities such as velocity, pressure, and other field variables. The key feature of LDD is its unique approximation scheme for spatial derivatives based on renormalization tensors.

3.2.1 LDD Approximation

LDD is a meshless numerical scheme that operates under the Lagrangian paradigm, rooted in the GFDM. Rather than relying on a structured mesh, the fluid domain is represented by an unstructured cloud of computational points, each carrying local field quantities such as pressure and velocity, with no predefined connectivity between them. A fundamental distinction between LDD and particle-based methods such as SPH is that these computational points carry no associated mass or volume; they function solely as locations at which field properties are defined and evaluated. The physical quantities at each point are computed through weighted contributions from neighbouring points residing within a prescribed compact support radius h, as shown in Figure 3.1. The contribution of each neighbouring point is determined by a smoothing kernel function evaluated at the inter-point distance r.
For this work, the compact support radius is set within the range $1.8\Delta r$ to $2.2\Delta r$, where Δr denotes the characteristic inter-point spacing. A larger compact radius incorporates contributions from a greater number of neighbouring points, which promotes numerical stability at fluid interfaces in complex flow configurations. The kernel function used in LDD takes a cubic spiky form, given by:

$$W(r,h) = \left(1 - \left(0.4 \times \frac{r}{h}\right)\right)^3 \quad 0 \le r \le h \tag{3.8}$$

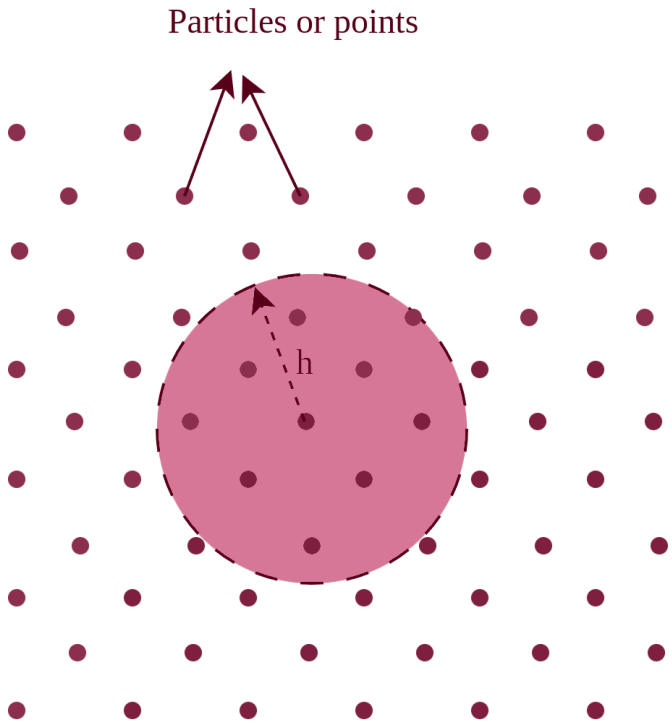

Figure 3.1. Neighbouring points within a defined compact radius(h).

$$\langle f(x)\rangle_i = \sum_j \psi_{ij}(r_{ij},h) f(x_j) \tag{3.9}$$

where $r_{ij} = \|\mathbf{x}_j - \mathbf{x}_i\| = \|\mathbf{x}_{ij}\|$ is the Euclidean distance between points i and j, $\mathbf{x}_i$ and $\mathbf{x}_j$ are the spatial coordinates of points i and j respectively, and $\mathbf{x}_{ij}$ is the vector connecting them. The coefficient 0.4 appearing in the weighting function is introduced to prescribe a compact support radius of $2.5h$. With this choice, the kernel satisfies $W = 0$ at $r = 2.5h$, since $1 - 0.4(r/h)$ becomes zero at that distance. The parameter therefore does not represent an additional physical constant, but rather a convenient scaling used to define the maximum extent of the local neighbourhood over which particle interactions are evaluated. The normalised weighting fraction ψ_{ij} assigned to neighbouring point j is given by:

$$\psi_{ij}(x) = \frac{W(r_{ij},h)}{\sum_j W(r_{ij},h)} \tag{3.10}$$

The accuracy of the LDD method hinges on the quality of its first and second-order spatial approximations, particularly the gradient and Laplacian operators. As established in Bašić et al. [39], both the gradient operator with first-order consistency and the Laplacian operator with second-order consistency are derived directly from the kernel function itself, rather than from its spatial derivatives as is conventional in SPH-based formulations.

3.2.2 Gradient Operator

The gradient of a scalar field f at point i is approximated using the weighted contributions of neighbouring points j within the compact support radius h:

$$\langle \nabla f \rangle_i = \mathbf{B}_i \sum_{j \in \mathcal{N}_i} W_{ij} \mathbf{r}_{ij} (f_j - f_i) \tag{3.11}$$

where $\mathcal{N}_i$ denotes the set of neighbouring points of point i within radius h, $\mathbf{r}_{ij} = \mathbf{r}_j - \mathbf{r}_i$ is the relative position vector between points i and j, $W_{ij} = W(\mathbf{r}_{ij}, h)$ is the kernel weighting function evaluated at distance $r_{ij} = |\mathbf{r}_{ij}|$, and $\mathbf{B}_i$ is the renormalization tensor that enforces second-order consistency of the gradient approximation. The renormalization tensor is constructed as:

$$\mathbf{B}_i = \left(\sum_{j \in \mathcal{N}_i} W_{ij} \mathbf{r}_{ij} \otimes \mathbf{r}_{ij} \right)^{-1} \tag{3.12}$$

where $\otimes$ denotes the outer tensor product of two vectors. The Equation (3.11) follows from a first-order Taylor expansion of f_j about point i,

$$f_j - f_i = \mathbf{r}_{ij} \cdot \nabla f_i + O(\|\mathbf{r}_{ij}\|^2). \tag{3.13}$$

Multiplying by the weighted vector $W_{ij}\mathbf{r}_{ij}$ and summing over the neighbouring set gives

$$\sum_{j \in \mathcal{N}_i} W_{ij} \mathbf{r}_{ij} (f_j - f_i) \approx \left(\sum_{j \in \mathcal{N}_i} W_{ij} \mathbf{r}_{ij} \otimes \mathbf{r}_{ij} \right) \nabla f_i. \tag{3.14}$$

Inverting the local second-moment matrix therefore yields Equation (3.11). The tensor $\mathbf{B}_i$ is thus a renormalization tensor that corrects the gradient approximation for anisotropy and irregular spacing of the local point cloud.

3.2.3 Laplacian Operator

The discrete Laplacian operator at point i is approximated as:

$$\langle \nabla^2 f \rangle_i = \frac{2d \sum_{j \in \mathcal{N}_i} W_{ij} (f_j - f_i)(1 - \mathbf{r}_{ij} \cdot \mathbf{B}_i \mathbf{o}_i)}{\sum_{j \in \mathcal{N}_i} W_{ij} (1 - \mathbf{r}_{ij} \cdot \mathbf{B}_i \mathbf{o}_i) \|\mathbf{r}_{ij}\|^2} \tag{3.15}$$

where d is the spatial dimensionality of the problem (2 or 3), and $\mathbf{o}_i$ is the offset vector defined as:

$$\mathbf{o}_i = \sum_{j \in \mathcal{N}_i} W_{ij} \mathbf{r}_{ij} \tag{3.16}$$

The offset vector accounts for non-uniformities in the local point distribution and ensures

consistency of the Laplacian approximation even for irregular point clouds. Together, the symmetric renormalization tensor $\mathbf{B}_i$ and the offset vector $\mathbf{o}_i$ characterise the local geometric arrangement of the point cloud and additionally serve as indicators for the identification of free surface points within the LDD framework.

The Equation (3.15) is obtained from the second-order Taylor expansion of f_j about point i,

$$f_j - f_i = \mathbf{r}_{ij} \cdot \nabla f_i + \frac{1}{2}\mathbf{r}_{ij}^T (\nabla^2 f)_i \mathbf{r}_{ij} + O(\|\mathbf{r}_{ij}\|^3). \tag{3.17}$$

Under the assumption that the local support is sufficiently isotropic, the quadratic term may be related to the scalar Laplacian by

$$\mathbf{r}_{ij}^T (\nabla^2 f)_i \mathbf{r}_{ij} \approx \frac{\|\mathbf{r}_{ij}\|^2}{d} \nabla^2 f_i, \tag{3.18}$$

so that

$$\nabla^2 f_i \approx \frac{2d}{\|\mathbf{r}_{ij}\|^2} \left[(f_j - f_i) - \mathbf{r}_{ij} \cdot \nabla f_i \right]. \tag{3.19}$$

The remaining difficulty is that the exact gradient is not known and must itself be approximated from the local point cloud. Using the renormalized gradient operator, Multiplying by W_{ij} and summing over all neighbours gives. Then the Equation (3.19) becomes

$$\nabla^2 f_i \sum_{j \in \mathcal{N}_i} W_{ij} \|\mathbf{r}_{ij}\|^2 \left(1 - \mathbf{r}_{ij} \cdot \mathbf{B}_i \mathbf{o}_i\right) \approx 2d \sum_{j \in \mathcal{N}_i} W_{ij} (f_j - f_i) \left(1 - \mathbf{r}_{ij} \cdot \mathbf{B}_i \mathbf{o}_i\right). \tag{3.20}$$

The correction associated with neighbour asymmetry may be written compactly through $\mathbf{B}_i \mathbf{o}_i$. Finally, dividing both sides by the denominator gives

$$\langle \nabla^2 f \rangle_i = \frac{2d \sum_{j \in \mathcal{N}_i} W_{ij} (f_j - f_i)(1 - \mathbf{r}_{ij} \cdot \mathbf{B}_i \mathbf{o}_i)}{\sum_{j \in \mathcal{N}_i} W_{ij} (1 - \mathbf{r}_{ij} \cdot \mathbf{B}_i \mathbf{o}_i) \|\mathbf{r}_{ij}\|^2}. \tag{3.21}$$

For a perfectly symmetric neighbour cloud, the weighted first-order term cancels under summation. In a general irregular point distribution, however, this cancellation is incomplete. The resulting asymmetry is measured by the offset vector $\mathbf{o}_i = \sum_{j \in \mathcal{N}_i} W_{ij} \mathbf{r}_{ij}$, which vanishes only for a locally balanced support. The quantity $\mathbf{B}_i \mathbf{o}_i$ therefore represents the renormalized geometric bias of the neighbour cloud, and the factor $(1 - \mathbf{r}_{ij} \cdot \mathbf{B}_i \mathbf{o}_i)$ acts as a correction that suppresses the residual first-order error in the Laplacian estimate.

3.2.4 Weighting Function

The cubic spiky kernel adopted as the weighting function in LDD is defined as:

$$W(r_{ij}, h) = \begin{cases} \left(1 - \left(0.4 \times \frac{r_{ij}}{h}\right)\right)^3 & \text{if } r_{ij} \leq h \\ 0 & \text{if } r_{ij} > h \end{cases} \tag{3.22}$$

This kernel possesses compact support, continuity, and positive definiteness, all of which are properties that contribute to the numerical stability and accuracy of the spatial discretization.

3.3 Pressure Poisson Equation Solution

Applying the LDD differential operators to discretize the pressure Poisson equation in space produces a sparse system of linear equations of the form:

$$\mathbf{Ap} = \mathbf{b} \tag{3.23}$$

where $\mathbf{A}$ denotes the sparse coefficient matrix generated by the discretization of the Laplacian operator, $\mathbf{p}$ refers to the vector of unknown pressure values at all computational points, and $\mathbf{b}$ is the right-hand side vector constructed from the velocity material derivative together with the imposed boundary conditions. The resulting system is solved using a matrix-free preconditioned Biconjugate Gradient Stabilized (BiCGSTAB) iterative solver [139], which provides a computationally efficient and low-memory approach well-suited to the large sparse systems encountered in realistic flow simulations.

3.4 Particle Based Dynamics (PBD)

A persistent challenge in Lagrangian numerical methods is the maintenance of a regular and well-distributed spatial arrangement of computational points throughout the duration of the simulation. As points are advected with the local fluid velocity, they tend to accumulate in regions of convergent flow and become sparsely distributed in regions of divergent flow. This progressive deterioration of point regularity degrades the accuracy of the spatial differential operators and can ultimately give rise to numerical instabilities. The LDD method addresses this challenge through the Position Based Dynamics (PBD) technique, a constraint-based regularization approach originally developed within the computer graphics community, which iteratively enforces uniform inter-point spacing to maintain a well-conditioned point distribution throughout the simulation.

3.5 Boundary Condition

The LDD method employs surface mesh elements in three dimensions and line elements in two dimensions, from which boundary or solid points are generated along structural surfaces. To enforce boundary conditions, fluid points located near a wall are orthogonally projected onto the closest boundary element, where a corresponding solid point is then placed. The boundary conditions are enforced directly at these solid points, ensuring accurate representation of wall constraints with respect to the true boundary geometry. The projection procedure

involves computing the orthogonal projection of a fluid point $\mathbf{x}$ onto a line segment AB by first defining the vectors $\mathbf{r_{AX}} = \mathbf{x} - \mathbf{x_A}$ and $\mathbf{r_{AB}} = \mathbf{x_B} - \mathbf{x_A}$, where $\mathbf{x_A}$ and $\mathbf{x_B}$ are the position vectors of the boundary segment endpoints A and B respectively. The scalar projection parameter e is evaluated as:

$$e = \frac{\mathbf{r_{AX}} \cdot \mathbf{r_{AB}}}{\mathbf{r_{AB}} \cdot \mathbf{r_{AB}}} \tag{3.24}$$

When $0 \leq e \leq 1$, the projected point $\mathbf{x_p}$ falls within the boundary segment AB and its position is computed as:

$$\mathbf{x_p} = \mathbf{x_A} + e\mathbf{r_{AB}} \tag{3.25}$$

3.6 Time Integration

Lagrangian advection within the LDD method is carried out through an Adams-Bashforth 2 (AB2) extrapolation, [140]. The position of each computational point i is updated at every time step according to:

$$\mathbf{x}_i^{n+1} = \mathbf{x}_i^n + \mathbf{dx}_i^{n+1} \tag{3.26}$$

where the displacement increment $\mathbf{dx}_i^{n+1}$ is computed via a Lagrangian advection approach with second-order accuracy, following the formulation in [141]:

$$\mathbf{dx}_i^{n+1} = \left[1.5\,\mathbf{u}_i^n - 0.5\,\mathbf{u}_i^{n-1}\right]\delta t \tag{3.27}$$

In this formulation, the displacement at time level $n+1$ is computed as a linearly weighted blend of velocities from the current time level n and the preceding time level $n-1$, with coefficients of 1.5 and 0.5 respectively. The larger weighting assigned to the current velocity reflects the second-order extrapolation character of the AB2 scheme. As an implicit method, this formulation supports larger time steps than explicit schemes, improving computational throughput without sacrificing second-order temporal accuracy, making it well-suited to problems demanding both numerical stability and precision [142].

3.7 Auto Time Stepping

The simulation employs an adaptive time-stepping strategy governed by the Lagrangian Courant-Friedrichs-Lewy (LCFL) condition [143],whereby the time step is continuously adjusted as:

$$\mathrm{LCFL} = \delta t \|\nabla \mathbf{u}\|_\infty \tag{3.28}$$

This condition controls the time step size through the maximum local deformation rate in the flow, measured via the L_∞-norm of the velocity gradient tensor. A key distinction of the LCFL condition relative to its classical Eulerian counterpart is that it carries no explicit dependence on the spatial distribution of the computational points. This characteristic grants the Lagrangian time stepping criterion greater flexibility, permitting larger time steps than those mandated by the more restrictive Eulerian CFL condition under equivalent flow conditions.

3.8 Summary

This chapter has presented the foundational LDD method, which provides the basis for the multiphase, FSI and phase change extensions developed in this thesis. The key features of the LDD method include:

- Construction of second-order spatially consistent gradient and Laplacian operators through the use of renormalization tensors
- Direct operation on surface meshes
- Efficient PBD-based point-cloud regularization
- Robust pressure-velocity coupling through the projection method
- Suitability for complex geometries, free surfaces, and large deformations

The subsequent chapters build upon this foundation to address fluid-structure interaction, multiphase flows with sharp interfaces, heat transfer and phase change phenomena.

4 FLUID STRUCTURE INTERACTION WITH MODAL COUPLING

This chapter presents the fluid-structure interaction (FSI) framework developed within the Lagrangian Differencing Dynamics method. The coupling strategy employs modal superposition techniques to achieve efficient weakly coupled simulations that leverage the inherently Lagrangian nature of both the fluid solver and structural motion. Unlike traditional mesh-based FSI approaches that require complex mesh deformation or remeshing procedures, the proposed method enables direct force transfer from particle distributions to modal coordinates without intermediate mesh mapping operations.

The subsequent sections of this chapter are organised as follows: Section 4.1 establishes the theoretical foundation of modal superposition for structural dynamics, including the derivation of modal equations of motion and the Complementary Function and Particular Integral (CFPI) integration scheme. Section 4.3 details the coupling methodology, describing the workflow for integrating the modal solver with the LDD fluid solver and the procedures for force transfer and mesh deformation.

4.1 Mode Superposition

Structural dynamics problems involving time-varying loads are commonly addressed through the method of modal superposition, which approximates the full dynamic response by combining a selected subset of vibration modes derived from a preliminary modal analysis. Each vibration mode is characterised by two quantities: an eigenfrequency, representing the rate of free oscillation of the system in the absence of external forcing, and a mode shape vector, describing the relative spatial deformation pattern associated with that frequency. These modal properties carry significant practical relevance in the analysis and design of structures subjected to dynamic loading. The modal superposition technique offers substantial reductions in computational cost relative to direct time integration of the full system, provided the structural behaviour remains linear [44, 46]. Its range of applicability is, however, confined to problems where the dominant excitation frequencies are well below the higher modal frequencies of the structure [114, 112].

For a discretized structural system, the equation of motion can be expressed in matrix form as:

$$M\ddot{u} + C\dot{u} + Ku = f(t) \tag{4.1}$$

Here M, C, and K are the $N \times N$ mass, damping, and stiffness matrices respectively, assembled through spatial discretization of the structural domain, where N is the total number of degrees of freedom. The nodal displacement vector is denoted u, and $f(t)$ is the externally applied load vector. Mass normalisation is applied throughout so that the modal mass is unity for every mode, which simplifies the evaluation of modal participation factors.

The eigenfrequencies and mode shapes entering the superposition are extracted by solving the undamped free vibration problem posed as an eigenvalue problem:

$$(-\omega^2 M + K)\Phi = 0, \qquad \Phi \neq 0 \tag{4.2}$$

The columns of the modal matrix $\Phi = \{\Phi_1, \Phi_2, \ldots, \Phi_n\}$ contain the n mode shape vectors of the system. Structural discretization and solution of Equation (4.2) are carried out using the FEM. Eigenvalue extraction algorithms fall into two broad families: transformation methods, which convert the problem into a standard form amenable to bulk extraction, and tracking methods, which isolate eigenvalues one at a time through iteration. The present study adopts the Lanczos algorithm, which draws on characteristics of both families. Mode shapes are scaled under the mass normalisation convention, whereby each mode shape satisfies unit modal mass, ensuring consistency across modes in the subsequent superposition.

Having obtained the modal basis, the nodal displacement field is projected onto the modal coordinates through the expansion:

$$u(t) = \sum_{i=1}^{n} \Phi y_i(t) \tag{4.3}$$

where $y(t)$ collects the generalised or modal displacements. In practice, only the lowest few modes are retained, as higher modes typically contribute negligibly to the response under low-frequency excitation. Substituting Equation (4.3) into Equation (4.1) and premultiplying by Φ^T gives:

$$\Phi^T M \Phi \ddot{y}(t) + \Phi^T C \Phi \dot{y}(t) + \Phi^T K \Phi y(t) = \Phi^T f(t) \tag{4.4}$$

Decoupling this system into n independent single-degree-of-freedom equations requires diagonalisation of the damping term. This is achieved by adopting the Rayleigh proportional damping hypothesis, expressing the damping matrix as:

$$C = a_K K + a_M M \tag{4.5}$$

where a_M and a_K are scalar coefficients controlling the mass-proportional and stiffness-proportional contributions to damping respectively. Exploiting the orthogonality of the mass-

normalised mode shapes reduces the coupled system to n decoupled equations, one per retained mode:

$$\ddot{y}_i(t) + 2\omega_i\zeta_i\dot{y}_i(t) + \omega_i^2 y_i(t) = \Phi_i^T f(t) \tag{4.6}$$

The scalar ζ_i is the modal damping ratio for mode i, measuring the fraction of critical damping present in that mode. Any time integration scheme may be applied to advance Equation (4.6). In the present work the Complementary Function and Particular Integral (CFPI) method is selected [112], decomposing the solution into a homogeneous complementary part and a forced particular part.

The complementary solution reads:

$$\begin{aligned} y_t &= y_{t-1}\cdot\mathbf{E}\cdot\left(C + \frac{\zeta}{s}\cdot\mathcal{S}\right) + \dot{y}_{t-1}\cdot\mathbf{E}\cdot\frac{1}{\omega_n\cdot s}\cdot\mathcal{S} \\ \dot{y}_t &= \dot{y}_{t-1}\cdot\mathbf{E}\cdot\left(C - \frac{\zeta}{s}\cdot\mathcal{S}\right) - y_{t-1}\cdot\mathbf{E}\cdot\frac{\omega_n}{s}\cdot\mathcal{S} \end{aligned} \tag{4.7}$$

where y_t, $\dot{y}_t$ denote modal displacement and velocity at the current time step, and y_{t-1}, $\dot{y}_{t-1}$ are the corresponding quantities from the preceding step.

The particular solution reads:

$$\begin{aligned} y_t &= -\mathbf{E}\cdot F_{t-1}\cdot\left(\frac{\zeta\omega_n\delta t + 2\zeta^2 - 1}{\omega_n^2\mathcal{W}}\cdot\mathcal{S} + \frac{\omega_n\delta t + 2\zeta}{\omega_n^3\delta t}\cdot\mathcal{C}\right) \\ &\quad + F_{t-1}\cdot\frac{2\zeta}{\omega_n^3\delta t} + \mathbf{E}\cdot F_t\cdot\left(\frac{2\zeta^2-1}{\omega_n^2\mathcal{W}}\cdot\mathcal{S} + \frac{2\zeta}{\omega_n^3\delta t}\cdot\mathcal{C}\right) + F_t\cdot\frac{\omega_n\delta t - 2\zeta}{\omega_n^3\delta t} \\ \dot{y}_t &= \mathbf{E}\cdot F_{t-1}\cdot\left(\frac{\zeta_i + \omega_n\delta t}{\omega_n\cdot wts}\cdot\mathcal{S} + \frac{1}{\omega_n^2\delta t}\cdot\mathcal{C}\right) - F_{t-1}\cdot\frac{1}{\omega_n^2\delta t} \\ &\quad - \mathbf{E}\cdot F_t\cdot\left(\frac{\zeta_i}{\omega_n\cdot wts}\cdot\mathcal{S} + \frac{1}{\omega_n^2\delta t}\cdot\mathcal{C}\right) + F_t\cdot\frac{1}{\omega_n^2\delta t} \end{aligned} \tag{4.8}$$

The auxiliary coefficients appearing in both solutions are:

$$s = \sqrt{1-\zeta^2}, \quad \mathcal{W} = \omega_n\cdot\delta t\cdot s, \quad \mathbf{E} = \exp(-\zeta\cdot\omega_n\cdot\delta t), \quad \mathcal{S} = \sin(W), \quad \mathcal{C} = \cos(W) \tag{4.9}$$

The total modal response at each step is the sum of the two contributions. The CFPI scheme is preferred over the Newmark-beta method in this context because it has been shown to accumulate smaller numerical errors when resolving high-frequency modal oscillations [112]. A further practical benefit is that each modal equation is advanced independently using only its own displacement and velocity, so the structural integration can proceed at a time step entirely decoupled from the constraints imposed by the fluid solver. High-frequency structural content can therefore be accurately captured regardless of the fluid time step size.

4.2 Force Transfer from Fluid to Structure

At each coupling step, the fluid load acting on the deformable structure is evaluated at the structural surface vertices by interpolating the surrounding LDD pressure field to the vertex locations and converting the resulting pressure into discrete nodal forces. Let $\mathbf{x}_i^v$ denote the position of structural vertex i, $\mathbf{n}_i$ its outward unit normal, and A_i its associated representative surface area. The pressure-induced force transferred from the fluid to the structure is approximated as

$$\mathbf{F}_i^f = p_i^* A_i \mathbf{n}_i, \tag{4.10}$$

where p_i^* is the fluid pressure interpolated to the structural vertex location.

The interpolated pressure is obtained from neighbouring fluid points located within a prescribed interpolation radius around the structural vertex. Denoting the neighbouring set by $\mathcal{N}_i^v$, the interpolated pressure is computed as a weighted average,

$$p_i^* = \frac{\sum_{j \in \mathcal{N}_i^v} W_{ij}\, p_j}{\sum_{j \in \mathcal{N}_i^v} W_{ij}}, \tag{4.11}$$

where p_j is the pressure at fluid point j and W_{ij} is the interpolation kernel evaluated from the distance between the structural vertex and the neighbouring fluid point. In this manner, the fluid pressure field is projected onto the structural surface in a meshless and locally weighted form.

To ensure that the applied force acts consistently with the local body orientation, the sign of the interpolated pressure force is adjusted using the relative arrangement of the neighbouring fluid points and the structural surface normal. This correction ensures that the transferred traction is directed inward or outward in a manner consistent with the physical pressure loading on the body surface.

Accordingly, the total discrete force vector applied to the structural model is assembled from the set of nodal forces $\mathbf{F}_i^f$ evaluated over all structural surface vertices. These nodal forces are then used as the external forcing input to the modal structural equations of motion.

In the present implementation, only the pressure contribution to the fluid traction is included in the force transfer procedure. Thus, the structural forcing is approximated as pressure-dominated loading, and the viscous shear contribution is neglected. In continuum form, the complete fluid traction would be written as

$$\mathbf{t}^f = \left(-p\mathbf{I} + \boldsymbol{\sigma}^{visc}\right)\mathbf{n}, \tag{4.12}$$

where $\boldsymbol{\sigma}^{visc}$ denotes the viscous stress tensor. In the current formulation, only the $-p\mathbf{n}$ component is transferred to the structure. This approximation is appropriate for the validation cases considered in this thesis, where the dominant structural response is governed primar-

ily by hydrodynamic pressure loading. The inclusion of viscous shear transfer constitutes a natural extension of the present coupling framework and is left for future work.

4.3 Methodology

The FSI framework couples the modal superposition formulation of Section 4.1 with the LDD fluid solver through a two-way weakly coupled scheme. At every fluid time step, Equation (4.6) is advanced independently for each retained mode using the CFPI integrator, producing a set of generalised displacements $y(t)$. The physical deformation field is then recovered via Equation (4.3) and imposed on the fluid mesh, so that the subsequent fluid solution reflects the updated structural geometry and yields revised pressure and velocity fields [112]. The modal basis, encompassing the natural frequencies and mass-normalised mode shapes of the structure, is determined independently prior to the commencement of the CFD computation, either through analytical expressions or via a dedicated modal analysis solver.

The coupled solution procedure is summarised in Figure 4.1 and proceeds through the following steps:

1. Compute mass-normalised mode shapes and natural frequencies $\omega_1, \omega_2, \ldots, \omega_n$ in the pre-processing stage.

2. Set initial and boundary conditions, including any prescribed initial structural displacement.

3. Where the fluid and structural meshes do not share a conforming interface, construct Radial Basis Function (RBF) interpolants to map mode shape data from the structural mesh onto the fluid mesh [144].

4. At each time step δt:

   (a) Compute the fluid pressure forces acting on the structural surface.

   (b) Advance Equation (4.6) for each mode using the CFPI method.

   (c) Reconstruct the global displacement via Equation (4.3) and update the mesh geometry accordingly.

   (d) Advance the fluid solver on the updated deformed geometry to recover the flow field solution at time $t + \delta t$.

In the pre-processing stage, the modal basis is assembled and supplied to the LDD solver alongside the prescribed initial and boundary conditions of the problem. RBF interpolation is invoked only when mesh non-conformity requires projection of the mode shapes onto fluid mesh nodes. Within each time step, pressure forces extracted from the fluid solution drive

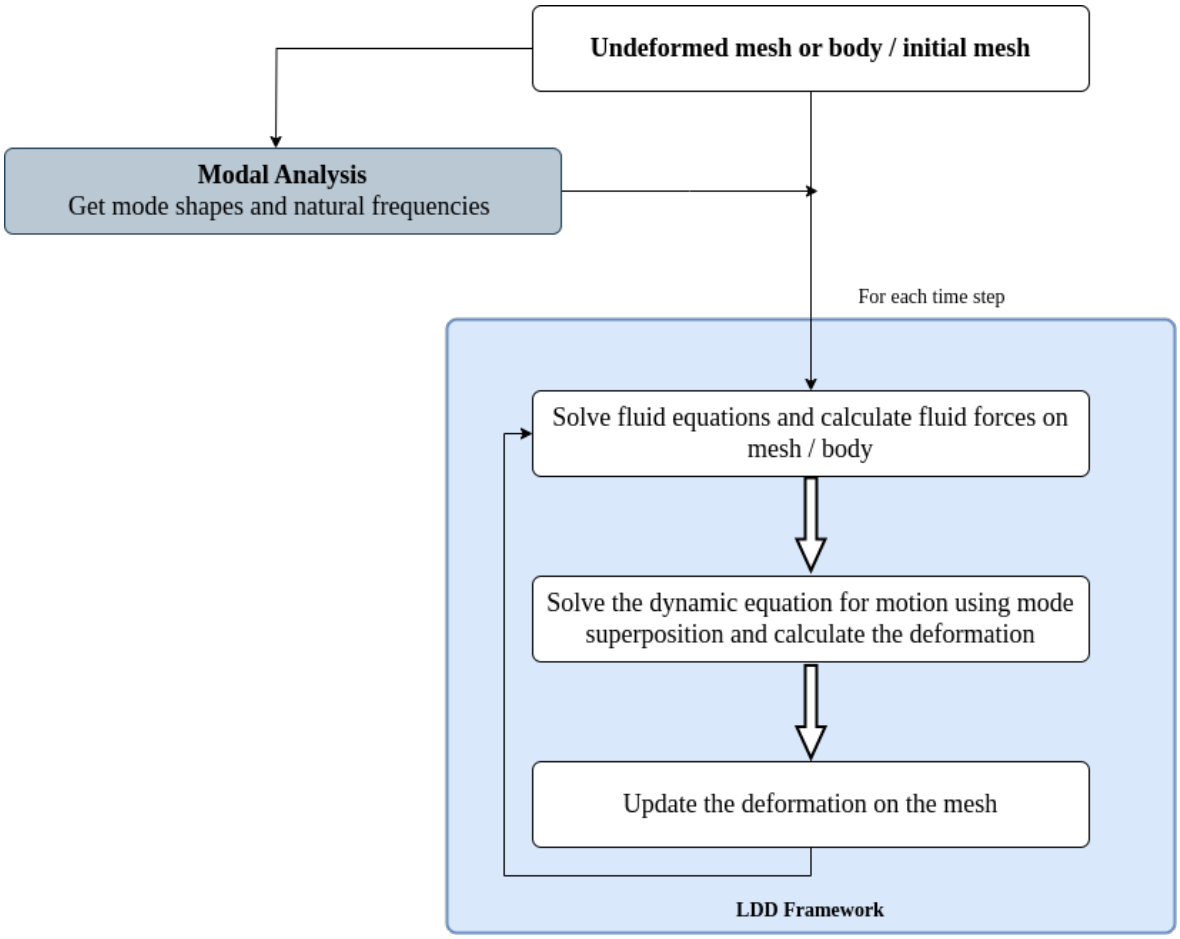

Figure 4.1. Flowchart of the LDD-based FSI solver illustrating the weakly coupled modal integration procedure.

the modal integrator, which returns updated generalised displacements. These are projected back onto physical space to deform the mesh, and the fluid solver is then advanced on the updated geometry to close the coupling loop.

4.4 Numerical Procedure of the Modal Superposition Method

4.4.1 Step 1: Governing Dynamic Equation

The governing system of Equation (4.1), comprises of M, C, and K as the $N \times N$ mass, damping, and stiffness matrices respectively. For large values of N, direct solution of this system becomes computationally prohibitive since it constitutes a coupled set of N ordinary differential equations. Consequently, the application of modal superposition aims to decouple the equations, thereby improving computational efficiency.

4.4.2 Step 2: Eigenvalue Problem (Undamped Free Vibration)

Setting $f(t) = 0$ and $C = 0$, and assuming a harmonic solution $u(t) = \Phi e^{i\omega t}$, substitution into Equation (4.1) gives:

$$M\left(-\omega^2\Phi\right)e^{i\omega t} + K\Phi e^{i\omega t} = 0 \tag{4.13}$$

Dividing through by $e^{i\omega t} \neq 0$ yields the generalised eigenvalue problem:

$$\left(-\omega^2 M + K\right)\Phi = 0, \qquad \Phi \neq 0 \tag{4.14}$$

Solving Equation (4.14) yields n eigenvalues $\omega_1^2, \omega_2^2, \ldots, \omega_n^2$ (natural frequencies) and n corresponding eigenvectors $\Phi_1, \Phi_2, \ldots, \Phi_n$ (mode shapes), which are assembled into the *modal matrix*:

$$\Phi = \left[\Phi_1,\ \Phi_2,\ \ldots,\ \Phi_n\right] \tag{4.15}$$

4.4.3 Step 3: Mass Normalisation and Orthogonality

Mode shapes are scaled so that the modal mass equals unity for each mode i:

$$\Phi_i^T M \Phi_i = 1 \tag{4.16}$$

A fundamental consequence of the eigenvalue problem is the orthogonality of mass-normalised mode shapes:

$$\Phi_i^T M \Phi_j = a_{ij}, \qquad \Phi_i^T K \Phi_j = \omega_i^2 a_{ij} \tag{4.17}$$

where a_{ij} is the Kronecker delta. In matrix form, Equations (4.16)–(4.17) become:

$$\Phi^T M \Phi = I, \qquad \Phi^T K \Phi = \Omega^2 = \mathrm{diag}\left(\omega_1^2,\ \omega_2^2,\ \ldots,\ \omega_n^2\right) \tag{4.18}$$

4.4.4 Step 4: Modal Coordinate Transformation

The physical displacement $u(t)$ is expressed as a linear combination of mode shapes:

$$u(t) = \sum_{i=1}^{n} \Phi_i y_i(t) = \Phi y(t) \tag{4.19}$$

where $y(t)$ is the vector of modal coordinates (generalized displacements). This represents a change of basis from physical space to modal space. Differentiating with respect to time:

$$\dot{u}(t) = \Phi \dot{y}(t), \qquad \ddot{u}(t) = \Phi \ddot{y}(t) \tag{4.20}$$

4.4.5 Step 5: Substitution into the Governing Equation

Substituting $u = \Phi y$ into Equation (**??**):

$$M\Phi\ddot{y}(t) + C\Phi\dot{y}(t) + K\Phi y(t) = f(t) \tag{4.21}$$

Pre-multiplying every term by Φ^T:

$$\Phi^T M\Phi\ddot{y}(t) + \Phi^T C\Phi\dot{y}(t) + \Phi^T K\Phi y(t) = \Phi^T f(t) \tag{4.22}$$

Applying the orthogonality relations from Equation (4.18), the mass and stiffness terms simplify immediately:

$$\ddot{y}(t) + \Phi^T C\Phi\dot{y}(t) + \Omega^2 y(t) = \Phi^T f(t) \tag{4.23}$$

The damping term $\Phi^T C\Phi$ is not yet diagonal and must be addressed separately.

4.4.6 Step 6: Diagonalisation of Damping via Rayleigh Proportional Damping

To decouple the damping term, the Rayleigh (proportional) damping model is adopted, in which C is written as a weighted combination of M and K:

$$C = a_M M + a_K K \tag{4.24}$$

where a_M and a_K are the mass- and stiffness-proportional damping coefficients, respectively. Pre- and post-multiplying by Φ^T and Φ, and using Equation (4.18):

$$\Phi^T C\Phi = a_M \underbrace{\Phi^T M\Phi}_{I} + a_K \underbrace{\Phi^T K\Phi}_{\Omega^2} = a_M I + a_K\Omega^2 = \mathrm{diag}\left(a_M + a_K\omega_i^2\right) \tag{4.25}$$

The diagonal matrix in Equation (4.25) is identified with the standard SDOF damping term $2\zeta_i\omega_i$:

$$2\zeta_i\omega_i = a_M + a_K\omega_i^2 \implies \zeta_i = \frac{a_M}{2\omega_i} + \frac{a_K\omega_i}{2} \tag{4.26}$$

4.4.7 Step 7: Fully Decoupled SDOF Equations of Motion

Substituting Equations (4.25) and (4.26) back into Equation (4.23), the coupled $N \times N$ system reduces to n independent SDOF equations. For the i-th mode:

$$\boxed{\ddot{y}_i(t) + 2\zeta_i\omega_i\dot{y}_i(t) + \omega_i^2 y_i(t) = \Phi_i^T f(t)} \tag{4.27}$$

Each mode i is now completely decoupled from all other modes.

4.4.8 Step 8: Solution via the Complementary Function and Particular Integral (CFPI) Method

Each decoupled equation (4.27) is solved analytically over a single time step δt, assuming the modal force $F_i(t) = \Phi_i^T f(t)$ varies linearly within the step. The following shorthand coefficients are introduced:

$$s = \sqrt{1-\zeta_i^2}, \quad \mathcal{W} = \omega_i\,\delta t\,s, \quad \mathcal{E} = e^{-\zeta_i\omega_i\delta t}, \quad \mathcal{S} = \sin(\mathcal{W}), \quad \mathcal{C} = \cos(\mathcal{W}) \tag{4.28}$$

where s is the damped frequency ratio and $\mathcal{W}$ is the damped natural frequency scaled by the time step.

Part A – Complementary Solution (response to initial conditions)

The exact analytical solution to the homogeneous equation is:

$$y_t^{(c)} = y_{t-1}\cdot\mathcal{E}\left(\mathcal{C}+\frac{\zeta_i}{s}\mathcal{S}\right)+\dot{y}_{t-1}\cdot\mathcal{E}\cdot\frac{\mathcal{S}}{\omega_i\,s} \tag{4.29}$$

$$\dot{y}_t^{(c)} = \dot{y}_{t-1}\cdot\mathcal{E}\left(\mathcal{C}-\frac{\zeta_i}{s}\mathcal{S}\right)-y_{t-1}\cdot\mathcal{E}\cdot\frac{\omega_i}{s}\mathcal{S} \tag{4.30}$$

Part B – Particular Solution (response to linearly interpolated load)

$$\begin{aligned} y_t^{(p)} = {} & -\mathcal{E}\cdot F_{t-1}\left(\frac{\zeta_i\omega_i\delta t+2\zeta_i^2-1}{\omega_i^2\,\mathcal{W}}\mathcal{S}+\frac{\omega_i\delta t+2\zeta_i}{\omega_i^3\,\delta t}\mathcal{C}\right)+F_{t-1}\cdot\frac{2\zeta_i}{\omega_i^3\,\delta t} \\ & +\mathcal{E}\cdot F_t\left(\frac{2\zeta_i^2-1}{\omega_i^2\,\mathcal{W}}\mathcal{S}+\frac{2\zeta_i}{\omega_i^3\,\delta t}\mathcal{C}\right)+F_t\cdot\frac{\omega_i\delta t-2\zeta_i}{\omega_i^3\,\delta t} \end{aligned} \tag{4.31}$$

$$\begin{aligned} \dot{y}_t^{(p)} = {} & \mathcal{E}\cdot F_{t-1}\left(\frac{\zeta_i+\omega_i\delta t}{\omega_i\,\mathcal{W}\,s}\mathcal{S}+\frac{1}{\omega_i^2\,\delta t}\mathcal{C}\right)-F_{t-1}\cdot\frac{1}{\omega_i^2\,\delta t} \\ & -\mathcal{E}\cdot F_t\left(\frac{\zeta_i}{\omega_i\,\mathcal{W}\,s}\mathcal{S}+\frac{1}{\omega_i^2\,\delta t}\mathcal{C}\right)+F_t\cdot\frac{1}{\omega_i^2\,\delta t} \end{aligned} \tag{4.32}$$

Total Solution at Each Time Step

At time t, the complete modal displacement and velocity are assembled through the superposition of the complementary function and particular integral solutions:

$$y_t = y_t^{(c)} + y_t^{(p)}, \qquad \dot{y}_t = \dot{y}_t^{(c)} + \dot{y}_t^{(p)} \tag{4.33}$$

4.4.9 Step 9: Recovery of Physical Displacements

Once the modal coordinates $y_i(t)$ are obtained for the first $m \ll n$ significant modes, the physical displacement field is recovered by the modal superposition:

$$u(t) = \sum_{i=1}^{m} \Phi_i y_i(t) = \Phi_{(m)} y_{(m)}(t) \tag{4.34}$$

where $\Phi_{(m)}$ contains only the first m mode shapes retained in the analysis. This truncation is the key computational saving of the modal superposition method.

4.4.10 Summary of the Mode Superposition Method

The complete derivation proceeds as follows:

1. Start with the coupled N-DOF system (Equation (**??**)).
2. Solve the generalised eigenvalue problem (Equation (4.14)) to obtain natural frequencies ω_i and mass-normalised mode shapes Φ_i.
3. Exploit the orthogonality of mode shapes (Equation (4.18)) to diagonalise mass and stiffness.
4. Apply the modal coordinate transformation $u = \Phi y$ (Equation (4.19)) and pre-multiply by Φ^T (Equation (4.22)).
5. Introduce Rayleigh proportional damping (Equation (4.24)) to diagonalise the damping term (Equation (4.25)).
6. Obtain n independent SDOF equations in modal space (Equation (4.27)).
7. Solve each SDOF equation using the CFPI method (Equations (4.29)–(4.33)).
8. Recover physical displacements by superposition (Equation (4.34)).

5 MULTIPHASE LDD (MP-LDD) WITH SHARP INTERFACES

This chapter presents the extension of the Lagrangian Differencing Dynamics (LDD) framework to multiphase flows, establishing the foundation for Multiphase LDD (MP-LDD). The key developments include variable coefficient operators that maintain second-order consistency across discontinuous property fields, a systematic approach to particle regularization that prevents interpenetration while preserving interface sharpness, and an efficient split-scheme solver for handling flows with density ratios as high as 1000:1.

The chapter is organized as follows: Section 5.1 introduces the variable coefficient Laplacian operator adapted for multiphase flows with discontinuous density and viscosity fields. The multiphase pressure and velocity solvers are detailed, demonstrating how a single pressure equation can robustly handle large property ratios. A novel Atwood number-based position-based dynamics (PBD) regularization scheme is presented, which ensures sharp interface representation without artificial mixing of phases. The split-scheme solution strategy is described, outlining the sequential coupling of advection, diffusion, and projection steps within the Lagrangian framework. The complete MP-LDD solver workflow is synthesized at the end of the chapter, providing a comprehensive view of the numerical implementation for each time step.

5.1 Multiphase Extension of LDD

The MP-LDD approach, which adapts the LDD framework for multiphase flows, emerges as a logical and systematic evolution of the single-phase incompressible formulation. The transition to multiphase flow introduces additional physical complexity, primarily arising from the presence of density and viscosity discontinuities across fluid interfaces, which must be handled within the existing LDD approximation architecture.

5.1.1 Variable Laplacian for MP-LDD

To handle spatially varying fluid properties across phase interfaces, a variable coefficient Laplacian operator is introduced into the MP-LDD framework. Drawing on the formulation discussed by Gibou et al. [145] and incorporating it into the LDD Laplacian presented by

Bašić et al. [39], the generalised variable coefficient Laplacian takes the following discrete form:

$$\langle \nabla \cdot (\phi \nabla f) \rangle_i = \frac{2d \sum_j W_{ij} L_{ij} \left(\frac{\phi_i + \phi_j}{2} \right) (f_j - f_i)}{\sum_j W_{ij} L_{ij} \|\mathbf{x}_{ij}\|^2} \tag{5.1}$$

This operator serves a dual purpose within MP-LDD: it is employed to evaluate the pressure Laplacian when fluid phases of differing densities are present, and to compute the velocity Laplacian in configurations involving spatially varying viscosity.

5.1.2 Multiphase Pressure Solver

Determination of both the pressure and velocity fields across the discretized computational domain is required to advance the incompressible Navier-Stokes equations in time. The pressure field is determined by solving the PPE, which following Bašić et al. [39] is expressed as:

$$\nabla \cdot \left(\frac{\nabla p}{\rho} \right) = -\frac{(\nabla \cdot \mathbf{u})^n - (\nabla \cdot \mathbf{u})^{n-1}}{\delta t} \tag{5.2}$$

where $(\nabla \cdot \mathbf{u})^n$ and $(\nabla \cdot \mathbf{u})^{n-1}$ are the velocity divergence fields at the current and preceding time steps respectively, and δt is the time step size. In an incompressible flow the velocity field must remain divergence-free at all times. Consequently, the divergence at the previous time step satisfies $(\nabla \cdot \mathbf{u})^{n-1} = 0$ exactly. In practice, however, numerical errors introduced during the Lagrangian advection step render $(\nabla \cdot \mathbf{u})^n$ non-zero. The role of the PPE is therefore to determine a pressure field that restores the solenoidal property of the velocity, reducing the PPE to:

$$\nabla \cdot \left(\frac{\nabla p}{\rho} \right) = -\frac{(\nabla \cdot \mathbf{u})^n}{\delta t} \tag{5.3}$$

Within the Lagrangian LDD framework, the time step is related to the spatial resolution Δr and the local velocity magnitude $\|\mathbf{u}\|$ through the expression $\delta t = \Delta r / \|\mathbf{u}\|$ as established in [146]. Substituting this relationship into the PPE yields the following working form evaluated at point i:

$$\nabla \cdot \left(\frac{\nabla p}{\rho} \right) = -\frac{(\nabla \cdot \mathbf{u})^n \|\mathbf{u}\|}{\Delta r} = b_i \tag{5.4}$$

The right-hand side b_i is discretized using the MP-LDD gradient approximation from Equation (3.11), with the scaling coefficient $C_i = \|\mathbf{u}\| / \Delta r$:

$$b_i = -C_i \langle \nabla \cdot \mathbf{u} \rangle_i^n = -C_i \sum_j W_{ij} (\mathbf{u}_j^n - \mathbf{u}_i^n) \cdot \mathbf{B}_i \cdot \mathbf{x}_{ij} \tag{5.5}$$

where C_i constitutes the known right-hand side coefficient of the PPE linear system. The left-hand side is discretized by applying the variable Laplacian operator of Equation (5.1) with the coefficient ϕ set to the inverse density $1/\rho$, yielding:

$$\left\langle \nabla \cdot \left(\frac{\nabla p}{\rho} \right) \right\rangle_i = \frac{2d \sum_j W_{ij} L_{ij} \left(\frac{\frac{1}{\rho_i} + \frac{1}{\rho_j}}{2} \right) (p_j - p_i)}{\sum_j W_{ij} L_{ij} \|\mathbf{x}_{ij}\|^2} \tag{5.6}$$

Absorbing the known prefactor $2d/\sum_j W_{ij} L_{ij} \|\mathbf{x}_{ij}\|^2$ into the right-hand side b_i produces the simplified working equation:

$$\sum_j W_{ij} L_{ij} \left(\frac{\frac{1}{\rho_i} + \frac{1}{\rho_j}}{2} \right) (p_j - p_i) = b_i \tag{5.7}$$

where p_i and p_j are the unknown pressures, collectively denoted x_i. The coefficient matrix entries associated with the unknown at point i are:

$$A_i = \begin{cases} A_{ii} = -\sum_j W_{ij} L_{ij} \left(\frac{\frac{1}{\rho_i} + \frac{1}{\rho_j}}{2} \right) & \text{for } i = j \\ A_{ij} = W_{ij} L_{ij} \left(\frac{\frac{1}{\rho_i} + \frac{1}{\rho_j}}{2} \right) & \text{for } i \neq j \end{cases} \tag{5.8}$$

The PPE is thereby cast as a sparse linear system $A_i x_i = b_i$, which is solved using a matrix-free Preconditioned Biconjugate Gradient Stabilized (PBiCGSTAB) solver [139]. The matrix-free implementation avoids explicit assembly and storage of the coefficient matrix, reducing both memory requirements and computational overhead. Preconditioning transforms the original system into a form with more favourable spectral properties, accelerating iterative convergence. Selecting the preconditioner $M_i = A_i$ produces a diagonally dominant preconditioned system:

$$M_i^{-1} A_i x_i = M_i^{-1} b_i \tag{5.9}$$

The resulting preconditioned system $M_i^{-1} A_i$ exhibits eigenvalues concentrated near unity, which substantially improves the convergence rate of the iterative solver.

At boundary points, illustrated in Figure 5.1, a Neumann-type pressure boundary condition is derived by projecting the momentum equation onto the wall-normal direction $\mathbf{n}$:

$$\mathbf{n} \cdot \nabla p = \rho \, \mathbf{n} \cdot \left(-\frac{D\mathbf{u}}{Dt} + \nu \nabla^2 \mathbf{u} + \mathbf{g} + \frac{1}{\rho} \mathbf{F}_{s+d} \right) \tag{5.10}$$

Imposing a no-slip condition at the wall, $\mathbf{u}_w = 0$, and introducing δ as the normal distance from the fluid point to the wall, the normal pressure gradient and material acceleration are approximated as:

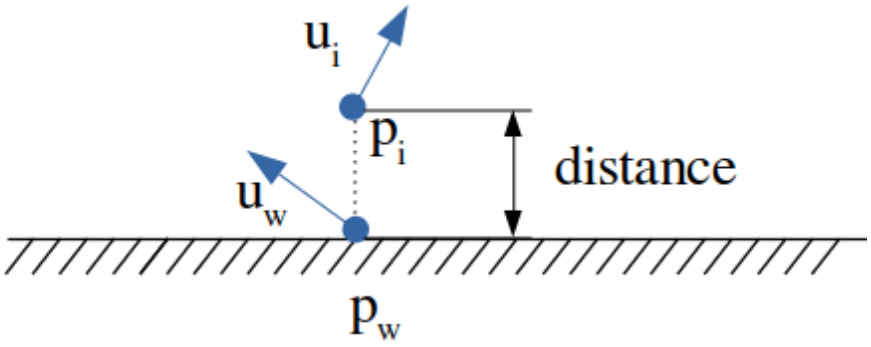

Figure 5.1. Modeling of boundary/solid points and the pressure at those points.

$$\mathbf{n} \cdot \nabla p = \frac{p_w - p_i}{\delta}, \qquad \frac{D\mathbf{u}}{Dt} = \frac{\mathbf{u}_w - \mathbf{u}_i}{\delta t}$$

For boundaries separating identical fluid phases and in inertia-dominated flow regimes, surface tension contributions are negligible. Setting $p_w = p_j$ and substituting into Equation (5.10) yields the boundary pressure condition:

$$(p_j - p_i) = \delta \left(\rho \, \mathbf{n} \cdot \left(\frac{\mathbf{u}_i - \mathbf{u}_w}{\delta t} + \frac{\mathbf{g}}{\rho} + \nu \nabla^2 \mathbf{u} \right) \right) \tag{5.11}$$

Once the pressure field is obtained, the pressure acceleration is evaluated using the LDD gradient operator of Equation (3.11), as established in Bašić et al. [39]:

$$\left\langle \frac{1}{\rho} \nabla p \right\rangle_i = \frac{1}{\rho_i} \left(\mathbf{B}_i \sum_j W_{ij} \, \mathbf{x}_{ij} \, (p_j - p_i) \right) \tag{5.12}$$

Solving the PPE at each time step corrects the spurious divergence introduced during advection and restores the incompressibility condition $\nabla \cdot \mathbf{u} = 0$ throughout the fluid domain.

5.1.3 Multiphase Velocity Solver

With the pressure field determined, the velocity field is advanced in time using a variable time step BDF2 scheme for temporal discretization [147], which approximates time derivatives using data from two preceding time levels and yields a second-order accurate implicit formulation. This contrasts with the original single-phase LDD implementation, which employs an explicit scheme [43]. The BDF2 material derivative approximation takes the form:

$$\frac{D\mathbf{u}}{Dt} = \frac{1}{\delta t} \left[\left(\frac{1 + 2\alpha_t}{1 + \alpha_t} \right) \mathbf{u}^{n+1} - (1 + \alpha_t) \mathbf{u}^n + \left(\frac{\alpha_t^2}{1 + \alpha_t} \right) \mathbf{u}^{n-1} \right] \tag{5.13}$$

where $\mathbf{u}^{n+1}$, $\mathbf{u}^n$, and $\mathbf{u}^{n-1}$ are the velocity vectors at the future, current, and previous time levels respectively, and $\alpha_t = \delta t^n / \delta t^{n-1}$ is the ratio of consecutive time step sizes. Substituting

into the momentum equation (2.2) and collecting terms gives:

$$\frac{1}{\delta t}\left[\left(\frac{1+2\alpha_t}{1+\alpha_t}\right)\mathbf{u}^{n+1}-(1+\alpha_t)\mathbf{u}^{n}+\left(\frac{\alpha_t^2}{1+\alpha_t}\right)\mathbf{u}^{n-1}\right]=-\frac{1}{\rho}\nabla p+\nu\nabla^2\mathbf{u}^{n+1}+\mathbf{g}+\frac{1}{\rho}\mathbf{F}_{s+d} \tag{5.14}$$

Introducing the coefficients $C_L=\delta t\left(\frac{1+\alpha_t}{1+2\alpha_t}\right)$, $C_n=\frac{(1+\alpha_t)^2}{1+2\alpha_t}$, $C_{n-1}=-\frac{\alpha_t^2}{1+2\alpha_t}$, and $C_{n+1}=\delta t\left(\frac{1+\alpha_t}{1+2\alpha_t}\right)$, and rearranging with the unknown $\mathbf{u}^{n+1}$ on the left and all known quantities on the right yields the discrete velocity equation:

$$\mathbf{u}^{n+1}-C_L\nu\nabla^2\mathbf{u}^{n+1}=C_n\mathbf{u}^{n}+C_{n-1}\mathbf{u}^{n-1}+C_{n+1}\left(-\frac{1}{\rho}\nabla p+\mathbf{g}+\frac{1}{\rho}\mathbf{F}_{s+d}\right) \tag{5.15}$$

For inertia-dominated flows where surface tension and dynamic contact angle forces are negligible, the right-hand side is denoted q_i. Applying the variable Laplacian of Equation (5.1) to discretize the viscous term with $\phi=\nu$ gives:

$$\mathbf{u}_i^{n+1}-C_L\frac{2d\sum_j W_{ij}L_{ij}\left(\frac{\nu_i+\nu_j}{2}\right)(\mathbf{u}_j^{n+1}-\mathbf{u}_i^{n+1})}{\sum_j W_{ij}L_{ij}\|\mathbf{x}_{ij}\|^2}=q_i \tag{5.16}$$

Absorbing the known denominator into C_i simplifies this to:

$$\mathbf{u}_i^{n+1}-C_i\sum_j W_{ij}L_{ij}\left(\frac{\nu_i+\nu_j}{2}\right)(\mathbf{u}_j^{n+1}-\mathbf{u}_i^{n+1})=q_i \tag{5.17}$$

Equation (5.17) is solved using the same matrix-free PBiCGSTAB solver as the pressure equation [139]. A single pressure equation and a single velocity equation are solved simultaneously for both fluid phases, rather than maintaining separate equations per phase. Point positions are subsequently updated through Lagrangian advection using Equation (3.27).

5.1.4 A Structured Method for Point Cloud Regularization

The discrete differential operators in LDD tend to align computational points with local streamlines, which progressively induces anisotropic point distributions over the course of a simulation. Such non-uniformity degrades the accuracy of the spatial approximations and compromises volumetric conservation. Analogous issues arise in ISPH and MPS methods and are typically addressed through particle shifting algorithms that redistribute particles after the advection step to recover a more uniform spatial arrangement [148, 149, 150].

The MP-LDD framework employs Position-Based Fluid (PBF) simulation, founded on the Position Based Dynamics (PBD) paradigm, to perform point cloud regularization following each advection step. PBF is well established in the computer graphics and fluid simulation communities due to its stable behaviour and ease of implementation [151, 152, 153].

Its central mechanism is a density constraint that drives the point distribution toward a target rest density, ensuring physical consistency of the fluid representation throughout the simulation [154, 43]. Each computational point i is characterised by its position $\mathbf{x}_i$, velocity $\mathbf{u}_i$, and current density ρ_{icurr}, with the target rest density denoted ρ_0.

The density constraint for point i within the PBF framework is defined as:

$$P_i(\mathbf{x}_1,\ldots,\mathbf{x}_n) = \frac{\rho_{icurr}}{\rho_0} - 1 \tag{5.18}$$

Assuming unit density for all points, the current density is approximated as:

$$\rho_{icurr} = \sum_j \rho_{jcurr} W(\mathbf{x}_j - \mathbf{x}_i, h) \simeq \sum_j W(\mathbf{x}_j - \mathbf{x}_i, h) \tag{5.19}$$

The position correction $\Delta\mathbf{x}$ required to satisfy the constraint $P_i(\mathbf{x}+\Delta\mathbf{x}) = 0$ is obtained through a first-order Taylor expansion:

$$P_i(\mathbf{x}+\Delta\mathbf{x}) \approx P_i(\mathbf{x}) + \Delta\mathbf{x}\cdot\nabla P_i = 0 \tag{5.20}$$

Constraining the correction to act along the gradient direction ∇P_i, the displacement is parameterised as:

$$\Delta\mathbf{x} \approx \lambda \nabla P_i(\mathbf{x}) \tag{5.21}$$

where λ denotes a Lagrange multiplier. Substituting Equation (5.21) into Equation (5.20) and solving for λ gives:

$$\lambda_i = -\frac{P_i(\mathbf{x}_1,\ldots,\mathbf{x}_n)}{\sum_k \|\nabla_{\mathbf{x}_k} P_i\|^2} \tag{5.22}$$

The constraint function gradient with respect to a neighbouring point k takes one of two forms depending on whether k coincides with the point of interest:

$$\nabla_{\mathbf{x}_k} P_i = \frac{1}{\rho_0} \begin{cases} \sum_j \nabla_{\mathbf{x}_k} W(\mathbf{x}_i - \mathbf{x}_j, h) & \text{if } k = i \\ -\nabla_{\mathbf{x}_k} W(\mathbf{x}_i - \mathbf{x}_j, h) & \text{if } k = j \end{cases} \tag{5.23}$$

Combining these expressions, the total position correction for point i incorporating contributions from all neighbouring points is:

$$\Delta\mathbf{x}_i = \frac{1}{\rho_0} \sum_j (\lambda_i + \lambda_j) \nabla W(\mathbf{x}_j - \mathbf{x}_i, h) \tag{5.24}$$

Applying Equation (5.24) iteratively after each Lagrangian advection step, through a small number of correction passes, effectively restores point uniformity. This scheme performs reliably for single-phase LDD under the unit density assumption and preserves conservation properties throughout the simulation. However, in the multiphase setting, the standard PBF

correction is insufficient because it does not account for density contrasts between neighbouring points belonging to different fluid phases.

Otaduy et al. introduced the DYVERSO method [155], an extension of the PBF framework designed for multiphase fluid simulation in visual effects applications, capable of handling fluid separation and mixing between distinct phases. An analogous approach was evaluated for MP-LDD; however, it was found to generate substantial artificial compression and tension at phase interfaces, resulting in significant departures from the expected pressure distribution and rendering the method unsuitable for the present application.

In Rayleigh-Taylor instability, the depth to which the heavier fluid penetrates into the lighter phase scales as $A\mathbf{g}\delta t^2$, where $\mathbf{g}$ denotes acceleration due to gravity, δt is the time step, and $A = (\rho_h - \rho_l)/(\rho_h + \rho_l)$ is the Atwood number, with ρ_h and ρ_l denoting the densities of the heavy phase and light phase respectively [156]. This expression quantifies the temporal growth of the instability. Generalising this to $A\mathbf{a}\delta t^2$, where $\mathbf{a}$ represents the local point acceleration, allows the formulation to be extended to configurations without gravitational forcing, in which acceleration is governed by the local pressure gradient normalised by density. Discontinuities in pressure acceleration across the interface destabilise this generalised formulation. Monaghan et al. [157] addressed analogous interfacial instability in SPH by introducing an interfacial force formulated in terms of the Atwood number, pressure, and local density, achieving a stable interface representation. Since PBF enforces a density constraint, and the local density ratio governs whether a given phase rises or sinks relative to its surroundings through buoyancy, the Atwood number and relative density provide a natural basis for reformulating the PBF correction factor in Equation (5.24) for the multiphase setting.

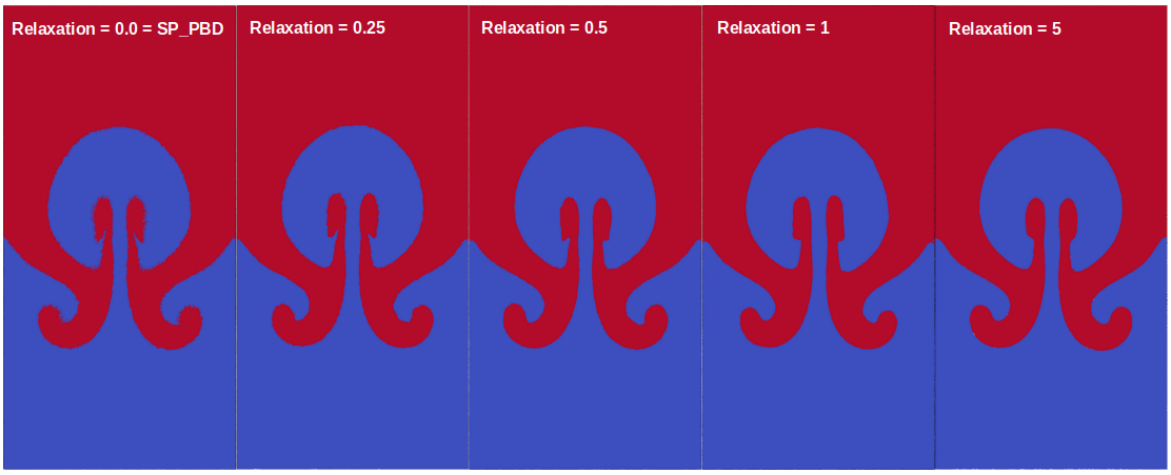

Figure 5.2. Behaviour of the modified PBD scheme with differing relaxation values under low-density ratio flow conditions.

The modified correction scheme applies density-weighted positional adjustments to each computational point based on the local density contrast with its neighbours. The objective is to produce a spatially uniform and physically consistent density field throughout the

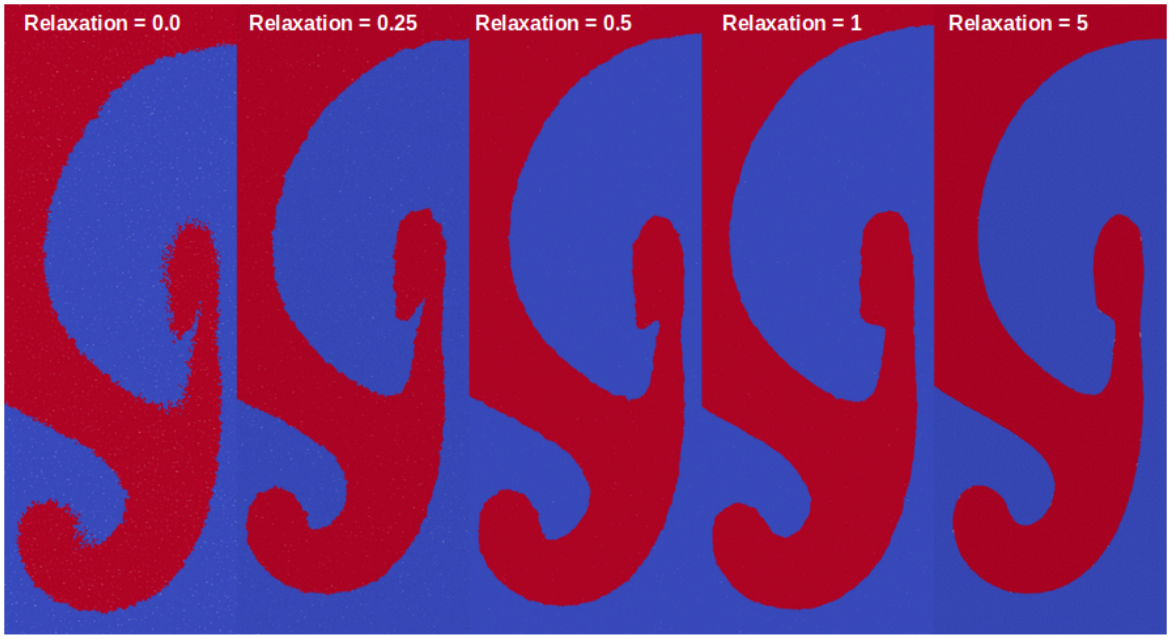

Figure 5.3. Zoomed view of Figure 5.2 showing the effect of the modified PBD with various relaxation factors.

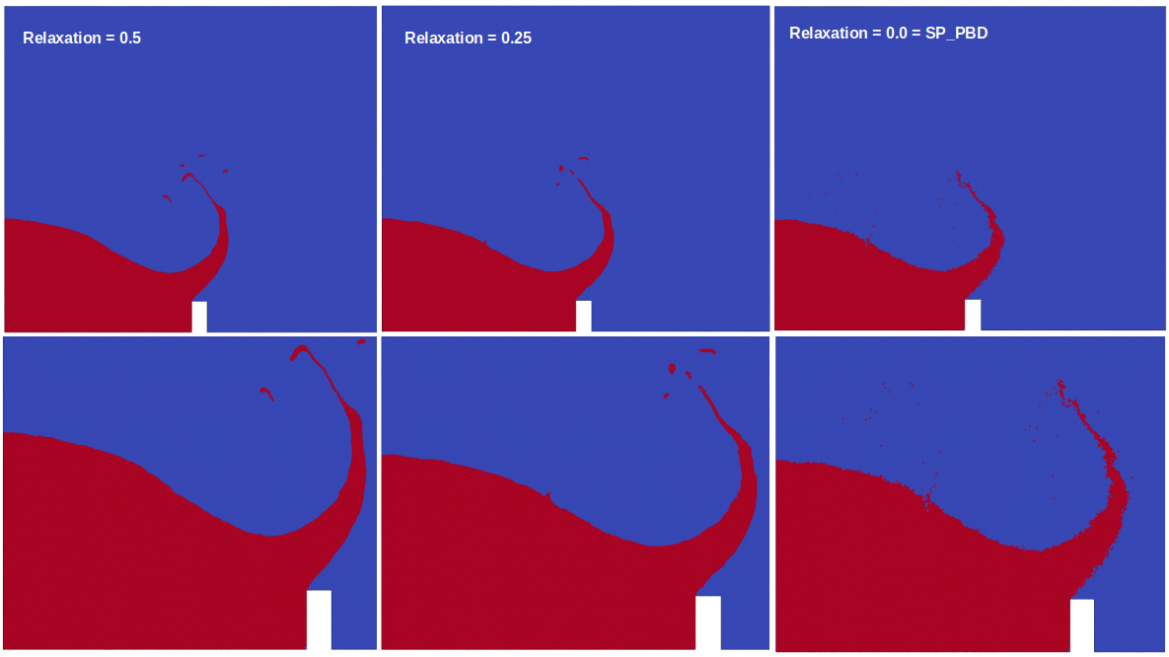

Figure 5.4. Influence of the relaxation parameter on the modified PBD scheme under high-density ratio flow conditions.

simulation domain. Corrections are localised through kernel weighting and modulated by a relaxation parameter to preserve numerical stability and physical accuracy, preventing pathological behaviours such as point clustering or spurious interfacial pressure gradients. Maintaining a well-defined and stable interface between phases requires careful control of the positional updates to avoid smearing or fragmentation of the phase boundary. The following correction is introduced subsequent to the advection step to maintain correct phase

sequencing and a stable interface boundary:

$$\Delta \mathbf{x}_{icorr} = \begin{cases} \mathbf{x}_{ij} \dfrac{|\rho_i - \rho_j|}{\rho_i + \rho_j} \left(\dfrac{\dfrac{\bar{\rho}_i - \bar{\rho}_j}{\bar{\rho}_j} + \dfrac{\rho_i - \rho_j}{\rho_j}}{2} \right) W_{ij} Z_{relax}, & \text{if } \rho_i < \rho_j \\ \mathbf{x}_{ij} \dfrac{|\rho_i - \rho_j|}{\rho_i + \rho_j} \left(\dfrac{\dfrac{\bar{\rho}_j - \bar{\rho}_i}{\bar{\rho}_i} + \dfrac{\rho_j - \rho_i}{\rho_i}}{2} \right) W_{ij} Z_{relax}, & \text{if } \rho_i > \rho_j \end{cases} \tag{5.25}$$

where ρ_i and ρ_j are the actual densities of points i and j, and $\bar{\rho}_i$, $\bar{\rho}_j$ are the corresponding smoothed densities evaluated using Equation (3.10), which serve to distinguish between phases across the interface. The factor $|\rho_i - \rho_j|/(\rho_i + \rho_j)$ represents the local Atwood number for each point pair, normalising the density contrast in a manner that ensures proportional scaling of the correction. The ratio $(\rho_i - \rho_j)/\rho_j$ measures the density deficit of the lighter phase compared to the heavier one, with larger absolute values indicating greater phase separation and correspondingly stronger tendencies toward buoyancy-driven stratification, interfacial instability, and phase segregation. The combined weighting factor $\frac{1}{2}\left[(\bar{\rho}_i - \bar{\rho}_j)/\bar{\rho}_j + (\rho_i - \rho_j)/\rho_j\right]$ blends the smoothed and actual density contrasts to stabilise the interfacial correction, suppressing spurious voids or discontinuities that would otherwise develop at the phase boundary. Spatial localisation of the correction is achieved through the kernel weight W_{ij}, which ensures that contributions decay with inter-point distance, preventing remote points from unduly influencing the local interface structure. The relaxation factor Z_{relax} governs the overall magnitude of the correction, allowing the strength of the interfacial regularization to be tuned without triggering oscillatory instabilities. Setting $Z_{relax} = 0$ recovers the original single-phase PBF formulation of Equation (5.24).

The total positional update for each point is then assembled as the sum of the standard PBF correction and the multiphase interfacial correction:

$$\Delta \mathbf{x}_i = \Delta \mathbf{x}_i + \Delta \mathbf{x}_{icorr} \tag{5.26}$$

In the present implementation, the total correction is not applied in a single pass. It is evaluated iteratively after each advection step using a prescribed number of regularization iterations and it is usually 3 to 5 iterations. During each iteration, the density constraint multipliers are recomputed from the current shifted point locations, neighbour-wise correction vectors are accumulated, and the resulting displacement is locally limited to prevent excessive point motion and wall penetration. After completion of the final regularization pass, the velocity field is interpolated onto the corrected point positions so that the subsequent momentum update remains consistent with the reordered point cloud.

It is noted that this regularization procedure may introduce a surface-tension-like numer-

ical effect, particularly when the interfacial relaxation parameter is increased. In the present work, this influence is assessed empirically through the interface-preservation studies shown in Figures 5.2–5.4, and moderate values of the relaxation parameter were found to provide a practical balance between interface stability and excessive artificial interfacial stiffening.
The performance of the modified PBF scheme across a range of relaxation factors is assessed against the standard single-phase PBF using a two-dimensional Rayleigh-Taylor benchmark instability test case with aphases differing in density by a factor of 3, as shown in Figures 5.2 and 5.3. The unmodified PBF scheme proves inadequate in multiphase configurations, producing unphysical mixing of points from the two phases at the interface. The modified formulation successfully preserves a well-defined and physically coherent interface free from cross-phase mixing. Increasing Z_{relax} strengthens the density enforcement at the interface, which introduces a degree of artificial surface tension while maintaining the overall physical fidelity of the simulation. Values of Z_{relax} in the range 0.25 to 1.0 is advised for practical use. The evaluation is further extended to a dam break configuration with a density ratio of 1000, representing a violent high-density-ratio flow, as shown in Figure 5.4. The modified PBF scheme demonstrates robust performance under these demanding conditions. For optimal accuracy, Z_{relax} values between 0.25 and 0.5 are advised.

5.1.5 Split Scheme Solver

Incompressible NS equations (2.1) and (2.2) are advanced in time within MP-LDD using a fractional step, or split scheme, methodology. This technique breaks down the full Navier-Stokes system into a sequential series of physically distinct sub-problems covering advection, diffusion, and pressure correction, each of which is solved independently within a single time step. The pressure correction step determines a pressure field whose gradient projects an field of intermediate velocity on the solution of free divergence in the flow field, enforcing incompressibility. This projection methodology was originally introduced by Chorin et al. [158]. An alternative operator splitting framework was introduced by Strang et al. [159], in which the governing operator is decomposed into constituent sub-operators, each of which is advanced over shorter sub-intervals before the results are recombined. Rather than employing a predictor-corrector structure, this approach emphasises sequential operator decomposition to enhance overall numerical performance. Guermond et al. [160] subsequently developed an efficient fractional time-stepping scheme for incompressible flows with variable-density that needs only one poisson equation of solution per time step, substantially reducing the computational cost of the pressure correction within split scheme frameworks.
The MP-LDD solver adopts a split scheme consistent with that employed in the single-phase LDD formulation [154], applying the second-order consistent MP-LDD differential operators while omitting the intermediate velocity prediction step. The complete solution proce-

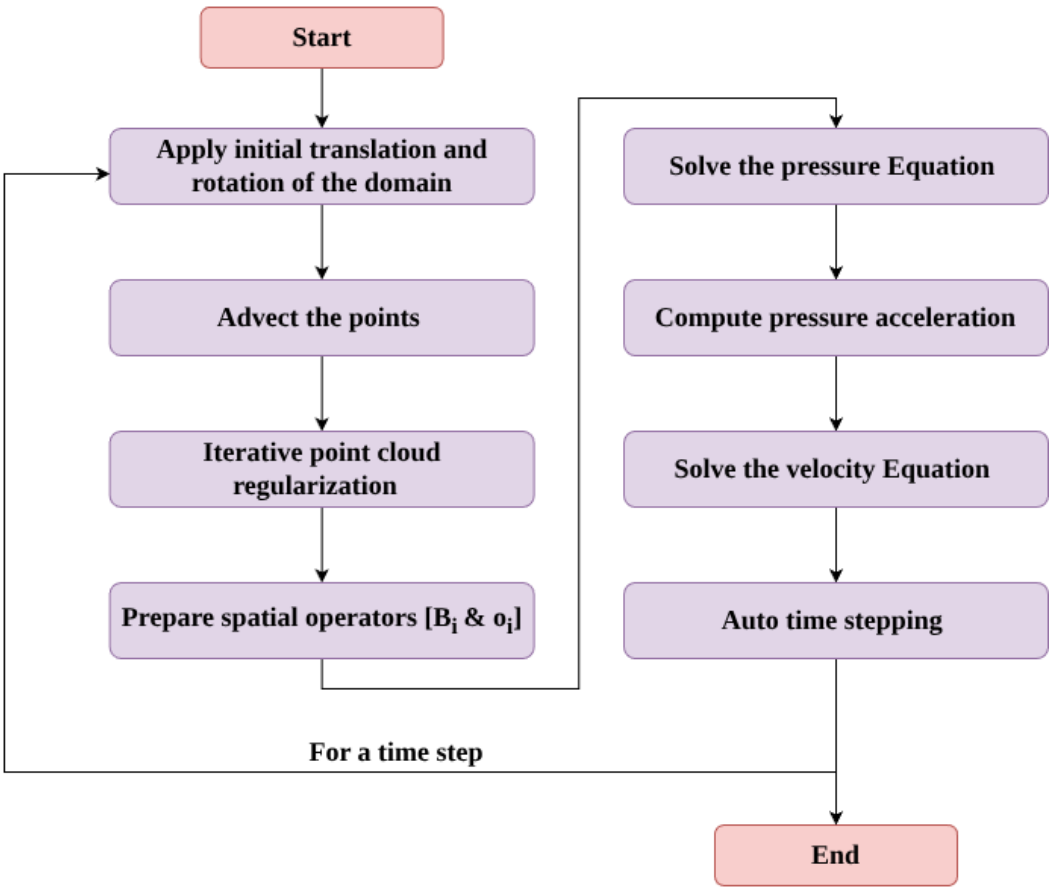

Figure 5.5. MP-LDD solver workflow for a single time step.

dure for a single time step is depicted in the workflow of Figure 5.5. Each time step begins with any prescribed rigid body translation or rotation of the computational domain. Computational points are then displaced according to their current velocities through the Lagrangian advection scheme, after which the point cloud regularization procedure is applied iteratively via PBD to restore a well-conditioned spatial distribution. The local geometric operators $\mathbf{B}_i$ and $\mathbf{o}_i$ are subsequently assembled in preparation for the differential operator evaluations. The PPE is then solved in a single step to enforce the incompressibility constraint directly, without recourse to intermediate velocity calculations, and the resulting pressure field is used to compute the acceleration of pressure. Then velocity field is subsequently obtained, and the next time interval size is computed through the adaptive automatic time-stepping method. This sequence of operations is repeated until the prescribed simulation end time is reached.

5.2 Numerical Procedure of the Multiphase LDD (MP-LDD) Formulation

5.2.1 Step 1: Variable-Coefficient Laplacian Operator

The starting point for MP-LDD is a generalisation of the standard LDD Laplacian to support spatially varying scalar fields (density, viscosity). Following Gibou et al. [145] and Basic et al. [39], the variable-coefficient Laplacian at point i is defined as:

$$\langle \nabla \cdot (\phi \nabla f) \rangle_i = \frac{2d \sum_j W_{ij} L_{ij} \left(\frac{\phi_i + \phi_j}{2} \right) (f_j - f_i)}{\sum_j W_{ij} L_{ij} \left\| \mathbf{x}_{ij} \right\|^2} \tag{5.27}$$

where d refers to dimensional space, W_{ij} denotes kernel weight between points i and j, L_{ij} is a correction factor, $\mathbf{x}_{ij} = \mathbf{x}_j - \mathbf{x}_i$ is the inter-point vector, and ϕ is the scalar field that multiplies the gradient (e.g. $1/\rho$ for the pressure equation or ν for the velocity equation).

Equation (5.27) is the single operator used throughout MP-LDD:

- with $\phi = 1/\rho$ it handles multi-density in the pressure Poisson equation;
- with $\phi = \nu$ it handles multi-viscosity in the velocity equation.

5.2.2 Step 2: Pressure Poisson Equation (PPE) - Continuous Form

2a. General PPE for Incompressible Multiphase Flow

For incompressible flow, the NS momentum equation requires the field of pressure to enforce the solenoidal constraint $\nabla \cdot \mathbf{u} = 0$. The continuous Pressure Poisson Equation (PPE) accounting for variable density is:

$$\nabla \cdot \left(\frac{\nabla p}{\rho} \right) = -\frac{(\nabla \cdot \mathbf{u})^n - (\nabla \cdot \mathbf{u})^{n-1}}{\delta t} \tag{5.28}$$

where n and $n-1$ are the present and previous time steps, and δt is the time-interval.

2b. Enforcement of Incompressibility

Within incompressible flow formulations, the solenoidal character of the velocity field must be enforced at each discrete time interval. The constraint is precisely fulfilled at the preceding time interval:

$$(\nabla \cdot \mathbf{u})^{n-1} = 0 \tag{5.29}$$

Nevertheless, discretisation errors introduced throughout the advection stage result in a non-zero divergence at the current time interval, $(\nabla \cdot \mathbf{u})^n$, to be non-zero. Substituting the above into Equation (5.28) yields the reduced PPE that corrects these errors:

$$\nabla \cdot \left(\frac{\nabla p}{\rho} \right) = -\frac{(\nabla \cdot \mathbf{u})^n}{\delta t} \tag{5.30}$$

5.2.3 Step 3: Lagrangian Time-Step Criterion and RHS

3a. Lagrangian Time-Step Definition

In LDD, points are analysed in a Lagrangian context. The time step is therefore coupled to the spatial resolution Δr and the velocity magnitude $\|\mathbf{u}\|$ as [146]:

$$\delta t = \frac{\Delta r}{\|\mathbf{u}\|} \tag{5.31}$$

3b. Substitution into the PPE

Substituting Equation (5.31) into Equation (5.30):

$$\nabla \cdot \left(\frac{\nabla p}{\rho} \right) = -\frac{(\nabla \cdot \mathbf{u})^n \|\mathbf{u}\|}{\Delta r} \equiv b_i \tag{5.32}$$

3c. Discrete RHS b_i

Defining the scaling coefficient $C_i = \dfrac{\|\mathbf{u}\|}{\Delta r}$, and using the discrete divergence approximation of MP-LDD:

$$b_i = -C_i \langle \nabla \cdot \mathbf{u} \rangle_i^n = -C_i \sum_j W_{ij} \left(\mathbf{u}_j^n - \mathbf{u}_i^n \right) \cdot \mathbf{B}_i \cdot \mathbf{x}_{ij} \tag{5.33}$$

where $\mathbf{B}_i$ is the renormalised matrix of the LDD gradient operator [39]. The quantity b_i is fully known at the start of each pressure solve.

5.2.4 Step 4: Discrete PPE - Left-Hand Side

The left-hand side (LHS) of Equation (5.30) is discretised by applying the variable-coefficient Laplacian operator (5.27) with $\phi = 1/\rho$:

$$\left\langle \nabla \cdot \left(\frac{\nabla p}{\rho} \right) \right\rangle_i = \frac{2d \sum_j W_{ij} L_{ij} \left(\frac{\frac{1}{\rho_i} + \frac{1}{\rho_j}}{2} \right) (p_j - p_i)}{\sum_j W_{ij} L_{ij} \|\mathbf{x}_{ij}\|^2} \tag{5.34}$$

The arithmetic mean $\left(\frac{1/\rho_i + 1/\rho_j}{2}\right)$ naturally interpolates the inverse density across the interface between two phases without requiring an explicit interface-tracking step.

5.2.5 Step 5: Algebraic Form of the Discrete PPE

5a. Absorbing the Normalisation Factor

The normalisation factor $\frac{2d}{\sum_j W_{ij} L_{ij} \|\mathbf{x}_{ij}\|^2}$ from the LHS is incorporated into the RHS coefficient b_i. The simplified equation for point i becomes:

$$\sum_j W_{ij} L_{ij} \left(\frac{\frac{1}{\rho_i} + \frac{1}{\rho_j}}{2}\right) (p_j - p_i) = b_i \tag{5.35}$$

5b. Coefficient Matrix A_i

Expanding the sum in Equation (5.35) and collecting terms multiplying p_i and each p_j, the coefficient matrix entries are:

$$A_i = \begin{cases} A_{ii} = -\sum_j W_{ij} L_{ij} \left(\frac{\frac{1}{\rho_i} + \frac{1}{\rho_j}}{2}\right) & \text{for } i = j, \\ A_{ij} = \quad W_{ij} L_{ij} \left(\frac{\frac{1}{\rho_i} + \frac{1}{\rho_j}}{2}\right) & \text{for } i \neq j. \end{cases} \tag{5.36}$$

The diagonal entry A_{ii} is negative and equals the negative sum of all off-diagonal entries in the same row, ensuring the matrix is *diagonally dominant* — a property exploited by the preconditioner in Step 6.

5c. Linear System

Collecting over all interior points, the PPE reduces to the linear system:

$$A_i x_i = b_i, \qquad x_i \equiv p_i \tag{5.37}$$

where x_i is the vector of unknown pressures at all points.

5.2.6 Step 6: Preconditioned Solver for the PPE

6a. PBICGSTAB Solver

The system (5.37) is resolved through the matrix-free PBICGSTAB method [139]. The matrix-free approach avoids forming A_i explicitly, reducing memory cost.

6b. Preconditioning

A preconditioner M_i transforms the original system into one with improved spectral properties:

$$M_i^{-1} A_i x_i = M_i^{-1} b_i \tag{5.38}$$

Choosing $M_i = A_i$ (i.e. the diagonal of A_i) produces a diagonally dominant preconditioned matrix $M_i^{-1} A_i$ whose eigenvalues cluster near unity, thereby accelerating convergence of the iterative solver.

5.2.7 Step 7: Boundary Condition for the PPE

7a. Wall-Normal Momentum Equation

At solid boundary points, the Neumann-type pressure boundary condition is established by projecting the momentum equation in the direction of the outward wall-normal $\mathbf{n}$:

$$\mathbf{n} \cdot (\nabla p) = \rho\, \mathbf{n} \cdot \left(-\frac{D\mathbf{u}}{Dt} + \nu \nabla^2 \mathbf{u} + \mathbf{g} + \frac{1}{\rho} \mathbf{F}_{s+d} \right) \tag{5.39}$$

7b. Discretisation of the LHS and Total Acceleration

With a no-slip condition $\mathbf{u}_w = \mathbf{0}$ and wall distance δ, the left-hand side pressure gradient and the material acceleration are approximated as:

$$\mathbf{n} \cdot \nabla p = \frac{p_w - p_i}{\delta} \tag{5.40}$$

$$\frac{D\mathbf{u}}{Dt} = \frac{\mathbf{u}_w - \mathbf{u}_i}{\delta t} = -\frac{\mathbf{u}_i}{\delta t} \tag{5.41}$$

7c. Boundary Pressure Difference

Neglecting surface tension at same-phase boundaries and setting $p_w = p_j$, substitution of Equations (5.40)–(5.41) into Equation (5.39) gives the boundary pressure difference:

$$(p_j - p_i) = \delta \left(\rho\, \mathbf{n} \cdot \left(\frac{\mathbf{u}_i - \mathbf{u}_w}{\delta t} + \mathbf{g} + \nu \nabla^2 \mathbf{u} \right) \right) \tag{5.42}$$

5.2.8 Step 8: Pressure Acceleration

Once the field of pressure is derived from the system of linear equation (5.37), the pressure acceleration at point i is recovered using the LDD gradient operator [39]:

$$\left\langle \frac{1}{\rho}\nabla p \right\rangle_i = \frac{1}{\rho_i}\left(\mathbf{B}_i \sum_j W_{ij}\,\mathbf{x}_{ij}\,(p_j - p_i)\right) \tag{5.43}$$

Resolution of the PPE ensures that pressure-based corrections eliminate the numerical divergence present in the velocity field, restoring the incompressibility condition $\nabla \cdot \mathbf{u} = 0$.

5.2.9 Step 9: Velocity Solver - BDF2 Temporal Discretisation

9a. Variable Time-Step BDF2 Scheme

The velocity field is updated using the second-order BDF2 [147], that approximated as:

$$\frac{D\mathbf{u}}{Dt} = \frac{1}{\delta t}\left[\left(\frac{1+2\alpha_t}{1+\alpha_t}\right)\mathbf{u}^{n+1} - (1+\alpha_t)\,\mathbf{u}^n + \left(\frac{\alpha_t^2}{1+\alpha_t}\right)\mathbf{u}^{n-1}\right] \tag{5.44}$$

where $\mathbf{u}^{n+1}$, $\mathbf{u}^n$, and $\mathbf{u}^{n-1}$ denotes velocity vectors at the future, present, and previous time steps respectively, and $\alpha_t = \delta t^n / \delta t^{n-1}$ is the ratio of consecutive time-intervals.

9b. Substitution into the Momentum Equation

Substituting the BDF2 approximation (5.44) into the NS momentum equation while preserving the implicit velocity contribution $\mathbf{u}^{n+1}$ on both sides:

$$\frac{1}{\delta t}\left[\left(\frac{1+2\alpha_t}{1+\alpha_t}\right)\mathbf{u}^{n+1} - (1+\alpha_t)\,\mathbf{u}^n + \frac{\alpha_t^2}{1+\alpha_t}\mathbf{u}^{n-1}\right] = -\frac{1}{\rho}\nabla p + \nu\nabla^2\mathbf{u}^{n+1} + \mathbf{g} + \frac{1}{\rho}\mathbf{F}_{s+d} \tag{5.45}$$

9c. BDF2 Coefficients

To simplify the algebra, the following coefficients are introduced:

$$C_L = \delta t\left(\frac{1+\alpha_t}{1+2\alpha_t}\right), \quad C_n = \frac{(1+\alpha_t)^2}{1+2\alpha_t}, \quad C_{n-1} = -\frac{\alpha_t^2}{1+2\alpha_t}, \quad C_{n+1} = \delta t\left(\frac{1+\alpha_t}{1+2\alpha_t}\right) \tag{5.46}$$

9d. Implicit Discrete Velocity Equation

Multiplying Equation (5.45) by $C_L = C_{n+1}$ and rearranging so that all terms involving the unknown $\mathbf{u}^{n+1}$ are on the LHS and all known quantities are on the RHS:

$$\mathbf{u}^{n+1} - C_L\nu\nabla^2\mathbf{u}^{n+1} = C_n\,\mathbf{u}^n + C_{n-1}\,\mathbf{u}^{n-1} + C_{n+1}\left(-\frac{1}{\rho}\nabla p + \mathbf{g} + \frac{1}{\rho}\mathbf{F}_{s+d}\right) \tag{5.47}$$

The right-hand side of Equation (5.47), which contains only quantities known from the previous steps (pressure from Step 6, body forces, surface tension), is denoted q_i.

5.2.10 Step 10: Discrete Velocity Equation with Variable Viscosity

10a. Applying the Variable Laplacian to the Viscous Term

The implicit viscous Laplacian $\nu\nabla^2\mathbf{u}^{n+1}$ on the LHS of Equation (5.47) is discretised using Equation (5.27) with $\phi = \nu$:

$$\mathbf{u}_i^{n+1} - C_L \frac{2d\sum_j W_{ij} L_{ij} \left(\frac{\nu_i + \nu_j}{2}\right)\left(\mathbf{u}_j^{n+1} - \mathbf{u}_i^{n+1}\right)}{\sum_j W_{ij} L_{ij} \|\mathbf{x}_{ij}\|^2} = q_i \tag{5.48}$$

The arithmetic mean $\left(\frac{\nu_i + \nu_j}{2}\right)$ interpolates the kinematic viscosity across the phase interface consistently with the density interpolation used in Step 4.

10b. Simplified Final Velocity Equation

Absorbing the normalisation factor $\frac{2d}{\sum_j W_{ij} L_{ij} \|\mathbf{x}_{ij}\|^2}$ into the coefficient C_L (redefining C_L locally), the final compact form is:

$$\boxed{\mathbf{u}_i^{n+1} - C_L \sum_j W_{ij} L_{ij} \left(\frac{\nu_i + \nu_j}{2}\right)\left(\mathbf{u}_j^{n+1} - \mathbf{u}_i^{n+1}\right) = q_i} \tag{5.49}$$

10c. Solution Strategy

Equation (5.49) is solved using the same matrix-free PBICGSTAB solver described in Step 6. A key feature is that one pressure equation and one velocity equation collectively handle both phases in a coupled manner, rather than employing distinct equations for each. The phase-dependent material properties (ρ, ν) enter only through the arithmetic means at inter-point interactions.

5.2.11 Step 11: Lagrangian Advection

After the velocity field $\mathbf{u}^{n+1}$ is obtained, the Lagrangian positions of all points are updated:

$$\mathbf{x}_i^{n+1} = \mathbf{x}_i^n + \delta t\, \mathbf{u}_i^{n+1} \tag{5.50}$$

This step completes one full time-step cycle of the MP-LDD solver.

5.2.12 Summary of the MP-LDD

The complete derivation proceeds through the following logical chain:

1. **Variable Laplacian** (Equation (5.27)): A single variable-coefficient discrete operator handles both multi-density and multi-viscosity effects.

2. **Continuous PPE** (Equation (5.30)): Derived from the incompressibility constraint; the previous-step divergence vanishes exactly.

3. **Lagrangian time step and RHS** (Equations (5.31)–(5.33)): The Lagrangian δt criterion is substituted to form the known RHS b_i.

4. **Discrete PPE LHS** (Equation (5.34)): The variable Laplacian with $\phi = 1/\rho$ is applied to the pressure.

5. **Linear system for pressure** (Equations (5.36)–(5.37)): Coefficient assembly yields the sparse system $A_i x_i = b_i$.

6. **Preconditioned solve** (Equation (5.38)): PBICGSTAB with $M_i = A_i$ recovers the pressure field.

7. **Boundary condition** (Equation (5.42)): Wall-normal momentum projection provides the Neumann pressure boundary condition.

8. **Pressure acceleration** (Equation (5.43)): The LDD gradient operator converts pressure to acceleration.

9. **BDF2 temporal discretisation** (Equations (5.44)–(5.46)): Variable time-step BDF2 provides second-order implicit time integration.

10. **Discrete velocity equation** (Equation (5.49)): The variable Laplacian with $\phi = \nu$ discretises the viscous term; PBICGSTAB solves for $\mathbf{u}^{n+1}$.

11. **Lagrangian advection** (Equation (5.50)): Points are moved with the updated velocity to complete the time step.

6 INTERFACE DYNAMICS MODELLING

This chapter addresses the modeling of interfacial phenomena crucial for accurate multiphase flow simulation, including surface tension effects and dynamic wetting behavior. Building upon the MP-LDD framework established in Chapter 4, the formulations presented here enable the simulation of capillary-driven flows, droplet dynamics, and wetting processes at solid boundaries.

The chapter begins with Section 6.2, which adapts the Continuum Surface Force (CSF) approach to the Lagrangian particle framework. The formulation includes curvature computation from particle distributions and volumetric force representation suitable for momentum equation integration. Section 6.4 presents the dynamic contact angle modeling framework, incorporating velocity-dependent corrections to the static equilibrium angle and a force-based stabilization approach for robust contact line motion. The integration of these interfacial models with the MP-LDD solver enables accurate prediction of surface tension-dominated phenomena and complex wetting dynamics encountered in boiling, condensation, and droplet impact scenarios.

6.1 Surface Tension

The interface modeling approach used in this study, including surface tension and dynamic contact angle formulation, builds upon the methodology presented by [161] in the context of Multiphase Lagrangian Differencing Dynamics. The surface tension force, $\mathbf{F}_s$, can be represented as a volumetric force acting at the fluid interface:

$$\mathbf{F}_s(x_s) = \int \mathbf{f}_s(x)\,\delta(\mathbf{x}-\mathbf{x}_s)\,dS, \tag{6.1}$$

where $\mathbf{x}_s$ denotes the interfacial position and $\delta(\mathbf{x}-\mathbf{x}_s)$ is the Dirac delta function. The interfacial force per surface unit area, $\mathbf{f}_s$, is defined as:

$$\mathbf{f}_s = \sigma\kappa\hat{\mathbf{n}}, \tag{6.2}$$

with σ representing the coefficient of surface tension, κ corresponds to the local curvature,

and $\hat{\mathbf{n}}$ designates the unit outward normal vector at the interface. Following the Continuum Surface Force (CSF) formulation proposed by [162], the interface delta function is approximated through the gradient of an indicator, or color function $C(x)$:

$$\delta = \frac{\nabla C(x)}{[C]} = \mathbf{n}, \tag{6.3}$$

where $[C]$ is the jump in C (equal to one for a volume fraction), and $\mathbf{n}$ denotes the interface normal. The MP-LDD framework evaluates the interfacial normal directly from the particle density ($\delta = {}^{\nabla\rho}/_{\rho_{abs}} = \mathbf{n}$). For discrete numerical implementation, the gradient operator formulation proposed by Basic [39] is employed and The interfacial normal direction for each particle is evaluated as:

$$\mathbf{n}_i = \begin{cases} \mathbf{B}_i \sum_j W_{ij} \mathbf{x}_{ij} \left(\dfrac{\rho_j - \rho_i}{\rho_{abs}} \right), & \rho_i \neq \rho_j, \\ 0, & \rho_i = \rho_j, \end{cases} \tag{6.4}$$

where $\rho_{abs} = |\rho_{\text{phase0}} - \rho_{\text{phase1}}|$ is the absolute density difference between phases. The unit interfacial normal and curvature are evaluated as:

$$\hat{\mathbf{n}} = \frac{\nabla C}{\|\nabla C\|} = \frac{\mathbf{n}}{\|\mathbf{n}\|}, \qquad \kappa = -\left(\nabla \cdot \hat{\mathbf{n}}\right). \tag{6.5}$$

The local curvature is then obtained from:

$$\kappa_i = \begin{cases} \sum_j W_{ij} \left(\hat{\mathbf{n}}_j - \hat{\mathbf{n}}_i \right) \cdot \mathbf{B}_i \mathbf{x}_{ij}, & \rho_i \neq \rho_j, \\ 0, & \rho_i = \rho_j. \end{cases} \tag{6.6}$$

In the MP-LDD framework, the interfacial force per unit area is divided by the local particle spacing Δr to convert it into a volumetric force suitable for the momentum equations. Ensuring dimensional consistency, correct scaling with particle density, and accurate localization of the surface tension near the interface. Accordingly, the volumetric surface tension force is expressed as:

$$\mathbf{F}_s = \frac{\sigma \kappa \hat{\mathbf{n}}}{\Delta r}. \tag{6.7}$$

The force $\mathbf{F}_s$ is included in the momentum Equation 3.2 and σ is the surface tension coefficient (N/m), κ is the curvature (1/m), $\hat{\mathbf{n}}$ is dimensionless, and Δr is the local particle spacing (m).

6.1.1 Capillary Time-Step Restriction

In the present formulation, the surface tension force is treated explicitly in time. As a consequence, the time step is subject to the classical capillary stability restriction associated with the temporal resolution of the shortest capillary waves supported by the spatial discretization. For a characteristic inter-point spacing Δr, the capillary time-step limit may be expressed as

$$\Delta t \;<\; \sqrt{\frac{\rho\,\Delta r^3}{\pi\sigma}}, \tag{6.8}$$

where ρ is the characteristic fluid density and σ is the surface tension coefficient. This restriction becomes increasingly severe as the spatial resolution is refined, since the admissible time step scales with $\Delta r^{3/2}$, and it is likewise more restrictive for flows involving larger values of surface tension.

Accordingly, in surface-tension-dominated multiphase simulations, the capillary constraint may become more restrictive than the convective or viscous time-step conditions. This is particularly relevant in cases involving fine interface resolution, small droplets, or strong curvature-driven interfacial motion, where capillary waves introduce the fastest time scales in the problem. In the adaptive time-stepping procedure adopted in this work, the selected time step should therefore be interpreted as being limited by the most restrictive active stability condition among the relevant advective, viscous, and capillary criteria. Although the capillary condition is not always the dominant limiter in every case considered, it constitutes an inherent stability requirement of the present explicit surface tension treatment and should be taken into account whenever interfacial dynamics are governed strongly by surface tension effects. A more detailed assessment of the relative influence of the capillary restriction under different flow regimes, as well as possible relaxation of this limitation through semi-implicit or fully implicit surface tension treatment, remains an important direction for future work.

6.2 Numerical Procedure of Surface Tension

6.2.1 Step 1: Physical Origin and Continuum Definition

Surface tension arises from the imbalance of intermolecular cohesive forces at the phase boundary. At the continuum level, it acts as a force per unit area directed along the interface. For an interface S, the total surface tension force on a control volume is:

$$\mathbf{F}_s = \int_S \mathbf{f}_s\, dS, \qquad \mathbf{f}_s = \sigma\kappa\hat{\mathbf{n}} \tag{6.9}$$

where σ denotes coefficient of surface tension (N/m), κ corresponds to the local curvature (m^{-1}), and $\hat{\mathbf{n}}$ is the unit outward interface normal. The mean curvature relates to the principal

radii R_1, R_2 as:

$$\kappa = \frac{1}{R_1} + \frac{1}{R_2} \tag{6.10}$$

6.2.2 Step 2: Converting Surface Force to Volumetric Body Force

The surface integral cannot be directly inserted into the volumetric momentum equation. A Dirac delta function localises the force to the interface:

$$\mathbf{F}_s(\mathbf{x}) = \int_S \sigma\kappa\hat{\mathbf{n}}\,\delta(\mathbf{x}-\mathbf{x}_s)\,dS \tag{6.11}$$

where $\mathbf{x}_s$ is the interfacial position. This is the Continuum Surface Force (CSF) representation [162].

6.2.3 Step 3: Approximation of the Delta Function

The Dirac delta function is not computable directly. Following CSF [162], it is approximated using the gradient of a scalar colour function $C(\mathbf{x})$, where $C = 1$ in phase 0 and $C = 0$ in phase 1 with jump $[C] = 1$:

$$\delta(\mathbf{x}-\mathbf{x}_s) \approx \|\nabla C\| \tag{6.12}$$

The interface normal follows directly:

$$\mathbf{n} = \frac{\nabla C}{[C]} = \nabla C, \qquad \hat{\mathbf{n}} = \frac{\nabla C}{\|\nabla C\|} \tag{6.13}$$

and the curvature from the divergence of the unit normal:

$$\kappa = -\nabla\cdot\hat{\mathbf{n}} = -\nabla\cdot\left(\frac{\nabla C}{\|\nabla C\|}\right) \tag{6.14}$$

6.2.4 Step 4: Density-Based Normal in MP-LDD

In the MP-LDD framework, no explicit colour function is tracked. Instead, the local density field serves as the phase indicator, since density is discontinuous across the interface. The delta function approximation becomes:

$$\delta \approx \frac{\nabla\rho}{\rho_{abs}} = \mathbf{n}, \qquad \rho_{abs} = |\rho_{\text{phase0}} - \rho_{\text{phase1}}| \tag{6.15}$$

Substituting into the CSF framework, the interfacial normal at particle i is evaluated using the LDD gradient operator [39]:

$$\mathbf{n}_i = \begin{cases} \mathbf{B}_i \sum_j W_{ij}\,\mathbf{x}_{ij} \left(\dfrac{\rho_j - \rho_i}{\rho_{abs}} \right), & \rho_i \neq \rho_j \\ \mathbf{0}, & \rho_i = \rho_j \end{cases} \tag{6.16}$$

where $\mathbf{B}_i$ is the LDD renormalization tensor ensuring first-order consistency of the gradient. The condition $\rho_i = \rho_j$ identifies bulk-phase particles far from the interface, where no interfacial force is applied.

6.2.5 Step 5: Unit Normal and Curvature

The unit normal vector at particle i is normalised from Step 4:

$$\hat{\mathbf{n}}_i = \frac{\mathbf{n}_i}{\|\mathbf{n}_i\|} \tag{6.17}$$

The discrete curvature is obtained by applying the LDD divergence approximation to $\hat{\mathbf{n}}$:

$$\kappa_i = \begin{cases} \sum_j W_{ij} \left(\hat{\mathbf{n}}_j - \hat{\mathbf{n}}_i \right) \cdot \mathbf{B}_i\,\mathbf{x}_{ij}, & \rho_i \neq \rho_j \\ 0, & \rho_i = \rho_j \end{cases} \tag{6.18}$$

This expression computes the divergence of $\hat{\mathbf{n}}$ using finite differences of the unit normal across neighbouring particles weighted by the LDD kernel.

6.2.6 Step 6: Dimensional Conversion to Volumetric Force

The interfacial force per unit area $\mathbf{f}_s = \sigma\kappa\hat{\mathbf{n}}$ carries units of N/m^2. To enter the momentum equation, which requires units of N/m^3, division by the local particle spacing Δr (m) is performed:

$$[\mathrm{N/m^2}] \div [\mathrm{m}] = [\mathrm{N/m^3}] \tag{6.19}$$

This conversion ensures dimensional consistency, correct scaling with particle resolution, and physical localisation of the force near the interface. The final volumetric surface tension force at particle i is:

$$\boxed{\mathbf{F}_{s,i} = \frac{\sigma\,\kappa_i\,\hat{\mathbf{n}}_i}{\Delta r}} \tag{6.20}$$

This force is incorporated into the momentum equation (3.2) in the form of a body force contribution.

6.2.7 Step 7: Summary of Surface Tension

1. Physical interface force: $\mathbf{f}_s = \sigma\kappa\hat{\mathbf{n}}$
2. CSF volumetric conversion via Dirac delta: $\mathbf{F}_s = \int \mathbf{f}_s\,\delta(\mathbf{x}-\mathbf{x}_s)\,dS$
3. Delta function approximation: $\delta \approx \|\nabla C\|$, $\hat{\mathbf{n}} = \nabla C/\|\nabla C\|$
4. Density substitution in MP-LDD: $\mathbf{n}_i$ from $\nabla\rho/\rho_{abs}$ using LDD gradient
5. Discrete curvature: κ_i from divergence of $\hat{\mathbf{n}}$ via LDD operator
6. Volumetric conversion: divide by Δr for momentum equation
7. Final force: $\mathbf{F}_{s,i} = \sigma\kappa_i\hat{\mathbf{n}}_i/\Delta r$

6.3 Dynamic Contact Angle Modeling

The dynamic contact angle (θ_d) plays a crucial role in simulating wetting phenomena, particularly near the moving contact line where fluid solid interactions dominate capillary behavior. Accurate prediction of θ_d is essential for reproducing droplet spreading, film retraction, and impact dynamics [163, 164]. Deviations from the static (equilibrium) contact angle arise from viscous dissipation and surface tension imbalance near the moving contact line [165, 166]. Present formulation extends the dynamicAlphaContactAngle boundary condition of OpenFOAM [167], incorporating both curvature-weighted static angles and a force-based stabilisation term to enhance interfacial sharpness and numerical stability. The radii associated with the maximum advancing (r_A) and receding (r_R) menisci are first obtained as:

$$r_A = \frac{\sin^2(\theta_{mda})}{\sqrt{2-3\cos(\theta_{mda})+\cos^3(\theta_{mda})}}, \qquad r_R = \frac{\sin^2(\theta_{mdr})}{\sqrt{2-3\cos(\theta_{mdr})+\cos^3(\theta_{mdr})}}, \tag{6.21}$$

where θ_{mda} and θ_{mdr} denote the maximum advancing and receding contact angles, respectively. The static (equilibrium) contact angle is then determined via curvature-weighted interpolation:

$$\theta_s = \cos^{-1}\left(\frac{r_A\cos(\theta_{mda})+r_R\cos(\theta_{mdr})}{r_A+r_R}\right), \tag{6.22}$$

To capture interface motion effects, a velocity-dependent correction is introduced:

$$\Delta\theta = (\theta_{mda}-\theta_{mdr})\tanh(\mathbf{u}_{tan}\cdot\mathbf{n}_{can}), \tag{6.23}$$

where $\mathbf{u}_{tan}$ is the local tangential velocity near the contact line and $\mathbf{n}_{can}$ the wall-normal vector. This formulation accounts for apparent angle variations during advancing and receding motion, consistent with empirical correlations by Kistler [165]. The dynamic contact angle is thus updated as:

$$\theta_d = \theta_s + \Delta\theta. \tag{6.24}$$

Following the approach of [168], a restoring force is applied to the fluid contact line point to drive the interface toward its dynamic equilibrium state. The tangential capillary force per unit volume is expressed as:

$$\mathbf{F}_d = \mathbf{n}_{tan} DCA_{coef} \frac{(\theta_d - \theta_{curr})}{\rho}, \tag{6.25}$$

where $\theta_{curr} = \cos^{-1}(-\mathbf{n}_{wall} \cdot \mathbf{n})$ is the instantaneous interface angle, ρ is the local fluid density, and $DCA_{coef} = \sigma \Delta r^2$ represents the dynamic contact angle coefficient associated with interface resolution. The force $\mathbf{F}_d$ is included in the calculations to determine the velocity. This approach provides a stable transition between static and dynamic regimes, ensuring robust simulation of complex wetting, dewetting, and impact phenomena. Although the present velocity-based form was found to provide stable and practically useful behaviour in the cases considered in this thesis, the use of a dimensional velocity inside the hyperbolic tangent limits the physical generality of the model. The hyperbolic tangent function is used here as a bounded smooth transition function, ensuring that the dynamic contact angle correction remains limited between the advancing and receding bounds. The present form was found to provide stable behavior for the cases considered, although a non-dimensional argument would offer a more physically transferable scaling across different flow regimes. This will be addressed in future work on DCA.

6.4 Numerical Procedure of Dynamic Contact Angle Modelling

6.4.1 Step 1: Physical formulation

When a fluid interface meets a solid wall, the contact angle θ characterises the degree of surface wettability. Under static equilibrium, the Young-Laplace equation determines the equilibrium angle from the equilibrium among solid-gas, solid-liquid, and liquid-gas interfacial energy contributions. Under dynamic conditions, contact line motion introduces additional

viscous dissipation near the wall, causing the resultant DCA θ_d to deviate from the static equilibrium value. Advancing motion (contact line moving outward) increases the apparent angle, while receding motion decreases it [163, 164, 165, 166].

6.4.2 Step 2: Meniscus Radii from Geometric Constraint

The upper and lower limits of the contact angle define the hysteresis band. The radii r_A and r_R of the maximum advancing and receding menisci are determined from the geometric relationship between contact angle and meniscus curvature:

$$r_A = \frac{\sin^2(\theta_{mda})}{\sqrt{2-3\cos(\theta_{mda})+\cos^3(\theta_{mda})}}, \qquad r_R = \frac{\sin^2(\theta_{mdr})}{\sqrt{2-3\cos(\theta_{mdr})+\cos^3(\theta_{mdr})}} \tag{6.26}$$

where θ_{mda} and θ_{mdr} are the maximum advancing and minimum receding contact angles respectively. The denominator arises from the volume of a spherical cap of unit radius at the respective contact angle, ensuring geometric self-consistency of the meniscus representation.

6.4.3 Step 3: Static Equilibrium Angle via Curvature-Weighted Interpolation

Rather than using θ_{mda} or θ_{mdr} directly as the static angle, a curvature-weighted interpolation between the two limits is performed. The weighting is proportional to the meniscus radii r_A and r_R, which represent the geometric extent of each limiting state:

$$\cos(\theta_s) = \frac{r_A\cos(\theta_{mda}) + r_R\cos(\theta_{mdr})}{r_A + r_R} \tag{6.27}$$

Inverting:

$$\theta_s = \cos^{-1}\left(\frac{r_A\cos(\theta_{mda}) + r_R\cos(\theta_{mdr})}{r_A + r_R}\right) \tag{6.28}$$

This weighted static angle accounts for the asymmetry between advancing and receding hysteresis limits and provides a physically consistent reference state for the dynamic correction applied in the next step.

6.4.4 Step 4: Velocity-Dependent Dynamic Correction

Contact line motion at velocity $\mathbf{u}_{tan}$ along the wall introduces a velocity-dependent deviation from the static angle. The correction $\Delta\theta$ must satisfy the following physical requirements:

- $\Delta\theta > 0$ when advancing ($\mathbf{u}_{tan} \cdot \mathbf{n}_{can} > 0$)
- $\Delta\theta < 0$ when receding ($\mathbf{u}_{tan} \cdot \mathbf{n}_{can} < 0$)

- $\Delta\theta \to 0$ at zero contact line velocity
- $|\Delta\theta| \leq \theta_{mda} - \theta_{mdr}$ (bounded by hysteresis range)

The hyperbolic tangent satisfies all four requirements:

$$\Delta\theta = (\theta_{mda} - \theta_{mdr}) \tanh(\mathbf{u}_{tan} \cdot \mathbf{n}_{can}) \tag{6.29}$$

where $\mathbf{n}_{can}$ is the wall-normal vector. The factor $(\theta_{mda} - \theta_{mdr})$ scales the correction to the full hysteresis range. For slow contact line motion ($|\mathbf{u}_{tan} \cdot \mathbf{n}_{can}| \ll 1$), $\tanh \approx \mathbf{u}_{tan} \cdot \mathbf{n}_{can}$ and the correction is approximately linear in velocity. For fast motion, $\tanh \to \pm 1$ and the correction saturates at the hysteresis limits, consistent with the empirical correlations of Kistler [165].

6.4.5 Step 5: Dynamic Contact Angle Update

Combining the static reference angle from Step 3 with the velocity-dependent correction from Step 4:

$$\theta_d = \theta_s + \Delta\theta \tag{6.30}$$

This is the DCA toward which the interface evolves at the present time level. Difference between θ_d and the instantaneous interface angle drives the restoring force derived in the next step.

6.4.6 Step 6: Restoring Force at the Contact Line

The instantaneous interface angle at the wall is measured through the inner product of the wall normal $\mathbf{n}_{wall}$ and the interface normal $\mathbf{n}$:

$$\theta_{curr} = \cos^{-1}(-\mathbf{n}_{wall} \cdot \mathbf{n}) \tag{6.31}$$

When $\theta_{curr} \neq \theta_d$, a capillary imbalance exists at the contact line. Following the approach of Esteban et al. [168], a tangential restoring force is applied to drive the interface toward θ_d. The magnitude of this force scaling proportionally with the angular deviation $(\theta_d - \theta_{curr})$:

$$\mathbf{F}_d = \mathbf{n}_{tan} DCA_{coef} \frac{(\theta_d - \theta_{curr})}{\rho} \tag{6.32}$$

where $\mathbf{n}_{tan}$ is the unit tangential vector at the contact line directed toward the equilibrium position, ρ is the local fluid density, and DCA_{coef} is the dynamic contact angle coefficient.

6.4.7 Step 7: Derivation of the DCA Coefficient

The coefficient DCA_{coef} must carry units consistent with the volumetric force contribution entering the momentum equation. Starting from the dimensional requirements:

$$[\mathbf{F}_d] = \mathrm{N/m^3} = \mathrm{kg/(m^2 s^2)} \tag{6.33}$$

The angular deviation $(\theta_d - \theta_{curr})$ is dimensionless (radians) and $1/\rho$ has units $\mathrm{m^3/kg}$. Therefore:

$$[DCA_{coef}] = \mathrm{N/m^3} \times [\rho] = \mathrm{kg/(m^2 s^2)} \times \mathrm{kg/m^3} = \mathrm{kg^2/(m^5 s^2)} \tag{6.34}$$

Since σ has units N/m = $\mathrm{kg/s^2}$ and Δr^2 has units $\mathrm{m^2}$:

$$[\sigma \Delta r^2] = \mathrm{kg/s^2} \times \mathrm{m^2} = \mathrm{kg \cdot m^2/s^2} \tag{6.35}$$

Dividing by ρ ($\mathrm{kg/m^3}$) in Equation (6.32) and recognising that the contact line force scales with σ and the interface resolution Δr, the coefficient is defined as:

$$\boxed{DCA_{coef} = \sigma \Delta r^2} \tag{6.36}$$

This ensures that the restoring force magnitude scales correctly with the surface tension coefficient and with the particle resolution, so that the contact line dynamics converge as $\Delta r \to 0$.

6.4.8 Step 8: Integration into the Momentum Equation

The total interfacial volumetric force contribution entering the MP-LDD momentum equation is the sum of the bulk surface tension force $\mathbf{F}_s$ and the contact line restoring force $\mathbf{F}_d$:

$$\mathbf{F}_{s+d} = \mathbf{F}_s + \mathbf{F}_d = \frac{\sigma \kappa \hat{\mathbf{n}}}{\Delta r} + \mathbf{n}_{tan}\, \sigma \Delta r^2 \, \frac{(\theta_d - \theta_{curr})}{\rho} \tag{6.37}$$

$\mathbf{F}_{s+d}$ is the combined surface tension and dynamic contact angle force term that appears in the Navier-Stokes momentum equation (2.2).

6.4.9 Step 9: Summary of DCA

1. Physical motivation: θ_d deviates from static equilibrium due to viscous dissipation at moving contact line
2. Meniscus radii: r_A, r_R from advancing and receding angle geometry - Equation (6.26)
3. Static angle: curvature-weighted interpolation between θ_{mda} and θ_{mdr} — Equation (6.28)

4. Dynamic correction: $\Delta\theta$ via tanh of contact line velocity, bounded by hysteresis range - Equation (6.29)
5. Dynamic angle update: $\theta_d = \theta_s + \Delta\theta$ - Equation (6.30)
6. Instantaneous angle: θ_{curr} from wall and interface normal vectors
7. Restoring force: proportional to $(\theta_d - \theta_{curr})$, tangential to contact line - Equation (6.32)
8. DCA coefficient: $DCA_{coef} = \sigma\Delta r^2$ from dimensional analysis
9. Combined force: $\mathbf{F}_{s+d}$ enters momentum equation

7 HEAT TRANSFER AND PHASE CHANGE

This chapter extends the MP-LDD framework to thermal flows and phase change phenomena by introducing an energy equation formulation compatible with the Lagrangian particle method. The developments include implicit thermal diffusion treatment, enthalpy-based phase change modeling, and a hierarchical framework for buoyancy-driven flows with variable density and viscosity.

The chapter is structured as follows: Section 7.1 derives the internal energy equation for incompressible flows in the Lagrangian framework, establishing the foundation for heat transfer modeling. Section 7.2 presents the enthalpy-based formulation that naturally incorporates latent heat effects during phase transitions, including the Implicit Phase-Coupled Energy (IPCE) algorithm that ensures robust coupling between temperature and phase fraction evolution. For liquid-vapor systems, a saturation check based on local pressure and temperature conditions is introduced to maintain thermodynamic consistency. Section 7.3 introduces the Hierarchical Buoyancy Modeling Framework (HBMF), which adaptively selects appropriate density and viscosity models based on local temperature deviation and phase type, enabling accurate simulation of natural convection with large temperature gradients. The chapter concludes with an integrated solver workflow that demonstrates the sequential coupling of momentum, energy, and phase change equations within each time step, establishing a unified computational framework for multiphase thermal flows with phase transitions.

7.1 Enthalpy Based Energy Equation For Phase Change

While the internal energy formulation captures sensible heating, it does not explicitly account for latent heat effects during phase transitions. To address this limitation, the energy equation is commonly recast in terms of enthalpy, defined as $H = U + p/\rho$ [169, 170]. For incompressible flows, the contribution of pressure work p/ρ is negligible, therefore, variations in enthalpy effectively represent changes in internal energy. A key advantage of the enthalpy formulation is its ability to naturally incorporate latent heat through the phase fraction f_p, thereby providing a unified framework for modeling both sensible and latent heat transfer. The total enthalpy can be expressed as:

$$H = c_p T + L f_p, \tag{7.1}$$

where c_p is the specific heat capacity, L is the latent heat of phase change, and f_p denotes the phase fraction (ranging from 0 to 1), representing the fraction of material that has undergone a phase transition. The sign of the latent heat contribution depends on the nature of the transformation. Endothermic transitions, such as melting (solid $\rightarrow$ liquid) and vaporization (liquid $\rightarrow$ vapor), require energy input from the surroundings, while exothermic transitions, such as solidification (liquid $\rightarrow$ solid) and condensation (vapor $\rightarrow$ liquid), release energy. This leads to the enthalpy formulation:

$$H = \begin{cases} c_p T + L f_p, & \text{endothermic processes (melting, vaporization),} \\ c_p T - L f_p, & \text{exothermic processes (solidification, condensation).} \end{cases} \tag{7.2}$$

Here, the positive latent heat term ($+Lf_p$) indicates energy absorption to sustain the phase change process, while the negative term ($-Lf_p$) reflects energy release to the environment. Correct treatment of this sign convention is essential to preserve energy conservation in numerical models of phase change. Incorporating this definition into the conservation of energy yields the enthalpy-based energy equation:

$$\frac{DH}{Dt} = \nabla \cdot \left(\frac{k}{\rho} \nabla T \right) + \rho Q, \tag{7.3}$$

where k is the thermal conductivity and Q represents the volumetric heat sources.

Figure 7.1 illustrates the enthalpy–temperature relationship for a generic material undergoing solid, liquid, and gas phases. In the solid, liquid, or vapor regions, enthalpy increases linearly with temperature as a result of sensible heating. During phase changing, however, enthalpy varies at constant temperature, reflecting the absorption or release of latent heat. This graphical representation highlights how the enthalpy method conveniently unifies sensible and latent heat contributions within a single formulation.

7.2 Implicit Phase-Coupled Energy (IPCE) Formulation

Implicit coupling of temperature and phase fraction using an enthalpy formulation has long been recognized as a robust strategy for phase change problems because it inherently stabilizes the energy update and accommodates latent heat effects without restrictive time step limitations. In classical enthalpy methods, recasting the energy equation in terms of total enthalpy and discretizing it implicitly prevents non-physical oscillations and unsteady temperature behavior near the phase interface that often arise in explicit schemes [3]. Building upon this concept, the Implicit Phase-Coupled Energy (IPCE) formulation in the present MP-

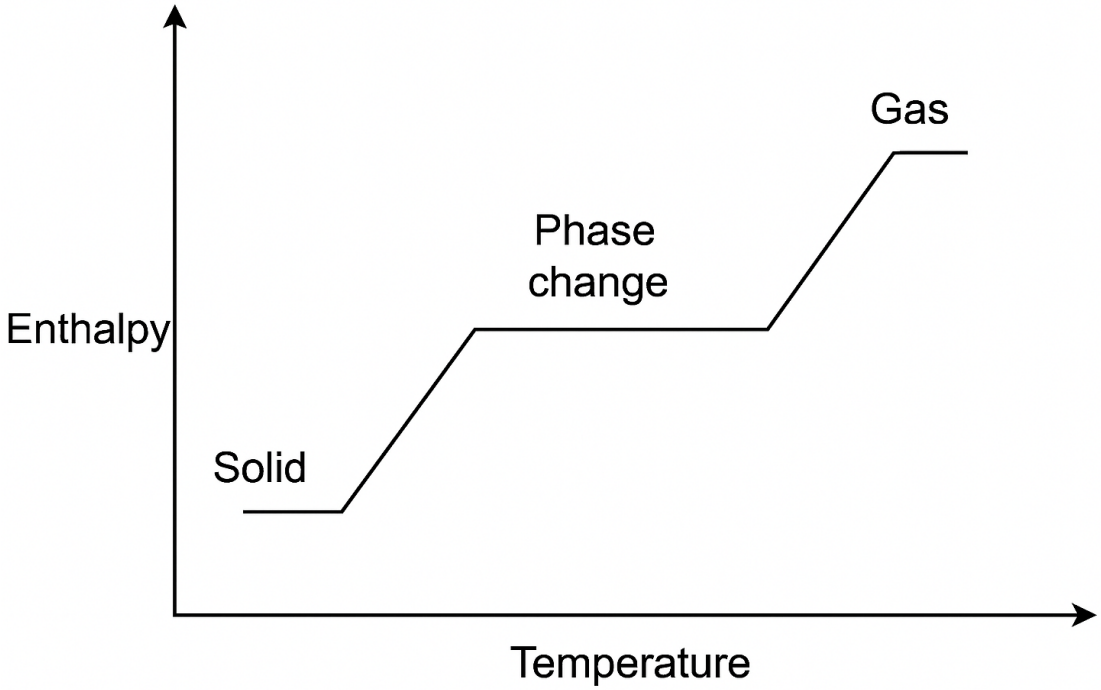

Figure 7.1. Schematic representation of the enthalpy–temperature relationship during phase change. The sloped regions correspond to sensible heating in single phases (solid, liquid, or gas), while the horizontal plateaus represent isothermal phase transitions, where enthalpy increases or decreases due to latent heat absorption or release.

LDD framework treats temperature T and phase fraction f_p as primary variables rather than solving directly for enthalpy. Substituting the enthalpy definition $H = c_p T + L f_p$ into the energy equation yields a coupled temperature phase fraction form that explicitly incorporates latent heat effects:

$$\rho \frac{D(c_p T + L f_p)}{Dt} = \nabla \cdot (k \nabla T) + \rho Q. \tag{7.4}$$

Rearranging for the temperature evolution gives the following:

$$\frac{DT}{Dt} = \nabla \cdot \left(\frac{k}{\rho c_p} \nabla T \right) + \frac{Q}{c_p} - \frac{L}{c_p} \frac{Df_p}{Dt}, \tag{7.5}$$

where $\alpha = k/(\rho c_p)$ is the thermal diffusivity. Applying a variable-coefficient Laplacian discretization to $\nabla \cdot (\alpha \nabla T)$ and backward differencing in time results in the fully implicit particle-level update:

$$\frac{T_i^{n+1}-T_i^n}{\delta t} = \frac{2d\sum_j L_{ij}\left(\frac{\alpha_i+\alpha_j}{2}\right)\left(T_j^{n+1}-T_i^{n+1}\right)}{\sum_j L_{ij}\|x_{ij}\|^2} + \frac{Q_i}{c_{p,i}} - \frac{L}{c_{p,i}}\frac{f_i^n - f_i^{n-1}}{\delta t}, \tag{7.6}$$

which can be rearranged as below:

$$T_i^{n+1} - \frac{\delta t\, 2d\sum_j L_{ij}\left(\frac{\alpha_i+\alpha_j}{2}\right)\left(T_j^{n+1}-T_i^{n+1}\right)}{\sum_j L_{ij}\|x_{ij}\|^2} = T_i^n + \frac{\delta t\, Q_i}{c_{p,i}} - \frac{L}{c_{p,i}}\left(f_i^n - f_i^{n-1}\right). \tag{7.7}$$

It is convenient to define the pairwise diffusion coefficient as follow:

$$D_{ij} \;=\; \frac{2d\,L_{ij}}{\sum_j L_{ij}\|x_{ij}\|^2}\,\frac{\alpha_i+\alpha_j}{2},$$

so the discrete Laplacian contribution becomes $\sum_j D_{ij}(T_j^{n+1}-T_i^{n+1})$. Assembling the contributions for all particles yields the sparse linear system:

$$\sum_j A_{ij}\,T_j^{n+1} \;=\; b_i, \tag{7.8}$$

with

$$A_{ii} = 1 + \delta t \sum_j D_{ij}, \qquad A_{ij} = -\,\delta t\, D_{ij} \quad (i \neq j),$$

and the right-hand side

$$b_i = T_i^n + \delta t\,\frac{Q_i}{c_{p,i}} - \frac{L}{c_{p,i}}\left(f_i^n - f_i^{n-1}\right).$$

Equation (7.8) provides the fully implicit temperature update; note that the latent contribution is treated here using the lagged phase fraction f^n, consistent with the IPCE update sequence described below. Once T_i^{n+1} is obtained, the particle enthalpy is computed using the (lagged) phase fraction:

$$H_i^{n+1} = c_{p,i}\,T_i^{n+1} + L\,f_i^n. \tag{7.9}$$

Define the enthalpy thresholds,

$$H_{\mathrm{p0}} = c_p T_{sat}, \qquad H_{\mathrm{p1}} = H_{\mathrm{p0}} + L, \tag{7.10}$$

which represent the enthalpy at the onset (H_{p0}) and completion (H_{p1}) of phase change and T_{sat} is the saturation temperature. The phase fraction is then updated according to the enthalpy criterion:

$$f_{p,i}^{\mathrm{new}} = \begin{cases} 0, & L < 0 \text{ (condensation/freezing)}, \quad H_i \geq H_{\mathrm{p0}}, \\ \dfrac{H_i - H_{\mathrm{p0}}}{L}, & L < 0, \quad H_{\mathrm{p1}} < H_i < H_{\mathrm{p0}}, \\ 1, & L < 0, \quad H_i \leq H_{\mathrm{p1}}, \\ 0, & L > 0 \text{ (melting/boiling)}, \quad H_i \leq H_{\mathrm{p0}}, \\ \dfrac{H_i - H_{\mathrm{p0}}}{L}, & L > 0, \quad H_{\mathrm{p0}} < H_i < H_{\mathrm{p1}}, \\ 1, & L > 0, \quad H_i \geq H_{\mathrm{p1}}. \end{cases} \tag{7.11}$$

To avoid abrupt jumps and improve numerical stability a relaxation is applied:

$$f_i^{n+1} = (1-\omega)\, f_i^n + \omega\, f_{p,i}^{\mathrm{new}}, \qquad 0 < \omega \leq 1. \tag{7.12}$$

Particle material properties are then updated by linear interpolation between phases:

$$\phi_i^{n+1} = (1 - f_i^{n+1})\, \phi_{\mathrm{phase0}} + f_i^{n+1}\, \phi_{\mathrm{phase1}}, \tag{7.13}$$

applied to ρ, μ, k, c_p (and hence to α) for the next time step. This IPCE procedure ensures a consistent, implicit advance of temperature and phase fraction while preserving the MP-LDD variable-diffusivity discretization and allowing thermodynamic checks for vapor liquid transitions [169, 171, 172]. In the proposed Lagrangian framework, heat transfer and phase change are naturally coupled through the motion of particles that carry their own thermodynamic and transport properties. The advection of enthalpy and temperature is inherently captured as each particle moves with the local flow, eliminating numerical diffusion and preserving stable thermal and phase interfaces.

7.2.1 Saturation Check via Temperature Criterion

For liquid vapor systems, relying solely on the enthalpy criterion can lead to non-physical phase transitions, as latent heat absorption or release does not guarantee thermodynamic

consistency. To address this, a local saturation condition is imposed based on the saturation temperature T_{sat} corresponding to the local pressure, ensuring that phase change is thermodynamically admissible. The saturation temperature is obtained by inverting the Antoine relation, which empirically correlates the equilibrium vapor pressure to temperature:

$$\log_{10} p_{\text{sat}}(T) = A - \frac{B}{C+T}, \tag{7.14}$$

where A, B, and C are fluid-specific coefficients. Solving for T_{sat} yields:

$$T_{\text{sat}}(p) = \frac{B}{A - \log_{10} p} - C, \tag{7.15}$$

where p is the local pressure at the computational point. At each timestep and for every computational point i, the local temperature T_i is compared with the saturation temperature $T_{\text{sat},i}$:

$$T_i \geq T_{\text{sat},i}. \tag{7.16}$$

Phase transition is allowed only if this condition is satisfied. Otherwise, the phase fraction $f_{p,i}^{n+1}$ is constrained to remain in the liquid state, even if the enthalpy indicates latent heat availability. Enthalpy threshold Equation 7.10 has been updated based on the new T_{sat} for computing the phase fraction. By combining this temperature-based saturation check with the enthalpy criterion, the model prevents spurious vapor generation and maintains physical consistency across a wide range of pressures and temperatures [173].

7.2.2 Phase Change Workflow

The computational procedure for modeling the phase transition is implemented, as illustrated in Figure 7.2. The process initiates with the calculation of the spatial temperature field via the governing energy equation defined in Equation 7.8. Once the temperature distribution is established, the total enthalpy comprising both sensible and latent heat components is computed using Equation 7.9. This enthalpy value serves as the basis for determining the local phase fraction in Equation 7.11, which identifies the transition state of the material (e.g., solid, liquid, or mushy zone). The workflow concludes by updating the effective material properties through Equation 7.13, ensuring that parameters such as thermal diffusivity, density and viscosity accurately reflect the current physical state of the domain.

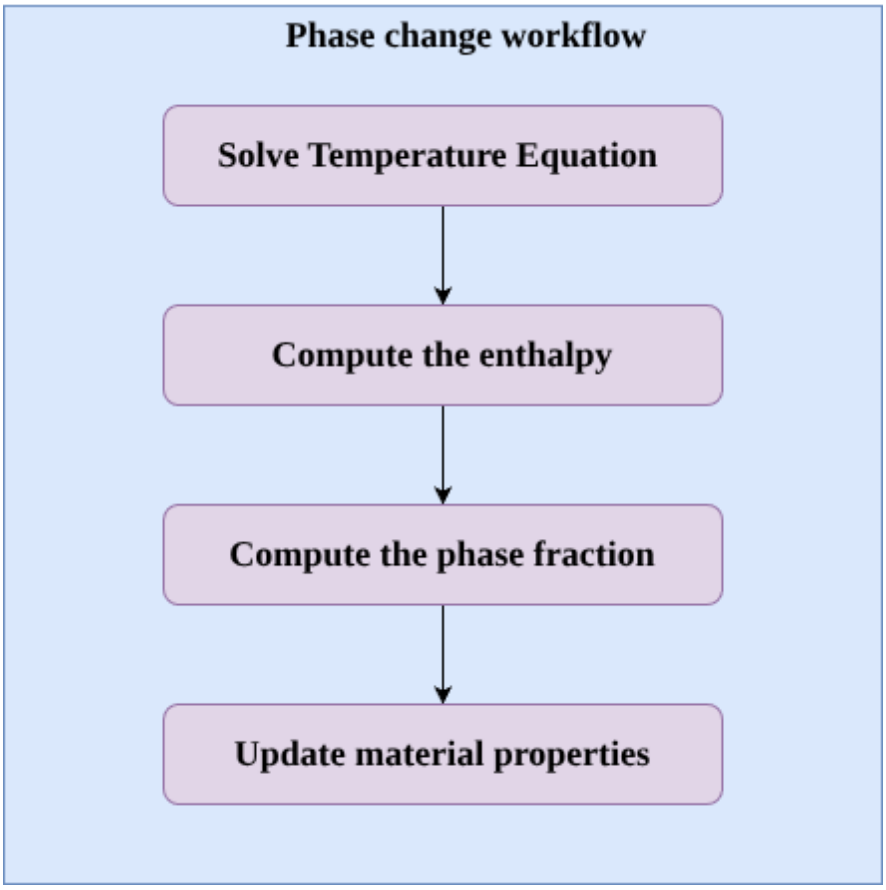

Figure 7.2. Sequential workflow for the phase change numerical solver.

7.3 Hierarchical Buoyancy Modelling Framework

Accurate prediction of buoyancy-driven flows in multiphase systems requires careful treatment of density and viscosity variations, as these properties directly influence momentum transport and phase interactions. Traditional approaches often rely on a single approximation, such as the Boussinesq assumption, which assumes density variations are negligible except in the buoyancy term. While computationally efficient, the Boussinesq approximation is only valid for small temperature differences, typically when $\frac{|T-T_{\text{ref}}|}{T_{\text{ref}}} < 5\%$ [174]. In regions with larger temperature gradients, such simplifications can lead to significant inaccuracies in predicting flow dynamics. To address these limitations, the Hierarchical Buoyancy Modeling Framework (HBMF) is proposed. HBMF adaptively selects the most appropriate model for density and viscosity based on the local phase and temperature deviation from a reference state. For points where the relative temperature deviation is small, i.e.,

$$\varepsilon = \frac{|T - T_{\text{ref}}|}{T_{\text{ref}}} \leq 0.05, \tag{7.17}$$

The Boussinesq approximation is applied for the computation of the density when there is a change in temperature under 5%, and it is applicable for both liquid and gas phases:

$$\rho = \rho_{\text{ref}}\left(1 - \beta(T - T_{\text{ref}})\right), \tag{7.18}$$

where ρ_{ref} is the reference density, β is the thermal expansion coefficient, and T_{ref} is the reference temperature. In this regime, density variations are small, and the fluid is treated as nearly incompressible, which maintains computational efficiency while capturing buoyancy effects as a source term in the momentum equation [174]. Viscosity is updated according to the phase. For liquids, an Arrhenius-type temperature dependence is used:

$$\mu_\ell = \mu_{\text{ref}} \exp\left(\frac{E_a}{R_g T}\right), \tag{7.19}$$

where μ_{ref} is the reference viscosity, E_a is the activation energy, and R_g is the universal gas constant [175]. For gases, Sutherland's law is applied:

$$\mu_g = \mu_{\text{ref}} \left(\frac{T}{T_{\text{ref,g}}}\right)^{3/2} \frac{T_{\text{ref,g}} + S}{T + S}, \tag{7.20}$$

where S is the Sutherland constant, capturing the variation in gas viscosity with temperature [176].

In regions where temperature deviations exceed the threshold ($\varepsilon > 0.05$), HBMF transitions to phase-specific models. For likely liquid regions, where $\rho_{ref} \geq 10$, density is updated using a linear temperature model:

$$\rho = \rho_{\text{ref}} - \gamma(T - T_{\text{ref}}), \tag{7.21}$$

where $\gamma = \beta\rho_{\text{ref}}$ is the linear thermal expansion coefficient, which follows the Boussinesq approximation. Additionally, γ can be treated as a constant value defined for simulation purposes. This allows for larger density variations while preserving numerical stability. For likely gas regions, where $\rho < 10$, the ideal gas law governs the density:

$$\rho = \frac{p}{RT}, \tag{7.22}$$

where p is the local pressure and R is the specific gas constant. The use of the ideal gas law should be interpreted in a low-Mach-number sense rather than as a fully compressible

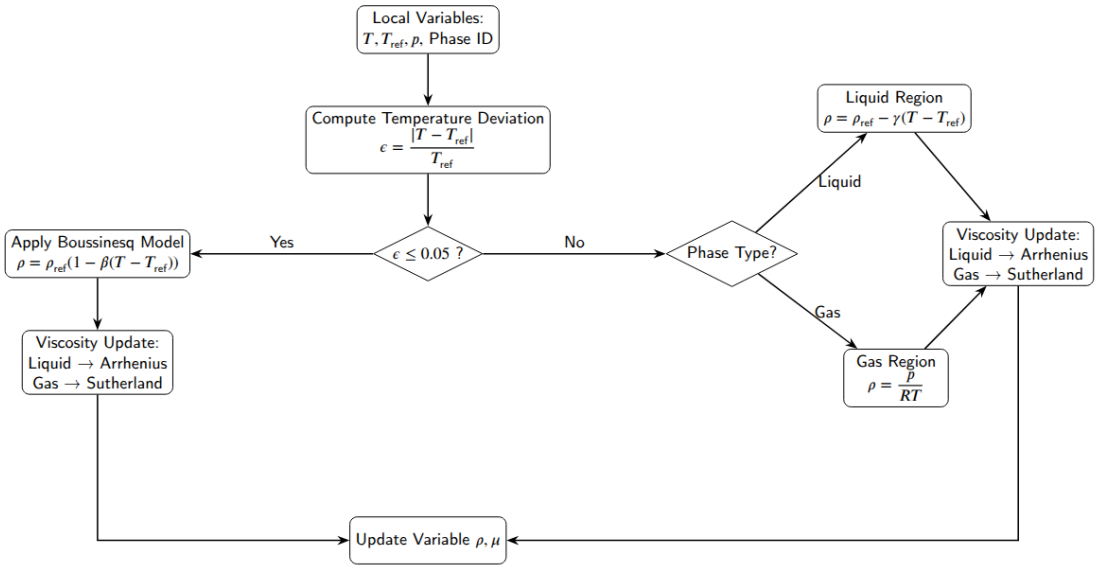

Figure 7.3. Flowchart of the Hierarchical Buoyancy Modelling Framework (HBMF). The model selection is based on the local temperature deviation ε. For small deviations, the Boussinesq approximation is applied. For larger deviations, phase-specific density models are used. Viscosity is updated according to phase.

flow model. In this setting, the gas density is allowed to vary thermodynamically according to the local pressure and temperature state, while the pressure field appearing in the momentum equation and pressure Poisson correction primarily serves to enforce the kinematic incompressibility constraint on the resolved velocity field. Accordingly, the present formulation is intended for flow regimes in which Mach numbers remain sufficiently small that acoustic compressibility effects are negligible, even though limited density variation is retained through the equation of state. The approach should therefore be understood as a weakly compressible or low-Mach approximation for gas-phase buoyancy modelling, not as a general compressible gas-dynamics formulation. Viscosity is again computed using Arrhenius or Sutherland models, corresponding to the liquid and gas phases. This hierarchical selection ensures smooth transitions between approximations while accurately capturing both buoyancy and viscous effects. This variation in density and viscosity is used in the conservation Equation 3.2 as a variable density and viscosity. The HBMF provides several advantages. By applying the Boussinesq approximation where low temperature variation. In areas with significant temperature differences, the framework uses physically accurate, phase-dependent models, enhancing predictive fidelity. This approach is particularly suitable for multiphase flows with high temperature gradients, phase change, or stratified density fields, where different regions of the domain require distinct physical treatments. Overall, HBMF represents a robust, adaptive, and physically consistent methodology for simulating buoyancy-driven multiphase flows.

The HBMF formulation adopted in this work employs threshold-based switching be-

tween buoyancy models in order to distinguish efficiently between low-density-contrast and strongly variable-density regimes. While this strategy is computationally convenient and a practical working solution. The abrupt switch at the prescribed threshold is not mathematically smooth and may introduce non-physical sensitivity in regions close to the transition point. For this reason, the present threshold should be regarded as a practical modelling choice rather than a uniquely defined physical boundary. In future developments, a smooth transition-zone formulation based on continuous blending between the Boussinesq and variable-density models would provide a more robust and physically gradual representation, and the present density-based liquid–gas criterion could likewise be replaced by a more systematically justified regime indicator.

7.4 Phase Change Solver workflow

The proposed MP-LDD framework follows a fully Lagrangian and sequential solution strategy in which fluid flow, heat transfer, and phase change are tightly coupled within each time step. The overall numerical workflow adopted in the present study is illustrated in Fig. 7.4 and is summarized below.

At the beginning of the simulation, the computational domain is initialized by applying the prescribed translation and rotation, when required, to account for moving reference frames or rigid body motion. This step ensures consistency between the physical configuration and the particle-based representation before time integration. The particle positions are then advected using the updated velocity field. To preserve numerical stability and maintain a high-quality particle distribution, a point cloud regularization procedure is applied after advection. This regularization step prevents particle clustering and void formation, which is particularly important for simulations involving large deformations or buoyancy-driven flows. Surface tension forces and dynamic contact angle effects are subsequently evaluated and incorporated into the momentum equation. This treatment enables accurate modeling of interfacial dynamics and wetting behavior at fluid solid boundaries. The pressure field is then obtained by solving a pressure Poisson equation derived from the incompressibility constraint. A single pressure field is employed for all phases, which allows the method to robustly handle large density ratios while preserving a sharp and stable interface. Following the pressure correction, the velocity field is updated. The updated velocity accounts for the combined effects of pressure gradients, viscous stresses, surface tension forces, and body forces. Thermal transport is solved next by updating the temperature field. Buoyancy effects induced by temperature dependent density variations are included through a body force term, providing two way coupling between the thermal and momentum equations. Phase change is modelled using an enthalpy based formulation in which latent heat effects are implicitly coupled with the temperature field. The local phase fraction and thermophysical properties are updated consistently based on the enthalpy, ensuring numerical robustness and preventing

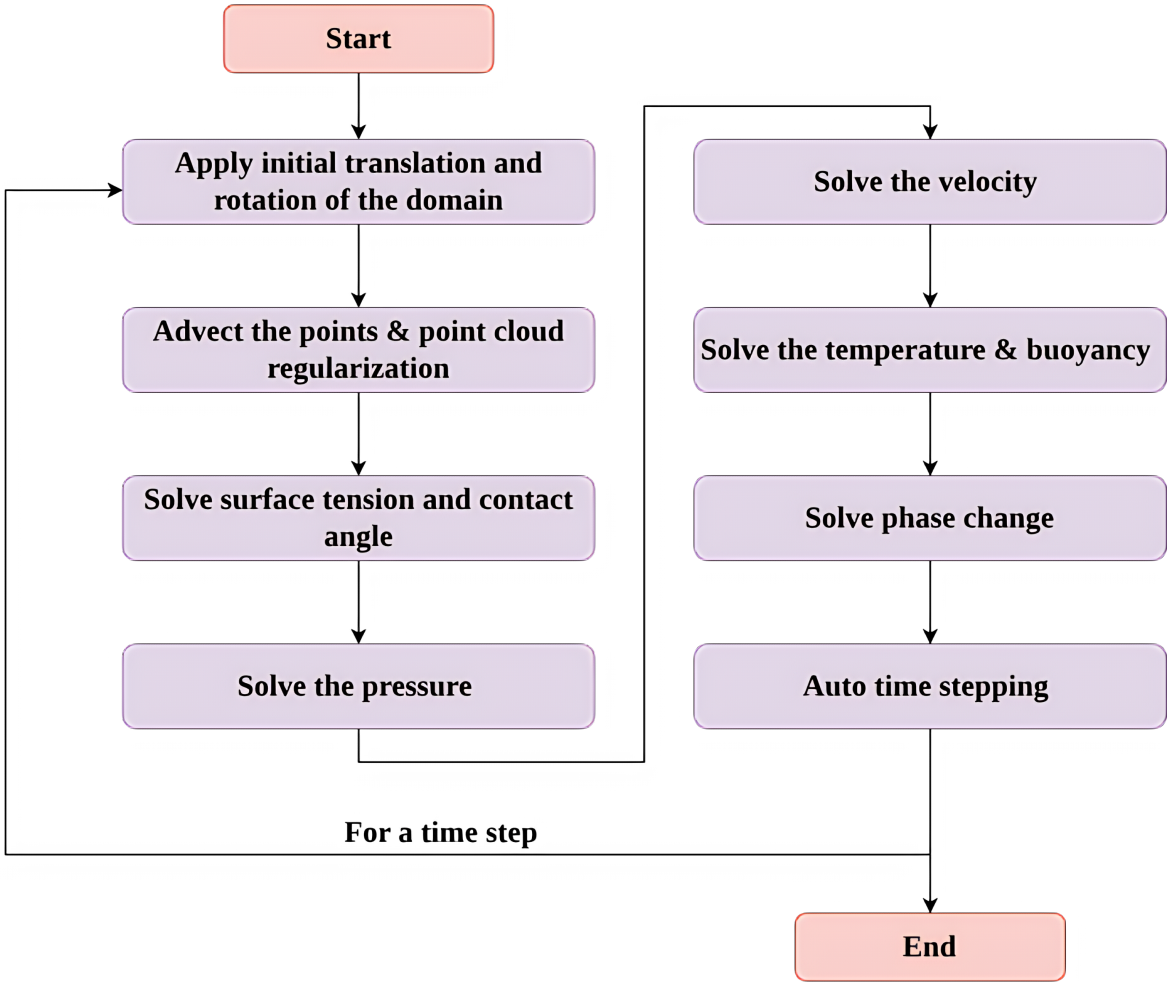

Figure 7.4. Flowchart of the MP–LDD solver workflow for coupled flow, heat transfer, surface tension, and phase change simulations.

non-physical temperature oscillations near the phase interface. Finally, an automatic time-stepping strategy is employed to adapt the time step. The above procedure is repeated until the prescribed end time or convergence criterion is reached.

7.5 Numerical Procedure of the Heat Transfer and Phase Change Formulation

7.5.1 Part I: Enthalpy-Based Energy Equation

Step 1: Motivation - From Internal Energy to Enthalpy

The internal energy form of the energy equation captures sensible heating but does not explicitly account for latent heat during phase transitions. To remedy this, the energy equation is recast in terms of specific enthalpy H, defined as:

$$H = U + \frac{p}{\rho} \tag{7.23}$$

where U is the specific internal energy, p is pressure, and ρ is density. For *incompressible* flows the pressure-work term p/ρ is negligible, so changes in H effectively represent changes in U. The key advantage is that latent heat can be incorporated naturally through a phase fraction $f_p \in [0,1]$, which represents the fraction of material that has undergone phase transition:

$$H = c_p T + L f_p \tag{7.24}$$

where c_p is the specific heat capacity, T is temperature, and L is the latent heat of phase change.

Step 2: Sign Convention for Latent Heat

The sign of the latent heat contribution depends on whether the process is endothermic or exothermic:

$$H = \begin{cases} c_p T + L f_p, & \text{endothermic (melting, vaporisation): energy absorbed from surroundings,} \\ c_p T - L f_p, & \text{exothermic (solidification, condensation): energy released to surroundings.} \end{cases} \tag{7.25}$$

Correct treatment of this sign convention is essential to preserve global energy conservation in any numerical phase-change model.

Step 3: Enthalpy-Based Conservation of Energy

Substituting the enthalpy definition into the material-derivative form of the energy conservation law gives:

$$\frac{DH}{Dt} = \nabla \cdot \left(\frac{k}{\rho} \nabla T \right) + \rho Q \tag{7.26}$$

where k is the thermal conductivity and Q is the volumetric heat source ($\mathrm{W\,kg^{-1}}$). Equation (7.26) is the governing continuous equation for all subsequent discretisation steps.

7.5.2 Part II: Implicit Phase-Coupled Energy (IPCE) Formulation

Step 4: Expanding the Material Derivative of Enthalpy

Substituting $H = c_p T + L f_p$ into Equation (7.26) and expanding the material derivative:

$$\rho \frac{D(c_p T + L f_p)}{Dt} = \nabla \cdot (k \nabla T) + \rho Q \tag{7.27}$$

Dividing through by ρc_p and rearranging so that the temperature evolution is isolated on the left-hand side:

$$\frac{DT}{Dt} = \nabla \cdot \left(\frac{k}{\rho c_p} \nabla T \right) + \frac{Q}{c_p} - \frac{L}{c_p} \frac{Df_p}{Dt} \tag{7.28}$$

where $\alpha = k/(\rho c_p)$ is the thermal diffusivity. The term $\frac{L}{c_p}\frac{Df_p}{Dt}$ acts as a latent-heat source (or sink) that couples temperature and phase fraction through the energy equation.

Step 5: Implicit Time Discretisation with Backward Differencing

Applying a first-order backward (implicit) difference in time to $\frac{DT}{Dt}$ and a lagged (explicit) approximation to the phase-fraction rate $\frac{Df_p}{Dt} \approx \frac{f_i^n - f_i^{n-1}}{\delta t}$:

$$\frac{T_i^{n+1} - T_i^n}{\delta t} = \frac{2d \sum_j L_{ij} \left(\frac{\alpha_i + \alpha_j}{2} \right) \left(T_j^{n+1} - T_i^{n+1} \right)}{\sum_j L_{ij} \left\| x_{ij} \right\|^2} + \frac{Q_i}{c_{p,i}} - \frac{L}{c_{p,i}} \frac{f_i^n - f_i^{n-1}}{\delta t} \tag{7.29}$$

where the spatial term uses the variable-coefficient Laplacian operator (analogous to Equation 5.27 in Appendix 5.2), with the arithmetic mean $\frac{\alpha_i + \alpha_j}{2}$ interpolating diffusivity across phase interfaces.

Step 6: Rearrangement into an Implicit Equation for T^{n+1}

Multiplying Equation (7.29) by δt and moving all terms containing T^{n+1} to the left-hand side:

$$T_i^{n+1} - \frac{\delta t \cdot 2d \sum_j L_{ij} \left(\frac{\alpha_i + \alpha_j}{2} \right) \left(T_j^{n+1} - T_i^{n+1} \right)}{\sum_j L_{ij} \left\| x_{ij} \right\|^2} = T_i^n + \frac{\delta t \, Q_i}{c_{p,i}} - \frac{L}{c_{p,i}} \left(f_i^n - f_i^{n-1} \right) \tag{7.30}$$

Step 7: Pairwise Diffusion Coefficient

To simplify notation, the pairwise thermal diffusion coefficient is defined as:

$$D_{ij} = \frac{2d \, L_{ij}}{\sum_j L_{ij} \left\| x_{ij} \right\|^2} \cdot \frac{\alpha_i + \alpha_j}{2} \tag{7.31}$$

The discrete Laplacian contribution then compresses to $\sum_j D_{ij}(T_j^{n+1} - T_i^{n+1})$.

Step 8: Assembly of the Global Linear System

Collecting Equation (7.30) for all computational points yields the sparse linear system:

$$\sum_j A_{ij} T_j^{n+1} = b_i \tag{7.32}$$

with coefficient matrix entries:

$$A_{ii} = 1 + \delta t \sum_j D_{ij}, \qquad A_{ij} = -\delta t\, D_{ij} \quad (i \neq j) \tag{7.33}$$

and the right-hand side vector:

$$b_i = T_i^n + \delta t \frac{Q_i}{c_{p,i}} + \frac{L}{c_{p,i}} \left(f_i^n - f_i^{n-1} \right) \tag{7.34}$$

The diagonal dominance of A_{ij} (since $A_{ii} > 0$ and $A_{ij} \leq 0$ for $i \neq j$) guarantees stability of the implicit scheme without restrictive time-step limitations.

Step 9: Particle Enthalpy Update

Once T_i^{n+1} is obtained from the linear system (7.32), the particle enthalpy is computed using the lagged phase fraction f_i^n (consistent with the implicit update sequence):

$$H_i^{n+1} = c_{p,i} T_i^{n+1} + L f_i^n \tag{7.35}$$

Step 10: Enthalpy Thresholds for Phase Change

The onset and completion of phase change are delineated by two enthalpy thresholds computed from the saturation temperature T_{sat}:

$$H_{p0} = c_p T_{\text{sat}}, \qquad H_{p1} = H_{p0} + L \tag{7.36}$$

where H_{p0} marks the beginning and H_{p1} marks the completion of the phase transition.

Step 11: Phase Fraction Update via Enthalpy Criterion

The new phase fraction $f_{p,i}^{\text{new}}$ is determined by comparing H_i^{n+1} against the thresholds (7.36). The sign of L distinguishes exothermic from endothermic processes:

$$f_{p,i}^{\text{new}} = \begin{cases} 0, & L < 0 \text{ (condensation/freezing)}, \quad H_i \geq H_{p0}, \\ \dfrac{H_i - H_{p0}}{L}, & L < 0, \quad H_{p1} < H_i < H_{p0}, \\ 1, & L < 0, \quad H_i \leq H_{p1}, \\ 0, & L > 0 \text{ (melting/boiling)}, \quad H_i \leq H_{p0}, \\ \dfrac{H_i - H_{p0}}{L}, & L > 0, \quad H_{p0} < H_i < H_{p1}, \\ 1, & L > 0, \quad H_i \geq H_{p1}. \end{cases} \tag{7.37}$$

Step 12: Relaxation of the Phase Fraction

To suppress abrupt jumps and improve numerical stability, the phase fraction update is relaxed:

$$f_i^{n+1} = (1-\omega)\, f_i^n + \omega\, f_{p,i}^{\text{new}}, \qquad 0 < \omega \leq 1 \tag{7.38}$$

where ω is the relaxation factor. Setting $\omega = 1$ recovers the unrelaxed update; smaller values damp oscillations near the phase interface.

Step 13: Material Property Update by Linear Interpolation

Once f_i^{n+1} is known, all temperature- and phase-dependent material properties are updated by linear interpolation between the two-phase values:

$$\phi_i^{n+1} = (1 - f_i^{n+1})\, \phi_{\text{phase0}} + f_i^{n+1}\, \phi_{\text{phase1}} \tag{7.39}$$

applied individually to ρ, μ, k, c_p (and hence to $\alpha = k/(\rho c_p)$) for the next time step.

7.5.3 Part III: Saturation Check via Antoine Relation

Step 14: Antoine Equation for Saturation Pressure

For liquid–vapour systems, the enthalpy criterion alone can produce non-physical phase transitions. Thermodynamic consistency is enforced by requiring the local temperature to exceed the saturation temperature T_{sat} corresponding to the local pressure. The saturation pressure is given by the empirical Antoine relation:

$$\log_{10} p_{\text{sat}}(T) = A - \frac{B}{C + T} \tag{7.40}$$

where A, B, C are fluid-specific coefficients.

Step 15: Inversion for Saturation Temperature

Inverting Equation (7.40) to express T_{sat} as a function of the local pressure p:

$$T_{\text{sat}}(p) = \frac{B}{A - \log_{10} p} - C \tag{7.41}$$

Step 16: Saturation Criterion

At each time step and for every computational point i, phase change is permitted only when:

$$T_i \geq T_{\text{sat},i} \tag{7.42}$$

If this condition is not met, the phase fraction $f_{p,i}^{n+1}$ is constrained to the liquid state regardless of the enthalpy value, preventing spurious vapour generation. The enthalpy thresholds (7.36) are recomputed with the updated $T_{\text{sat},i}$ at each step.

7.5.4 Part IV: Hierarchical Buoyancy Modelling Framework (HBMF)

Step 17: Temperature Deviation and Regime Selection

Traditional Boussinesq-based buoyancy models are only accurate for small temperature deviations, typically when:

$$\varepsilon = \frac{|T - T_{\text{ref}}|}{T_{\text{ref}}} \leq 0.05 \tag{7.43}$$

The HBMF adaptively selects the density and viscosity model based on whether the local ε falls below or above this threshold, and on the local phase.

Step 18: Small Deviation Regime ($\varepsilon \leq 0.05$) - Boussinesq Approximation

When ε is small, density variations are treated with the linear Boussinesq approximation (valid for both liquid and gas phases):

$$\rho = \rho_{\text{ref}}\big(1 - \beta(T - T_{\text{ref}})\big) \tag{7.44}$$

where ρ_{ref} is the reference density, β is the volumetric thermal expansion coefficient, and T_{ref} is the reference temperature. This approximation treats the fluid as nearly incompressible and introduces buoyancy as a source term in the momentum equation, preserving computational efficiency.

Step 19: Viscosity Models in the Small Deviation Regime

Viscosity is updated according to phase:

Liquid phase - Arrhenius model:

$$\mu_\ell = \mu_{\text{ref}} \exp\left(\frac{E_a}{R_g T}\right) \tag{7.45}$$

where μ_{ref} is the reference viscosity, E_a is the activation energy, and R_g is the universal gas constant [175].

Gas phase - Sutherland's law:

$$\mu_g = \mu_{\text{ref}} \left(\frac{T}{T_{\text{ref},g}}\right)^{3/2} \frac{T_{\text{ref},g} + S}{T + S} \tag{7.46}$$

where S is the Sutherland constant and $T_{\text{ref},g}$ is the reference temperature for the gas [176].

Step 20: Large Deviation Regime ($\varepsilon > 0.05$) - Phase-Specific Density Models

When temperature deviations exceed the Boussinesq validity threshold, the HBMF transitions to phase-specific density laws.

Liquid regions ($\rho_{\text{ref}} \geq 10\,\text{kg}\,\text{m}^{-3}$) - Linear thermal expansion:

$$\rho = \rho_{\text{ref}} - \gamma(T - T_{\text{ref}}), \qquad \gamma = \beta\,\rho_{\text{ref}} \tag{7.47}$$

where γ is the linear thermal expansion coefficient. This expression retains the functional form of the Boussinesq approximation while allowing larger density variations without sacrificing numerical stability. The coefficient γ may alternatively be specified as a constant calibrated to the material of interest.

Gas regions ($\rho < 10\,\text{kg}\,\text{m}^{-3}$) - Ideal gas law:

$$\rho = \frac{p}{RT} \tag{7.48}$$

where p is the local pressure and R is the specific gas constant. The ideal gas law accounts for compressibility effects that become significant at large temperature gradients.

Viscosity: In the large-deviation regime, viscosity is again computed using the Arrhenius model (7.45) for liquids and Sutherland's law (7.46) for gases.

Step 21: Integration with the Momentum Equation

The density and viscosity values obtained from Steps 18–20 are used directly in the variable-property Navier-Stokes momentum equation, replacing constant-property coefficients. This

introduces buoyancy and viscous effects that vary continuously in space and time, consistent with the local thermodynamic state.

For practical heat-transfer simulations, the interior discretisation described above must be supplemented by appropriate thermal boundary conditions at solid walls and interfaces. In the present particle framework, thermal boundary conditions are imposed at boundary particles according to the prescribed type of thermal constraint.

For a Dirichlet boundary condition, the temperature is prescribed directly at the boundary,

$$T = T_b \qquad \text{on } \Gamma_D, \tag{7.49}$$

where T_b is the imposed boundary temperature. In the discrete system, this is enforced by replacing the corresponding row of the linear system with the identity relation

$$A_{ii} = 1, \qquad A_{ij} = 0 \; (j \neq i), \qquad b_i = T_b. \tag{7.50}$$

For a Neumann boundary condition, the normal heat flux is prescribed,

$$-k \nabla T \cdot \mathbf{n} = q_n \qquad \text{on } \Gamma_N, \tag{7.51}$$

where q_n is the imposed outward heat flux and $\mathbf{n}$ is the outward unit normal vector. In the particle framework, this condition is incorporated as an additional boundary contribution to the discrete energy balance at the boundary particle, so that the prescribed thermal flux modifies the right-hand side of the implicit temperature system.

For a Robin boundary condition, convective heat exchange with an external environment is prescribed,

$$-k \nabla T \cdot \mathbf{n} = h_c \, (T - T_\infty) \qquad \text{on } \Gamma_R, \tag{7.52}$$

where h_c is the convective heat-transfer coefficient and T_∞ is the ambient temperature. This condition is treated as a mixed boundary condition, contributing both to the diagonal coefficient of the boundary particle and to the right-hand side through the ambient-temperature term.

Accordingly, Dirichlet conditions impose temperature directly, whereas Neumann and Robin conditions act through prescribed boundary heat fluxes. The detailed implementation of these boundary operators in the particle setting follows the same local-support philosophy as the interior discretisation, with boundary particles carrying either prescribed temperature values or equivalent flux contributions depending on the physical problem under consideration.

7.5.5 Summary of the Heat Transfer and Phase Change

The complete formulation proceeds through the following logical sequence:

1. **Enthalpy definition** (Equations (7.24)–(7.25)): Total enthalpy $H = c_p T \pm L f_p$ unifies sensible and latent heat in a single scalar.

2. **Continuous energy equation** (Equation (7.26)): Material derivative of H equals diffusive flux plus volumetric source.

3. **Temperature–phase fraction form** (Equations (7.27)–(7.28)): Expanding DH/Dt separates sensible and latent contributions; $\alpha = k/(\rho c_p)$ emerges.

4. **Implicit time discretisation** (Equation (7.29)): Backward differencing of DT/Dt; latent term lagged to f^n.

5. **Pairwise diffusion coefficient** (Equation (7.31)): D_{ij} absorbs the variable Laplacian normalisation.

6. **Linear system for temperature** (Equations (7.32)–(7.34)): Diagonally dominant system $\sum_j A_{ij} T_j^{n+1} = b_i$ solved by PBICGSTAB.

7. **Enthalpy update** (Equation (7.35)): H_i^{n+1} computed from updated T^{n+1} and lagged f^n.

8. **Phase change thresholds** (Equation (7.36)): H_{p0} and H_{p1} bracket the isothermal transition.

9. **Phase fraction update** (Equation (7.37)): $f_{p,i}^{\text{new}}$ set by comparing H_i^{n+1} to thresholds; sign of L distinguishes endo/exothermic.

10. **Relaxation** (Equation (7.38)): $f^{n+1} = (1-\omega) f^n + \omega f^{\text{new}}$ damps interface oscillations.

11. **Property interpolation** (Equation (7.39)): ρ, μ, k, c_p updated linearly between phase values.

12. **Saturation check** (Equations (7.40)–(7.42)): Antoine inversion gives $T_{\text{sat}}(p)$; phase change suppressed if $T_i < T_{\text{sat},i}$.

13. **Boussinesq regime** ($\varepsilon \leq 0.05$, Equations (7.44)–(7.46)): Linear density correction; Arrhenius or Sutherland viscosity.

14. **Phase-specific regime** ($\varepsilon > 0.05$, Equations (7.47)–(7.48)): Linear expansion for liquids; ideal gas law for gases; viscosity unchanged in model form.

8 VALIDATION AND VERIFICATION

This chapter presents comprehensive validation and verification of the computational framework developed in the preceding chapters. The validation strategy encompasses individual model components as well as coupled multiphysics scenarios, establishing the reliability, robustness, and numerical performance of the integrated MP-LDD framework through systematic verification against mathematical solutions, experimental data, and numerical findingss.

The chapter is categorised into four main sections: Section 8.1 validates the fluid-structure interaction capabilities through classical FSI benchmarks. Section 8.2 demonstrates the multiphase flow modeling accuracy for flows with density ratios from 2:1 to 1000:1. Section 8.3 verifies the surface tension and dynamic contact angle implementations through capillary-driven flow problems. Section 8.4 validates the energy formulation and buoyancy modeling through heat transfer, natural convection and phase change benchmarks.

8.1 Fluid Structure Interaction

8.1.1 Testing of the LDD and Modal Solver

Validation of Sloshing in a Cuboidal Tank

The predictive capability of the LDD flow solver is assessed against published experimental measurements from the sloshing test campaign reported by Rhee [177]. The test setup involves a rectangular box-shaped container whose interior measures 1200 mm, 600 mm, and 300 mm in the x, y, and z directions respectively, as depicted in Figure 8.1.
Water is introduced into the tank up to one-fifth of its full capacity. A prescribed sinusoidal rigid body translation is imposed in the direction of x-axis, with an excitation magnitude of 0.06 m and the period of oscillation is 1.94 s. The objective of the case is to establish whether the LDD solver can accurately reproduce the experimentally measured impact pressure at a specified sensor location in the given domain, fluid properties, and kinematic excitation conditions. The time-averaged pressure signal recorded at the P1 sensor which is, located 570 mm from the tank origin in the x-direction, is extracted from the numerical simulation and compared with experiment in Figure 8.2. The quantitative pressure deviations at the two principal sloshing peaks are reported in Table 8.1.

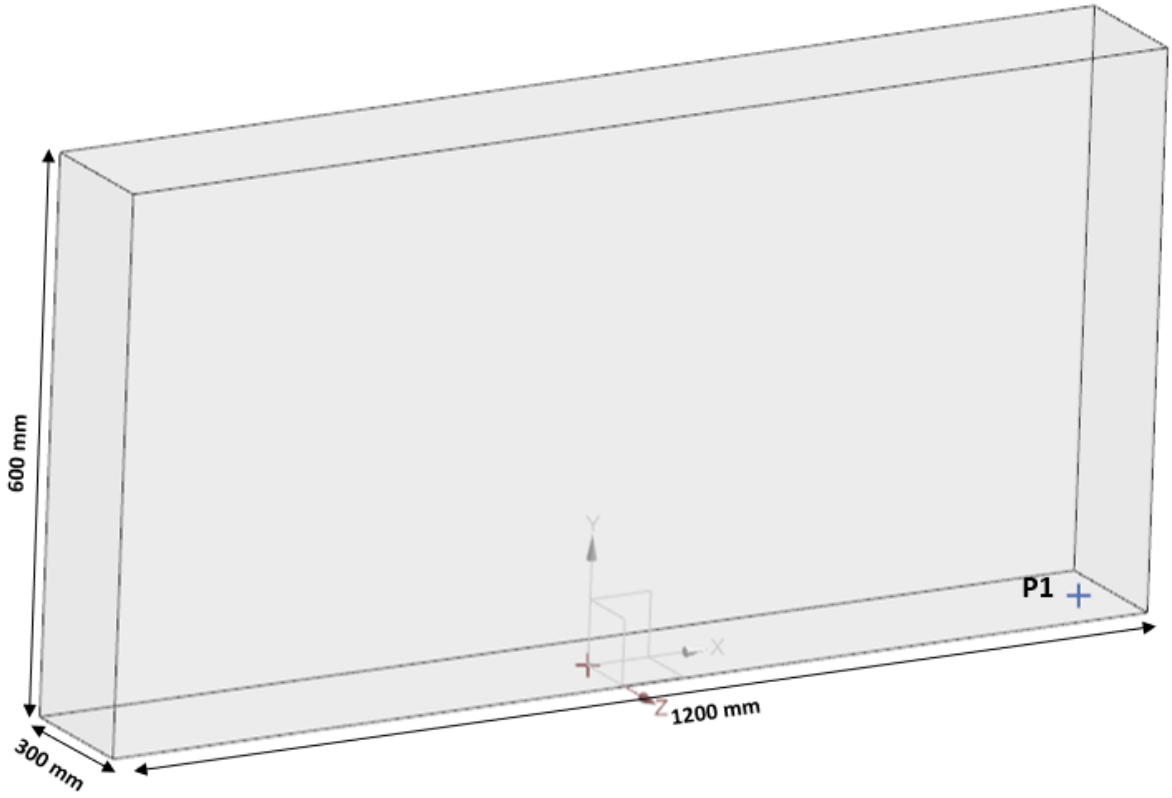

Figure 8.1. Cuboidal tank geometry used for the sloshing validation study.

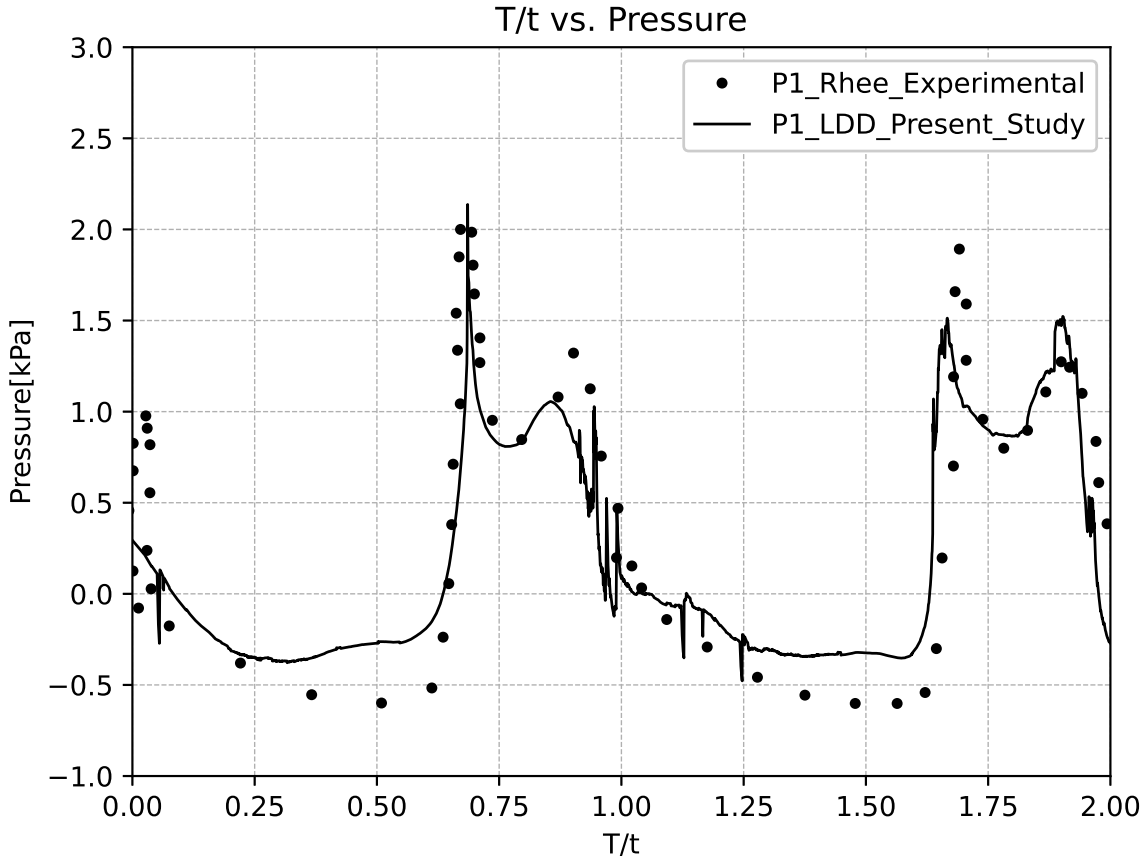

Figure 8.2. Pressure time history at sensor location P1 obtained from the LDD simulation compared against the experimental measurements.

Table 8.1. Deviation of numerically predicted pressure from the experimentally measured values at the sloshing pressure peaks.

Region	1st Peak	2nd Peak
Deviation of pressure [kPa]	0.1	0.35

The numerically predicted peak pressure values of each sloshing exhibits a close match with the experimental impact pressure measurements, validating the capacity of the flow solver to accurately resolve sloshing-induced pressure loads. This level of agreement is of particular significance in the context of the modal superposition framework, as the pressure field computed by the fluid solver serves directly as the forcing input to the structural equations of motion. Inaccuracies in the predicted pressure field would propagate directly into errors in the computed structural deformation, potentially compromising the safety assessment and performance evaluation of the structural components under consideration. Confidence in the fidelity of the flow solver under sloshing excitation therefore provides a reliable foundation for the subsequent coupled FSI simulations.

Modal Analysis of a Cantilever Beam Under Free Vibration

validation of the modal solver implementation is conducted through an independent simulation. In this analysis, a cantilever beam is exposed to a constant point load that is applied instantaneously and sustained for the duration of the study. The beam measures 0.079 meters in length and a cross-sectional width of 0.005 meters, and it experiences a tip force of 1 Newton, as depicted in Figure 8.3. The first five natural frequencies and their corresponding mode shapes are extracted from a prior modal analysis, presented in Table 8.2 and visualised in Figures 8.4 and 8.5.

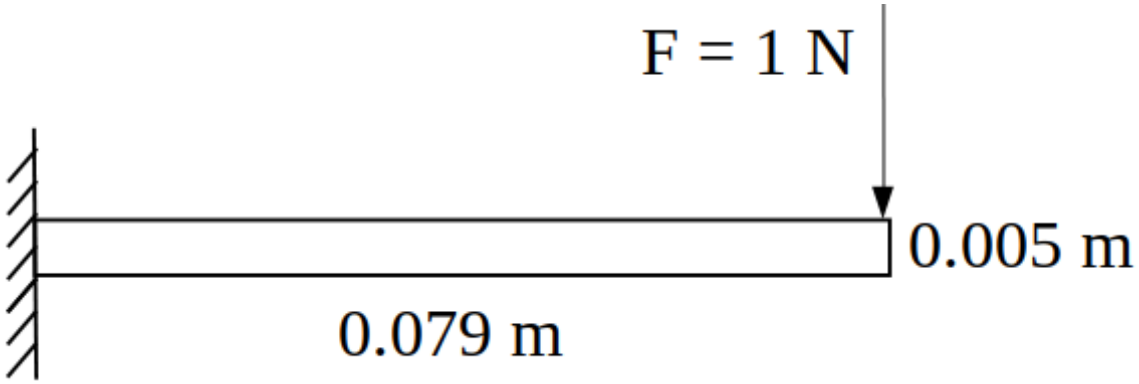

Figure 8.3. Cantilever beam configuration experiencing constant tip load, used for verifying the modal superposition implementation.

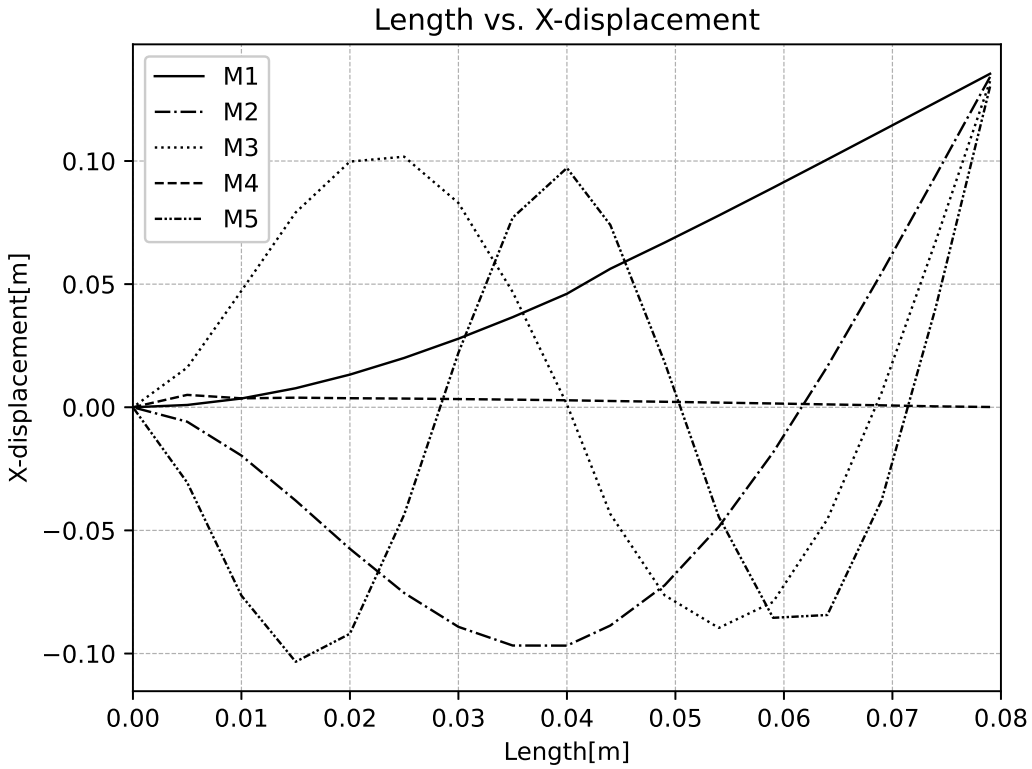

Figure 8.4. X-Directional Displacement of the Cantilever Beam : Vibration Mode Shapes

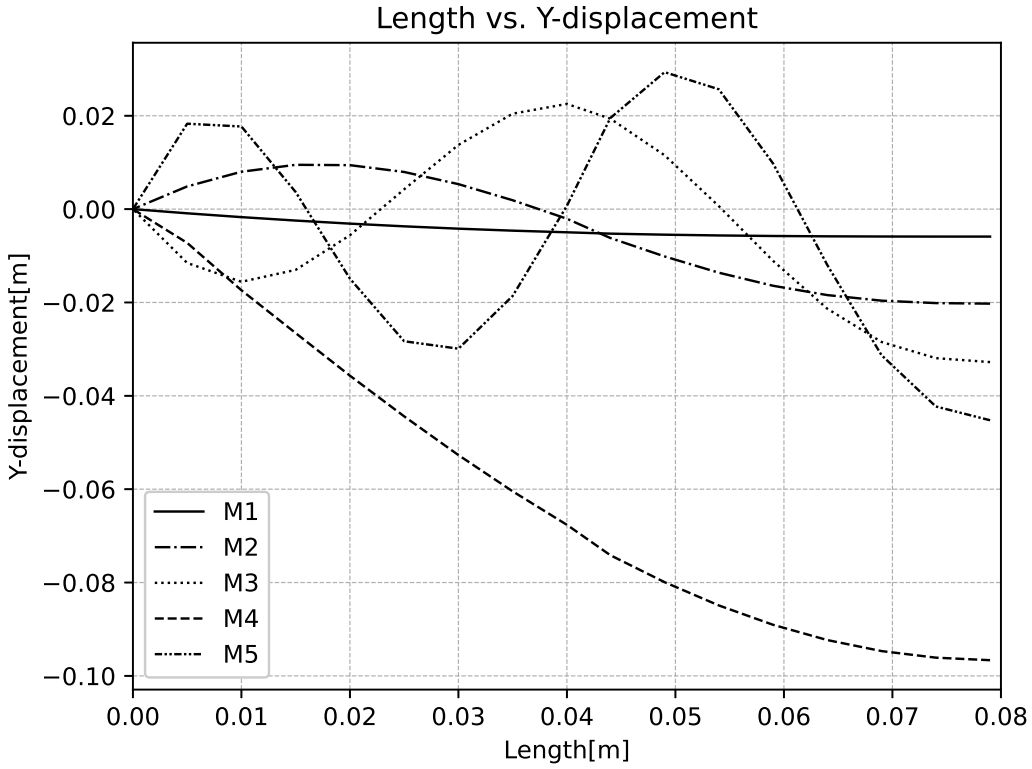

Figure 8.5. Y-Directional Displacement of the Cantilever Beam : Vibration Mode Shapes.

The analytical displacement response of a damped cantilever beam under a sustained tip load

Table 8.2. First five natural frequencies of the cantilever beam.

Mode	1	2	3	4	5
Natural Frequency (Hz)	15.09	93.433	257.66	374.8	495.57

is obtained by superposing the contributions from each natural frequency according to:

$$y(t) = \sum_{i=0}^{n} \frac{F}{\omega_{n_i}^2} \left(1 - e^{-\zeta \omega_{n_i} t} \cos(\omega_{d_i} t)\right) \tag{8.1}$$

where $y(t)$ is the structural deflection at time t, F is the magnitude of the applied tip load, and n denotes the total number of modes retained in the superposition. The factor F/ω_n^2 normalises the static contribution of each mode. The exponential term $e^{-\zeta \omega_n t}$ introduces amplitude decay due to viscous damping, with higher values of the damping ratio ζ producing more rapid attenuation of the oscillatory response. The cosine term $\cos(\omega_d t)$ governs the oscillatory component of the response at the damped natural frequency ω_d, which is related to the undamped natural frequency ω_n through:

$$\omega_d = \omega_n \sqrt{1 - \zeta^2} \tag{8.2}$$

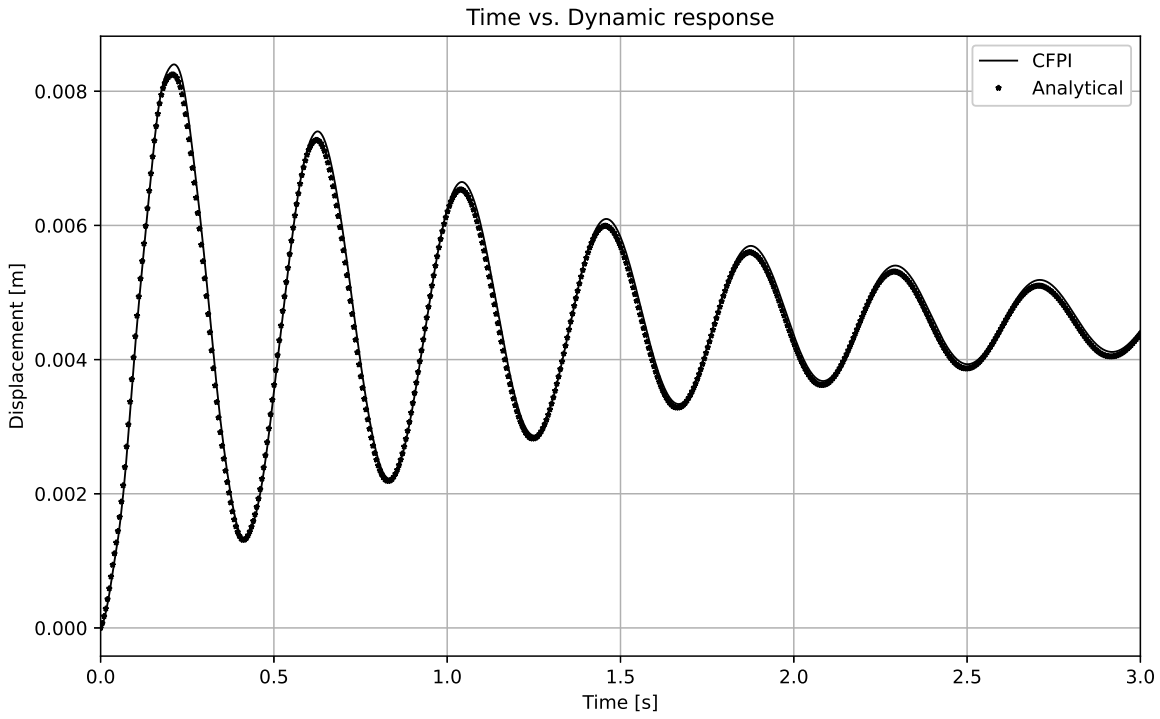

Figure 8.6. Validation of the numerically obtained dynamic displacement response against the analytical solution for a cantilever beam subjected to a constant tip load.

Since the dynamic response is governed primarily by the initial mode shapes, all analyses were carried out retaining the five lowest modes. The theoretical displacement history was

computed using Equation (8.1) and compared against the numerically integrated response obtained using the CFPI solver. The outcomes are depicted in Figure 8.6. The numerical solution reproduces the theoretical prediction with a displacement discrepancy of the order 1×10^{-4}, offering robust confirmation of the correctness and numerical accuracy of the modal solver implementation. It is noted that this case represents a relatively straightforward loading scenario, and more demanding validation cases involving coupled fluid loading are addressed in the subsequent sections.

8.1.2 Deformation of a Cantilever Gate

The bidirectional interaction between the fluid and structural solvers is verified against the experimental benchmark of Antoci et al. [178], which involves the progressive deformation of a flexible rubber gate under transient hydrodynamic loading. The test configuration resembles a dam-break scenario in which a column of fluid is initially retained by a compliant gate fixed along its upper edge to a rigid wall. As the fluid column is released, it exerts time-varying pressure forces on the gate, inducing elastic deformation. The fluid domain within the tank spans a length of $A = 100$ mm and reaches a height of $H = 140$ mm, while the rubber gate has a height of $L = 79$ mm and extends downward to contact the tank floor. The gate material is modelled as a linearly elastic isotropic material with a density of $\rho_{gate} = 1100$ kg/m^3 and a Young's modulus of $E = 12$ MPa. The fluid is water with a density of $\rho = 1000$ kg/m^3 and a dynamic viscosity of $\mu = 10^{-3}$ Pa·s. Given the quasi-static nature of the deformation in this configuration, only the fundamental bending mode and its associated natural frequency are retained in the simulation. The temporal evolution of the gate deformation under the action of the fluid pressure field is presented in Figure 8.7. The computed deformation pattern and its order of magnitude are consistent with the experimentally recorded data reported by Antoci et al. [178], confirming that the coupling implementation accurately transfers pressure loads from the fluid solver to the structural solver and reproduces the resulting elastic deformation. The small discrepancy observed in the predicted displacement magnitude is attributed to the inherently static character of the first mode approximation in this loading regime, which introduces a minor deviation from the experimentally measured response while preserving the correct qualitative behaviour.

8.1.3 Elastic Baffle in a Sloshing Tank

To examine the transient structural behaviour of a flexible body subjected to periodic hydrodynamic loading [179, 180, 181], a flexible baffle is incorporated at the bottom of the sloshing tank described in Section 8.1.1 and shown in Figure 8.1. An identical sinusoidal motion is imposed, characterised by an amplitude of 0.06 m and a period of 1.94 s. The tank enclosure is treated as as non-deformable, leaving the baffle as the only deformable member in the structural system, as illustrated in Figure 8.8.

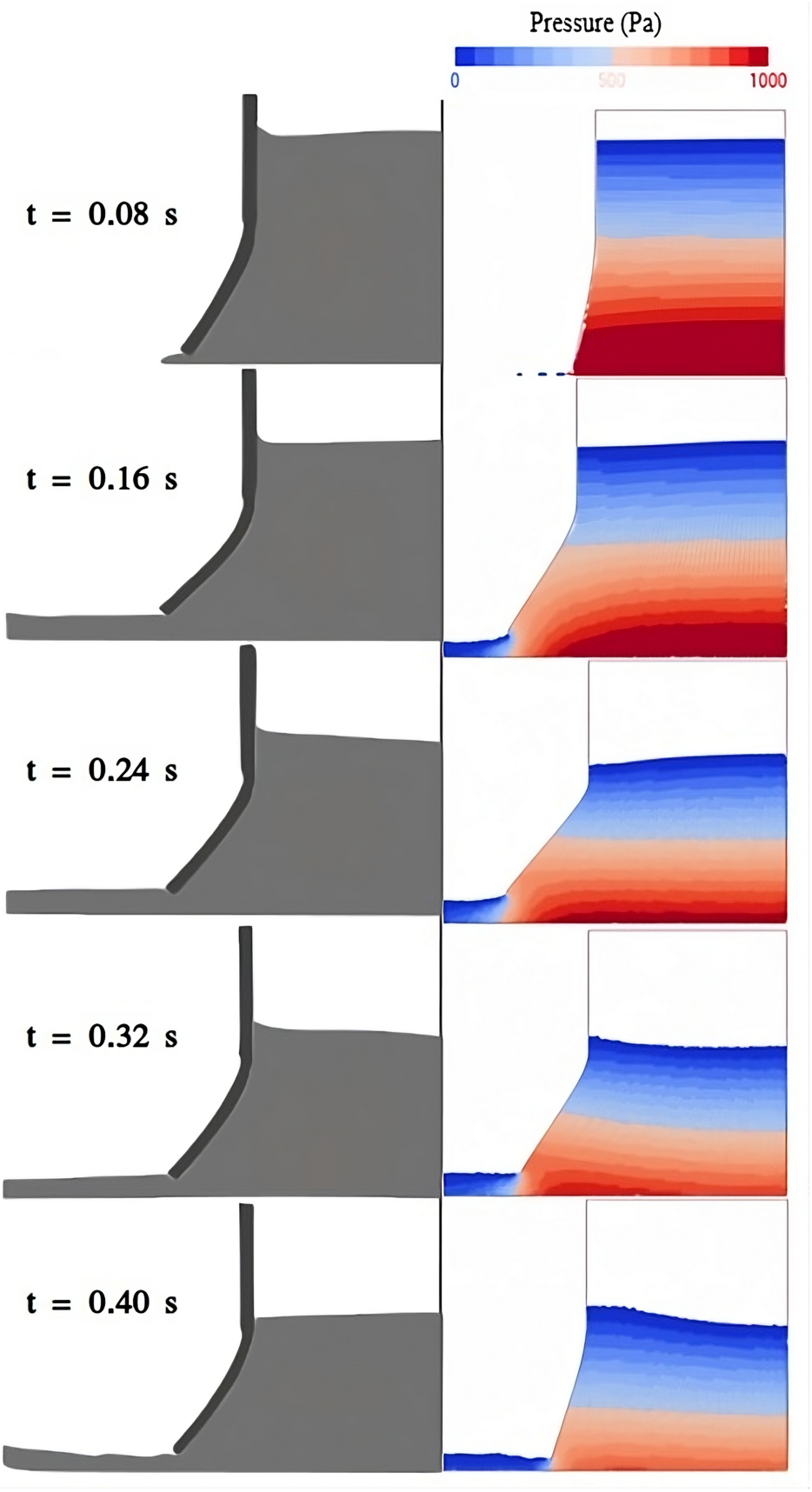

Figure 8.7. Time-varying behaviour of the cantilever gate deformation at $t = 0.08$ s, 0.16 s, 0.24 s, 0.32 s, and 0.40 s, compared against the reference experimental data.

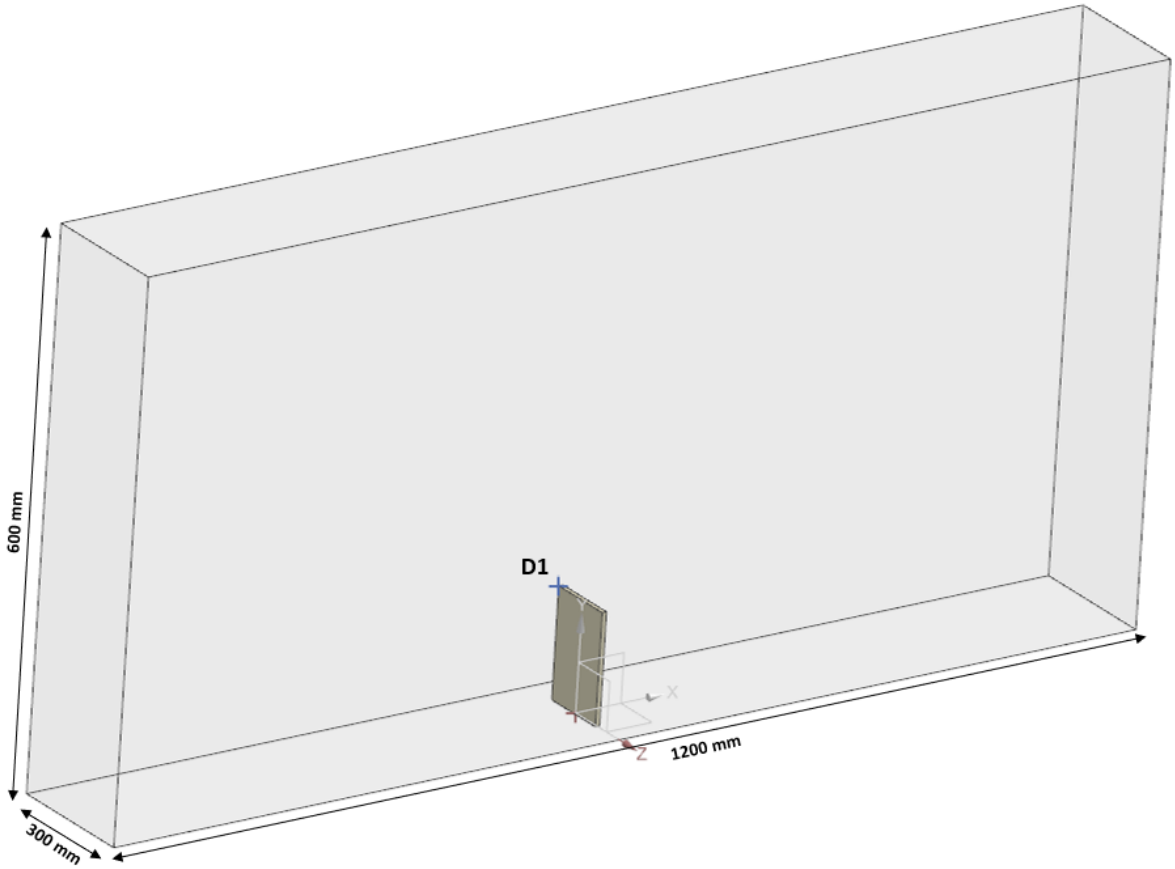

Figure 8.8. Schematic of the sloshing tank featuring a flexible baffle fixed at the base.

baffle geometry is defined by outer dimensions of 5 mm, 150 mm, and 120 mm along the x, y, and z axes respectively. The baffle material is characterised by a density of 4096 kg/m³, an elastic modulus of 38.4 MPa, and a Poisson's ratio of 0.3. The first five mode shapes and natural frequencies are extracted from a preliminary modal analysis and subsequently used as input to the FSI simulation. The resulting mode shapes are depicted in Figure 8.9 and the corresponding natural frequencies are listed in Table 8.3.

Table 8.3. First Five Vibration Modes of the Elastic Baffle.

Mode	1	2	3	4	5
Natural Frequency (Hz)	100.12	270.05	301.33	392.05	505.44

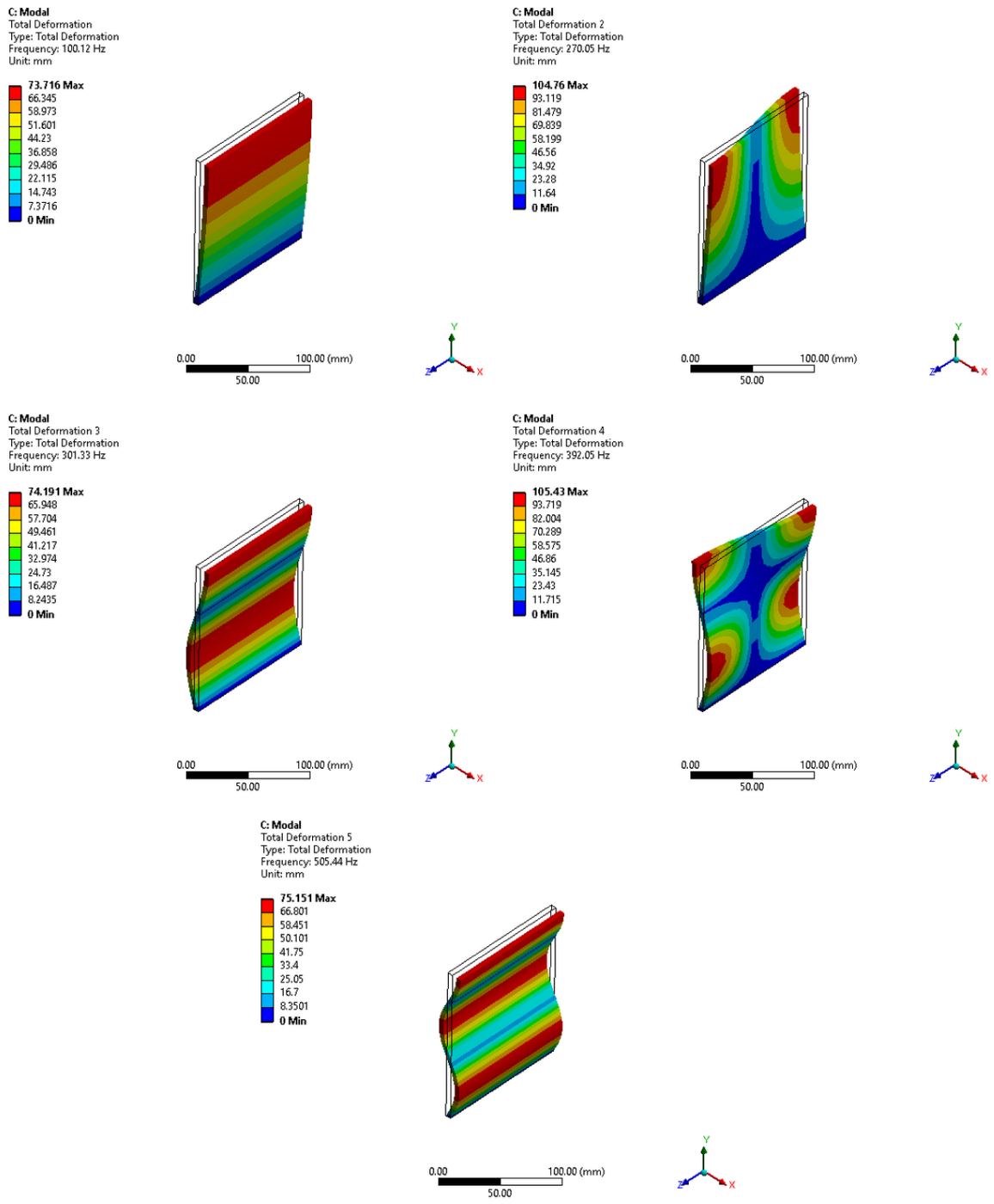

Figure 8.9. First five mode shapes of the elastic baffle with the undeformed geometry shown as a wireframe reference.

The baffle geometry, material parameters, and reference displacement data at monitoring location D1 defined as the top-left extremity of the baffle when observed from the frontal plane are adopted from the numerical study of Sampann [182]. The X-displacement predicted at location D1 by the current numerical prediction is validated against the reference solution in Figure 8.10, with quantitative deviations reported in Table 8.4.

Table 8.4. Deviation of numerically predicted baffle deformation from the reference solution of Sampann.

Region	Peak	Transition
Max Deviation of deformation [m]	0.005	0.01

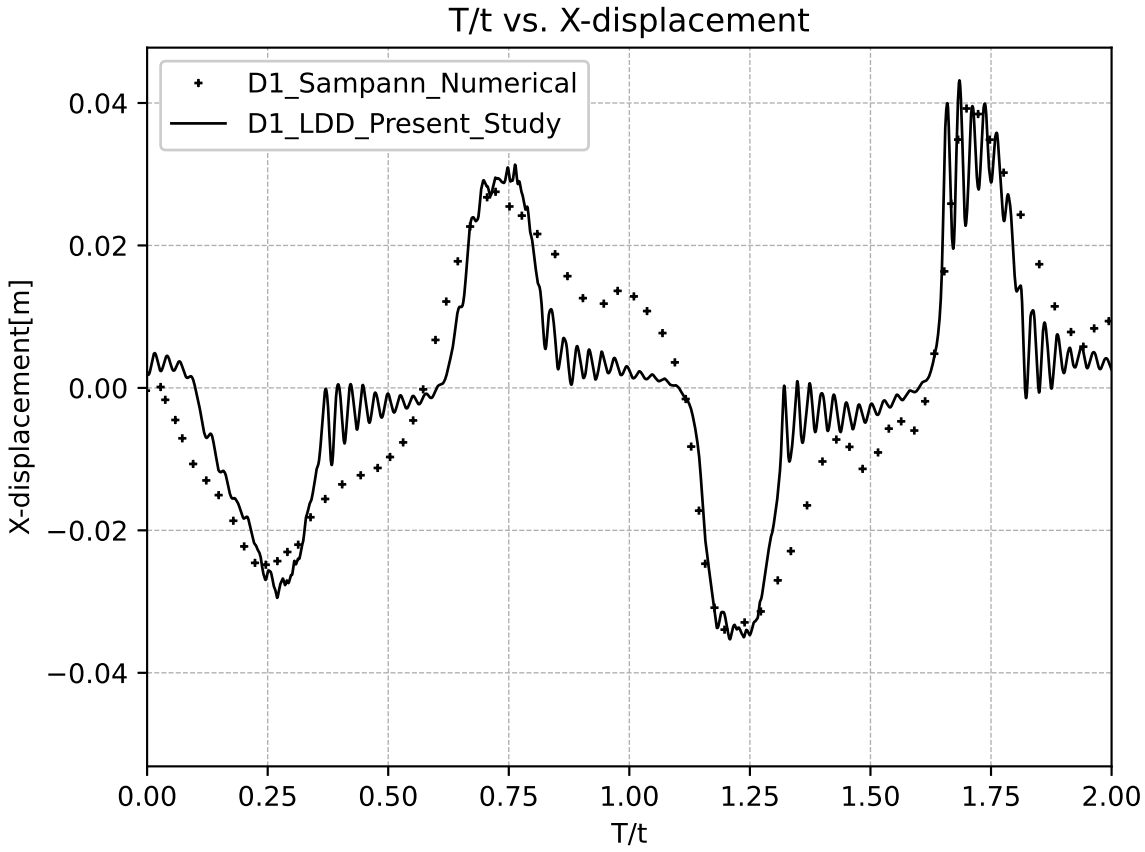

Figure 8.10. X-displacement at monitoring location D1 predicted by the current numerical solution compared against the reference numerical data.

The two displacement histories follow the same qualitative trend throughout the simulation, with particularly close agreement at the instants of peak deformation. A slightly larger discrepancy is observed during the transitional phases between peak values, which is attributable to the inherent limitation of the linear modal superposition assumption in capturing strongly nonlinear transient behaviour. The results collectively confirm the accuracy of the modal coupling framework in resolving the dynamic deformation of a flexible structure under sustained cyclic fluid excitation.

8.1.4 Elastic Beam Subjected to Sloshing Loads in Shallow Oil

Further validation of the bidirectional coupled FSI framework is undertaken through comparison with the measured and computational benchmark data reported by Idelsohn et al. [183, 184]. This benchmark involves a flexible elastic beam mounted at the base of

a liquid-filled tank subjected to rotational oscillatory excitation, and is closely analogous to the configuration of Section 8.1.3, differing in the fluid medium and geometry. The test geometry consists of a rectangular tank housing a base-fixed elastic beam made of dielectric polyurethane and fully immersed in sunflower oil.

The tank has internal dimensions of 609 mm, 344.5 mm, and 39 mm along the x, y, and z axes respectively. The elastic beam is fixed ai the tank floor and has cross-sectional and height dimensions of 4 mm, 57.4 mm, and 33.2 mm in the x, y, and z directions, as depicted in Figure 8.11. The beam is characterised by a material density of 1100 kg/m³, an elastic modulus of 60 MPa, and a Poisson's ratio of 0.49.The surrounding sunflower oil has a density of 917 kg/m³ and a kinematic viscosity of 5×10 m²/s. The tank is filled with oil up to the full height of the beam. The first five mode shapes obtained from the modal analysis are incorporated into the simulation, as shown in Figure 8.12, with the associated natural frequencies listed in Table 8.5.

Table 8.5. First Five Vibration Modes of the Elastic Baffle.

Mode	1	2	3	4	5
Natural Frequency (Hz)	186.4	560.61	673.29	856.07	939.09

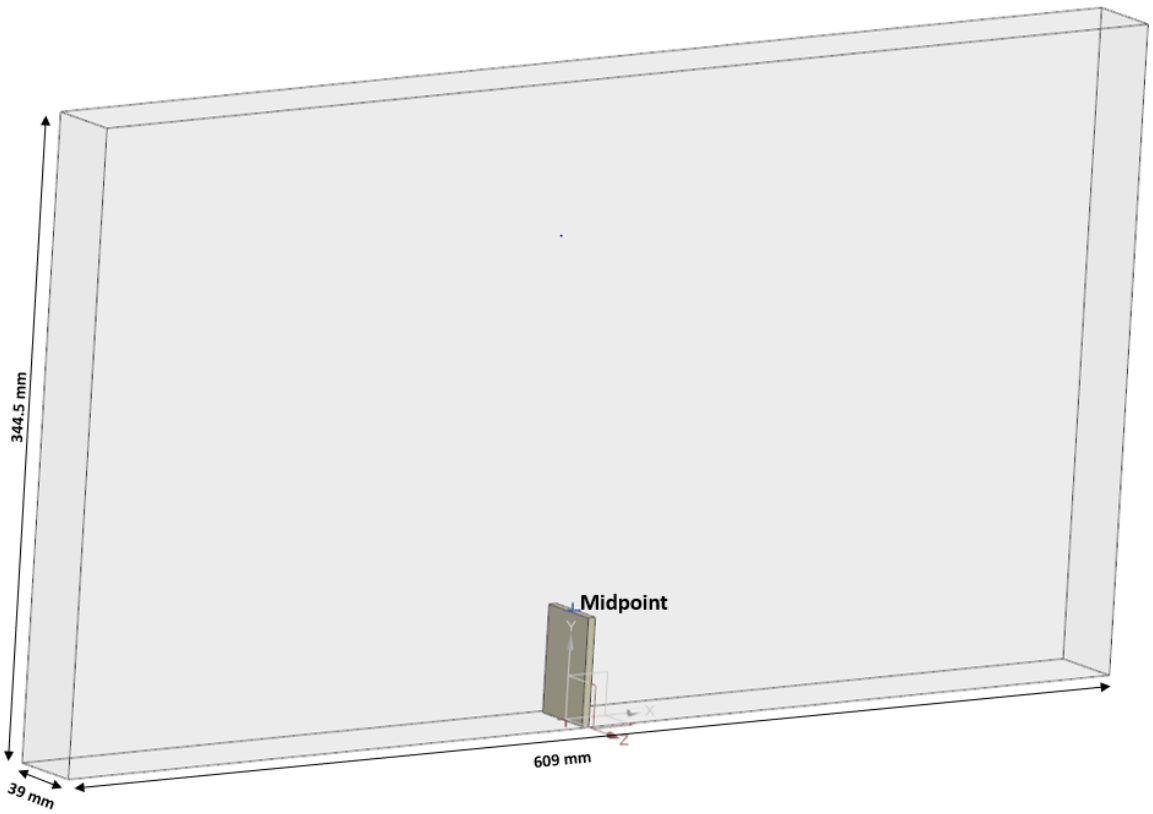

Figure 8.11. Tank and elastic beam configuration used for the sloshing validation study in shallow oil.

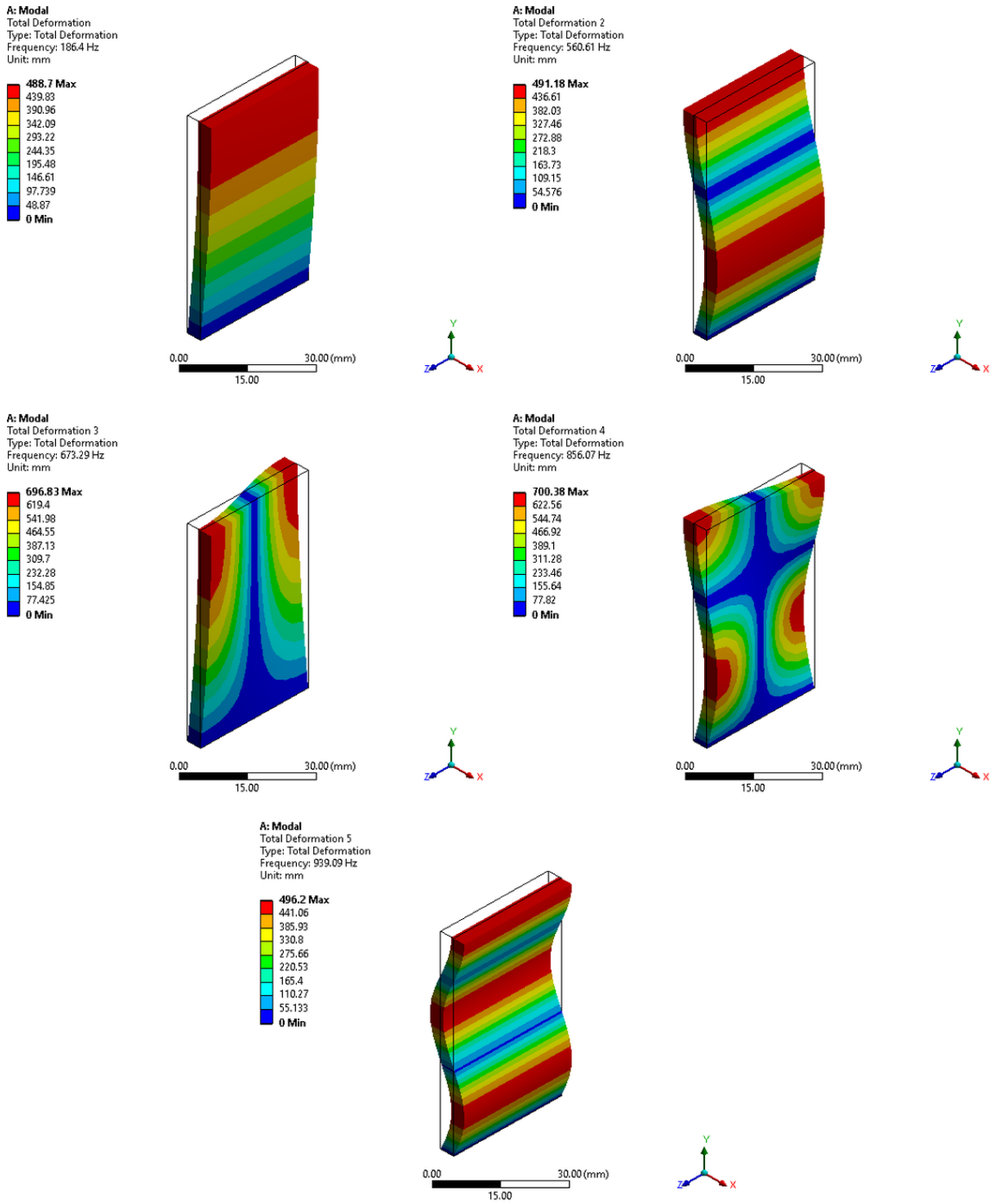

Figure 8.12. First five mode shapes of the elastic beam shown relative to the undeformed wireframe geometry.

A sinusoidal rotational motion is imposed on the tank about the z-axis, with a peak amplitude of 4 degrees and an oscillation frequency of 0.61 Hz. The horizontal displacement at the free end of the beam is monitored throughout the simulation and compared against both the experimental measurements and the numerical predictions from Idelsohn et al. [183], as presented in Figure 8.13. The computed results demonstrate satisfactory correspondence with the benchmark data throughout the entire simulated time period. At the locations of maxi-

mum deformation, the the obtained results show strong consistency with those of Idelsohn, with the deviation remaining of the order 1×10^{-4}. Minor offsets observed at intermediate time instants are attributable to the inherent constraints of the linear modal superposition methodology. The results provide robust confirmation of the accuracy of the two-way coupled FSI implementation across a range of excitation conditions and fluid-structure configurations.

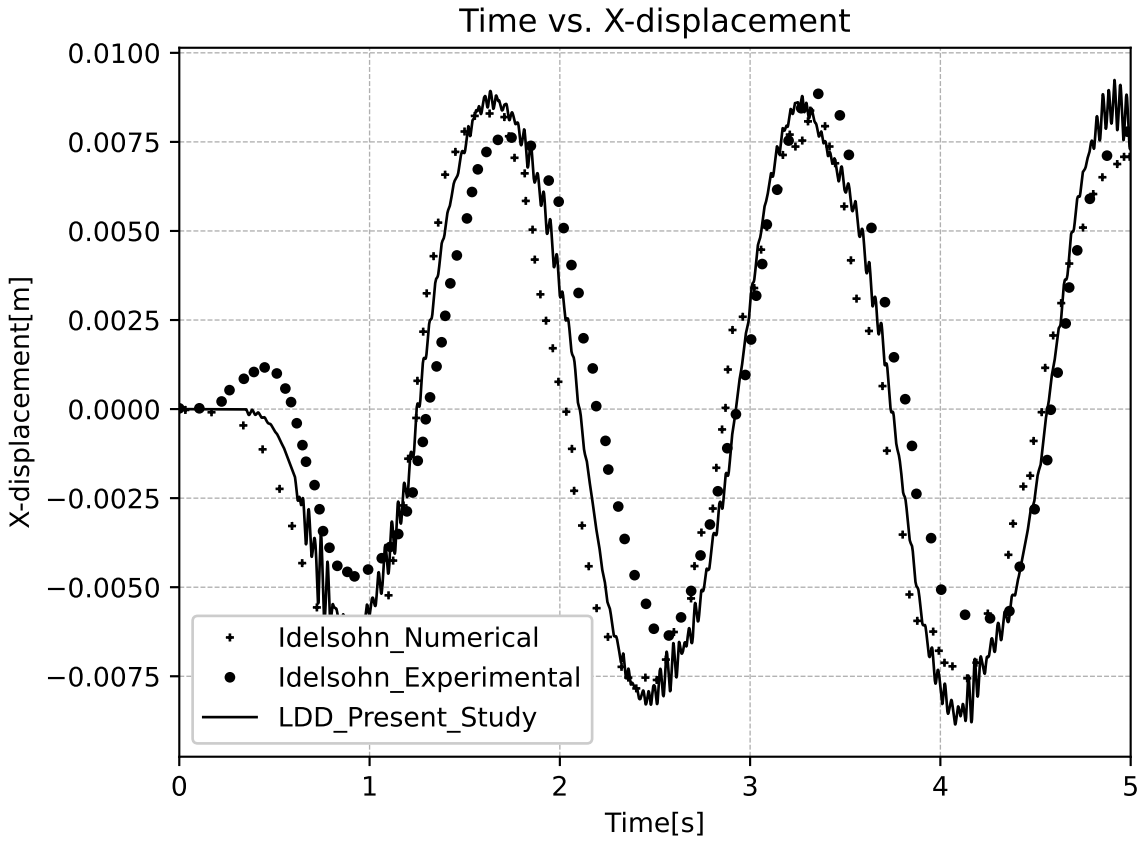

Figure 8.13. X-directional displacement at the beam tip: comparison between the present simulation and experimental and numerical reference solutions.

8.1.5 Impact of a Fluid Column on a Cantilever Beam

Having established the reliability of the FSI solver through the benchmark validations presented in Section 8.1.1, a further application is undertaken in which a cantilever beam experience an impulsive fluid impact followed by continuous periodic loading. The beam geometry and material properties are consistent with those described in Section 8.1.1, retaining a cross-sectional thickness of 5 mm. The computational domain measures 0.5×0.2 m and contains a rectangular fluid mass of dimensions 0.1×0.14 m initially positioned at the left edge of the computational domain. The beam is positioned along the centreline of the domain, with its clamped end aligned with the base of the tank. This configuration replicates a dam-break loading scenario. The total simulation duration is 10 s with a fixed time interval of 1×10^{-3} s.

The first five natural frequencies listed in Table 8.2 and the associated mode shapes shown in Figures 8.4 and 8.5 are employed throughout. The spatial deformation pattern and pressure distribution of the beam at successive time instants are shown in Figure 8.14. The displacement histories at both the mid-section and the free tip along both the x and y directions are presented in Figures 8.15 and 8.16, with zoomed views of the early response phase shown in Figures 8.17 and 8.18.

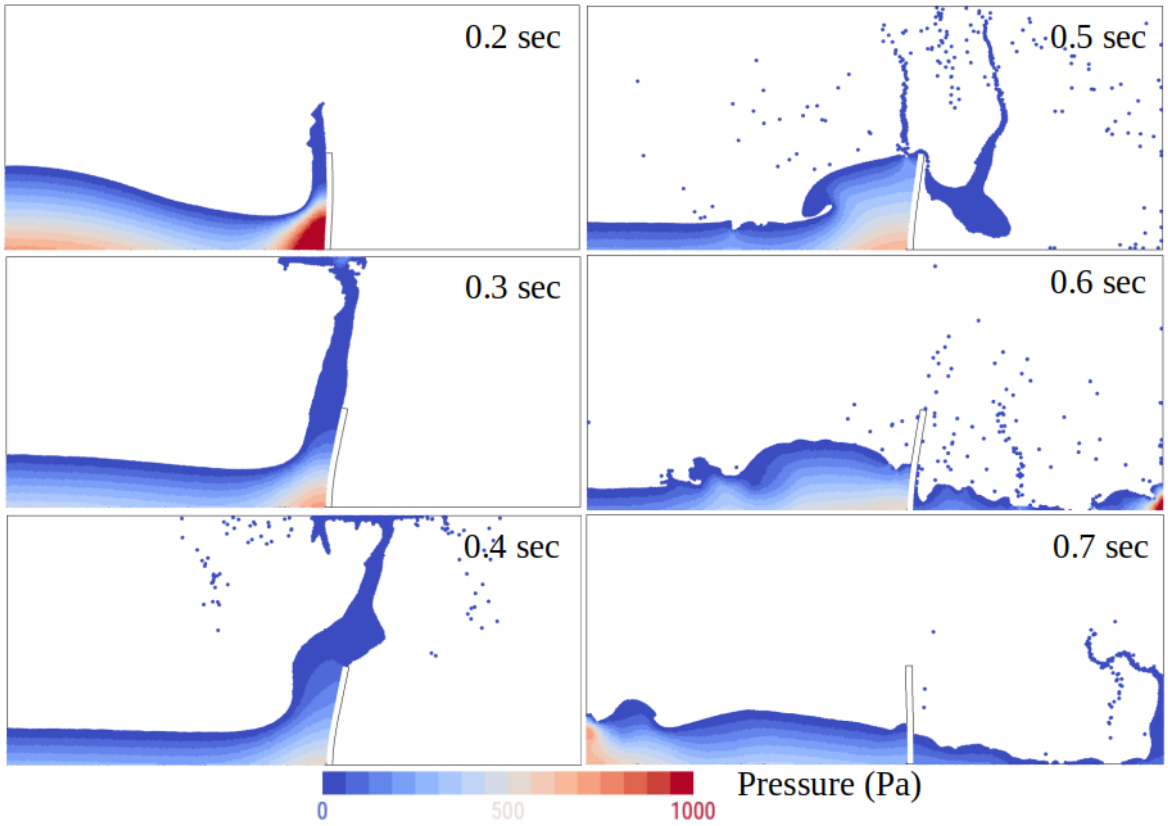

Figure 8.14. Deformation of the cantilever beam and pressure distribution at successive time instants during the dam-break simulation.

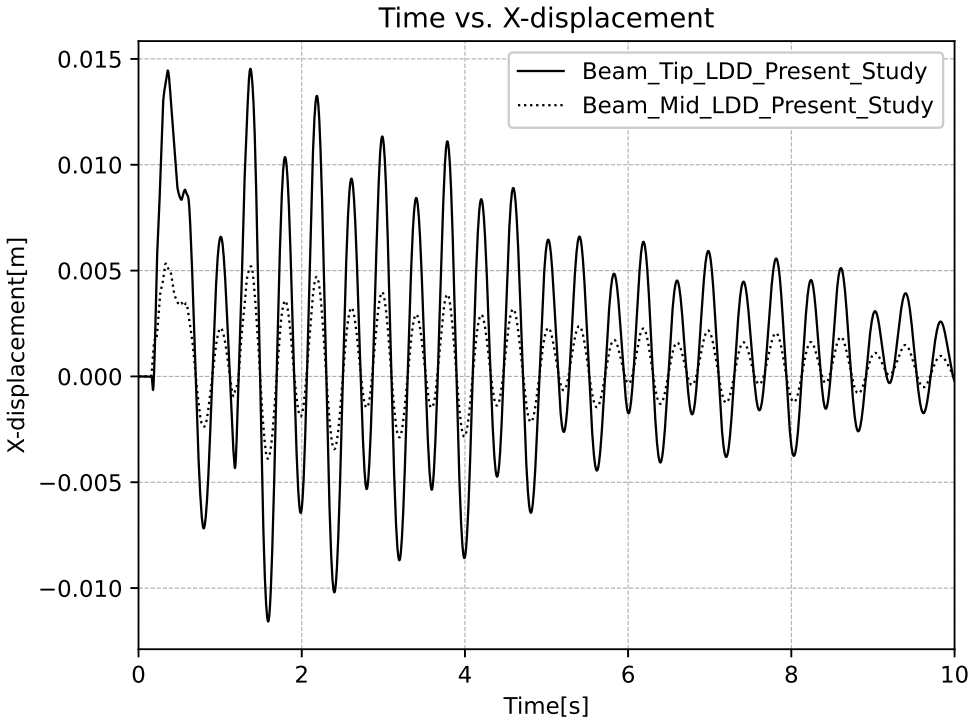

Figure 8.15. X-directional deformation at the mid-section and free tip of the beam over the full simulation duration.

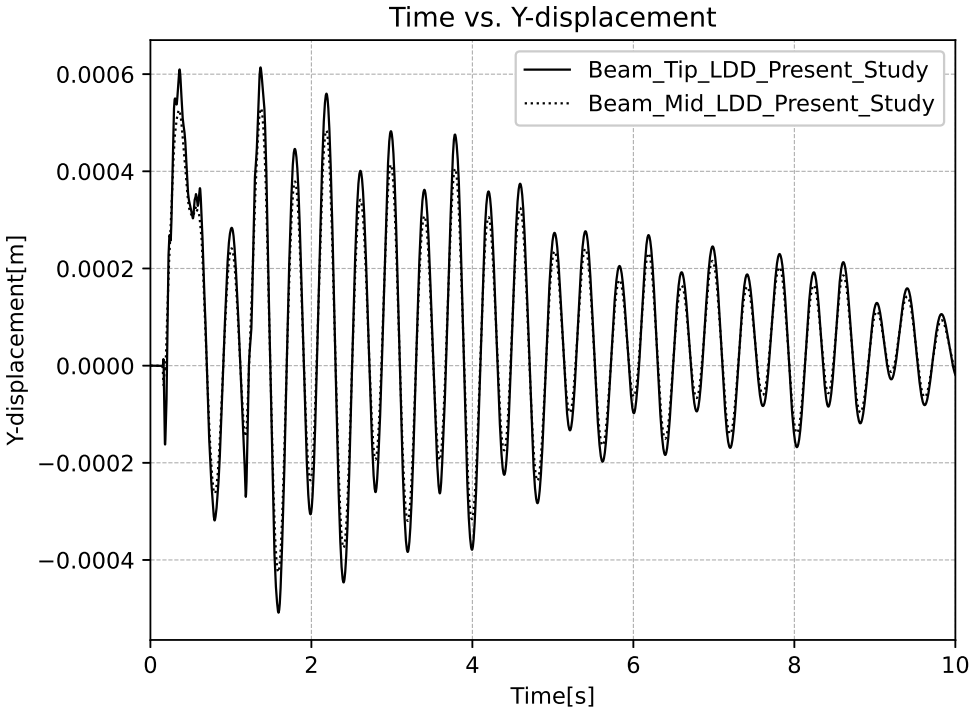

Figure 8.16. Y-directional deformation at the mid-section and free tip of the beam over the full simulation duration.

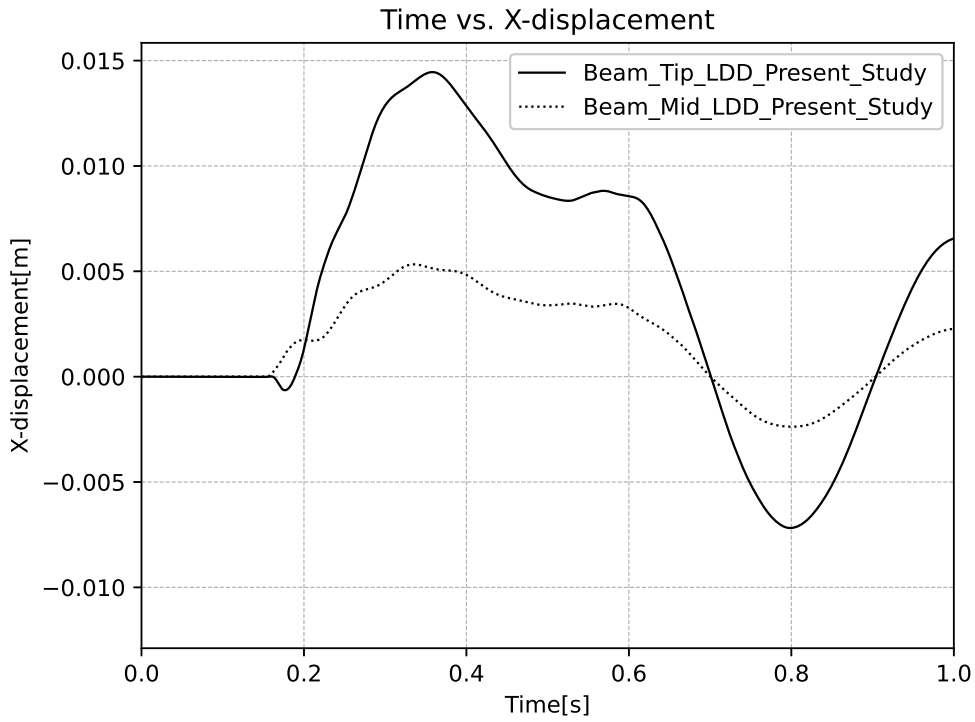

Figure 8.17. X-directional deformation at the mid-section and free tip of the beam during the initial 1 s of the simulation.

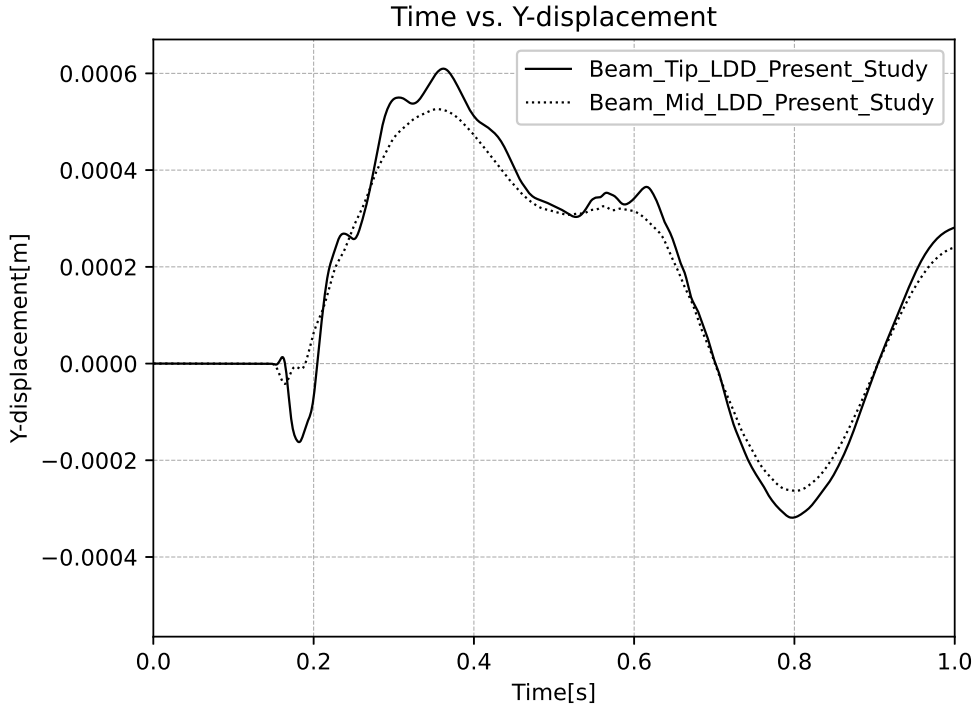

Figure 8.18. Y-directional deformation at the mid-section and free tip of the beam during the initial 1 s of the simulation.

The structural response at $t = 0.2$ s reveals a clear superposition of multiple mode shapes, reflecting the broadband frequency content of the initial impulsive loading. As the simula-

tion progresses beyond $t = 5$ s, the response becomes progressively dominated by the fundamental bending mode, consistent with the preferential decay of higher frequency modal contributions under sustained loading. This behaviour is reproduced consistently in both the full-duration displacement histories and the zoomed early-time records, demonstrating the capacity of the modal superposition technique to accurately resolve the relative contributions of individual modes to the overall structural response under complex transient loading conditions.

8.1.6 Water Entry of a Wedge

The capability of the coupled LDD-modal solver to resolve impulsive hydrodynamic loads and the associated structural response is assessed through simulation on impact of an deformable wedge entering flowing water , replicating the experimental study of Hosseinzadeh [185]. The wedge features a V-shaped cross-section with a variable deadrise angle at the keel, and has overall dimensions of 1500 mm, 940 mm, and 450 mm in length, breadth, and depth respectively. The keel and base panels are reinforced by T-shaped longitudinal and transverse stiffeners with profile T54 $\times$ 3 + 35 $\times$ 4 mm, each of 4 mm wall thickness, positioned at the centrelines of the respective panels.

The wedge is fabricated from an aluminium alloy with a material density of 2700 kg/m^3, a Young's modulus of 68 GPa, and a Poisson's ratio of 0.33. Accurate representation of these material properties is essential, as they govern the elastic response of the structure during water entry and directly influence the predicted deformation under impact loading [185]. The water-filled tank has plan dimensions of 5 m $\times$ 5 m and a fill depth of 1.5 m measured in the z-direction, as shown in Figure 8.19. The structural modal analysis and fluid simulation both utilise a shared surface discretisation of the wedge consisting of 9200 triangular mesh elements, illustrated in Figure 8.20.

The wedge is released from a height of 0.25 m above the undisturbed free water level, measured from the keel. Under gravity, the wedge accelerates during free fall, reaching an impact velocity of $U = 2.2$ m/s at the instant of water entry. The simulation is conducted using a constant time step of $\delta t = 2.5 \times 10^{-3}$ s. The first five structural modes extracted from the modal analysis are presented in Figure 8.21, with the corresponding natural frequencies listed in Table 8.6. These modal data are provided as input to the LDD-modal coupling framework.

Table 8.6. First five natural frequencies of the wedge.

Mode	1	2	3	4	5
Natural Frequency (Hz)	213.8	376.6	440.95	529.12	535.23

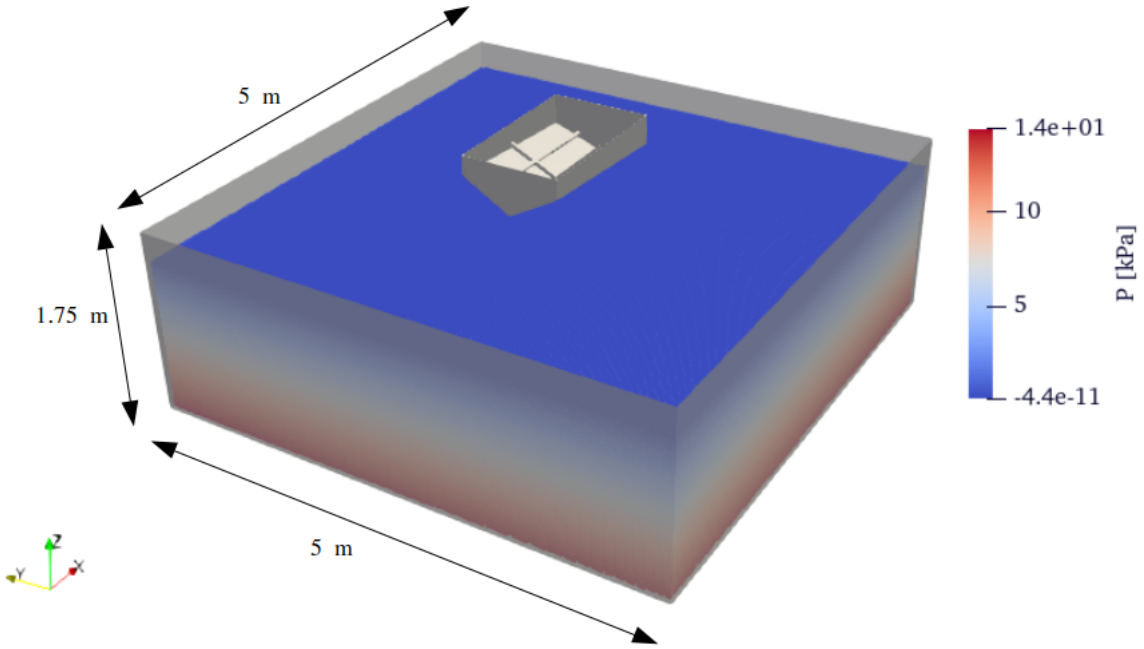

Figure 8.19. Numerical configuration for the wedge water entry study, showing the tank filled to 1.5 m depth with the wedge positioned 0.25 m above the free surface.

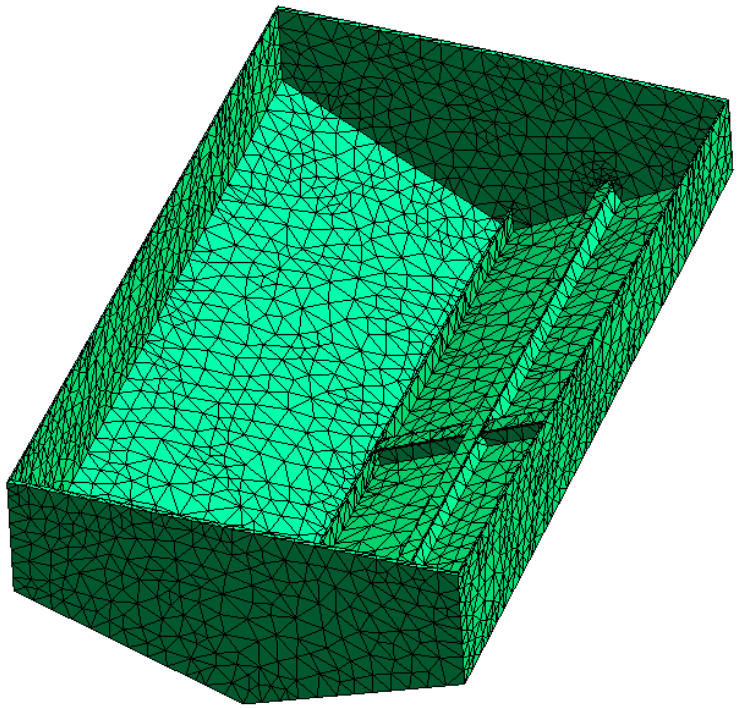

Figure 8.20. Surface triangulation of the wedge used for both modal analysis and the LDD-modal coupling simulation.

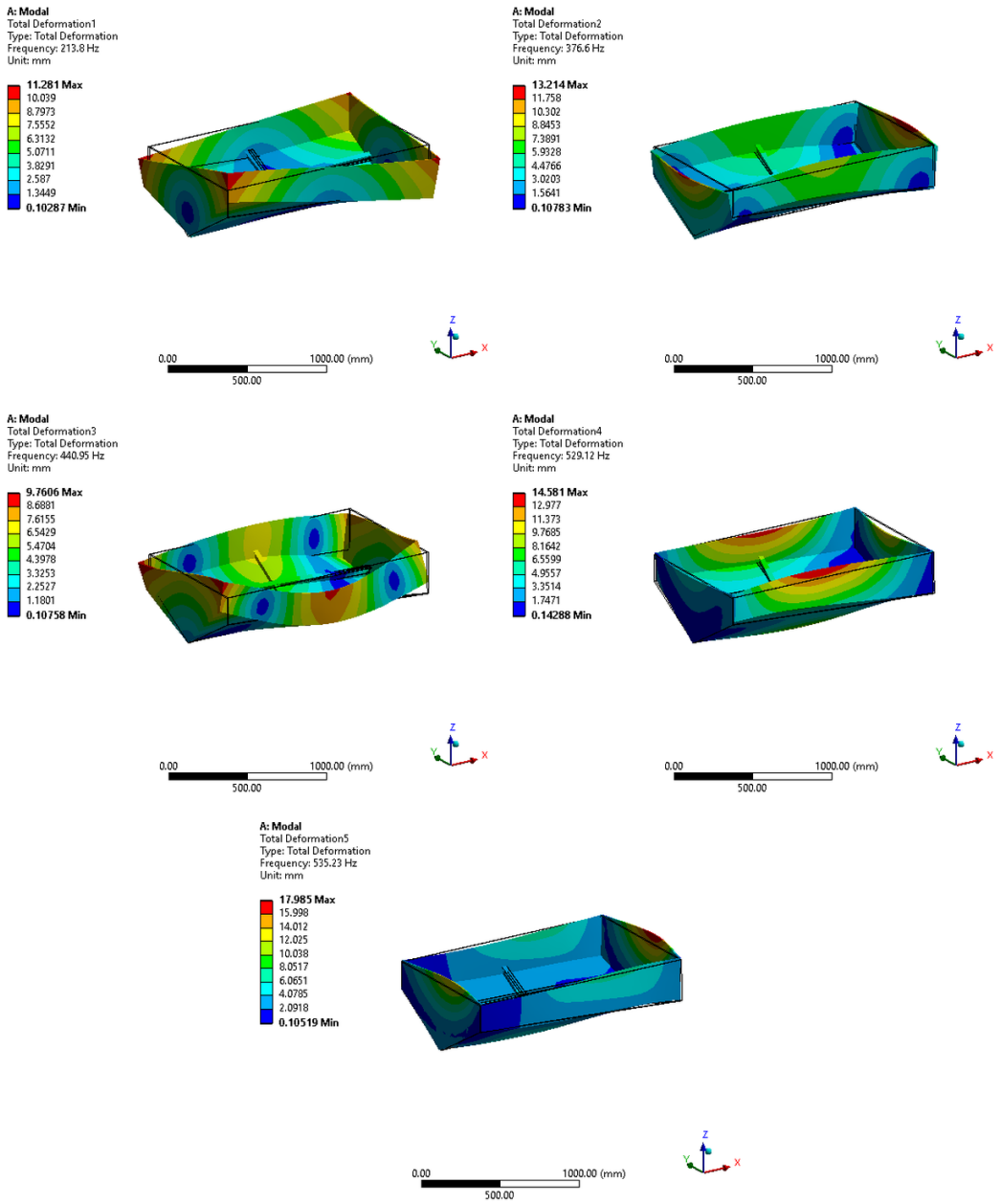

Figure 8.21. First five mode shapes of the wedge structure shown relative to the undeformed wireframe geometry.

The evolution of hydrodynamic pressure and structural deformation throughout the water entry event is monitored and analysed. The dynamic pressure histories at monitoring points PS1 and PP1 on the wedge surface are validated against the experimental observations recorded by Hosseinzadeh et al. [185] in Figures 8.22 and 8.23 respectively. The peak pressure values predicted by the simulation agree with the experimental measurements within a deviation of 4%. A discrepancy is noted in the rate of pressure decay following the impact peaks, with the simulated pressure signal diminishing more rapidly than the experimentally recorded one. This behaviour is consistent with known differences between idealised numerical boundary conditions and the physical dissipation mechanisms present in laboratory experiments.

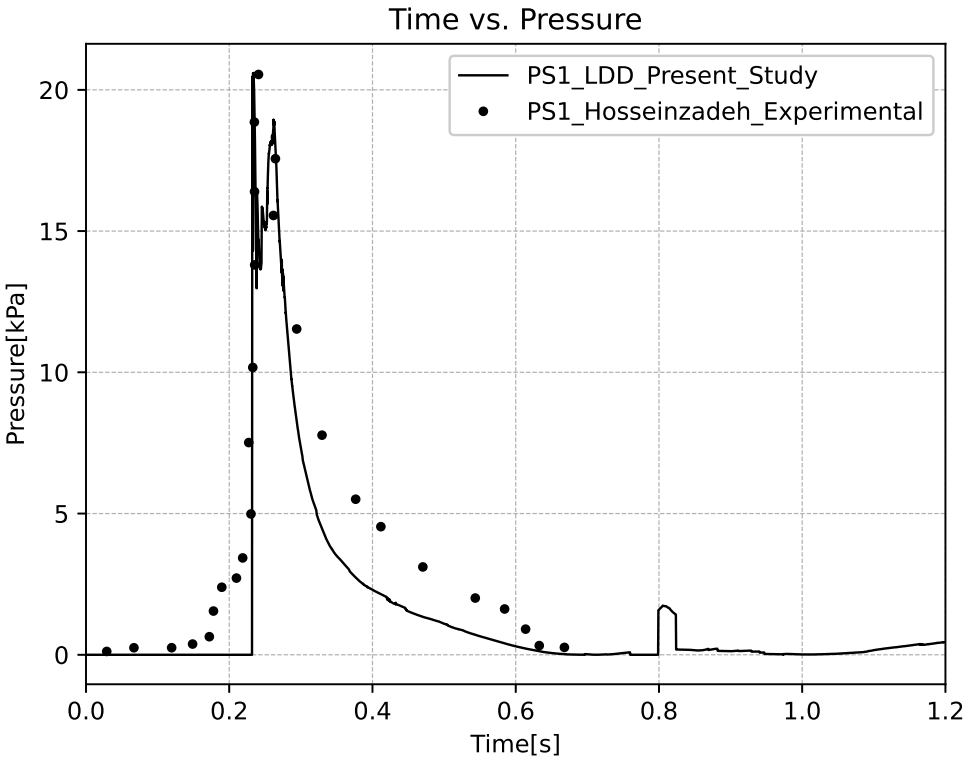

Figure 8.22. Dynamic pressure history at monitoring point PS1 compared against the experimental reference measurements.

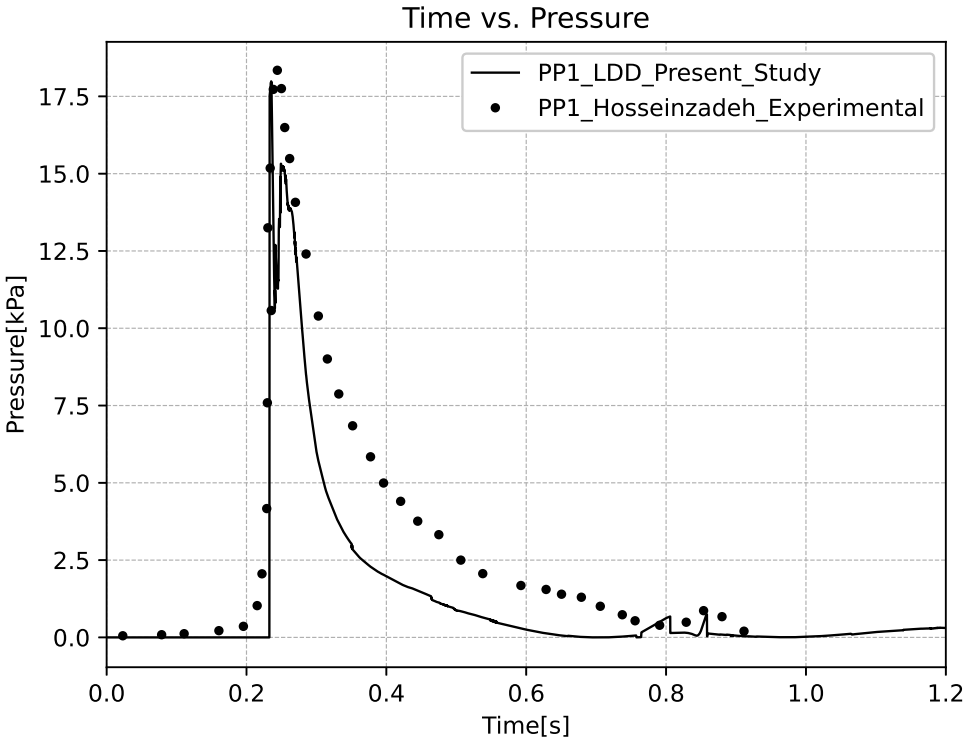

Figure 8.23. Dynamic pressure history at monitoring point PP1 compared against the experimental reference measurements.

Upon impacting the water surface at 2.2 m/s, the wedge undergoes elastic deformation in all three coordinate directions. The deformation state at the instant of peak impact loading is presented in Figure 8.24, which shows the displacement fields in the X, Y, and Z axes alongside the total deformation magnitude. The peak deformation observed across all coordinate directions under maximum impact conditions reaches 36 m, which aligns with the anticipated elastic behaviour of the stiffened aluminium structure subjected to the applied hydrodynamic forces.

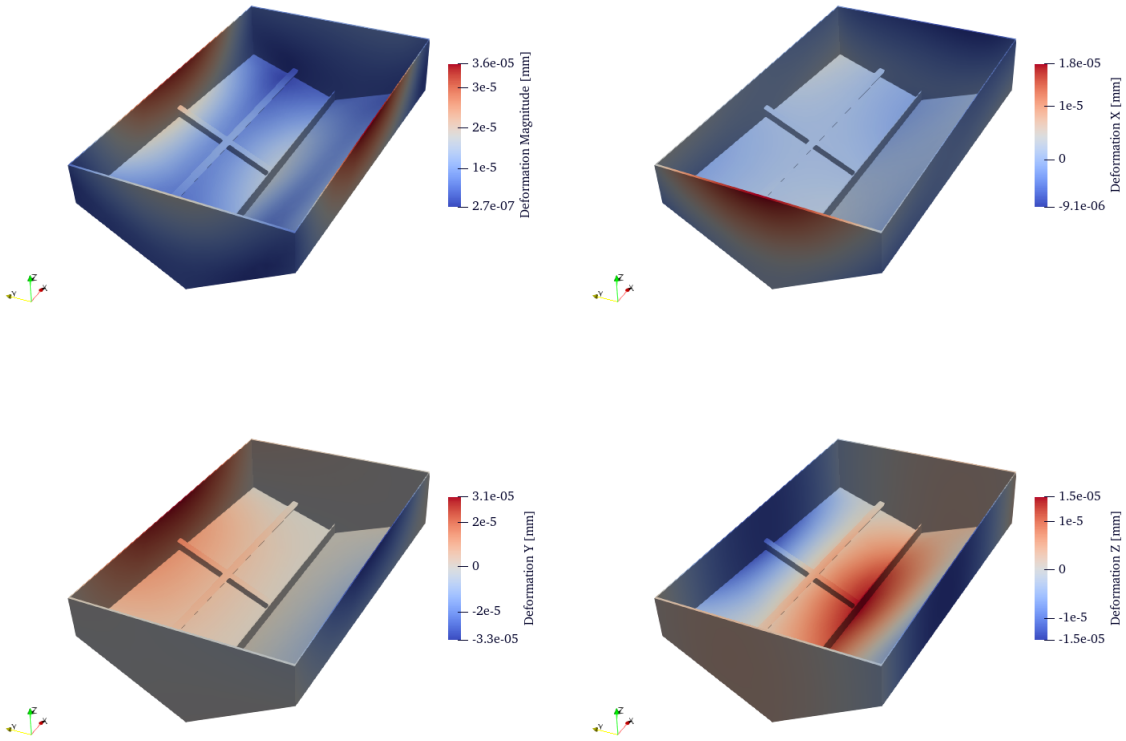

Figure 8.24. Distribution of structural displacements in the X, Y, and Z coordinate directions and resultant deformation magnitude of the wedge under peak impact conditions.

8.1.7 Summary

The structural dynamics are represented through modal superposition, which reduces the number of active structural degrees of freedom and avoids repeatedly solving the full structural system in its original form. Modal reduction methods are widely used for this purpose because they lower computational cost by projecting the response onto a limited set of dominant vibration modes. In addition, the structural model is incorporated directly within the partitioned fluid–structure interaction procedure, allowing the coupled dynamics to be resolved without the expense of a fully monolithic formulation. While partitioned FSI frameworks are commonly valued for their practical integration of flow and structural solvers.

Therefore, the efficiency claim made in the thesis refers to the reduced structural problem size, the avoidance of unnecessary full-order structural computations, and the practical coupling strategy adopted for time-dependent simulations.

A systematic investigation of resolution dependence and numerical convergence remains a relevant avenue for further research. Future work will broaden the verification of the present framework through more comprehensive numerical assessment, supported by appropriate quantitative error measures for the principal response variables. The staggered partitioned FSI formulation employed in this work is known to be potentially sensitive to added-mass instability when fluid inertia becomes comparable to structural inertia. The benchmark cases considered in this thesis were computed stably within the investigated parameter range, but no general stability analysis is claimed here. A broader assessment of stability limits and suitable mitigation strategies for strongly added-mass-dominated regimes is left for future work.

8.2 Multiphase LDD

The predictive capability of the MP-LDD method is assessed through a systematic series of validation studies, each targeting a distinct physical regime representative of the range of multiphase flow configurations encountered in engineering practice. The validation campaign is structured in order of increasing physical complexity. The sequence begins with a two-dimensional Rayleigh-Taylor instability at a low density ratio, which provides a controlled environment for assessing the accuracy of the interfacial dynamics formulation under conditions of moderate density contrast. This is followed by a dam-break simulation over a trapezoidal step, which introduces a high-density ratio water-air system and evaluates the solver under conditions of rapidly evolving free surface flow. The complexity is then elevated further through a dam-break configuration with a vertical obstacle, which combines high-density ratio flow with violent wave impact and complex topological changes at the interface. Two sloshing validation cases are subsequently presented: a two-dimensional rectangular tank under harmonic sway excitation from Kishev et al. [186], and a dedicated comparison against the experimental sloshing records of Rhee et al. [187] at a higher fill ratio, together examining the robustness of the method under sustained oscillatory multiphase loading. The validation sequence concludes with dispersal of oil within water across a submerged barrier, a configuration characterised by a low density ratio and a density-stratified interface, which tests the method's ability to resolve buoyancy-driven interfacial evolution between two immiscible liquids. Detailed discussion of results, quantitative comparisons, and assessment of predictive accuracy for each configuration are provided in the subsections that follow.

8.2.1 Low Density Ratio Rayleigh-Taylor Perturbation

The 2D RT perturbation constitutes the first validation case for the MP-LDD multiphase formulation. This classical test problem is of particular importance for multiphase methods, as it directly exercises the accuracy of the interfacial representation and the stability of the phase boundary treatment under conditions where gravitational destabilisation drives complex interfacial morphology. The configuration and reference data adopted for this study are drawn from the study of Cummins et al. [188] and Hu et al. [189], that provide established benchmarks for this instability within the framework of particle-based multiphase simulations.

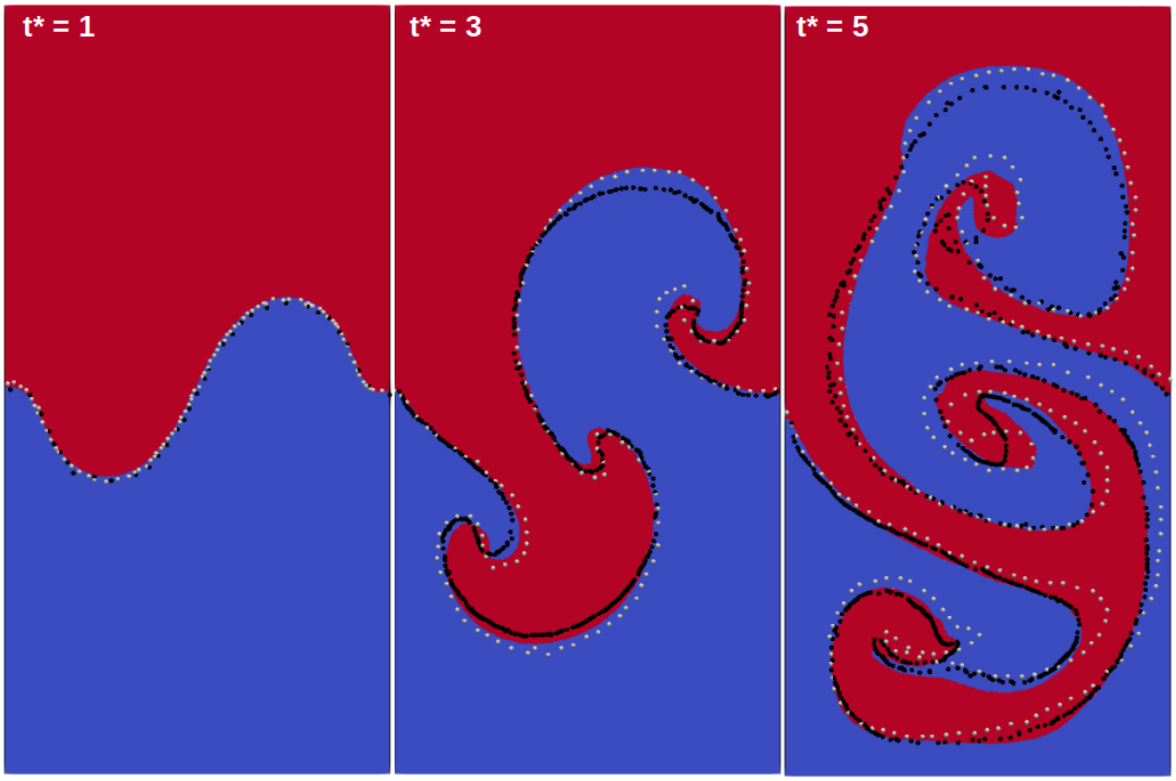

Figure 8.25. Temporal development of the RT instability interface at dimensionless times $t^* = 1$, 3, and 5, compared against the Level Set results (white dotted line) and SPH results (black dotted line) from the reference study.

The numerical simulation is conducted on a 2D rectangular domain with a height-to-width of 2:1, with the coordinate system normalised by the domain width $L = 1$ m. The domain is occupied by two non-mixing fluids of differing densities: a heavier fluid of density $\rho_B = 1.8$ kg/m^3 is initialised above a lighter fluid of density $\rho_A = 1.0$ kg/m^3, with downward acceleration due to gravity $\mathbf{g} = 9.81$ m/s^2 acting to destabilise the configuration. Both fluids share the same kinematic viscosity, giving a Reynolds number $Re = \sqrt{L^3\mathbf{g}/\nu} = 420$. The initial interface between the two fluid layers is perturbed by a sinusoidal displacement of the form $y/L = 1 - 0.15\sin(2\pi x/L)$, which seeds the instability from a well-defined initial condition. The initial inter-point spacing is set to 0.0015 m. Zero-velocity boundary conditions are

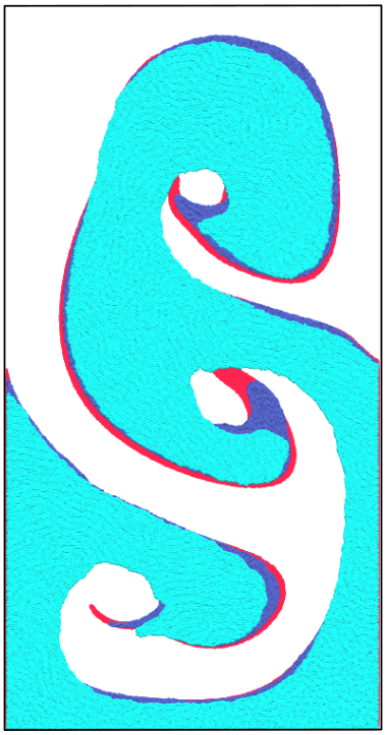

Figure 8.26. Point spacing convergence study showing the interface profile at $t^* = 5$ for spacings of 0.0015 m (red), 0.003 m (blue), and 0.006 m (fluorescent blue).

enforced along all domain boundaries, constraining the fluid velocity to zero at the enclosing walls throughout the simulation. This configuration represents the canonical RT instability setup, enabling examination of the progressive downward advancement of the heavier fluid into the lighter phase and the consequent development of the characteristic finger-like and mushroom-cap interfacial formation that define the nonlinear stage of the instability.

The temporal evolution of the RT instability is presented in Figure 8.25 at dimensionless times $t^* = t\sqrt{\mathbf{g}/L}$ of 1, 3, and 5. At $t^* = 1$, the heavier fluid (red) has begun to form nascent finger-like protrusions that penetrate downward into the lighter phase (blue), while the lighter fluid simultaneously rises as counter-flowing plumes. By $t^* = 3$, these initial structures have evolved into the characteristic mushroom-shaped heads of the RT instability as the nonlinear regime takes hold, with the interface exhibiting significant curvature and topological complexity. At $t^* = 5$, the instability has progressed into a strongly nonlinear regime characterised by extensive interpenetration of the two phases, prominent mushroom-cap formations, and the onset of interfacial roll-up. Comparison against the reference results of Grenier et al. [62], represented by the Level Set (white dotted line) and SPH (black dotted line) solutions, reveals strong qualitative agreement with the MP-LDD predictions at all three time instances, confirming the ability of the method to accurately reproduce the dynamics of RT instability including the spatial development of the interface and the characteristic morphological features.

The influence of spatial discretisation on the fidelity of the interface representation is

examined through a point spacing convergence study, presented in Figure 8.26. Three resolutions are compared at $t^* = 5$: a fine spacing of 0.0015 m (red), an intermediate spacing of 0.003 m (blue), and a coarse spacing of 0.006 m (fluorescent blue). The finest resolution produces the sharpest and most geometrically accurate interface representation, capturing the detailed morphological features of the instability with minimal numerical diffusion. The coarsest resolution introduces perceptible interface smearing and a reduction in the fidelity of the captured interfacial structures, while the intermediate resolution offers a balance between numerical accuracy and computational expense. The convergence behaviour observed supports the selection of the finest spacing as the reference resolution for subsequent validation cases requiring high-fidelity interface representation.

8.2.2 Dam Break Over a Trapezoidal Step

The second validation case addresses the two-dimensional dam-break flow interaction with a trapezoidal obstruction, replicating the experimental configuration of Hatice [190]. The computational domain is a rectangular channel of length 8.9 m and height 0.30 m. The upstream reservoir section is initialised with a water column of height 0.25 m, while the downstream region remains initially free of water. A trapezoidal obstacle of height 0.075 m and base length 1 m is positioned 1.53 m downstream of the initial dam location, as illustrated in Figure 8.27.

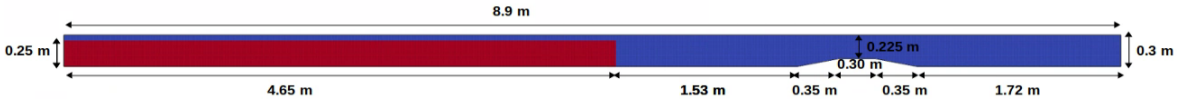

Figure 8.27. Computational domain and initial configuration for the dam-break over a trapezoidal obstacle.

The water phase is represented as an incompressible fluid characterised by a density of $\rho_w = 1000$ kg/m^3 and kinematic viscosity $\nu_w = 1 \times 10^{-6}$ m^2/s. The ambient air phase has a density of $\rho_a = 1.225$ kg/m^3 and a kinematic viscosity of $\nu_a = 1.5 \times 10^{-5}$ m^2/s. In the single-phase reference case, the air domain is neglected and treated as an empty void in order to minimise computational expense. The dam-break is initiated by the sudden withdrawal of the retaining wall, releasing the water column into the dry downstream region. Zero-velocity boundary conditions are enforced at all solid boundaries, encompassing the channel walls and the faces of the trapezoidal obstacle. The inter-point spacing is set to 0.005 m and gravitational acceleration is $\mathbf{g} = 9.81$ m/s^2.

Figure 8.28 presents a three-way comparison between the experimental observations of Hatice et al. [190], the MP-LDD multiphase simulation, and the single-phase LDD results of Bašić et al. [154] at six sequential time instants. The experimental data provide a quantitative physical benchmark for validating both simulation approaches, while the single-phase LDD solution serves as an additional numerical reference that enables a direct assessment of the

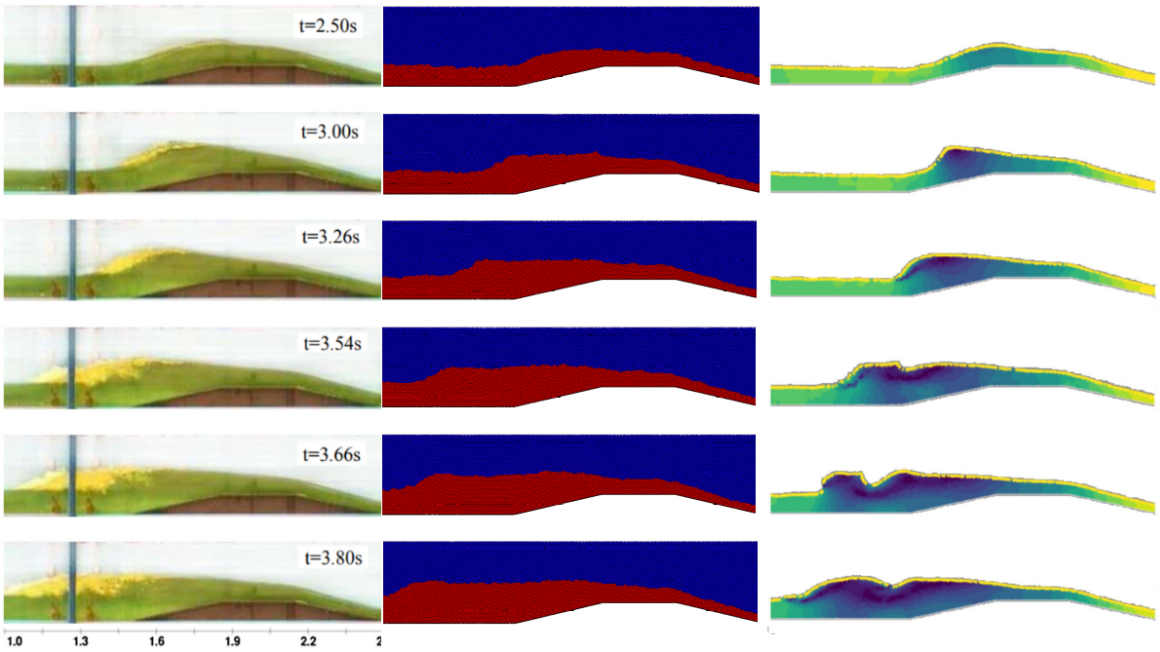

Figure 8.28. Sequential snapshots of the dam-break flow over the trapezoidal obstacle at $t = 2.50, 3.00, 3.26, 3.54, 3.66$, and 3.80 s: experimental observations (left column), MP-LDD simulation (centre column), and single-phase LDD reference solution (right column).

improvement afforded by the multiphase formulation. The MP-LDD results exhibit close agreement with both the experimental measurementsand the single-phase reference across all time snapshots, reproducing the wave propagation dynamics, the overtopping of the obstacle, and the subsequent downstream flow patterns with high fidelity. The consistency between the three sets of results confirms the accuracy and reliability of the MP-LDD formulation for high-density ratio free surface flows involving interaction with solid obstacles.

8.2.3 Dam Break With a Vertical Obstacle

The dam-break interacting with a vertical obstacle replicates the benchmark configuration of Hänsch et al. [191] and represents a more demanding validation scenario involving a high water-to-air density ratio and energetic impulsive flow with complex wave breaking and splashing dynamics. The computational domain is a square enclosure of dimensions 0.584×0.584 m, with a rectangular obstruction of height 0.048 m and width 0.024 m positioned 0.292 m from the left boundary. Water occupies the left portion of the domain as the initial fluid column, while air fills the remaining space. The material properties are: water density $\rho_w = 1000$ kg/m^3 with kinematic viscosity $\nu_w = 1 \times 10^{-6}$ m^2/s; air density $\rho_a = 1.225$ kg/m^3 with kinematic viscosity $\nu_a = 1.48 \times 10^{-5}$ m^2/s. The domain is discretized with a point spacing of 0.0015 m. Zero-velocity boundary conditions are imposed on all solid boundaries including the obstacle surfaces, while the top boundary is treated as an open surface with a zero-pressure condition ($p = 0$). The initial configuration is shown in Figure 8.29.

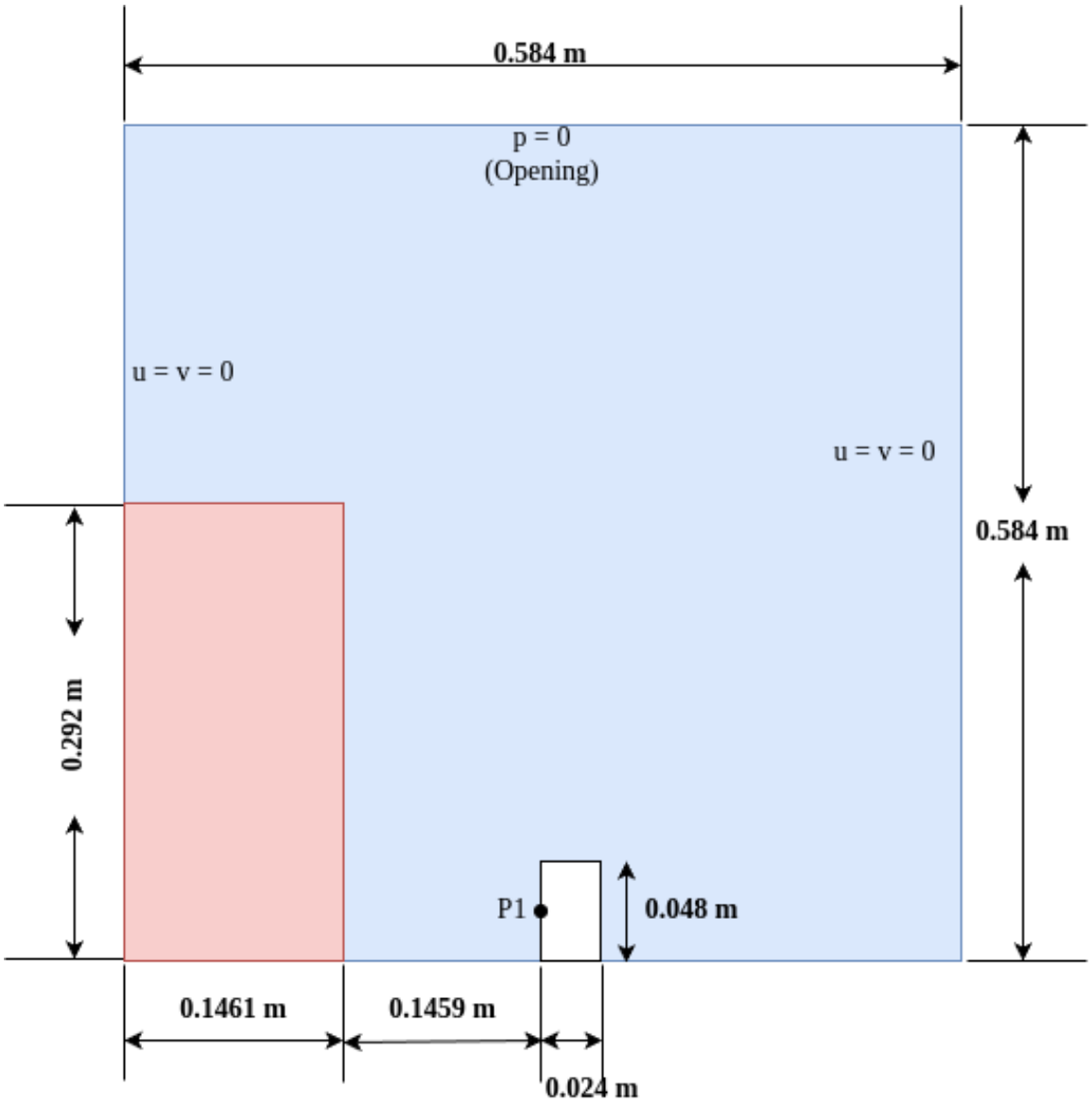

Figure 8.29. Initial configuration for the dam-break with vertical obstruction case, showing the water phase(red) and air region (blue).

The qualitative evolution of the flow is compared against the experimental photographic record of Hänsch et al. [191] in Figure 8.30 at successive time instants spanning the full sequence of the dam-break event. The MP-LDD simulation reproduces the principal physical phenomena with high visual fidelity, including the initial advance of the water front, the impact of the wave on the obstacle face, the overturning and folding of the water column, the creation of the air cavity trapped behind the advancing wave front, and the subsequent splashing and jet formation above the obstacle. The phase interface remains sharp and geometrically well-defined throughout the simulation without exhibiting numerical diffusion or spurious fragmentation, consistent with the physical observations. The strong visual correspondence between the simulation and experiment across all stages of the dam-break event demonstrates the robustness of MP-LDD in handling violent multiphase flow scenarios with

large interfacial deformations and topological changes.

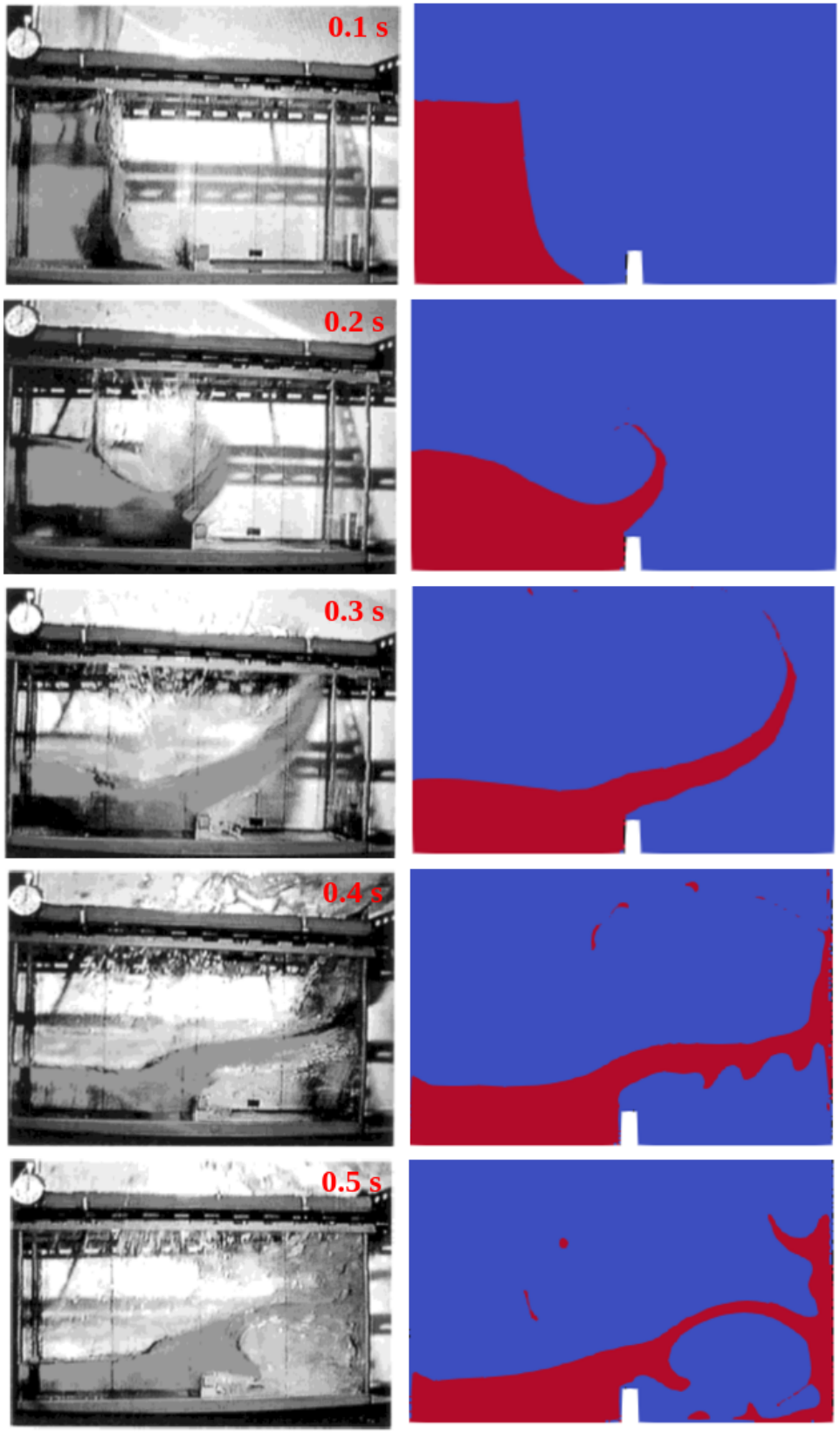

Figure 8.30. Temporal sequence of dam-break flow over the vertical obstacle from the MP-LDD simulation compared against the experimental photographic record.

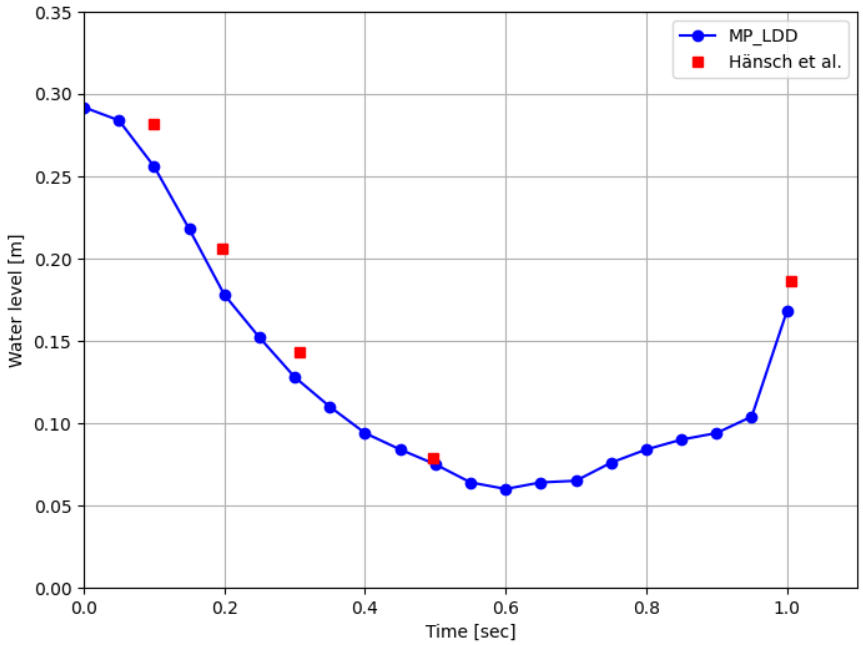

Figure 8.31. Time history of the free surface water level from the MP-LDD simulation compared against the experimental measurements.

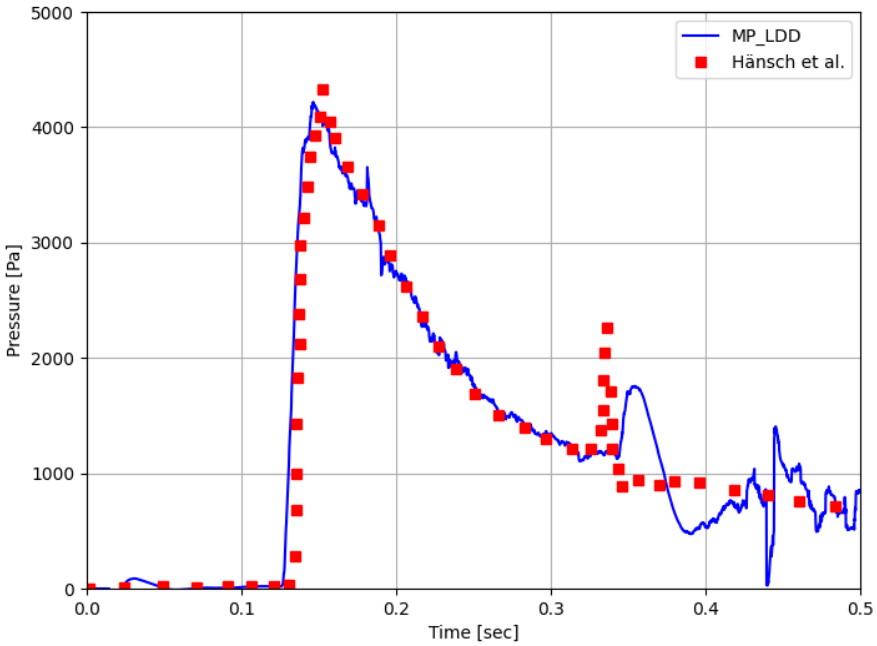

Figure 8.32. Time-dependent pressure history at monitoring point P1 from the MP-LDD simulation compared against the experimentally recorded measurements.

Quantitative validation is provided through comparison of the free surface water level history and the transient pressure signal at monitoring point P1. The water level evolution presented

in Figure 8.31 demonstrates that the MP-LDD method accurately captures the rapid fall of the water surface during the initial collapse phase, as well as the subsequent partial recovery as the flow redistributes within the domain. The predicted water level trajectory remains in close agreement with the experimental measurements across the full time range considered, confirming the capability of the method to reliably resolve the global mass balance and free surface kinematics under violent flow conditions.

The time-varying pressure history at point P1 is presented in Figure 8.32. The simulation correctly reproduces the pronounced pressure peak at approximately 0.1 s associated with the hydrodynamic impact of the collapsing water column, accurately predicting both the timing and the magnitude of the peak pressure. The subsequent pressure attenuation and the oscillatory decay that follows are also well-captured by the MP-LDD prediction. Minor discrepancies are observed in the late-time oscillatory regime beyond approximately 0.3 s, where the simulated pressure signal decays somewhat more rapidly than the experimental record. This behaviour is attributed to a combination of numerical dissipation in the pressure solver and slight differences in the effective interface thickness between the simulation and the physical experiment. Notwithstanding these minor deviations, the close overall agreement validates the capacity of MP-LDD to resolve high-pressure-gradient transient events and to maintain interfacial stability under conditions of violent multiphase flow.

8.2.4 Sloshing in a Harmonically Excited Rectangular Tank

The behaviour of the MP-LDD method under sustained oscillatory multiphase loading is assessed through replication of the sloshing experiment of Kishev et al. [186]. The computational domain represents a 2D rectangular domain of length 0.6 m and height 0.3 m. The tank is partially filled with water to a depth of 0.12 m from the base, with the remaining upper volume occupied by air. The water density is $\rho_w = 1000$ kg/m^3 with kinematic viscosity $\nu_w = 1.0 \times 10^{-6}$ m^2/s, and the air density is $\rho_a = 1.225$ kg/m^3 with kinematic viscosity $\nu_a = 1.5 \times 10^{-5}$ m^2/s. The coordinate origin is located at the lower left corner of the tank, and a pressure monitoring point is placed on the left wall at a height of 0.1 m from the base. The domain is discretized with a uniform point spacing of 0.002 m, and no-slip boundary conditions are applied at all solid boundaries. Both fluid phases are initialised at rest, and gravity acts vertically downward at $\mathbf{g} = 9.81$ m/s^2.

A prescribed sinusoidal horizontal sway motion defined $\eta(t) = A\sin(2\pi t/T)$ is imposed on the tank, with an excitation amplitude of $A = 0.05$ m and an oscillation period of $T = 1.5$ s. This excitation generates a time-varying free surface within the tank, producing a complex interplay of wave propagation, run-up along the tank walls, wave breaking, and free surface fragmentation at certain phases of the oscillation cycle.

Figure 8.33 presents side-by-side comparisons of the free surface geometry at four consecutive points within the excitation cycle ($t = 1.1T$, $1.2T$, $1.3T$, and $1.4T$) between the exper-

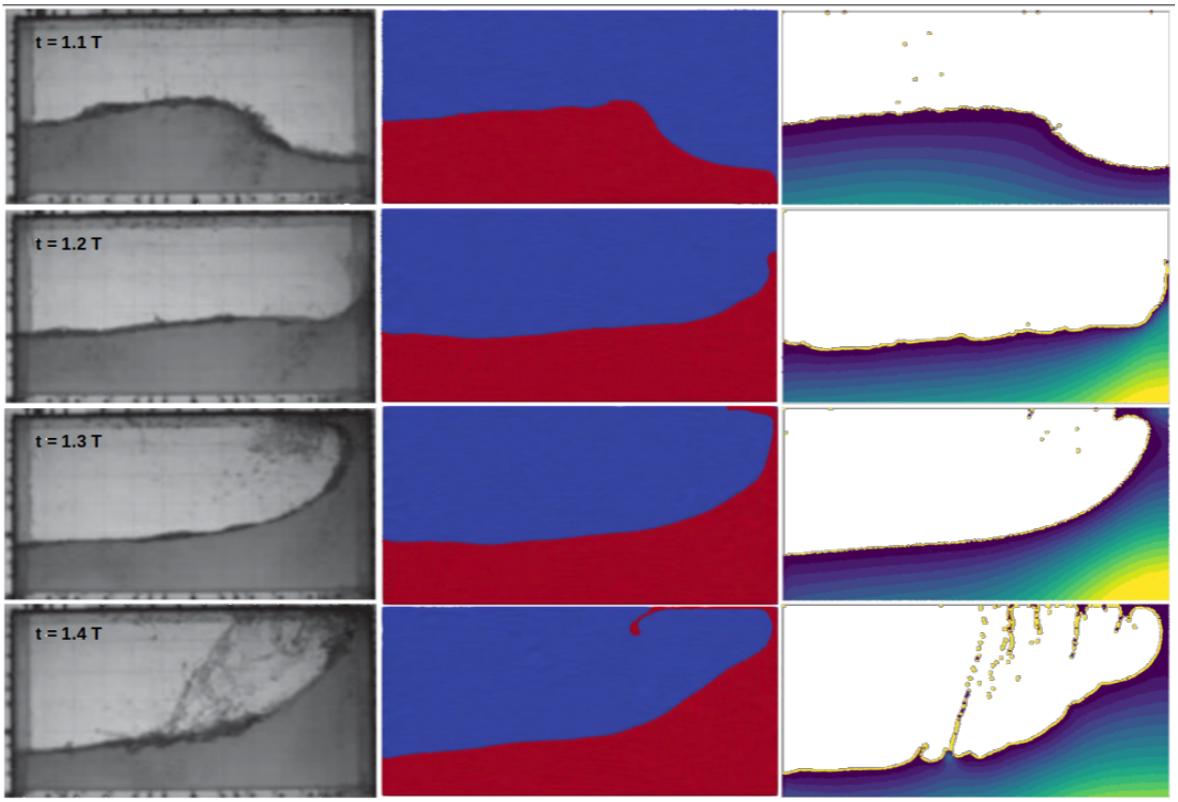

Figure 8.33. Free surface snapshots at $t = 1.1T$, $1.2T$, $1.3T$, and $1.4T$: experimental observations (left column), MP-LDD simulation (middle column), and single-phase LDD reference solution (right column).

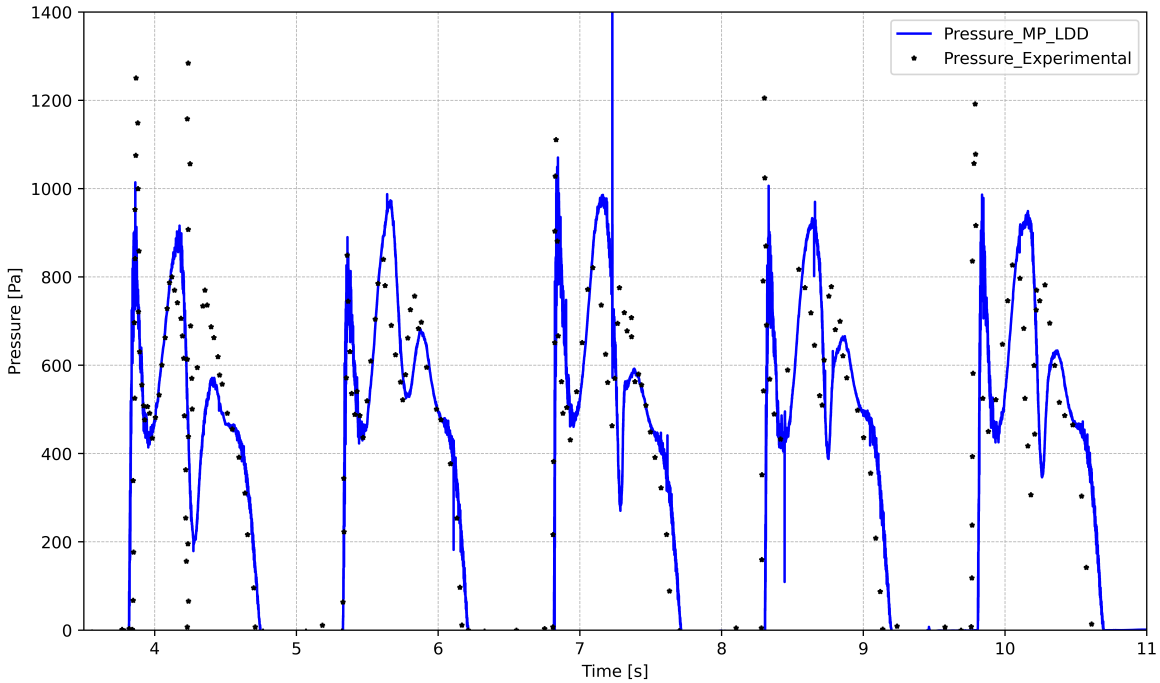

Figure 8.34. Pressure time history at the wall-mounted sensor located 0.1 m above the tank base, comparing the MP-LDD prediction against the experimental pressure data.

imental observations, the MP-LDD simulation, and the single-phase LDD solution of Bašić et al. [42]. The MP-LDD results reproduce the experimentally observed wave morphology with high fidelity at the first three time instants, accurately capturing the wave elevation profile, the run-up along the left wall, and the progressive steepening of the wave front. At $t = 1.4T$, a localised discrepancy is observed: the experiment shows water droplets suspended from the upper wall following wave impact, while the MP-LDD simulation does not reproduce this feature. This difference is attributed to the action of the PBD regularization procedure, which enforces a uniform spatial distribution of computational points and consequently prevents the formation of isolated droplet structures detached from the main fluid body. Despite this limitation at the specific instant of droplet formation, the MP-LDD method accurately captures the overall wave dynamics, the phase interface topology, and the multiphase interaction patterns throughout the majority of the excitation cycle.

The quantitative comparison of the pressure history at the wall sensor is shown in Figure 8.34. The MP-LDD prediction (blue line) tracks the experimental pressure record (black dots) with close agreement, accurately reproducing the timing and amplitude of the pressure spikes associated with wave impact events, as well as the inter-peak pressure fluctuations. These findings validate the MP-LDD formulation as a dependable and quantitatively accurate tool for predicting pressure loads in oscillatory multiphase sloshing configurations.

8.2.5 Two-Dimensional Sloshing Validation

A two-dimensional sloshing case is conducted in a rectangular tank of length 1.2 m and height 0.6 m, with an initial water fill level of 0.12 m, corresponding to 20% of the tank height. This configuration replicates the experimental study of Rhee et al. [187]. The tank is subjected to harmonic sway excitation with a period of $T = 1.94$ s and an amplitude of 0.06 m. A pressure monitoring point is located on the bottom wall of the tank at a distance of 0.57 m from the origin in the x-direction. The fluid properties are: water density $\rho_w = 1000$ kg/m^3 with kinematic viscosity $\nu_w = 1.0 \times 10^{-6}$ m^2/s; air density $\rho_a = 1.225$ kg/m^3 with kinematic viscosity $\nu_a = 1.48 \times 10^{-5}$ m^2/s. The computational domain employs a uniform point spacing of 0.004 m, and no-slip boundary conditions are applied to all solid walls.

The time evolution of the free surface profile within the tank is illustrated in Figure 8.35 through a sequence of snapshots at normalised time instants t/T. The water phase (red) undergoes progressive oscillatory redistribution within the tank in response to the sway excitation, forming travelling waves that reflect from the tank walls and interact to produce time-varying free surface profiles. The contour plots reveal a consistently sharp and well-defined interface between the water and air phases (blue) throughout the duration of the simulation, confirming the ability of the MP-LDD formulation to maintain interfacial integrity under sustained cyclic loading without exhibiting numerical diffusion or interface broadening.

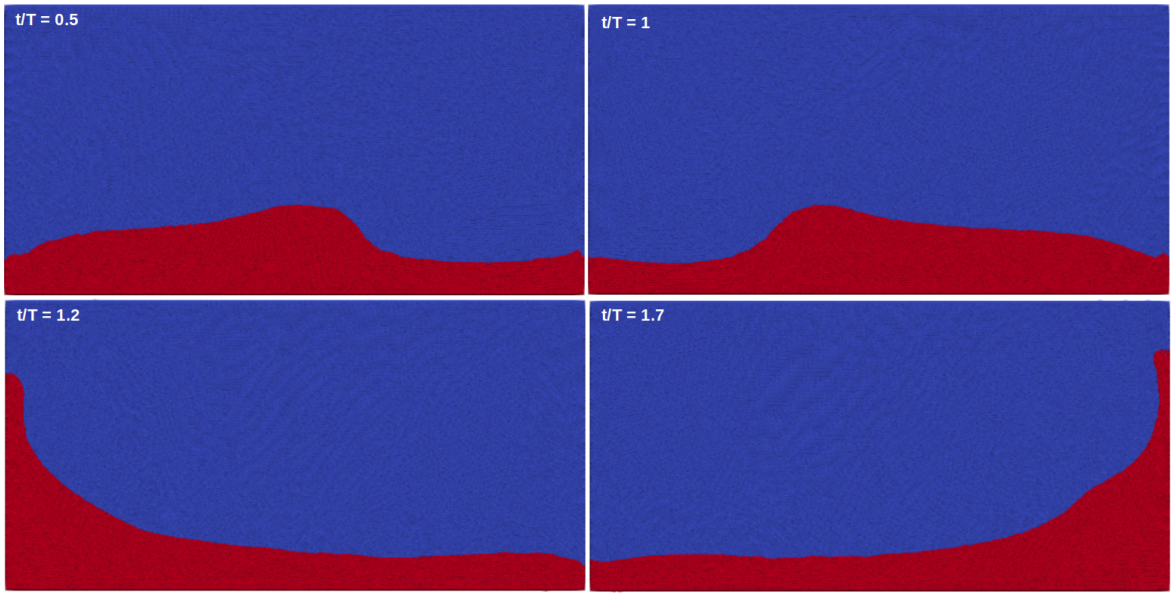

Figure 8.35. Temporal evolution of the fluid motion within the two-dimensional sloshing tank at successive normalised time instants t/T.

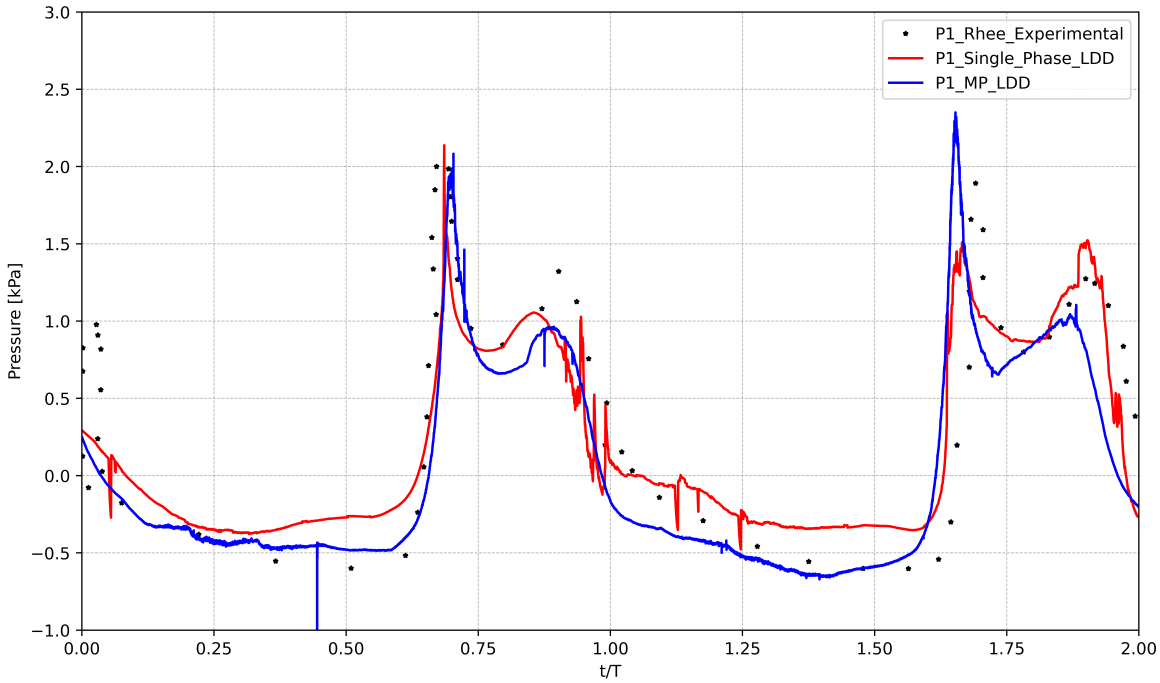

Figure 8.36. Pressure time history at monitoring point P1 from the MP-LDD simulation (blue), the single-phase LDD simulation (red), and the experimental measurements (black).

The pressure history at monitoring point P1 is presented in Figure 8.36, comparing the MP-LDD prediction (blue line) against the experimental measurements of Rhee et al. [187] (black dots) and the single-phase LDD results of Paneer et al. [47] (red line). All three datasets follow a consistent trend throughout the observation window, with close agreement at the principal pressure peaks associated with the most intense sloshing events. The quantitative pressure deviations at the two peak locations for both simulation approaches are

summarised in Table 8.7.

Table 8.7. Deviation of numerically predicted pressure from the experimental measurements at the first and second sloshing pressure peaks.

Region	1st Peak [kPa]	2nd Peak [kPa]	Method
1st peak	0.1	0.35	Single-Phase LDD
2nd peak	0.1	0.2	Multiphase MP-LDD

The pressure deviations listed in Table 8.7 indicate that both the single-phase and multiphase simulations produce comparable accuracy at the first pressure peak, with deviations of 0.1 kPa in both cases. At the second pressure peak, which is associated with a more intense sloshing event, the MP-LDD simulation achieves a reduced deviation of 0.2 kPa compared to 0.35 kPa for the single-phase LDD formulation. This improvement reflects the capability of the multiphase formulation to capture the pressure dynamics more accurately during severe sloshing events through explicit representation of the air phase and its compressibility effects on the pressure field near the interface.

8.2.6 Injection of Oil into Water

The final validation case addresses the injection of oil into a water-filled domain through a submerged barrier, replicating the numerical study of Duan et al. [14]. This configuration involves two immiscible liquid phases with a relatively modest density ratio, and is designed to evaluate the accuracy of the MP-LDD method in resolving buoyancy-driven interfacial evolution between fluids of similar density. The domain consists of a rectangular tank of total length 1.6 m and height 0.25 m, divided into two compartments by a vertical barrier. The left compartment is initially filled with water to a height of 0.1 m, and the right compartment contains oil reaching a height of 0.25 m. The barrier separating the two compartments contains a small rectangular aperture of width 0.02 m centred at a height of 0.05 m above the base, through which the two fluids are permitted to exchange under the action of gravity. The computational configuration is illustrated in Figure 8.37.

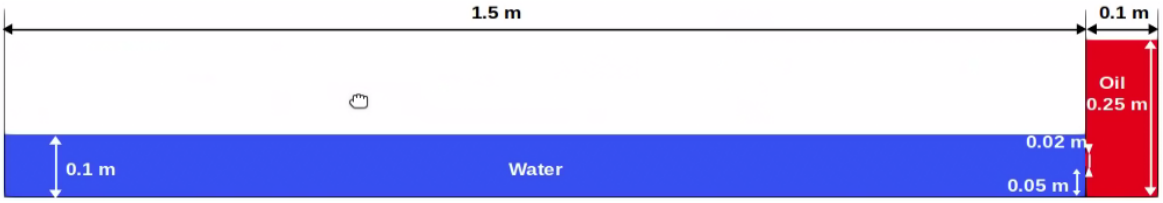

Figure 8.37. Computational domain configuration for the oil injection into water study, showing the initial fluid distribution in the two compartments separated by the perforated barrier.

Water has a density of $\rho_w = 1000$ kg/m^3 and a kinematic viscosity of $\nu_w = 1 \times 10^{-6}$ m^2/s. Oil has a density of $\rho_o = 897$ kg/m^3 and a kinematic viscosity of $\nu_o = 5.5741 \times 10^{-5}$ m^2/s.

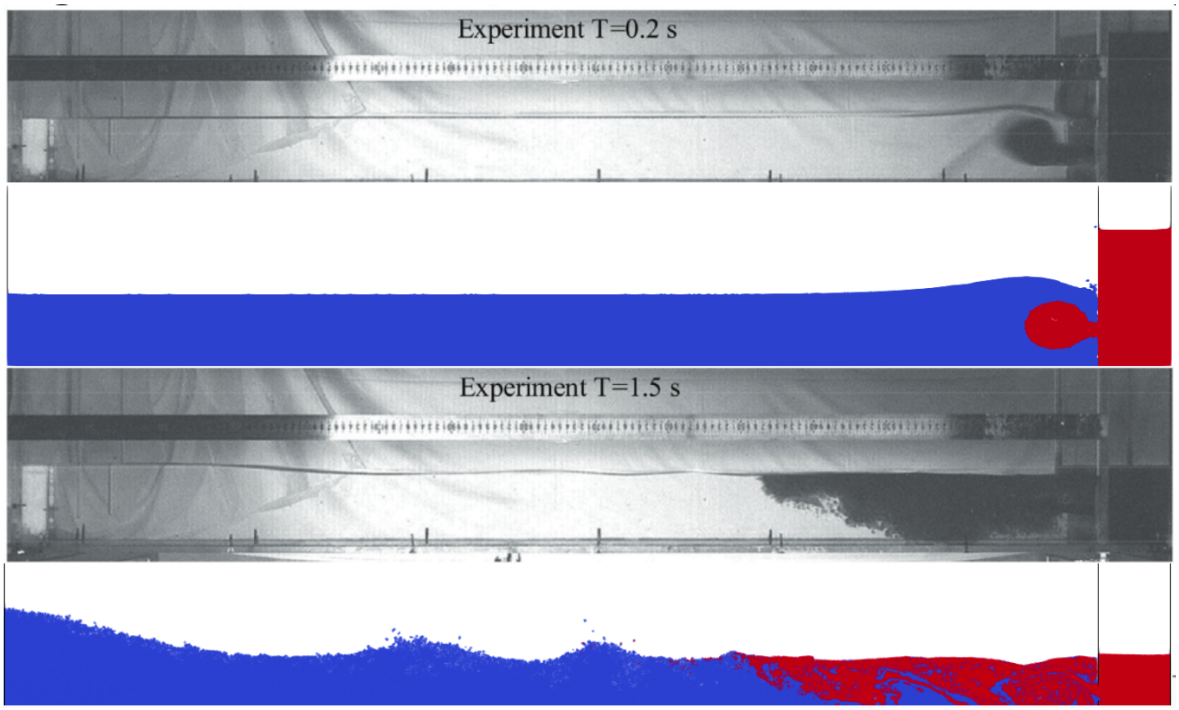

Figure 8.38. Comparison of the oil-water interface development at $T = 0.2$ s and $T = 1.5$ s between the MP-LDD simulation and the reference numerical study.

Since oil is less dense than water, it naturally migrates to the upper portion of the water column when the two phases come into contact, driven by the density differential and the gravitational body force of $\mathbf{g} = 9.81$ m/s^2. A fine uniform point spacing of 0.001 m is applied across the computational domain to capture the detailed interfacial behaviour as the oil infiltrates the water compartment through the barrier aperture.

The predicted oil-water interface development is benchmarked against the reference dataset of Duan et al. [14] at two time instants, $T = 0.2$ s and $T = 1.5$ s, in Figure 8.38. At the earlier time, $T = 0.2$ s, the oil has started to pass through the barrier aperture into the water compartment, driven primarily by the hydrostatic pressure difference arising from the unequal fill heights on either side of the barrier. Owing to its lower density, the oil accumulates at the top of the water column as it enters the left compartment, producing a clearly stratified configuration in which the oil-water interface separates the floating oil layer from the underlying water mass. At this stage, both the simulated and reference results display a well-defined and smooth interface at this stage. By $T = 1.5$ s, the oil has propagated further into the water compartment and the flow has transitioned to a more complex pattern characterised by a less regular interfacial geometry and greater spatial extent of the oil layer. The reference data at this time show increased irregularity at the interface consistent with the onset of buoyancy-driven secondary instabilities, and the MP-LDD simulation reproduces this behaviour with good qualitative fidelity. The consistency between the predicted and reference interface geometries at both time instants, together with the accurate reproduction of the oil distribution and stratification dynamics, demonstrates the ability of the MP-LDD method

to reliably replicate the behaviour between two immiscible liquids with a low density ratio under the combined influence of pressure-driven and buoyancy-driven flow mechanisms.

8.2.7 Summary

The proposed MP-LDD formulation is intended to extend the original Lagrangian Differencing Dynamics. This framework to multiphase flow problems through an explicit representation of immiscible phases and their interface dynamics within a fully Lagrangian setting. The central objective is to maintain a sharp and well-defined interface while avoiding the artificial density and viscosity smearing that commonly arises in diffuse-interface treatments, thereby preserving the distinct material properties of each phase across the interface. The validation studies presented for Rayleigh-Taylor instability, dam-break flows, sloshing configurations, and oil-water interaction collectively demonstrate that the method is capable of reproducing complex interfacial motion, strong density-ratio effects, and transient pressure evolution with good qualitative and quantitative agreement against reference data.

In particular, future assessment of the MP-LDD framework should include tracking of the total mass or volume of each phase throughout the simulation and reporting the associated relative conservation error as a function of time. Further verification of long-time conservation, interface accuracy & second order consistency at the interface, performance of broader benchmark cases remains an important direction for future work.

8.3 Surface Tension and DCA

8.3.1 Square Droplet - Non Equilibrium Oscillation

The oscillation of liquid droplets under the action of surface tension forces constitutes a fundamental phenomenon in multiphase fluid dynamics. Accurate simulation of this phenomenon is crucial for validating surface tension models in computational frameworks, particularly under simplified conditions where gravity is absent and unbalanced surface tension acts as the primary restoring force. In order to assess the surface tension model, the oscillation of a square ethanol droplet in a quiescent fluid due to unbalanced surface tension forces is simulated, as illustrated in Figure 8.39.

The ethanol droplet, having a side length of 0.075 m, is surrounded by a low-density fluid with no-slip wall boundaries. The ethanol properties are density ($\rho_d = 797.88\,\mathrm{kg/m^3}$), kinematic viscosity ($\nu_d = 1.4 \times 10^{-6}\,\mathrm{m^2/s}$), and surface tension coefficient ($\sigma = 0.02361\,\mathrm{N/m}$), while the surrounding fluid has a density ($\rho_e = 1\,\mathrm{kg/m^3}$) and a kinematic viscosity ($\nu_e = 1 \times 10^{-5}\,\mathrm{m^2/s}$).

The oscillation frequency is determined analytically using:

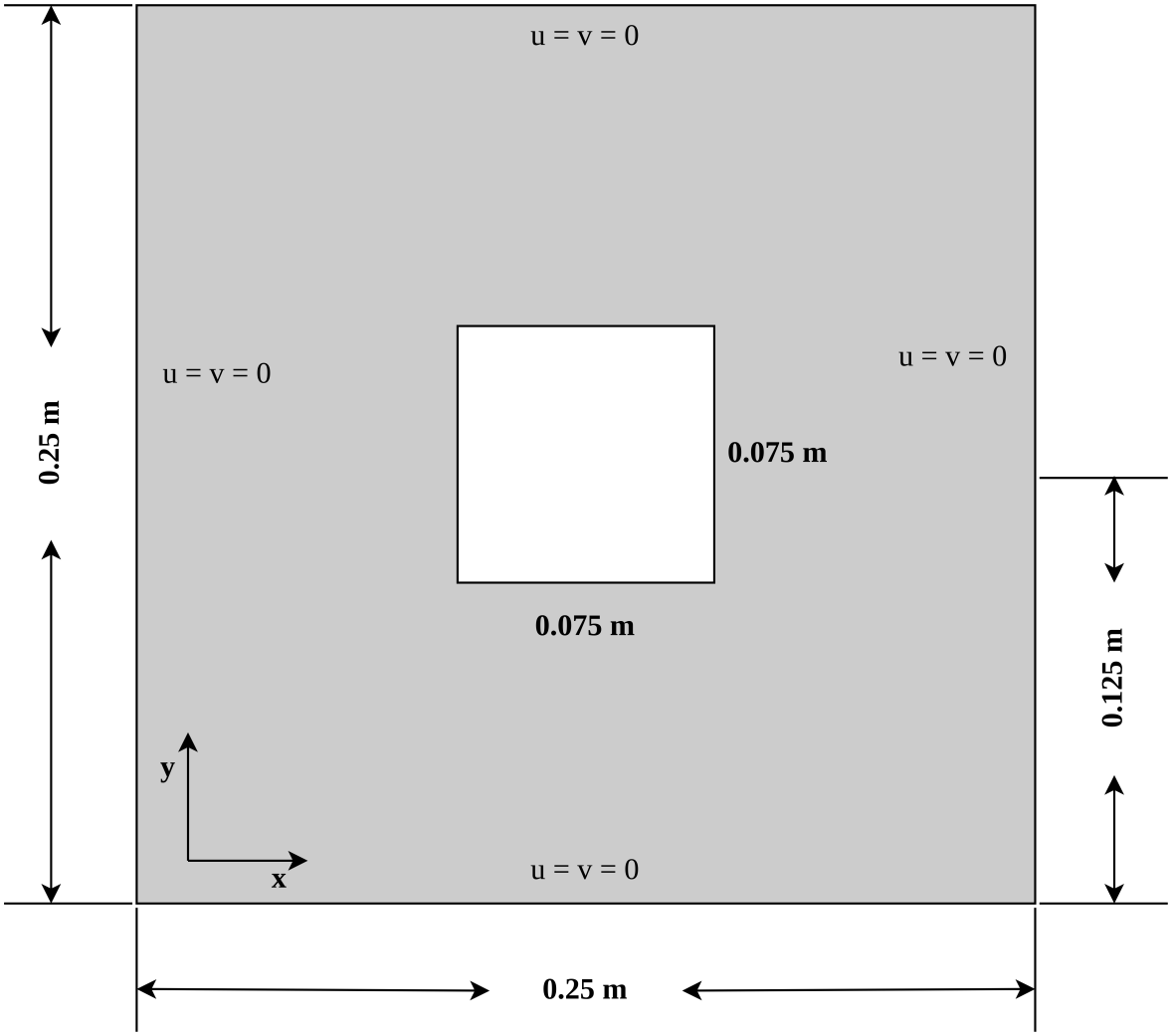

Figure 8.39. Schematic of the Case Setup for Square Ethanol Droplet Oscillation

$$\omega_n^2 = \frac{(n^3 - n)\sigma}{(\rho_d + \rho_e)R_0^3}, \tag{8.3}$$

where n is the oscillation mode, $R_0 = \sqrt{\frac{\text{Area}}{\pi}}$ is the equivalent radius, and ω_n is the angular frequency. For $n = 4$, the oscillation period is 1.299 using the following equation:

$$T = \frac{2\pi}{\omega_n}. \tag{8.4}$$

The analytically derived period matches well with the results obtained from our numerical method, as shown in Figure 8.40. This agreement demonstrates the reliability of the implemented surface tension model in predicting droplet oscillation dynamics.

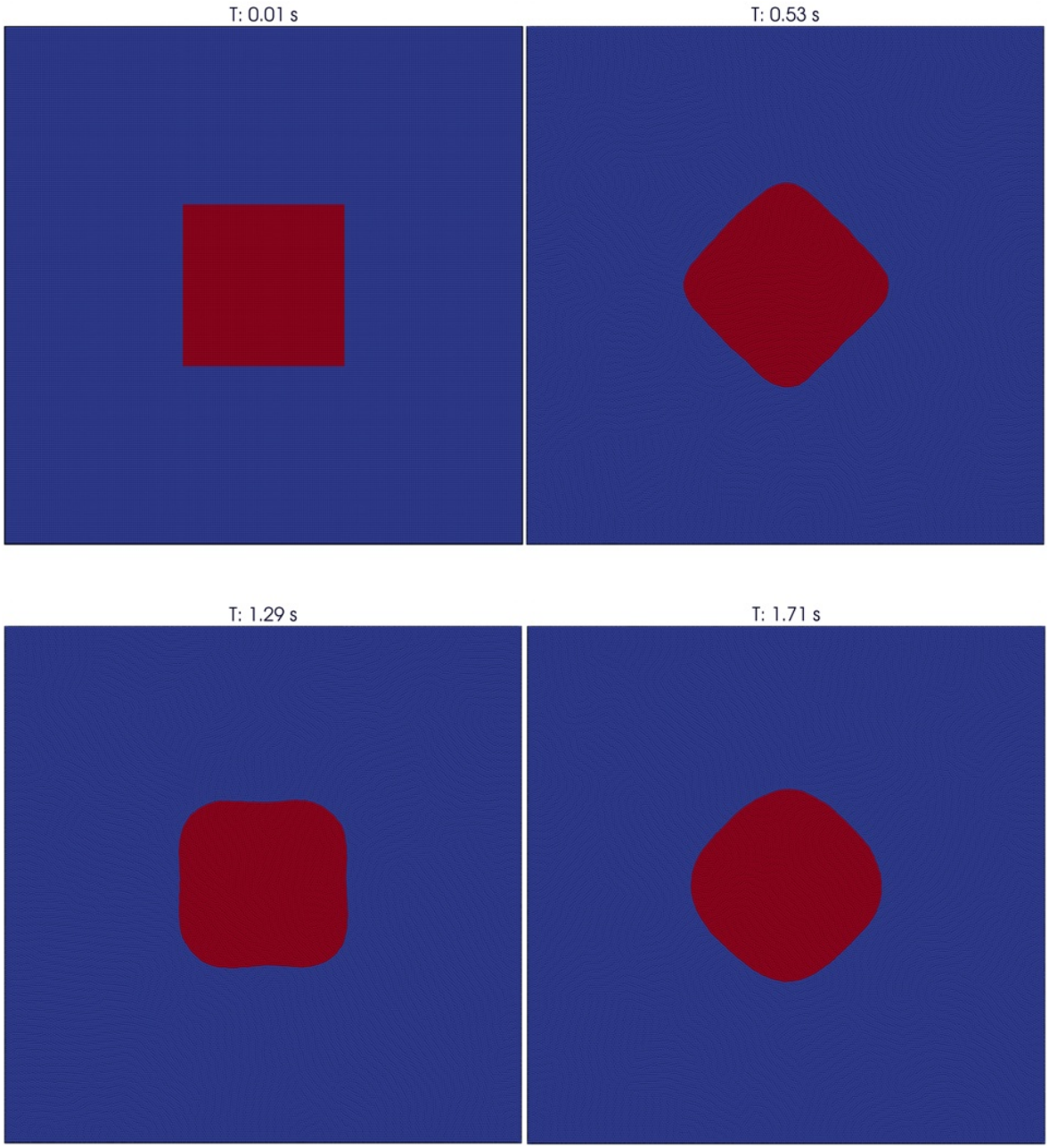

Figure 8.40. Non-equilibrium oscillation of square droplet at different time step

8.3.2 Bubble Rising

To validate the surface tension model within the MP-LDD framework under buoyancy-driven interfacial dynamics, the classical benchmark problem of a rising bubble was reproduced following the quantitative study of Hysing et al. [192]. This benchmark is widely used in the multiphase flow community due to the availability of well-established reference data and its ability to test both the interfacial tension formulation and the pressure-velocity coupling in the presence of density and viscosity contrasts. The computational domain is a two-dimensional rectangle of dimensions 1×2 m. A circular bubble of radius $r = 0.25$ m is initially centered at the coordinate $(0.5,\ 0.5)$ m. The bubble is composed of a lighter

fluid (fluid 2), while the surrounding medium consists of a heavier fluid (fluid 1). No-slip boundary conditions are enforced at the top and bottom walls, while free-slip (zero tangential stress) conditions are applied on the lateral walls. Gravity acts in the negative y-direction with a magnitude of $g = 0.98$ m/s^2. The fluid properties used in this simulation are summarised in Table 8.8.

Table 8.8. Fluid parameters used in the bubble rising simulation based on Hysing et al

ρ_1 (kg/m^3)	ρ_2 (kg/m^3)	μ_1 (Pa·s)	μ_2 (Pa·s)	g (m/s^2)	σ (N/m)
1000	100	10	1	0.98	24.5

This configuration corresponds to the high-surface-tension test case (Test Case 1) defined by Hysing et al., characterised by a Bond number $Bo = \rho_1 g r^2/\sigma \approx 1$ and a Reynolds number $Re = \rho_1 \sqrt{gr^3}/\mu_1 \approx 35$. These dimensionless numbers place the problem in a regime where surface tension dominates over inertial effects, resulting in minimal interfacial deformation and a nearly ellipsoidal bubble shape during the rise.

The simulation was advanced until $t = 3$ s, and the obtained results were benchmarked against the reference data of Hysing et al. [192] using three quantitative metrics: bubble shape, centre-of-mass position, and rising velocity. Figure 8.41 illustrates the bubble's shape and position at $t = 3$ s, where the white dots superimposed on the MP-LDD result represent the reference interface profile from Hysing et al. The MP-LDD framework resolves the distinct interface accurately and the bubble adopts a slightly flattened ellipsoidal shape consistent with the expected behaviour at high surface tension. The close agreement between the MP-LDD interface contour and the reference data confirms the capacity of the method to preserve a well-defined, non-diffuse interface without the need for ghost particles or explicit interface reconstruction.

The vertical location of the bubble's centre of mass was tracked throughout the simulation and compared to the benchmark values, as shown in Figure 8.42. The MP-LDD result follows the benchmark trajectory closely from the initial stages through to the end of the simulation at $t = 3$ s. The bubble accelerates from rest due to buoyancy and progressively decelerates as it approaches a terminal velocity. The MP-LDD framework reproduces this transient behaviour accurately, with negligible deviation from the Hysing et al. data. The correct prediction of the centre-of-mass trajectory validates both the momentum equation and the pressure correction strategy incorporating the Young-Laplace pressure jump. The temporal evolution of the bubble's rising velocity is presented in Figure 8.43. The MP-LDD method correctly captures the initial acceleration phase, the peak velocity, and the subsequent velocity plateau as the bubble approaches its terminal rise speed. The maximum velocity and the instant at which it is reached show close correspondence with the reference data. Minor oscillations visible in the velocity signal near the peak are consistent with the transient dynamics associated with the vortex shedding and interfacial deformation at that stage, and similar behaviour is also observed in the reference solutions.

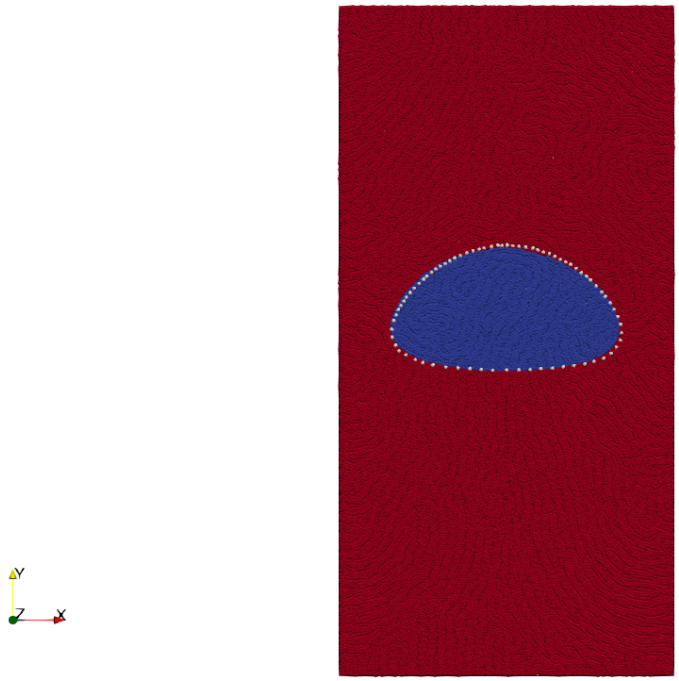

Figure 8.41. Comparison of bubble shape and position at $t = 3$ s obtained using MP-LDD (coloured region) against the benchmark dataset of Hysing et al. (white dots).

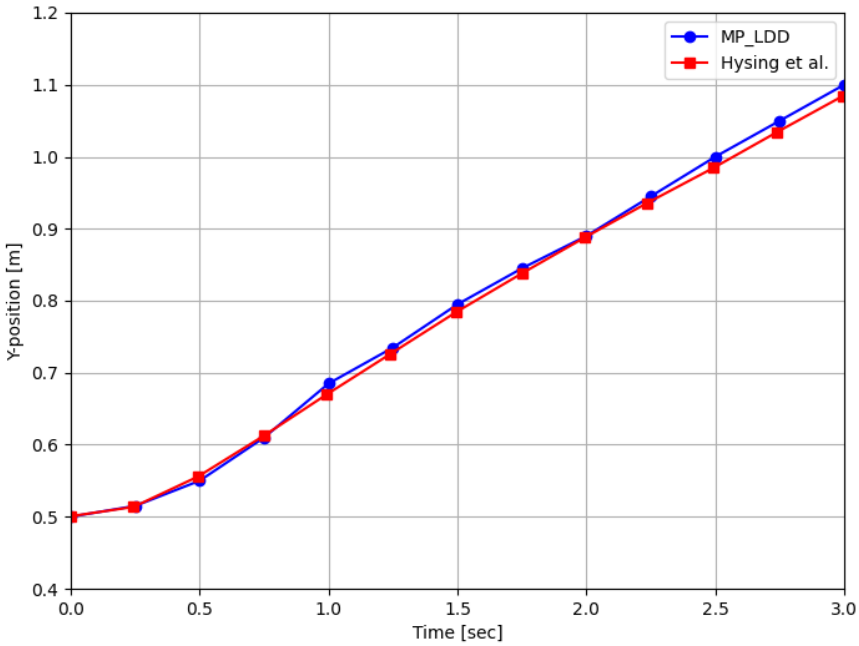

Figure 8.42. Quantitative comparison of bubble rising dynamics: centre-of-mass trajectory obtained with MP-LDD (blue solid line) against the reference data of Hysing et al. (red markers).

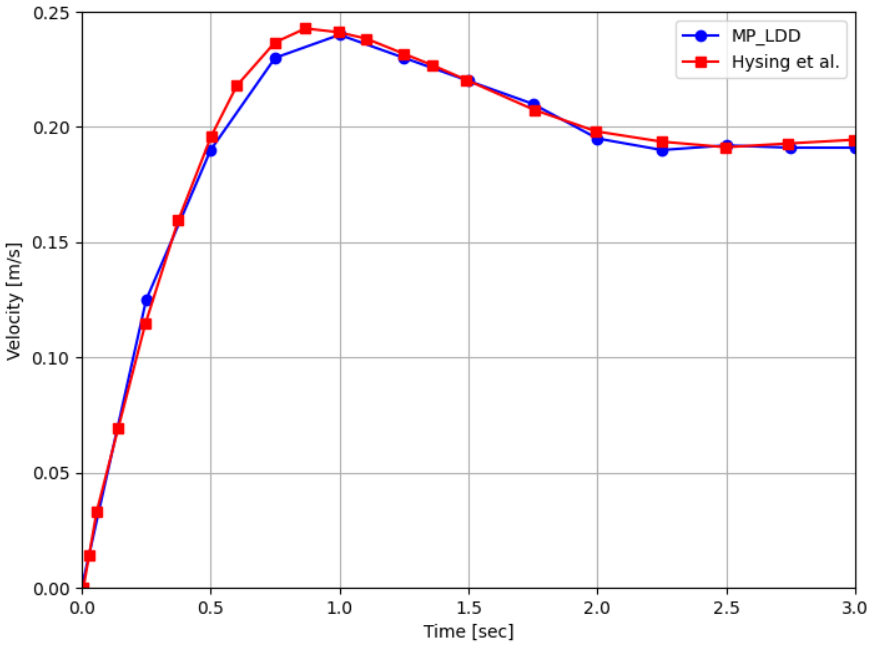

Figure 8.43. Quantitative comparison of bubble rising dynamics: rising velocity (Right) obtained with MP-LDD (blue solid line) against the reference data of Hysing et al. (red markers).

Overall, the three-way comparison in terms of shape, displacement, and velocity demonstrates that the MP-LDD method faithfully replicates the behaviour of a buoyancy-driven bubble under strong surface tension. The results validate the pressure jump initialisation strategy based on the Young-Laplace equation and confirm the robustness of the Continuum Surface Force (CSF) formulation integrated within the MP-LDD velocity equation. The sharp-interface treatment employed by MP-LDD proves to be effective in maintaining numerical stability over the full simulation duration without artificial smearing of the interface or spurious velocity artefacts.

8.3.3 Static Contact Angle on a Square Droplet

To assess the contact angle model within the MP-LDD framework independently of dynamic wetting effects, a series of simulations were performed in which a square droplet was allowed to reach its equilibrium shape on a flat solid surface under prescribed static contact angles. This test isolates the capillary-driven deformation mechanism and provides a direct means of verifying that the numerical framework correctly reproduces the equilibrium droplet morphology as predicted by the Young equation. A square ethanol droplet of dimensions 0.06×0.06 m was initialised at rest on a horizontal solid surface within a background fluid. The droplet had a density of $\rho_d = 797.88$ kg/m^3 and a surface tension coefficient of $\sigma = 0.02361$ N/m. The surrounding background fluid had a density of $\rho_b = 1.0$ kg/m^3 and a

dynamic viscosity of $\mu_d = 10^{-2}$ Pa·s. Gravitational acceleration and all other external body forces were deliberately excluded from this case so that the resulting equilibrium shape is governed exclusively by surface tension and the imposed contact angle, enabling a clean assessment of the contact angle model. The simulations were conducted for six values of the equilibrium static contact angle, θ_s, spanning the full wettability spectrum from complete wetting to complete non-wetting: $\theta_s \in \{30°, 60°, 90°, 120°, 150°, 180°\}$. Each simulation was run until a quasi-static equilibrium and at $T = 2$ s, where the droplet shape was analysed.

The equilibrium configurations obtained for each prescribed contact angle are presented in Figure 8.44. The droplet morphology transitions systematically from a highly flattened, spread shape at low contact angles to a nearly spherical cap at large contact angles, consistent with the theoretical predictions of the Young-Laplace framework. At $\theta_s = 30°$, the droplet

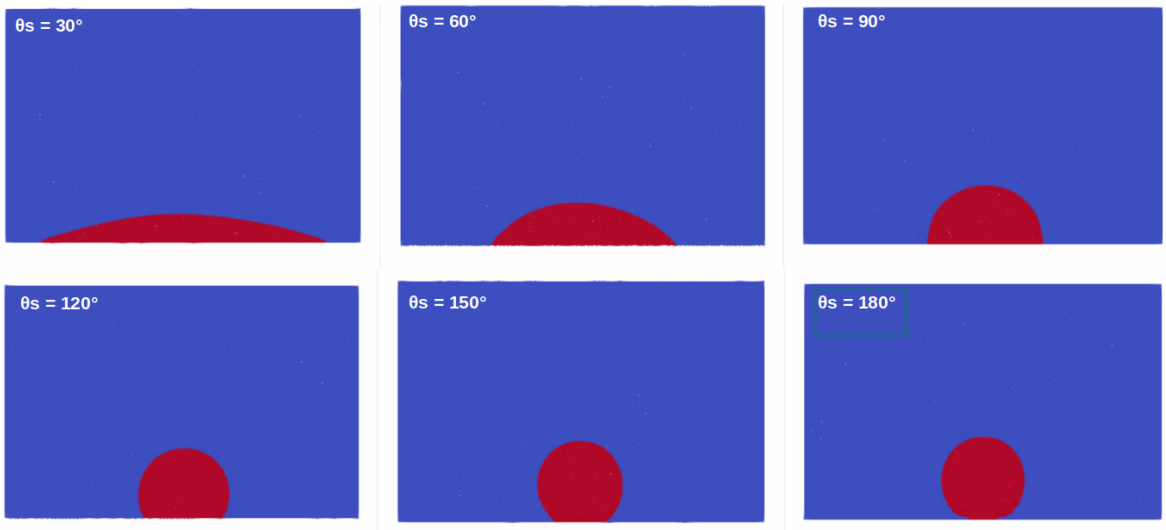

Figure 8.44. Equilibrium shapes of a square ethanol droplet on a flat solid surface at $T = 2$ s for static contact angles of $\theta_s = 30°$, 60°, 90°, 120°, 150°, and 180°.

extends substantially along the wall and adopts a shallow, low-profile dome characteristic of highly hydrophilic surfaces. As the contact angle increases to $\theta_s = 60°$, the spreading is reduced and the droplet becomes noticeably taller. At $\theta_s = 90°$, the contact angle is neutral, and the droplet assumes a semicircular profile where the interface meets the wall perpendicularly. This is a particularly important reference case because the equilibrium condition is geometrically exact and easy to verify analytically. For $\theta_s = 120°$ and $\theta_s = 150°$, the droplet transitions into the hydrophobic regime: the base contact length decreases further, the droplet height increases, and the curvature of the interface at the wall becomes distinctly obtuse. Finally, at $\theta_s = 180°$, the droplet makes contact with the wall only at a single mathematical point and assumes a near-circular cross-section, corresponding to the condition of complete non-wetting.

Importantly, in all cases, the measured contact angle of the equilibrium droplet shape closely matches the prescribed value of θ_s, and the droplet profiles exhibit excellent symmetry about the vertical axis. The smooth, well-resolved interface at the triple line confirms

that the force application at the contact point is handled correctly by the direct surface mesh operation of MP-LDD, without the need for ghost particles or extrapolation schemes. These results collectively validate the static contact angle model embedded in the MP-LDD framework across the full range of wettability conditions, and provide a necessary foundation for the more complex dynamic contact angle simulations that follow.

8.3.4 Effect of Surface Tension and Dynamic Contact Angle on Droplet Spreading

To assess the individual and combined contributions of surface tension (ST) and the dynamic contact angle (DCA) model on droplet spreading dynamics, a parametric study was conducted involving a semi-circular water droplet spreading on a flat horizontal surface under gravity. Three distinct physical configurations were examined in parallel: (1) No ST + No DCA, (2) ST + No DCA, and (3) ST + DCA. By progressively introducing each physical mechanism, the role of each model in governing the contact line motion and droplet morphology can be clearly isolated. A semi-circular droplet of radius $r = 0.5$ m was placed on a flat horizontal surface. Acceleration due to gravity was applied in the downward direction to drive the spreading process. The three configurations differ solely in which physical models are activated:

- **Configuration 1 — No ST + No DCA:** Neither surface tension nor dynamic contact angle effects are included. The droplet spreads under gravity and viscosity alone, with no interfacial restoring forces.
- **Configuration 2 — ST + No DCA:** Surface tension is activated and the velocity equation via the Continuum Surface Force (CSF) formulation. No contact angle constraint is applied at the triple line.
- **Configuration 3 — ST + DCA:** Both surface tension and the dynamic contact angle model are active. The DCA model applies a tangential force at the contact line proportional to the deviation between the dynamic and current contact angles, providing additional resistance to contact line motion.

The droplet profiles for all three configurations are shown at two time instants, $t = 0.05$ s and $t = 0.10$ s, in Figure 8.45 and Figure 8.46, respectively. Together, these snapshots reveal the transient and quasi-steady spreading behaviour under each configuration.

Configuration 1 - No ST + No DCA. In the absence of both surface tension and contact angle effects, the droplet undergoes the most aggressive spreading under gravity alone. At $t = 0.05$ s, the droplet has already spread to a wide footprint and its height is visibly reduced. By $t = 0.10$ s, the spreading has progressed further and the droplet has flattened dramatically,

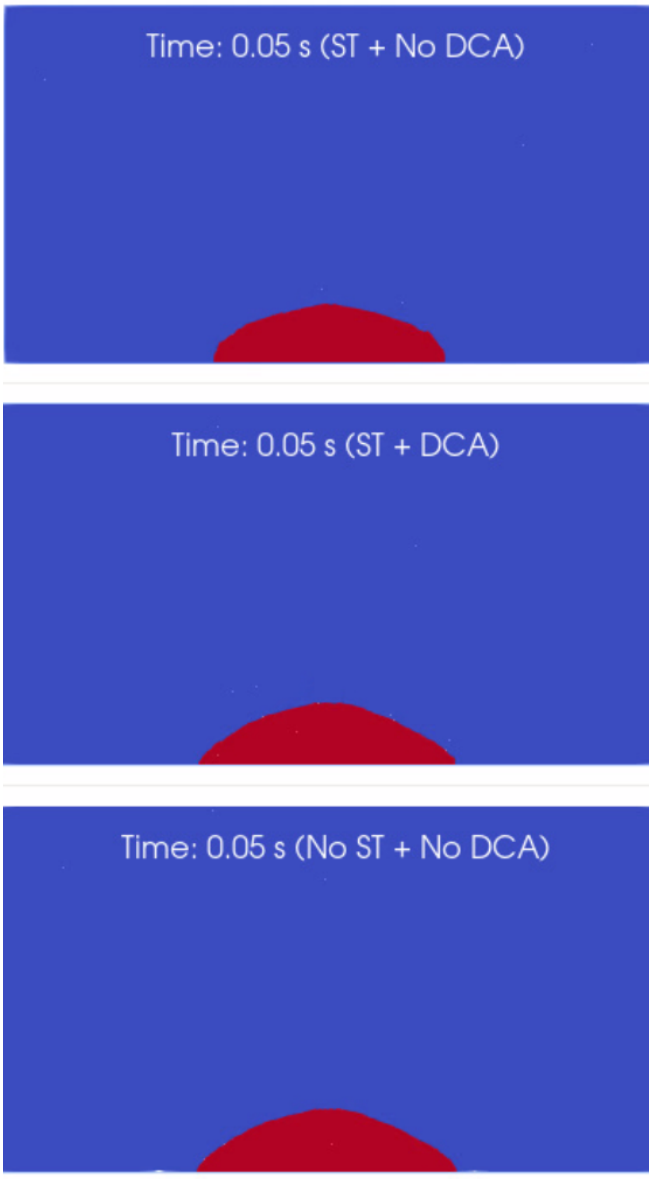

Figure 8.45. Droplet profiles at $t = 0.05$ s for the three configurations: ST + No DCA (top), ST + DCA (middle), and No ST + No DCA (bottom).

extending nearly across the full width of the domain with a very low profile. The lack of any interfacial restoring mechanism allows the gravitational force to dominate entirely, producing a thin, pancake-like morphology. This configuration serves as the reference baseline for evaluating the restraining effects introduced in the other two cases.

Configuration 2 - ST + No DCA. With surface tension included but no contact angle constraint, the droplet's behaviour changes markedly. At $t = 0.05$ s, the droplet retains a well-rounded, compact dome shape with a clearly visible and smooth curved interface, in strong contrast to the flattened profile of Configuration 1 at the same instant. The surface tension force resists the gravitational deformation of the interface, reducing the lateral spread and maintaining a greater central height. By $t = 0.10$ s, however, the droplet has spread

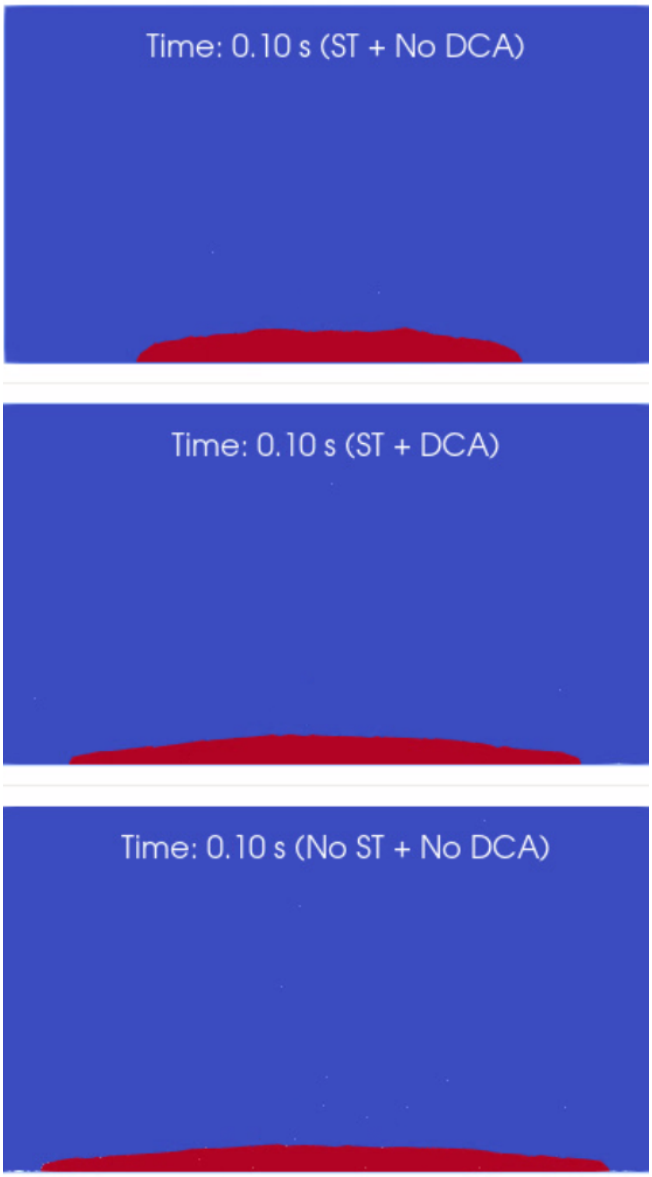

Figure 8.46. Droplet profiles at $t = 0.10$ s for the three configurations: ST + No DCA (top), ST + DCA (middle), and No ST + No DCA (bottom).

significantly — the profile has flattened and the footprint has grown considerably compared to the earlier time step. Without a contact angle model to pin or retard the contact line, the triple point is free to advance, and the droplet eventually spreads to a wide, low-profile shape. This reveals that while surface tension slows the spreading process, it is insufficient on its own to arrest contact line motion over longer time scales in the absence of a wetting constraint.

Configuration 3 - ST + DCA. When both surface tension and the dynamic contact angle model are activated, the droplet exhibits the most physically constrained behaviour of the three cases. At $t = 0.05$ s, the droplet profile is noticeably more compact and taller than in Configuration 2, with a smoother and more symmetric interface. The DCA model im-

poses a tangential force at the contact line that penalises rapid contact line advancement, effectively retarding the spreading process beyond what surface tension alone can achieve. At $t = 0.10$ s, the droplet in this configuration has spread less than Configuration 2 while maintaining a greater height, and the interface remains well-defined and symmetric. This behaviour demonstrates that the DCA model plays a crucial complementary role alongside surface tension: it directly constrains the dynamics at the triple point, which is the primary driver of lateral spreading, while surface tension governs the global shape of the free surface.

The progressive comparison across the three configurations at both time steps clearly demonstrates the hierarchical role of the two physical models. Surface tension is the dominant restoring mechanism that counteracts gravity and reduces overall spreading relative to the unconstrained baseline. The dynamic contact angle model provides an additional and physically distinct constraint at the contact line itself, further limiting the spreading footprint and producing a more compact, symmetric droplet profile at both early and late times. Together, the two models yield a simulation that captures the full richness of real droplet wetting behaviour, including the retardation of contact line motion commonly observed in experimental studies of droplet spreading on partially wettable surfaces. These results validate the implementation of both the ST and DCA models within the MP-LDD framework and highlight their importance for accurate simulation of wettability-driven flows in applications such as surface coating, inkjet printing, and microfluidic systems.

8.3.5 Summary

The results presented in this section show that the MP-LDD framework is able to capture the principal capillary and wetting phenomena relevant to multiphase interface dynamics. The surface tension model was assessed through non-equilibrium droplet oscillation and the rising-bubble benchmark, while the contact-angle formulation was examined through static contact-angle tests and comparative droplet-spreading simulations with and without surface tension and dynamic contact angle effects. Taken together, these studies demonstrate that the present formulation can reproduce interface restoration, bubble dynamics, equilibrium wettability, and the influence of contact-line modelling on transient spreading behaviour.

Further work will focus on strengthening the capillary-scale verification of the method through quantitative assessment of parasitic currents, more rigorous validation of the dynamic contact angle formulation against reference wetting data, and systematic evaluation of capillary time-step restrictions in relation to adaptive time stepping.

8.4 Energy Formulation

8.4.1 Heat Conduction

The study analyzes steady-state heat conduction within a two-dimensional square domain filled with a fluid defined by constant thermophysical properties: density $\rho = 1000\,\mathrm{kg/m^3}$, kinematic viscosity $\nu = 1 \times 10^{-6}\,\mathrm{m^2/s}$, specific heat capacity $C_p = 100\,\mathrm{J/kg{\cdot}K}$, thermal conductivity $k = 2\,\mathrm{W/m{\cdot}K}$, and acceleration due to gravity $\mathbf{g} = 0\,\mathrm{m/s^2}$ [193]. The boundary conditions, as illustrated in Figure 8.47, impose fixed wall temperatures of 0 K on the left, top, and bottom edges, while the right edge held at 100 K. The initial temperature throughout the domain, including the center point T_i, is uniformly set to 0 K.

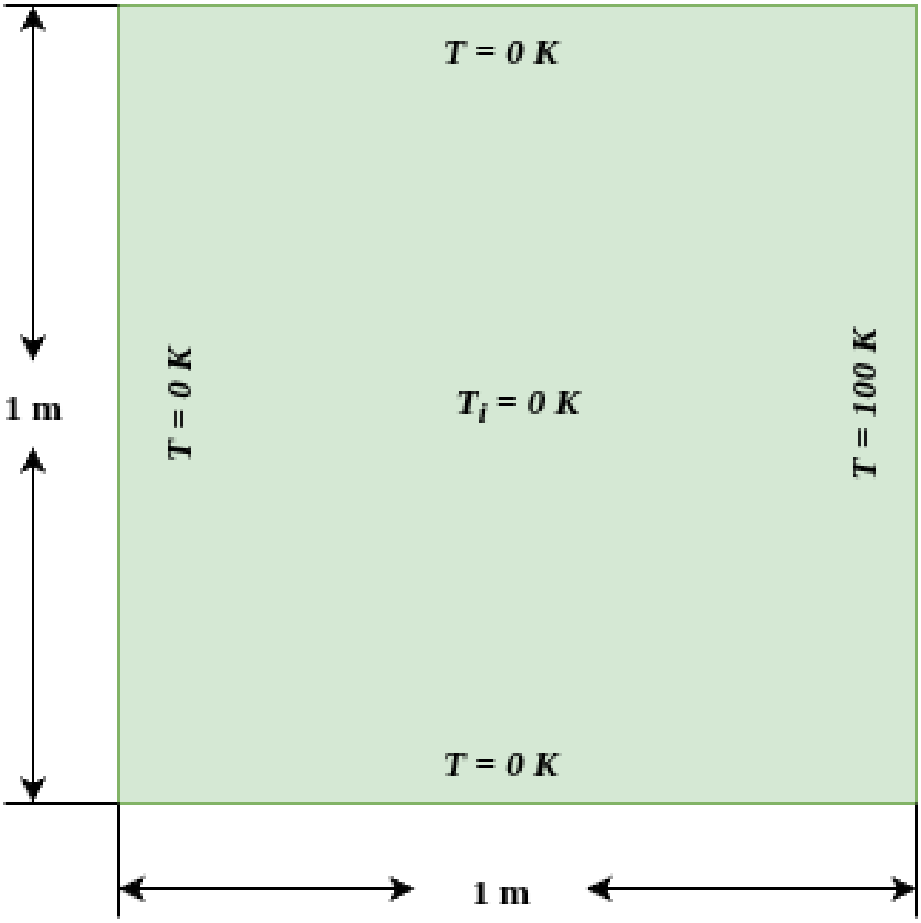

Figure 8.47. Case setup for the 2D heat conduction.

The absence of gravity eliminates convective motion, thereby isolating conductive heat transfer governed by Laplace's equation $\nabla^2 T = 0$. This setup provides a controlled framework for studying pure conduction effects and serves as a benchmark for validating a numerical implementation of the energy equation within the MP-LDD framework. The problem is simulated using the MP-LDD method. A uniform distribution of particles is initialized over the domain (100×100), and the field of temperature is evolved using the discretized energy

equation in the Lagrangian framework. Dirichlet boundary conditions are applied by fixing the temperature values of boundary particles. The simulation continues until a steady-state solution is attained. For the same grid size, the analytical solution for the temperature distribution is obtained using the method of separation of variables. The solution $T_{\text{analytical}}(x,y)$ is expressed as:

$$T_{\text{analytical}}(x,y) = \frac{4T_H}{\pi} \sum_{n=1}^{\infty} \frac{1}{2n-1} \frac{\sinh\left((2n-1)\pi x\right)}{\sinh\left((2n-1)\pi\right)} \sin\left((2n-1)\pi y\right), \tag{8.5}$$

where, $x\&y$ represents the gird positions, $T_H = 100\,\text{K}$ is the hot wall temperature and n represents the summation index over odd integers. In this study, the series is truncated after 100 terms, which provides sufficient convergence for comparison.

Figure 8.48 represents that, MP-LDD temperature distribution closely mirrors the analytical reference both in gradient behavior and overall spatial pattern, confirming the numerical method's accuracy. Despite the difference in visual representation colour shading in MP-LDD versus contour lines in the analytical model the temperature range and zone placements remain consistent across both.

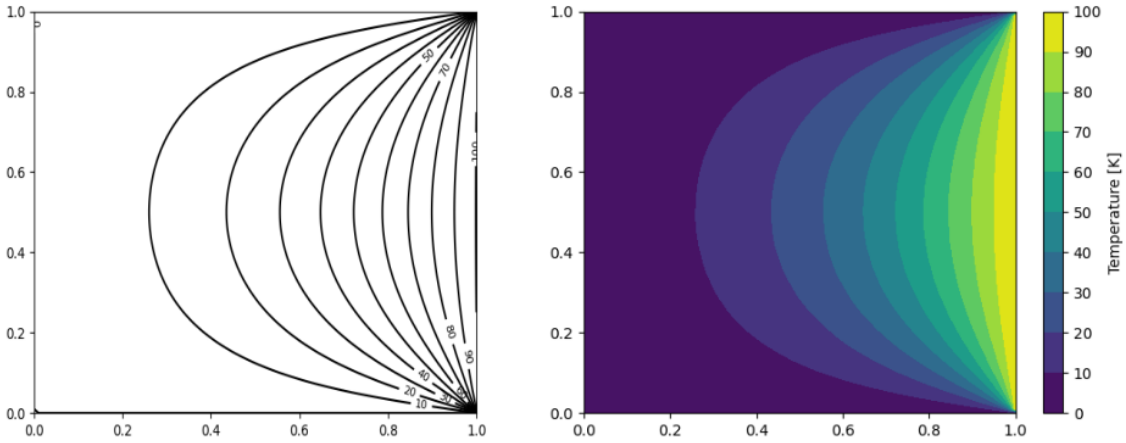

Figure 8.48. Comparison between analytical output (left) and MP-LDD output (right) for temperature distribution.

Table 8.9. Error norms comparing MP-LDD and analytical solution.

Grid Resolution	L1 norm [K]	L2 norm [K]
100×100	0.0332	0.1778

To evaluate the accuracy of the MP-LDD solution $T_{\text{MP-LDD}}(x,y)$, it is compared pointwise with the analytical solution. The absolute error at each particle position is described as:

$$e = \left| T_{\text{MP-LDD}}(x,y) - T_{\text{analytical}}(x,y) \right| \tag{8.6}$$

The global error is quantified using the L^1 norm (i.e. Mean Absolute Error) and L^2 norm (i.e. Root Mean Square Error) as follows:

$$\|e\|_{L^1} = \frac{1}{N}\sum_{i=1}^{N}|e|, \qquad \|e\|_{L^2} = \sqrt{\frac{1}{N}\sum_{i=1}^{N}e^2}, \tag{8.7}$$

where, N is the total number of particles used in the comparison. These norms provide quantitative measures of the deviation between the MP-LDD and analytical results.

The results show that the MP-LDD solution closely matches the analytical profile, validating the implementation of the energy equation. The small values of the L^1 and L^2 norms confirm that MP-LDD accurately captures steady-state conductive heat transfer in the domain. It can be seen in Table 8.9.

8.4.2 Buoyancy Driven Convection in a Square Cavity

To assess the precision of the proposed numerical framework in modelling buoyancy-driven flows, a classical benchmark of natural convection within 2D square cavity subjected to differential heating is considered. This test problem is commonly adopted in the literature as a canonical case for validating convective heat transfer models, due to the availability of reliable reference data and its sensitivity to both thermal and momentum coupling mechanisms.

The computational domain consists of a square cavity of dimensions $0.0386\,\mathrm{m} \times 0.0386\,\mathrm{m}$, as illustrated in Fig. 8.49. The vertical walls are differentially heated: the left wall set to a higher temperature of $303\,\mathrm{K}$, while the right wall fixed at a lower temperature of $283\,\mathrm{K}$. The horizontal walls are adiabatic, enforcing a zero heat flux condition. No-slip velocity boundary conditions are imposed along all four walls. The fluid within the cavity is initially quiescent and uniformly set to $293\,\mathrm{K}$. Air is used as the working fluid and is modeled as an incompressible Newtonian medium with constant thermophysical properties representative of standard ambient conditions. These include a density of $\rho = 1.204\,\mathrm{kg/m^3}$, a kinematic viscosity of $\nu = 1.506 \times 10^{-5}\,\mathrm{m^2/s}$, a specific heat capacity of $c_p = 1006\,\mathrm{J/(kg \cdot K)}$, and a thermal conductivity of $k = 0.02587\,\mathrm{W/(m \cdot K)}$. Gravitational acceleration of $g = 9.81\,\mathrm{m/s^2}$ acts in the vertical direction. Under these conditions, buoyancy arises naturally due to temperature-induced density variations, which are modeled via the Boussinesq approximation. The flow is assumed to be laminar, consistent with the low Rayleigh number regime imposed by the cavity dimensions and boundary conditions. To verify the accuracy of the numerical solution, a mesh convergence study was performed. The domain was discretized with progressively refined point spacings, and the resulting variations in key thermofluid quantities such as velocity profiles and temperature gradients along the cavity midlines were monitored. Convergence was considered achieved when successive refinements yielded negligible changes in these quantities. The final configuration employs a uniform point spacing of $\delta r = 0.005\,\mathrm{m}$. This resolution was found to be sufficient for

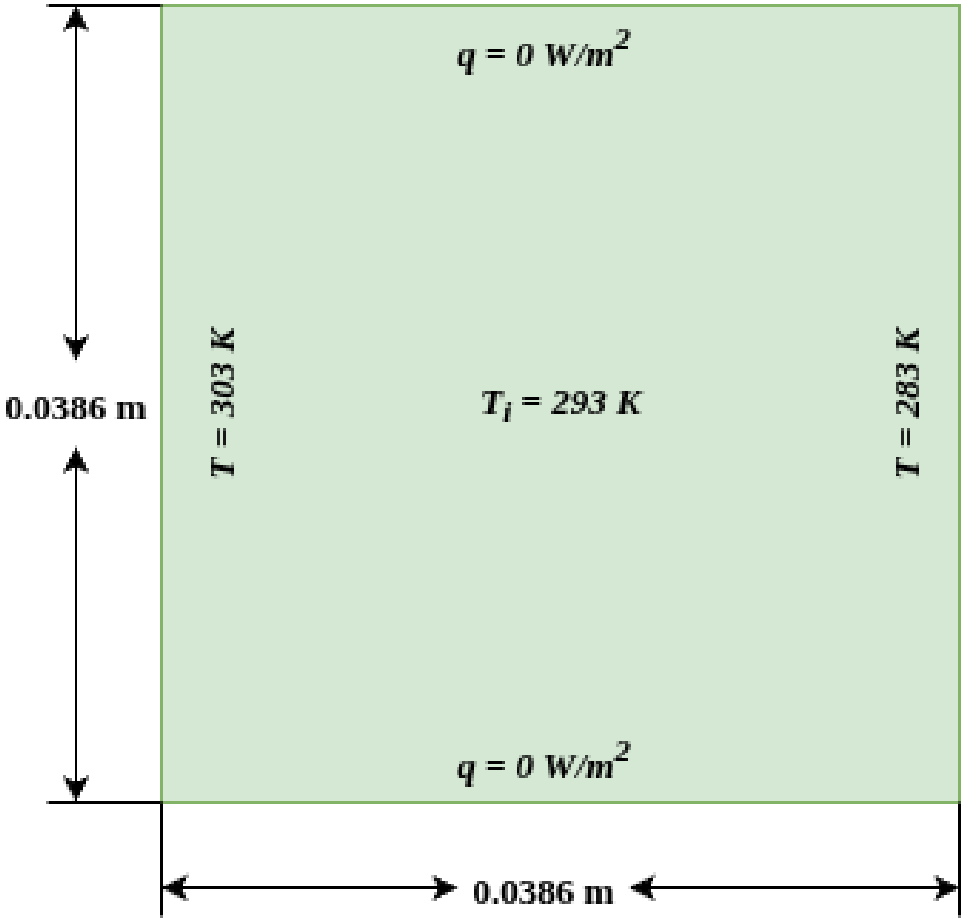

Figure 8.49. Representation of a square cavity (2D) subjected to thermal gradient boundary conditions used for the buoyancy-driven convection benchmark.

capturing sharp thermal gradients adjacent to the heated and cooled walls, as well as the thin boundary layers that govern buoyant circulation.

For generalization and to facilitate comparison with literature data, the governing variables are expressed in non-dimensional form using characteristic thermal and geometric scales. The characteristic length is taken as the cavity height $L = 0.0386\,\mathrm{m}$, and the temperature scale is defined by the imposed temperature difference $\Delta T = T_{hot} - T_{cold} = 20\,\mathrm{K}$. The velocity, temperature, and time are non-dimensionalized as:

$$\begin{aligned} \mathbf{v}^* &= \frac{\mathbf{v} L \rho C_p}{k} \\ T^* &= \frac{T - T_C}{T_H - T_C} \\ t^* &= \frac{tk}{L^2 \rho C_p}. \end{aligned} \tag{8.8}$$

The dimensionless formulation facilitates the scaling of the results and highlights the influence of thermal diffusivity and specific heat on the transient evolution. The simulation was carried out using the MP-LDD solver, which incorporates the heat conduction equation

coupled with buoyancy-driven convection. Measurements were extracted at $t^* = 0.5$, corresponding to a dimensional time of $t = 34.88\,\text{s}$, which marks the point where the flow reaches a steady state, as reported in benchmark studies presented by [194]. Figure 8.50 presents the

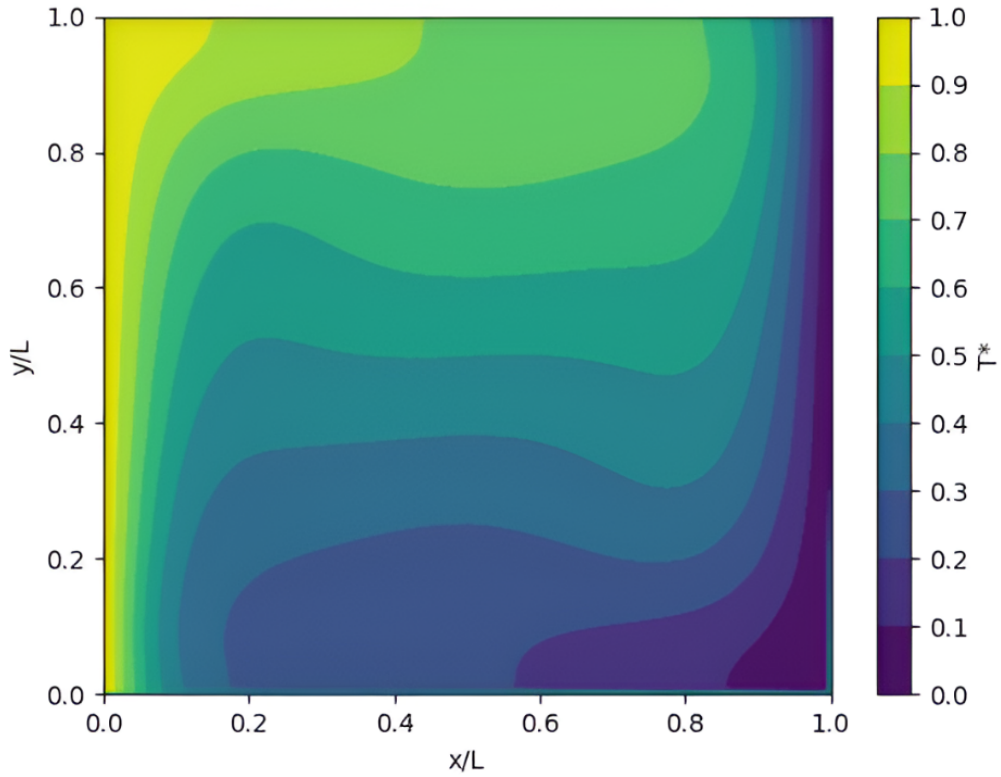

Figure 8.50. Normalized temperature distribution (T^*) at steady state ($t^* = 0.5$).

normalized temperature distribution (T^*) within the cavity domain at steady state ($t^* = 0.5$). The spatial gradient from high to low temperature along the horizontal axis demonstrates a clear thermally stratified flow, driven by buoyancy forces. The contour pattern reveals a stable and symmetric thermal boundary layer near the hot and cold walls, with smooth transitions in the core region, indicative of the model's robustness. To validate the simulation results, Figure 8.51 compares the dimensionless temperature profile (T^*) along the horizontal direction (x/L) at the mid-height location ($y/L = 0.5$) against the benchmark data of [194]. The numerical predictions from the MP-LDD solver (blue curve) exhibit excellent agreement with the reference data (black dots), particularly in regions with strong thermal gradients near the vertical walls. Quantitative validation is further supported by the L1 and L2 norm error values, depicted in Figure 8.52. The L1 norm error is calculated to be 0.012, while the L2 norm is slightly higher at 0.014, confirming the accuracy and convergence of the simulation. The marginally lower L1 value suggests that the solver effectively minimizes the overall deviation across the domain, and the smooth error distribution underscores the mesh adequacy (spacing of 0.0005 m) established through the mesh convergence study.

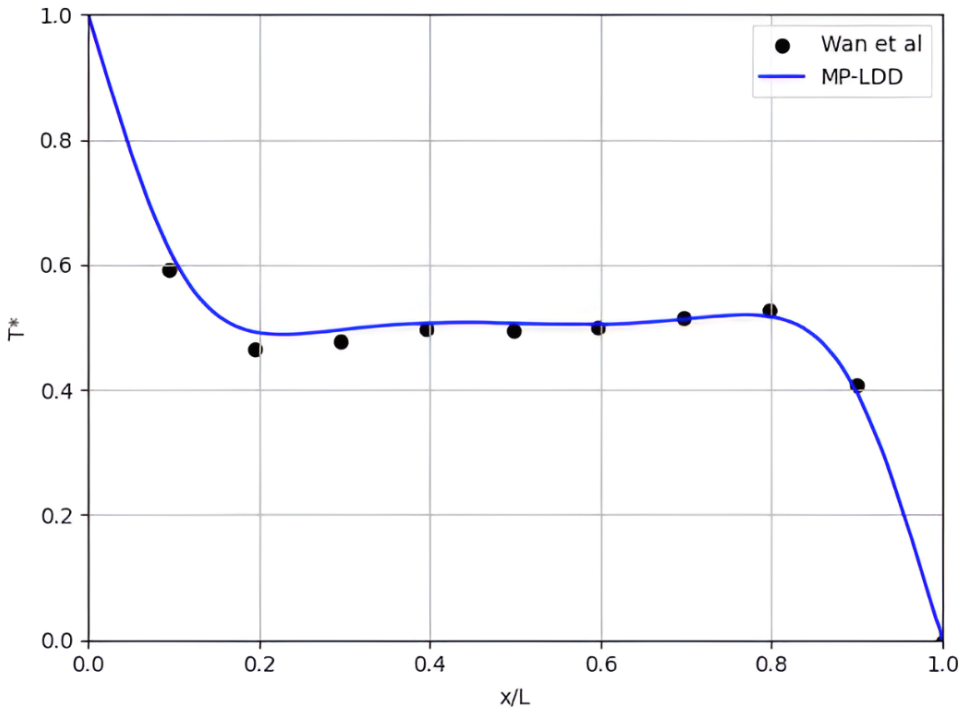

Figure 8.51. Comparison of MP-LDD simulation and benchmark results: Normalised temperature profile (T^*) along x/L at mid-height ($y/L = 0.5$).

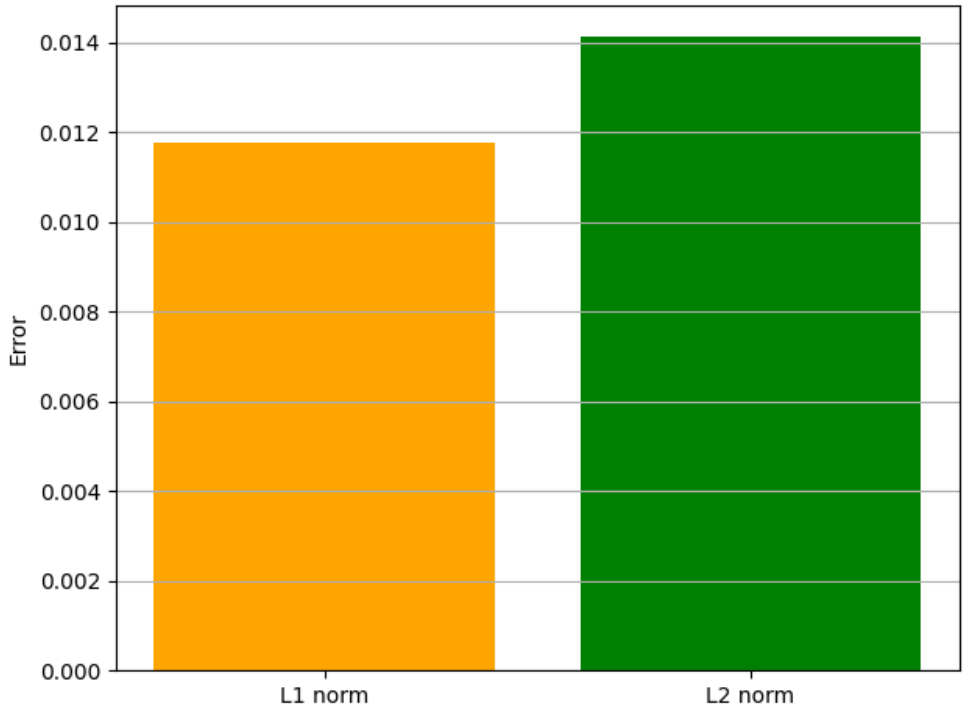

Figure 8.52. Comparison of MP-LDD simulation and benchmark results: Associated L1 and L2 norm errors quantifying deviation from the reference data.

Collectively, the visual and numerical validations substantiate the fidelity of the MP-LDD method in capturing buoyancy-driven convection phenomena. The results agree well with

prior benchmark studies, confirming that the solver can reliably simulate laminar natural convection under differential heating conditions.

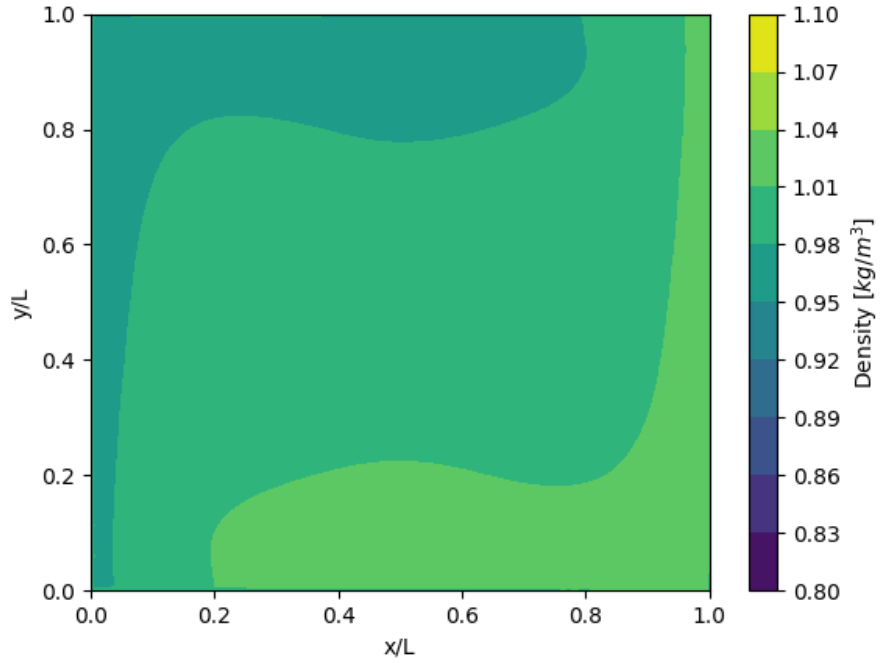

Figure 8.53. Density distribution in the cavity at steady state.

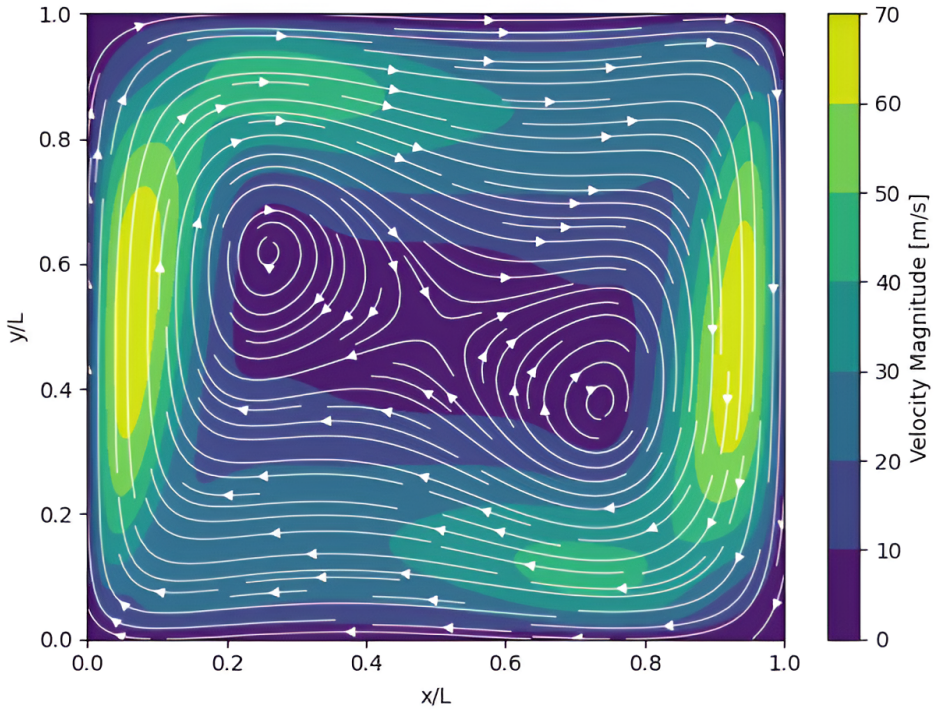

Figure 8.54. Velocity distribution in the cavity at steady state.

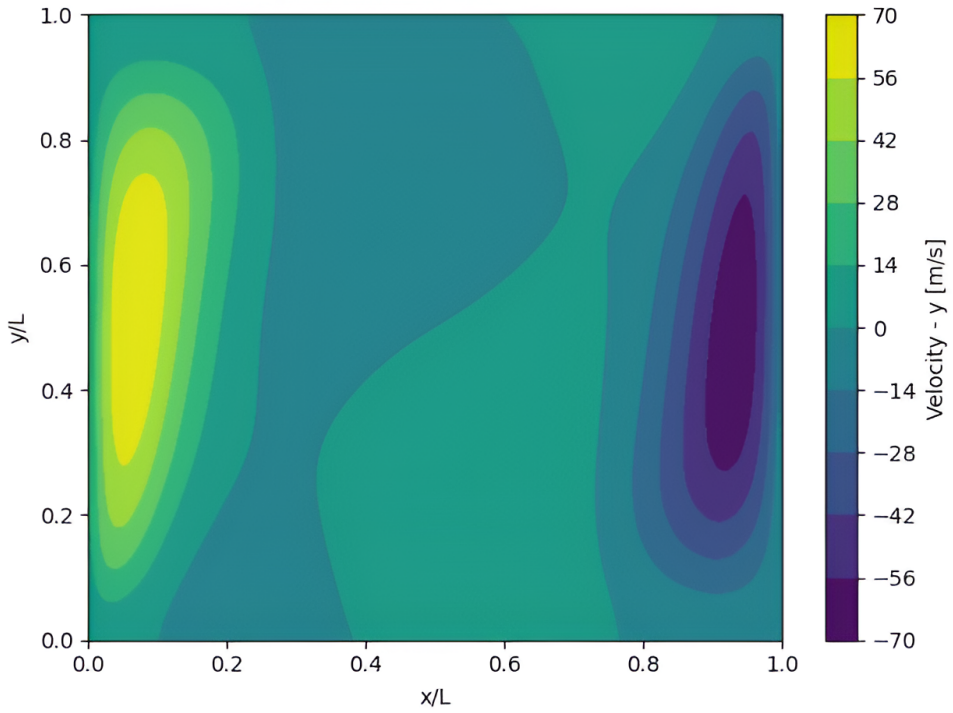

Figure 8.55. Visualisation of flow dynamics.

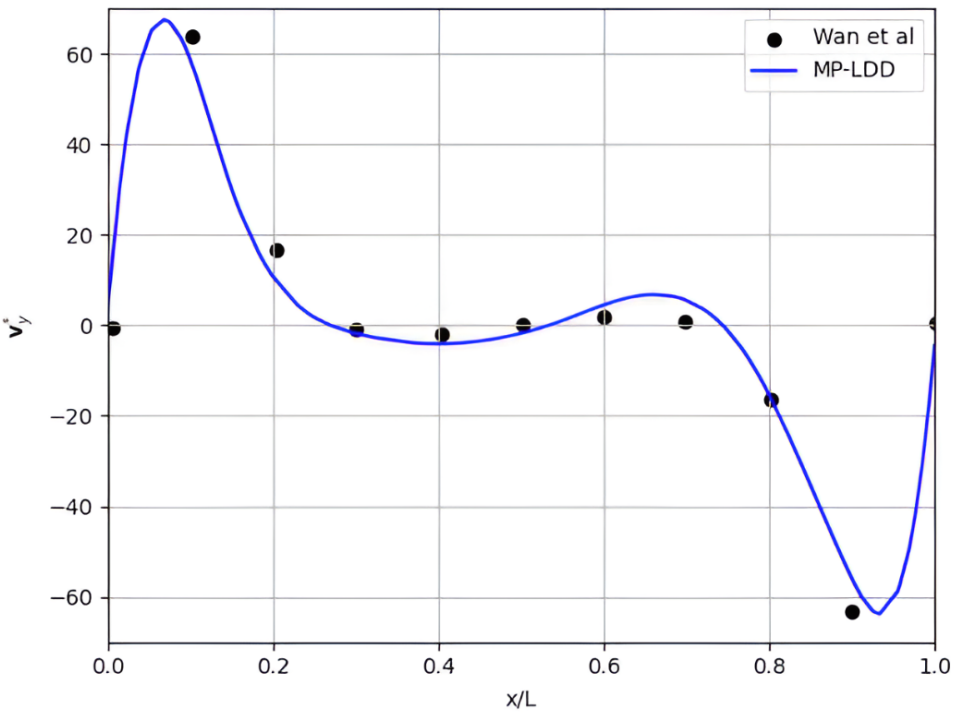

Figure 8.56. Buoyancy-driven motion is reflected in magnitude and direction, with benchmark comparison confirming model accuracy.

Figure 8.53 illustrates the density distribution within the cavity at the steady state, revealing the interplay between temperature-induced variations and buoyancy-driven flow. Due

to the thermal stratification between the heated left wall (303 K) and the cooled right wall (283 K), density gradients emerge throughout the domain. Regions adjacent to the hot wall exhibit lower density, while the cooler areas near the right wall retain higher density values. This inverse relationship between temperature and density drives the buoyancy effect, whereby lighter fluid rises and denser fluid sinks, forming the characteristic convective loop and it can also be seen in Figure 8.54. The smooth and continuous variation observed in the density contour supports the laminar nature of the flow and validates the physical consistency of the numerical model.

Figures 8.55–8.56 together provide a comprehensive view of the flow dynamics within the cavity, emphasizing both the magnitude and directionality of the velocity field driven by thermal gradients. The velocity magnitude contour (Figure 8.55) highlights regions of intense motion, with peak values nearing 70 m/s near the hot wall where buoyant fluid rises. The downward flow adjacent to the cooled wall shows significantly lower velocities, illustrating the asymmetry created by thermal stratification. Complementing this, the vertical velocity component (v-direction) map in Figure 8.56 further distinguishes upward and downward motions. Bright regions along the hot wall confirm strong buoyant ascent, while darker zones reflect gravitational settling of cooler, denser fluid. This vertical transport plays a pivotal role in sustaining the convective loop. To validate these findings, Figure 8.56 compares the normalized vertical velocity along the horizontal mid-plane ($y/L = 0.5$) against benchmark data from Wan et al. The MP-LDD simulation closely aligns with experimental trends, capturing characteristic peaks and troughs at expected positions. These results verify the reliability of the numerical model and indicate that the flow is laminar.

8.4.3 Stefan Problem - Vaporization

To evaluate the performance of the proposed MP-LDD framework in handling phase change phenomena, a classical two-dimensional Stefan problem is considered [195]. This benchmark involves the vaporization of a liquid initially at saturation temperature, with a constant temperature difference imposed at the boundary. The problem admits an analytical solution based on the Neumann formulation of the Stefan condition, making it a widely accepted test case for assessing numerical methods.

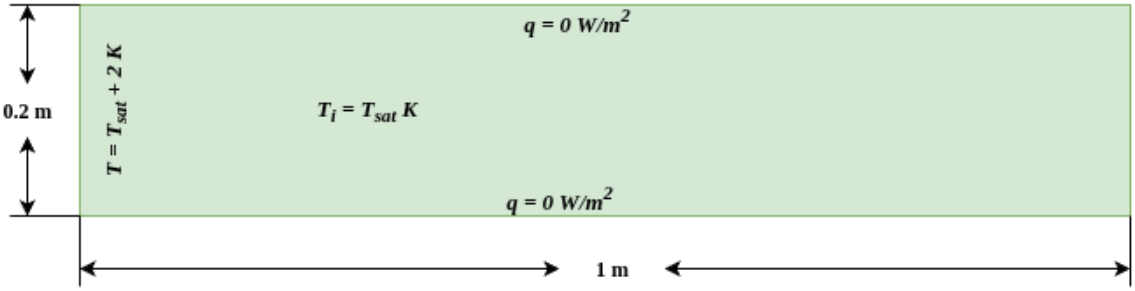

Figure 8.57. Case setup of the 2D Stefan problem for the vaporization process.

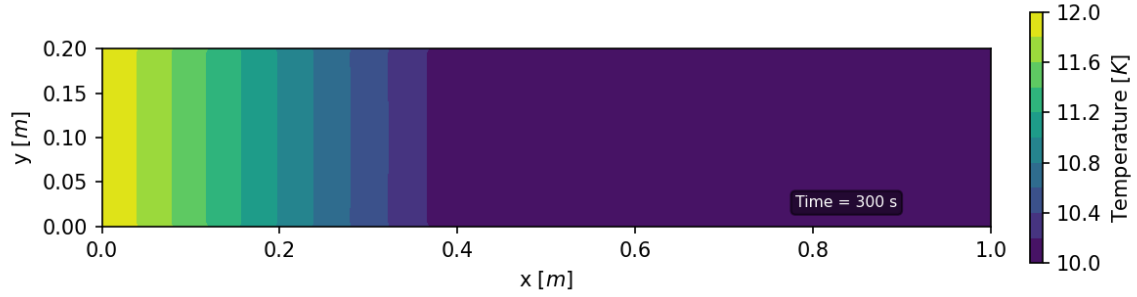

Figure 8.58. Temperature distribution along the x direction of the MP-LDD result at 300 sec.

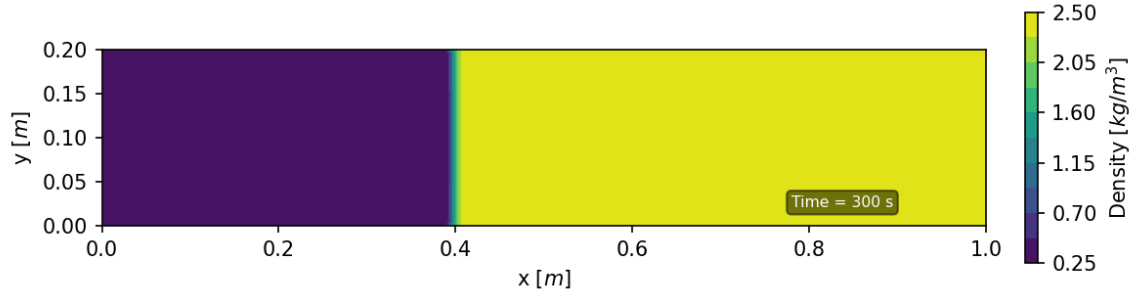

Figure 8.59. Density distribution along the x direction of the MP-LDD result at 300 sec.

The simulation domain is defined as a rectangular region with dimensions 1×0.2 m (Figure 8.57). The liquid is initially at saturation temperature $T_i = T_{\text{sat}} = 10$ K. At the upper boundary, a constant temperature $T = T_{\text{sat}} + 2$ K is imposed to drive the phase change, while the other boundaries are adiabatic ($q = 0$ W/m^2). The simulation employs the following physical parameters: liquid density $\rho_l = 2.5$ kg/m^3, kinematic viscosity $\nu_l = 3.92 \times 10^{-2}$ m^2/s, heat capacity $c_{p,l} = 10$ J/kgK, and thermal conductivity $k_l = 1.5 \times 10^{-3}$ W/mK. The vapor phase properties are: density $\rho_v = 0.25$ kg/m^3, kinematic viscosity $\nu_v = 2.8 \times 10^{-2}$ m^2/s, heat capacity $c_{p,v} = 10$ J/kgK, and thermal conductivity $k_v = 3.5 \times 10^{-3}$ W/mK. The specific latent heat of phase change is $L = 100$ J/kg. Figure 8.58 and 8.59 illustrate the spatial distribution of temperature and density along the x-direction at $t = 300$ s. The vaporization process results in the growth of a vapor region with reduced density, while the temperature field exhibits a sharp gradient near the moving interface. The MP-LDD framework successfully resolves both the temperature discontinuity and the density jump across the interface, without introducing spurious oscillations.

The analytical solution of the one-dimensional Stefan problem is computed by assuming a vapor domain $0 \leq x \leq x_\Gamma(t)$ in contact with a heated wall at $x = 0$, maintained at temperature T_w, while the liquid region is kept at the saturation temperature T_{sat}. The vapor temperature $T_g(x,t)$ satisfies the heat conduction equation

$$\frac{\partial T_g}{\partial t} = \alpha_g \frac{\partial^2 T_g}{\partial x^2}, \tag{8.9}$$

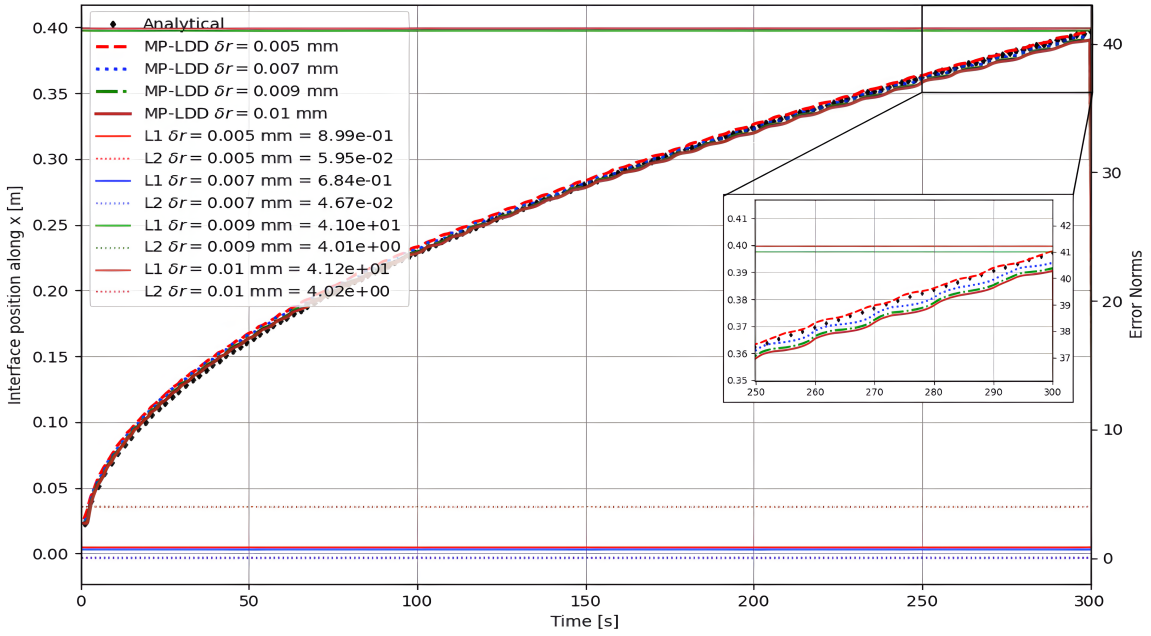

Figure 8.60. Temporal evolution of the two-phase vapour-liquid boundary position for the 2D Stefan problem at various grid resolutions. Symbols represent the analytical Neumann solution, while lines denote MP-LDD results. The inset highlights the asymptotic convergence of the 0.005 *mm mesh at* $t = 300$ *s. The corresponding* L_1 *and* L_2 *error norms (bottom) indicate a* $> 97\%$ *reduction in numerical error when refining the mesh from* 0.01 *mm to* 0.005 *mm.*

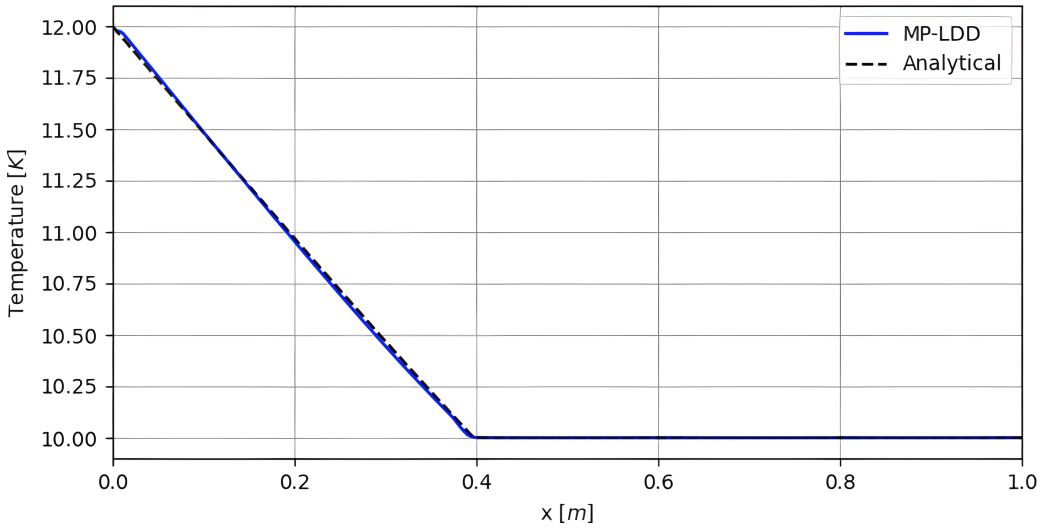

Figure 8.61. Comparison of temperature distribution along the x-direction obtained from MP-LDD and analytical solution at $t = 300$ *s for the resolution of 0.005 mm.*

with boundary conditions $T_g(0,t) = T_w$ and $T_g(x_\Gamma(t),t) = T_{\text{sat}}$. The interface position is computed using the similarity form

$$x_\Gamma(t) = s_0 + 2\beta\sqrt{\alpha_g t}, \tag{8.10}$$

where β is obtained by solving the transcendental Stefan condition

$$\beta e^{\beta^2} \operatorname{erf}(\beta) = \frac{c_{p,g}\,(T_w - T_{\text{sat}})}{h_{lg}\,\sqrt{\pi}}. \tag{8.11}$$

Here $\alpha_g = k_g/(\rho_g c_{p,g})$ is the vapor thermal diffusivity, $c_{p,g}$ the specific heat, k_g the thermal conductivity, ρ_g the density, and h_{lg} the latent heat of vaporization. Once β is computed numerically, the the theoretical temperature profile within the vapour region is expressed as

$$T_g(x,t) = T_w + \frac{T_{\text{sat}} - T_w}{\operatorname{erf}(\beta)} \operatorname{erf}\left(\frac{x}{2\sqrt{\alpha_g t}}\right), \qquad 0 \le x \le x_\Gamma(t), \tag{8.12}$$

while the liquid region is assumed to remain isothermal at T_{sat} for $x \ge x_\Gamma(t)$ [195].

The time-dependent advancement of the phase boundary separating the vapour and liquid regions is assessed against the closed-form analytical solution in Figure 8.60 across four different grid resolutions ($0.005, 0.007, 0.009$, and 0.01 mm). This comparison provides a rigorous basis for selecting the appropriate resolution, while the time step is set at 0.01 seconds. While all resolutions show close agreement during the initial stages of the simulation, the deviation between the coarser meshes and the analytical solution increases over time, reaching its maximum at $t = 300$ s. This widening gap is attributed to the accumulation of numerical truncation errors as the boundary layer grows, necessitating a finer discretization to maintain long-term fidelity. Quantitatively, refining the mesh from 0.01 mm to 0.005 mm results in a reduction of the L_1 and L_2 error norms by approximately 97.8% and 98.5%, respectively. The 0.005 mm resolution was therefore selected as the optimal grid size, as it demonstrates an asymptotic approach to the analytical curve. Finally, Figure 8.61 compares the temperature profile along the x-direction at $t = 300$ s with the analytical solution. The MP-LDD predictions demonstrate strong correspondence with the Neumann solution, capturing both the slope of the thermal gradient in the liquid domain and the plateau at $T = T_{\text{sat}}$ in the vapor region. The 2D Stefan problem validates the robustness of the MP-LDD framework in capturing moving phase-change interfaces. The method demonstrates excellent agreement with analytical solutions for both interface evolution and thermal fields, while maintaining stability.

8.4.4 Two Dimensional Solidification

To further validate the MP-LDD framework for phase-change problems, a 2D solidification case is examined. This reference case describes the growth of a solid region inside a liquid domain that is initially in a uniformly superheated state, and subsequently cooled from the boundaries. The case is widely reported in the literature and provides well-documented reference data, making it a reliable test for assessing the predictive capability of the present method.

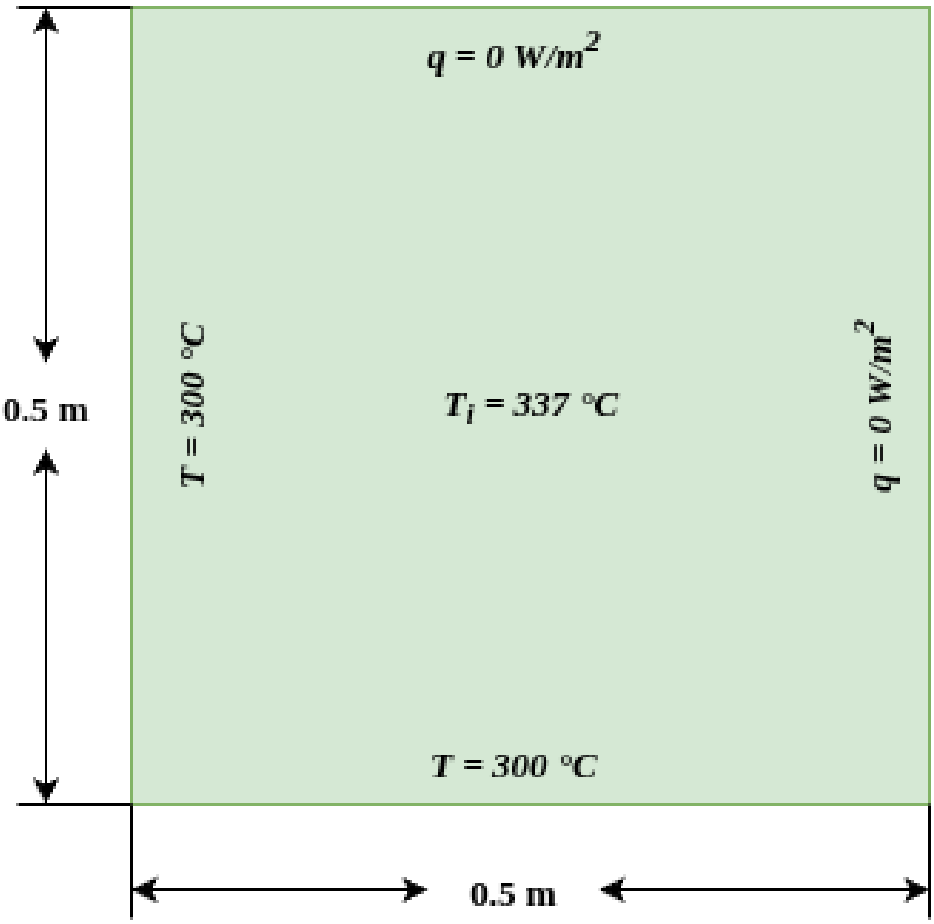

Figure 8.62. Schematic setup of the two-dimensional solidification benchmark problem.

The simulation domain is configured as a square of size 0.5×0.5 m, as shown in Figure 8.62. The initial condition is a uniform liquid temperature of $T_i = 337$ °C, which lies above the melting temperature $T_m = 327$ °C. The bottom and left boundaries are maintained at a constant temperature of $T = 300$ °C, thereby initiating solidification at these walls. The top and right boundaries are specified as adiabatic, enforcing a zero normal heat flux condition ($q_n = 0$). This configuration drives solid growth from the cooled bottom and left sides into the bulk of the liquid domain.

The material thermophysical characteristics assigned to both the liquid and solid phases are summarized below:

$$\text{Liquid: } \rho_\ell = 10650\ \text{kg/m}^3, \quad c_{p,\ell} = 30.7\ \text{J/(kg}\cdot\text{K)}, \quad k_\ell = 16\ \text{W/(m}\cdot\text{K)},$$
$$\text{Solid: } \rho_s = 11340\ \text{kg/m}^3, \quad c_{p,s} = 26.65\ \text{J/(kg}\cdot\text{K)}, \quad k_s = 35.3\ \text{W/(m}\cdot\text{K)},$$
$$L = -4.77 \times 10^3\ \text{J/kg}.$$

Here, the sign convention $L < 0$ indicates that latent heat is released during the solidification process. Simulations are advanced until $t = 2350$ s, with several point resolutions considered to perform grid sensitivity studies. Figure 8.63 illustrates the temporal evolu-

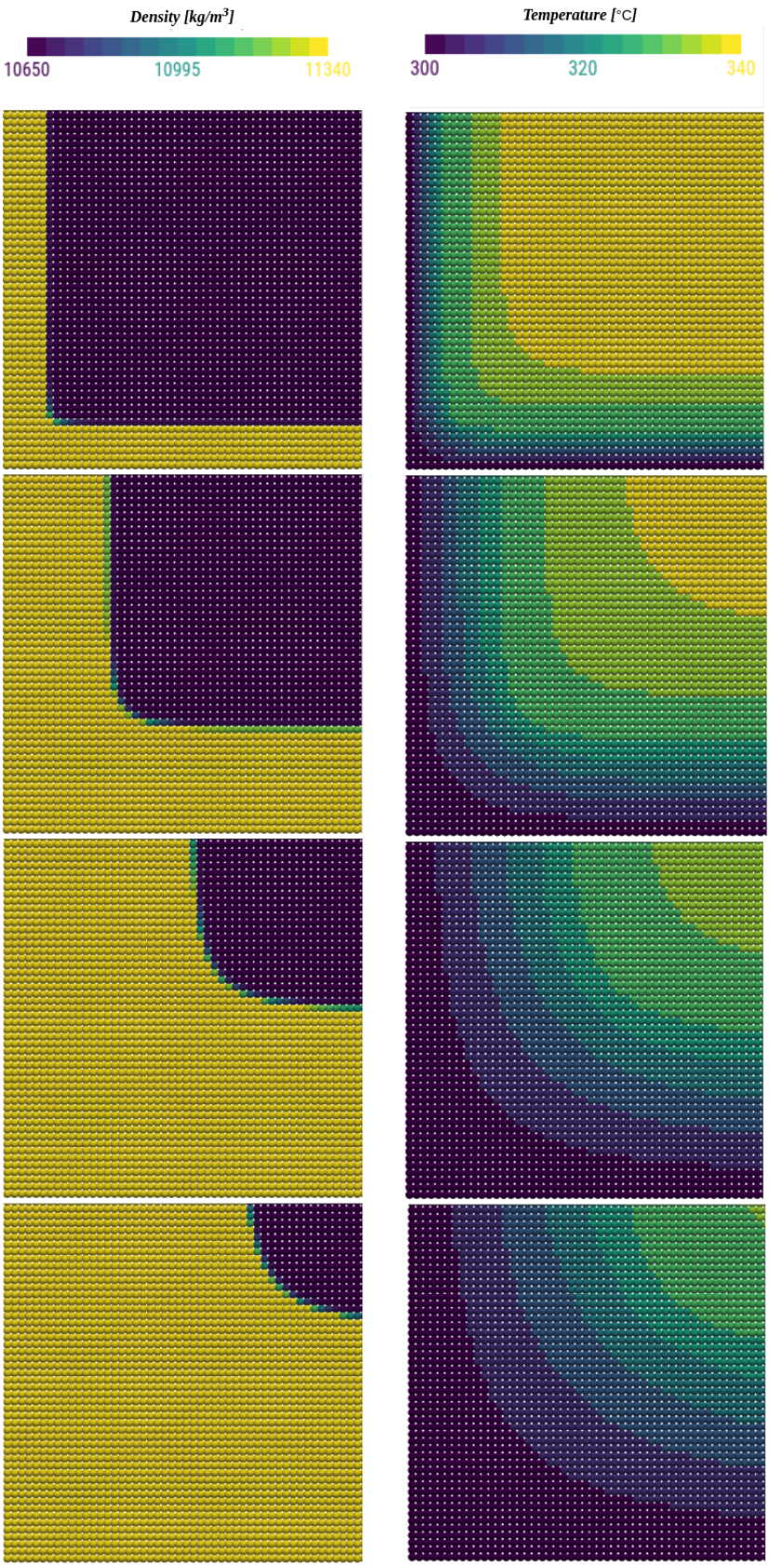

Figure 8.63. Evolution of density and temperature fields during the solidification process at different time instances.

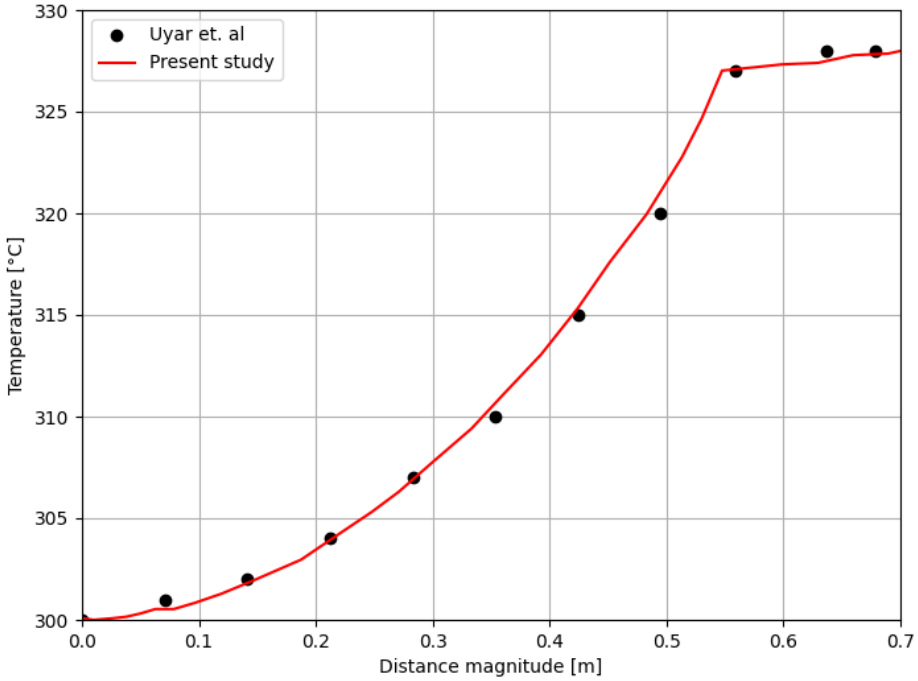

Figure 8.64. Comparison of temperature distribution along the vertical centerline with the results of Uyar et al.

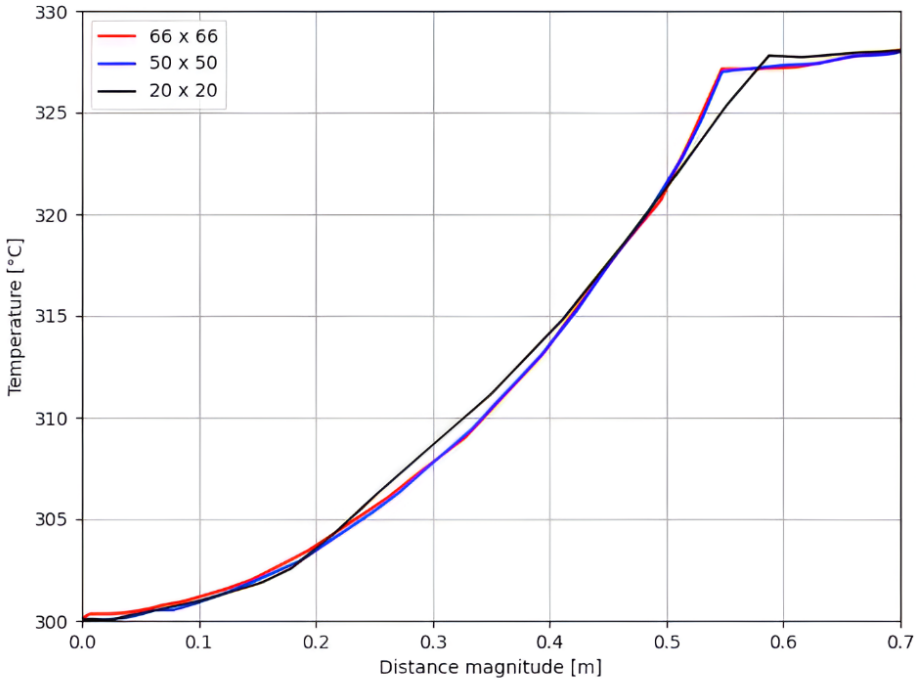

Figure 8.65. Grid convergence analysis for the 2D Stefan solidification benchmark.

tion of the temperature and density fields at four representative time instants ($t = 500$, 1500, 2000, and 2350 s). As cooling progresses, solidification initiates from the lower and left boundaries and gradually extends toward the bulk liquid. The MP-LDD framework successfully tracks the progression of the phase-change boundary with well-defined sharpness. The density field clearly differentiates the solid and liquid regions, while the temperature distribution reflects the expected steep gradients near the interface and smoother variations within the bulk phases.

For quantitative validation, temperature distributions along the vertical centerline of the domain are compared against the reference numerical data of [127]. As depicted in Fig. 8.64, the MP-LDD predictions are in excellent match with the reference data throughout the simulation. The model precisely reproduces the pronounced thermal gradients in the proximity of the advancing solid liquid interface, as well as the nearly uniform temperature in the bulk solid and liquid regions. This agreement demonstrates the capability of MP-LDD to resolve sharp thermal fronts while maintaining stability. To further assess the robustness of the framework, a grid convergence study was conducted by varying the number of discretization points in the domain. Figure 8.65 depicts the progression of the interface location across varying resolutions. The outcomes confirm that as the point density is increased, the interface evolution converges to a single profile. The difference between medium and fine resolutions is negligible, confirming the grid independence of the MP-LDD solution. A quantitative grid convergence study is conducted and Table 8.10 reports the L1 and L2 temperature error norms of the MP-LDD formulation with respect to the reference solution of Uyar et al. As the grid is refined from 20×20 to 66×66, the L1 norm decreases from 0.6026 K to 0.2725 K, while the L2 norm decreases from 0.7468 K to 0.3510 K, indicating a clear reduction in numerical error with mesh refinement.

Table 8.10. Grid convergence and error norms comparing the MP-LDD results with the reference solution of Uyar et al.

Grid Resolution	L1 norm [K]	L2 norm [K]
20×20	0.6026	0.7468
50×50	0.3419	0.4567
66×66	0.2725	0.3510

The two-dimensional solidification benchmark provides a stringent test of the MP-LDD framework for simulating phase-change phenomena. The method successfully captures the evolution of the solidification front and reproduces thermal gradients consistent with published reference data. The comparison with [127] demonstrates the accuracy of the predictions, while the grid convergence study confirms the computational stability and reliability of the numerical methodology. These results establish confidence in the capacity of the MP-LDD framework to effectively address large-scale solidification problems involving sharp phase interfaces, strong thermal gradients, and density variations.

8.4.5 Film Boiling

The present study simulates film boiling of water at near-critical pressure using a two-dimensional planar domain with a sinusoidal vapor-liquid interface, following the setup described by [196]. The computational domain extends horizontally over half the Taylor wavelength and vertically over twice that length. The lower wall is held at a fixed superheated condition with $\Delta T_{\text{sup}} = 10\,\text{K}$, while the upper boundary is treated as a solid wall. No slip boundary conditions are applied on the vertical sides. Thermophysical characteristics of water under near-critical operating conditions are employed in the simulations, with liquid and vapor densities of $\rho_l = 402.4\,\text{kg/m}^3$ and $\rho_v = 242.7\,\text{kg/m}^3$, respectively. The dynamic viscosities are $\mu_l = 46.7\,\mu\text{Pa·s}$ and $\mu_v = 32.38\,\mu\text{Pa·s}$, and the thermal conductivities are $k_l = 545\,\text{mW/m·K}$ and $k_v = 538\,\text{mW/m·K}$. The specific heats are $c_{p,l} = 218\,\text{J/kg·K}$ and $c_{p,v} = 352\,\text{J/kg·K}$. The surface tension is set to $\sigma = 0.07\,\text{mN/m}$, and the latent heat of vaporization is $L_v = 276.4\,\text{kJ/kg}$. The Antoine coefficients for water are summarized in Table 8.11.

Table 8.11. Antoine equation coefficients for water used in the present study.

Substance	A	B	C	Valid Temperature Range [°C]
Water	8.07131	1730.63	233.426	1 – 100

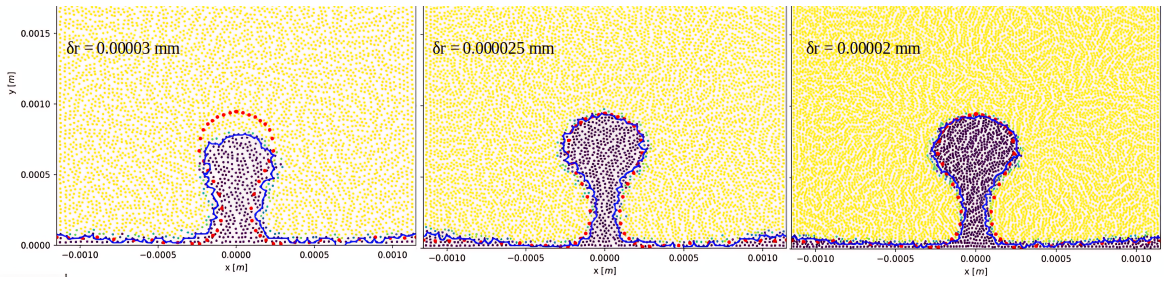

Figure 8.66. Grid dependence study for the film boiling simulation. The panels show the progression of the vapor bubble boundary (blue line) assessed against the benchmark data by Biswas et al. (red dots) at varying particle spacings: (a) 3×10^{-5} mm, (b) 2.5×10^{-5} mm, and (c) 2×10^{-5} mm. Increased resolution demonstrates better convergence with the experimental interface profile.

Table 8.12. Particle resolution study for the MP-LDD simulation at $t = 0.1$ s. The table shows the interface height error (%) and L_1/L_2 norms for different particle spacings. The results demonstrate convergence of both global and local interface features, with a particle spacing of 0.000020 m providing the best overall accuracy.

Particle size (mm)	Interface height error (%)	L_1 norm (m)	L_2 norm (m)
0.000030	16.6	4.66×10^{-5}	5.64×10^{-5}
0.000025	1.86	3.18×10^{-5}	3.51×10^{-5}
0.000020	0.27	2.86×10^{-5}	3.16×10^{-5}

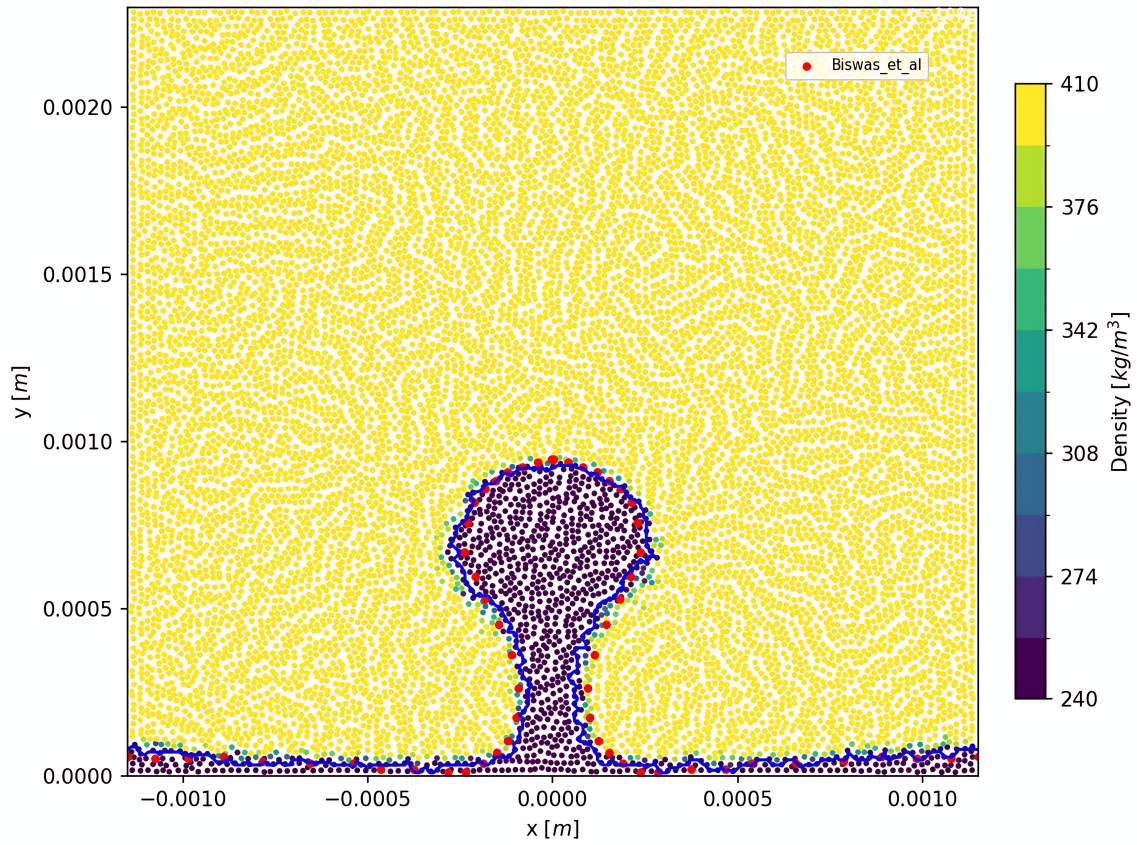

Figure 8.67. Density field of a vapor bubble in film boiling at near-critical conditions. The red markers indicate reference points from Biswas et al and blue line show the vapor boundary. The domain shows the formation of the bubble from a sinusoidal interface on a superheated wall at 0.1 sec.

To verify the dependability of the MP-LDD simulation, a particle resolution study was performed as illustrated in Figure 8.66. The particle spacing was refined incrementally until further refinement produced negligible improvement in key solution metrics, including interface height and interface shape. As shown in Table 8.12, the interface height error and geometric L_1/L_2 norms decrease steadily as the particle spacing is reduced. The lowest errors are achieved at a particle spacing of 0.000020 m, indicating that this resolution accurately captures both global interface features and local interface geometry. Therefore, $\delta r = 0.000020$ m was selected as the optimal particle spacing, balancing numerical accuracy. The evolution of the vapor bubble under film boiling conditions is visualized in Figures 8.67 and 8.68, which show both the density and velocity fields at selected time instants. The simulation captures the progressive transformation from the initial sinusoidal interface to the generation and rise of a vapor bubble due to localized heating. Figure 8.67 compares the predicted vapor-liquid interface against reference data from [196] at 0.1 seconds. The red markers represent the interface profile obtained in the reference study. The interfacial roughness observed in the vapor boundary as marked in blue line in Figure 8.67 is fundamentally linked to the treatment of the progressing interface within the MP-LDD framework. In a standard

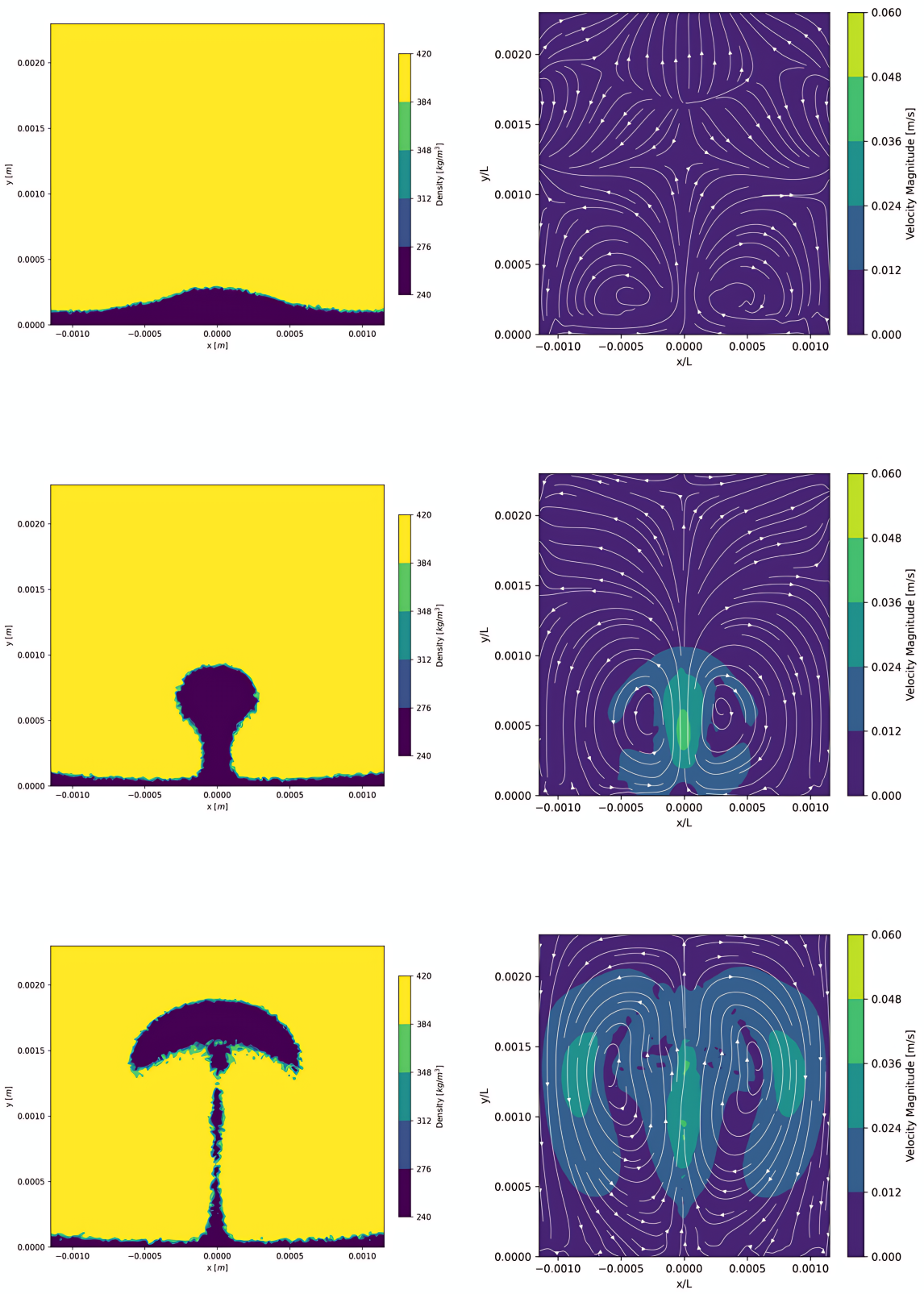

Figure 8.68. Evolution of density and velocity fields across three stages of phase change $(0.05s, 0.1s\&0.15s)$. *Left column: temperature distribution. Right column: velocity magnitude with streamlines.*

non-transitioning two-phase flow, the surface tension force is typically concentrated within a sharp interface involving only two particle layers (one from each phase). However, in the current transitioning case, the interface is characterized by a wider density gradient involving a greater number of particle layers.

While this multi-layer involvement ensures a continuous transition of properties, it also increases the sensitivity of the surface normal vector ($\hat{\mathbf{n}}$) and curvature (κ) calculations to local particle discretization. Because a constant surface tension coefficient (σ) is applied across these multiple layers, small-scale variations in local particle spacing (δr) and density lead to localized force fluctuations. These fluctuations manifest as the observed numerical wiggles at the interface. Furthermore, the motion of lower-density particles near the base of the bubble stem results from the localised equilibrium between buoyant forces and the distributed surface tension force, alongside recirculation zones generated by the bubble's progression. Despite these micro-scale numerical artifacts, the global bubble morphology remains consistent with the comparative data from [196], suggesting that the volumetric force scaling in Equation (6.20) correctly captures the macroscopic physics. Figure 8.68 presents the temporal progression of the phase change process through snapshots at $t = 0.05$ s, 0.1 s, and 0.15 s. The left column displays the density field, highlighting the liquid (high density) and vapor (low density) regions, while the right column shows the velocity magnitude and streamlines.

At $t = 0.05$ s, the initial vapor bubble begins to emerge from the superheated surface due to localized phase change. The velocity field exhibits symmetric vortical structures on either side of the vapor column, indicating the onset of buoyancy-driven convection. By $t = 0.1$ s, the vapor bubble has grown significantly, forming a pronounced neck and cap structure. The velocity streamlines demonstrate stronger vertical upward movement through the bubble stem and recirculating regions in the surrounding liquid, consistent with enhanced buoyant flow and latent heat transport. At $t = 0.15$ s, the vapor bubble exhibits a mushroom-shaped morphology with continued upward propagation. The flow field is dominated by large-scale convection loops that transport vapor upwards and draw liquid from the sides toward the heated wall. These features are characteristic of film boiling behavior near the critical point, where surface tension is low and thermal conductivity between phases is nearly matched. The simulated results exhibit excellent agreement with the reference data from [196], with only minimal qualitative deviations observed along the vapor-liquid interface. This strong correlation validates the reliability and computational robustness of the numerical framework in resolving near-critical film boiling behaviour.

Table 8.13 summarizes the wall-clock time required for the 2D film boiling simulations at different particle resolutions. The GPU-based solver was carried out on a laptop configured with an 11th Gen Intel® Core™ i7-11800H CPU (8 cores, 16 threads), 32 GB RAM, and an NVIDIA RTX A2000 Laptop GPU (4 GB VRAM). The results demonstrate that the GPU-based MP-LDD solver achieves practical computation times across a wide range of

Table 8.13. Computational time required for 2D film boiling simulations at different particle resolutions.

Point spacing (mm)	Total points	Average time step (s)	Wall-clock time (s)
0.00001	53,350	8×10^{-6}	681
0.00002	13,450	5×10^{-5}	37
0.000025	8,280	6×10^{-5}	28
0.00003	6,065	6×10^{-5}	23

particle spacings. Even for the finest resolution of 0.00001 mm, involving more than 53,000 particles, the simulation completed within approximately 11 minutes. These results highlight the practical feasibility of the framework for resolving phase change phenomena while maintaining manageable computational costs. In the future, detailed computational efficiency will be assessed for 3D industrial problems.

8.4.6 Summary

In this study, an implicit coupling strategy that connects the temperature field with the phase fraction variable. This approach enhances the stability and efficiency of managing enthalpy balance and latent heat during phase transitions. By representing thermophysical properties as smooth functions of the phase fraction, I ensured continuous material property fields across phase boundaries. The evaluation of the latent heat source used phase fraction data from the previous time step, which improved temporal stability without compromising accuracy. Validation against benchmark cases for melting, solidification, and film boiling confirmed the effectiveness of the method in accurately reproducing phase front movement, temperature distribution, and overall heat transfer metrics.

Looking ahead, while the current formulation effectively addresses latent heat in a semi-implicit manner for stability and efficiency, future work could explore tighter coupling strategies to tackle strongly nonlinear phase change problems more effectively.

9 CONCLUSION AND FUTURE WORK

9.1 Conclusion

This thesis presented the development and validation of a unified fully Lagrangian meshless computational framework, denoted Multiphase Lagrangian Differencing Dynamics (MP-LDD), for the simulation of physically complex flows involving multiphase dynamics, interfacial effects, thermally driven phase change, and fluid–structure interaction. The work extends the original single-phase LDD method into a dimension-independent and mesh-free formulation capable of treating strong discontinuities in density and viscosity, sharply evolving phase interfaces, surface tension and wetting effects, enthalpy-based phase transition, and two-way structural coupling within a common numerical framework.

A central contribution of the thesis is the derivation and implementation of variable-coefficient Laplacian operators within the MP-LDD discretization. These operators enable physically consistent treatment of pressure and viscous terms in multiphase configurations with abrupt material-property variation across the interface. In addition, a density-weighted modification of the Position-Based Dynamics regularization procedure was introduced in order to improve point redistribution near phase boundaries. This modification was shown to suppress spurious inter-phase mixing, reduce artificial void formation, maintain a sharp interface, and preserve a well-conditioned point distribution, particularly in flows involving large density contrasts and strong interfacial deformation.

The multiphase formulation was assessed through a range of established benchmark problems, including Rayleigh–Taylor instability, dam-break flows, sloshing in oscillating tanks, and immiscible liquid–liquid interaction. Across these cases, the method demonstrated robust interface preservation and good agreement with available experimental, numerical, and reference data over the investigated parameter range.

The framework was further extended to include capillary and wetting phenomena through the incorporation of surface tension and a dynamic contact angle model. This enabled simulation of wall-bounded interfacial flows in which curvature, capillary forces, and contact-line dynamics play a dominant role. Validation studies, including film boiling configurations, showed that the method is able to reproduce key features such as bubble nucleation, growth, detachment, and the associated thermal transport behaviour.

Thermally driven phase change was incorporated through the development of an Implicit

Phase Change Enthalpy (IPCE) formulation. Within the Lagrangian setting, this approach provides a natural treatment of thermal advection and phase transport while avoiding the numerical diffusion commonly associated with fixed-grid methods. The implicit coupling between temperature and phase fraction yielded stable and efficient treatment of latent heat effects, and the corresponding validation cases demonstrated accurate prediction of phase-front evolution, temperature fields, and integral heat-transfer behaviour.

A two-way weakly coupled FSI capability was also established through coupling of the LDD solver with a modal superposition structural model. By projecting structural deformation onto precomputed vibration modes, the structural response could be integrated efficiently while remaining compatible with the fluid time scale. Because both solvers operate on a shared surface description, the coupling avoids remeshing and geometric interface reconstruction. Validation against compliant baffle, elastic gate, and deformable wedge benchmarks demonstrated that the coupled formulation is capable of capturing hydrodynamic loading and the associated structural response with good accuracy.

Overall, the work presented in this thesis establishes MP-LDD as a unified meshless Lagrangian framework for the simulation of coupled multiphase, capillary, thermal, and fluid–structure interaction problems. The results demonstrate that the method provides a robust and extensible basis for the analysis of complex engineering flows involving sharp interfaces, strong material contrasts, phase transition, and structural deformation, while remaining compatible with efficient GPU-based computation.

9.2 Future Work

Although the MP-LDD framework has demonstrated robustness and good predictive capability across the range of benchmark problems considered in this thesis, several important directions remain for further development. These relate not only to extension of the framework toward broader multiphysics applications, but also to deeper verification of the present formulations, particularly in relation to conservation, interfacial accuracy, capillary effects, and coupled fluid–structure stability.

9.2.1 Further Verification and Conservation Assessment

An important next step is a more systematic quantitative assessment of the core numerical properties of the MP-LDD framework. In particular, future work should include tracking of the total mass or volume of each phase throughout the simulation and reporting the corresponding relative conservation error as a function of time. Such analysis would provide a clearer measure of long-time conservation behaviour and would complement the qualitative interface comparisons presented in the current study.

Further verification should also address interfacial accuracy and consistency more di-

rectly. This includes assessment of the accuracy of interface location, evaluation of second-order consistency in the vicinity of phase boundaries, and extension of the validation campaign to a broader class of benchmark problems with well-defined reference solutions. These steps would strengthen the numerical foundations of the method and help clarify its range of accuracy across different multiphase regimes.

9.2.2 Capillary and Wetting-Scale Validation

While the present surface tension and dynamic contact angle formulations produce physically reasonable results in the cases examined, additional capillary-scale verification is still required. Future work should therefore include quantitative assessment of parasitic currents, more rigorous validation of the dynamic contact angle model against reference wetting data, and systematic examination of interface behaviour in strongly capillary-dominated flows.

A related requirement is the study of capillary time-step restrictions and their interaction with adaptive time stepping. Such analysis would help establish practical stability and accuracy limits for simulations involving small length scales, rapid interface motion, or strong curvature effects. These developments would substantially improve confidence in the framework for coating, microfluidic, and free-surface capillary applications.

9.2.3 Fluid–Structure Interaction Enhancements

The present FSI formulation is based on a staggered partitioned coupling strategy and transfers pressure loading from the fluid to the structure. Although the benchmark cases examined in this thesis were computed stably within the investigated parameter range, no general stability analysis is claimed. In particular, staggered partitioned schemes are known to be potentially sensitive to added-mass effects when fluid inertia becomes comparable to structural inertia, and a broader assessment of stability limits remains necessary.

Future work should therefore include a systematic investigation of coupling stability in strongly added-mass-dominated regimes, together with evaluation of suitable mitigation strategies such as sub-iterations, interface relaxation, or more strongly coupled partitioned procedures. In addition, the present coupling transfers only normal pressure loading, whereas viscous shear transfer has not yet been incorporated. Inclusion of tangential fluid traction constitutes a natural extension of the framework and would improve predictive accuracy for problems in which wall shear and viscous structural loading are important.

9.2.4 Three-Dimensional and Large-Scale Applications

The validation studies in this thesis have been carried out primarily in two dimensions. Although the governing formulations are not restricted to two-dimensional settings, full three-dimensional implementation and verification remain an essential next step. This is particu-

larly important because many physically important phenomena, including vortex stretching, three-dimensional ligament breakup, droplet coalescence, and complex interface reconnection, cannot be represented fully in two dimensions.

Future work should therefore extend the multiphase, phase-change, wetting, and FSI capabilities of the framework to fully three-dimensional configurations. This would open the way to large-scale simulations of realistic engineering systems such as sloshing in LNG tanks, offshore hydrodynamics, boiling and condensation devices, casting processes, and thermally driven multiphase flows in energy systems.

9.2.5 Thermal and Phase-Change Extensions

The current framework already incorporates thermal transport and phase-change capability, but further development is possible for strongly nonlinear problems. In particular, more tightly coupled formulations for latent heat release and phase evolution may improve robustness in cases involving large heat fluxes, rapid melting or solidification, or strongly moving phase boundaries. Future research should therefore consider fully implicit nonlinear enthalpy formulations, tighter iterative coupling between temperature and phase fraction, and adaptive time-stepping strategies tailored to phase-transition dynamics.

An additional extension of clear practical relevance is the incorporation of temperature-dependent surface tension and Marangoni effects. Surface tension gradients can induce strong tangential interfacial stresses and fundamentally alter interface motion in boiling, welding, crystal growth, and microscale heat-transfer processes. Inclusion of these mechanisms would significantly broaden the applicability of the framework to thermocapillary flow problems.

9.2.6 Wetting and Contact-Line Physics

Although a dynamic contact angle model has been implemented successfully, further refinement of wall–interface physics remains an important area for development. Real wetting behaviour often depends on contact angle hysteresis, surface heterogeneity, roughness, and microscopic contact-line dissipation, none of which are yet represented in a fully general manner in the present work.

Future developments may therefore include physically based contact-line friction models, wall-energy or disjoining-pressure formulations, and improved treatment of advancing and receding contact angles. Such additions would enhance the predictive capability of the framework for capillary rise, coating flows, droplet spreading, and microfluidic systems.

9.2.7 Adaptive Resolution and Computational Performance

As the complexity of target applications increases, improved computational efficiency will become increasingly important. One promising direction is adaptive resolution, in which computational points are refined dynamically near interfaces, regions of high curvature, or zones of strong velocity, pressure, or thermal gradients. This would allow the method to maintain accuracy where needed while reducing cost in smoother parts of the domain.

Further work is also warranted in high-performance implementation. In particular, multi-GPU strategies, hybrid parallelization, and memory-efficient data structures could substantially improve scalability for large three-dimensional problems. Benchmarking against established grid-based solvers would also be valuable in order to quantify both the computational efficiency and the practical advantages of the MP-LDD framework across representative classes of multiphysics flow problems.

Final Perspective

The MP-LDD framework developed in this thesis demonstrates the potential of a meshless Lagrangian approach for coupled multiphysics simulation. By combining multiphase flow, surface tension, wetting dynamics, phase change, and fluid–structure interaction within a unified formulation, it provides a flexible basis for the analysis of complex interfacial and coupled physical processes. With further verification, extension to three-dimensional and large-scale problems, incorporation of more advanced interfacial physics, and continued development of stronger coupling strategies and computational efficiency, the MP-LDD framework has the potential to evolve into a robust and versatile tool for challenging engineering applications.

BIBLIOGRAPHY

[1] A. Prosperetti and G. Tryggvason, *Computational Methods for Multiphase Flow*, Cambridge University Press, 2007.

[2] G. Tryggvason, R. Scardovelli and S. Zaleski, *Direct Numerical Simulations of Gas–Liquid Multiphase Flows*, Cambridge University Press, 2011.

[3] V. R. Voller, M. Cross and N. C. Markatos, An enthalpy method for convection/diffusion phase change, *International Journal for Numerical Methods in Engineering*, 24, 271–284, 1987.

[4] F. P. Incropera, D. P. DeWitt, T. L. Bergman and A. S. Lavine, *Fundamentals of Heat and Mass Transfer*, John Wiley & Sons, 6th edn., 2007.

[5] V. K. Dhir, Boiling heat transfer, *Annual Review of Fluid Mechanics*, 30, 365–401, 1998.

[6] E. H. Dowell and K. C. Hall, Modeling of fluid–structure interaction, *Annual Review of Fluid Mechanics*, 33, 445–490, 2001.

[7] Y. Bazilevs, K. Takizawa and T. E. Tezduyar, *Computational Fluid–Structure Interaction*, Wiley, 2013.

[8] J. W. Cahn and J. E. Hilliard, Free energy of a nonuniform system. I: interfacial free energy, *The Journal of Chemical Physics*, 28, 258–267, 1958.

[9] C. Hirt and B. Nichols, Volume of fluid (vof) method for the dynamics of free boundaries, *Journal of Computational Physics*, 39, 201–225, 1981.

[10] M. Sussman, P. Smereka and S. Osher, A level set approach for computing solutions to incompressible two-phase flow, *Journal of Computational Physics*, 114, 1, 146–159, 1994.

[11] G. Tryggvason, R. Scardovelli and S. Zaleski, *Direct numerical simulations of gas–liquid multiphase flows*, Cambridge University Press, 2011.

[12] M. Theillard, F. Gibou and D. Saintillan, Sharp numerical simulation of incompressible two-phase flows, *Journal of Computational Physics*, 2019.

[13] J. J. Monaghan and A. Kocharyan, Sph simulation of multiphase flow, *Computer Physics Communications*, 87, 225–235, 1995.

[14] G. Duan, B. Chen, S. Koshizuka and H. Xiang, Stable multiphase moving particle semi-implicit method for incompressible interfacial flow, 2017.

[15] C. Hirt, J. Cook and T. Butler, A lagrangian method for calculating the dynamics of an incompressible fluid with free surface, *Journal of Computational Physics*, 5, 1, 103–124, 1970.

[16] G. Ryskin and L. Leal, Numerical solution of free-boundary problems in fluid mechanics. part 1. the finite-difference technique, *Journal of Fluid Mechanics*, 148, 1–17, 1984.

[17] G. Ryskin and L. Leal, Numerical solution of free-boundary problems in fluid mechanics. part 2. buoyancy-driven motion of a gas bubble through a quiescent liquid, *Journal of Fluid Mechanics*, 148, 19–35, 1984.

[18] F. Zonta, A. Soldati and M. Onorato, Growth and spectra of gravity-capillary waves in countercurrent air/water turbulent flow, *Journal of Fluid Mechanics*, 777, 245–259, 2015.

[19] J. Glimm, Tracking of interfaces for fluid flow: Accurate methods for piecewise smooth problems, *Transonic, Shock, and Multidimensional Flows*, 259–287, Academic Press, 1982.

[20] J. Glimm and O. A. McBryan, A computational model for interfaces, *Advances in Applied Mathematics*, 6, 4, 422–435, 1985.

[21] H. S. Udaykumar, H. C. Kan, W. Shyy and R. Tran-Son-Tay, Multiphase dynamics in arbitrary geometries on fixed cartesian grids, *Journal of Computational Physics*, 137, 2, 366–405, 1997.

[22] R. Fedkiw, T. Aslam, B. Merriman and S. Osher, A non-oscillatory eulerian approach to interfaces in multimaterial flows (the ghost fluid method), *Journal of Computational Physics*, 152, 2, 457–492, 1999.

[23] S. Popinet and S. Zaleski, A front-tracking algorithm for accurate representation of surface tension, *International Journal for Numerical Methods in Fluids*, 30, 6, 775–793, 1999.

[24] L. Lee and R. J. LeVeque, An immersed interface method for incompressible navier–stokes equations, *SIAM Journal on Scientific Computing*, 25, 3, 832–856, 2003.

[25] D. Drikakis, M. Frank and G. Tabor, Multiscale computational fluid dynamics, *Energies*, 12, 17, 2019.

[26] J. Brackbill, D. Kothe and C. Zemach, A continuum method for modeling surface tension, *Journal of Computational Physics*, 100, 2, 335–354, 1992.

[27] S. Kistler, *Hydrodynamics of wetting*, Marcel Dekker, 1993.

[28] R. L. Hoffman, A study of the advancing interface. i. interface shape in liquid-gas systems, *Journal of Colloid and Interface Science*, 50, 2, 228–241, 1975.

[29] L. H. Tanner, The spreading of silicone oil drops on horizontal surfaces, *Journal of Physics D: Applied Physics*, 12, 9, 1473, 1979.

[30] Y. D. Shikhmurzaev, *Capillary flows with forming interfaces*, CRC Press, 2007.

[31] R. Cox, The dynamics of the spreading of liquids on a solid surface. part 1. viscous flow, *Journal of Fluid Mechanics*, 168, 169–194, 1986.

[32] J. Göhl, A. Mark, S. Sasic and F. Edelvik, Dynamic wetting of droplet impingement: Theoretical and numerical modeling, *Physics of Fluids*, 30, 8, 082103, 2018.

[33] K. Yokoi, D. Vadillo, J. Hinch and I. Hutchings, Numerical studies of the influence of the dynamic contact angle on a drop impacting on a dry surface, *Physics of Fluids*, 21, 07 2009.

[34] J. M. Ludwicki, V. R. Kern, J. McCraney, J. B. Bostwick, S. Daniel and P. H. Steen, Is contact-line mobility a material parameter?, *NPJ Microgravity*, 8, 2022.

[35] M. Moran, H. Shapiro, D. Boettner and M. Bailey, *Fundamentals of Engineering Thermodynamics*, John Wiley & Sons, 2010.

[36] F. White, *Viscous Fluid Flow*, McGraw-Hill, 3rd edn., 2006.

[37] S. Patankar, *Numerical Heat Transfer and Fluid Flow*, Taylor & Francis, 1980.

[38] A. Bejan, *Convection Heat Transfer*, John Wiley & Sons, 4th edn., 2013.

[39] J. Bašić, N. Degiuli and D. Ban, A class of renormalised meshless laplacians for boundary value problems, *Journal of Computational Physics*, 354, 269–287, 2018.

[40] J. Bašić, N. Degiuli, B. Blagojević and D. Ban, Lagrangian differencing dynamics for incompressible flows, *J. Comput. Phys.*, 462, 111198, 2022.

[41] J. Basic, N. Degiuli, D. Ban and Malenica, A renormalisation procedure for lagrangian simulations of multiphase flows, *Comput. Fluids*, 233, 105073, 2023.

[42] J. Bašić, B. Blagojević, M. Andrun and N. Degiuli, A lagrangian finite difference method for sloshing: Simulations and comparison with experiments, *Proceedings of The 29th International Ocean and Polar Engineering Conference*, International Society of Offshore and Polar Engineers, Honolulu, Hawaii, USA, 2019.

[43] J. Bašić, N. Degiuli and D. Ban, Lagrangian differencing dynamics for incompressible flows, *Journal of Computational Physics*, 429, 109821, 2021.

[44] M. Bašić, B. Blagojević, B. Klarin and J. Bašić, Coupling of non–newtonian meshless flow with structural solvers, *Proceedings of the VII International Conference on Particle-Based Methods, PARTICLES*, 4–6 October, Hamburg, Germany, 2021.

[45] C. Peng, M. Bašić, B. Blagojević, J. Bašić and W. Wu, A lagrangian differencing dynamics method for granular flow modeling, *Journal of Computational Physics*, 457, 111198, 2022.

[46] M. Paneer, J. Bašić, Lozina, D. Sedlar and C. Peng, Elastic behaviours of linear structure using modal superposition and lagrangian differencing dynamics, *Proceedings of the VIII International Conference on Particle-Based Methods (PARTICLES 2023)*, Institute of Particle-Based Methods, Online, 2023.

[47] M. Paneer, J. Bašić, D. Sedlar, Lozina, N. Degiuli and C. Peng, Fluid structure interaction using modal superposition and lagrangian cfd, *Journal of Marine Science and Engineering*, 12, 2, 318, 2024.

[48] J. C. Joubert, D. N. Wilke and P. Pizette, A generalized finite difference scheme for multiphase flow, *Mathematical and Computational Applications*, 28, 2, 2023.

[49] S. Osher and J. Sethian, Fronts propagating with curvature-dependent speed: algorithms based on hamilton-jacobi formulations, *Journal of Computational Physics*, 79, 12–49, 1988.

[50] S. Unverdi and G. Tryggvason, A front-tracking method for viscous, incompressible, multi-fluid flows, *Journal of Computational Physics*, 100, 25–37, 1992.

[51] E. Olsson and G. Kreiss, A conservative level set method for two phase flow, *Journal of Computational Physics*, 210, 225–246, 2005.

[52] K. Kamran, R. Rossi and E. Oñate, A locally extended finite element method for the simulation of multi-fluid flows using the particle level set method, *Computer Methods in Applied Mechanics and Engineering*, 2015.

[53] R. A. Gingold and J. J. Monaghan, Smoothed particle hydrodynamics: Theory and application to non-spherical stars, *Monthly Notices of the Royal Astronomical Society*, 181, 375–389, 1977.

[54] L. B. Lucy, A numerical approach to the testing of the fission hypothesis, *The Astronomical Journal*, 82, 6, 1013–1024, 1977.

[55] S. Koshizuka and Y. Oka, Moving-particle semi-implicit method for fragmentation of incompressible fluid, *Nuclear Science and Engineering*, 123, 3, 421–434, 1996.

[56] T. Belytschko, Y. Y. Lu and L. Gu, Element-free galerkin methods, *International Journal for Numerical Methods in Engineering*, 37, 2, 229–256, 1994.

[57] E. O. Sergio Idelsohn, Monica Mier-Torrecilla, Multi-fluid flows with the particle finite element method, *Computer Methods in Applied Mechanics and Engineering*, 198, 33-36, 2750–2767, 2009.

[58] J. J. Monaghan, Smoothed particle hydrodynamics, *Annual Review of Astronomy and Astrophysics*, 30, 543–574, 1992.

[59] J. P. Morris, P. J. Fox and Y. Zhu, Modeling low reynolds number incompressible flows using sph, *Journal of Computational Physics*, 136, 1, 214–226, 1997.

[60] B. W. Ritchie and P. A. Thomas, Multiphase smoothed-particle hydrodynamics, *Monthly Notices of the Royal Astronomical Society*, 323, 3, 743–756, 05 2001.

[61] X. Check Hu and N. Adams, A multi-phase sph method for macroscopic and mesoscopic flows, *Monthly Notices of the Royal Astronomical Society*, 213, 2, 844–861, 2006.

[62] N. Grenier, M. Antuono, A. Colagrossi, D. L. Touzé and B. Alessandrini, An hamiltonian interface sph formulation for multi-fluid and free-surface flows, *Journal of Computational Physics*, 228, 22, 8380–8393, 2009.

[63] J. J. Monaghan et al., A robust sph algorithm for simulating immiscible multiphase flows, *Journal of Computational Physics*, 231, 4, 345–360, 2012.

[64] M. Rezavand, Isph scheme for simulating multiphase flows with complex interfaces and high density ratios, *Journal of Computational Physics*, 365, Issue Number, 106–123, 2018.

[65] M. Rezavand, C. Zhang and X. Hu, A weakly compressible sph method for violent multi-phase flows with high density ratio, *Journal of Computational Physics*, Volume Number, Issue Number, 2019.

[66] Y. Shimizu, Enhanced multiphase isph-based method for accurate modeling of oil spill, *Journal of Computational Physics*, 400, Issue Number, 104129, 2020.

[67] M. Olejnik and J. Pozorski, A robust method for wetting phenomena within smoothed particle hydrodynamics, *Flow, Turbulence and Combustion*, 104, 1, 115–137, 2020.

[68] R. Vacondio et al., Grand challenges for smoothed particle hydrodynamics numerical schemes, *Computational Particle Mechanics*, 8, 4, 575–588, 2021.

[69] C. Zhang, Y. Zhu and X. Hu, A multi-resolution sph framework: Application to multi-phase fluid-structure interactions, *physics.flu-dyn*, 5082–5101, 2022.

[70] G. Duan, S. Koshizuka, A. Yamaji, B. Chen, X. Li and T. Tamai, An accurate and stable multiphase moving particle semi-implicit method based on a corrective matrix for all particle interaction models, *International Journal for Numerical Methods in Engineering*, 115, 10, 1287–1314, 2018.

[71] R. P. Fedkiw, T. Aslam, B. Merriman and S. Osher, A non-oscillatory eulerian approach to interfaces in multimaterial flows (the ghost fluid method), *Journal of Computational Physics*, 152, 2, 457–492, 1999.

[72] D. Anderson, G. McFadden and A. Wheeler, Diffuse-interface methods in fluid mechanics, *Annual Review of Fluid Mechanics*, 30, 1, 139–165, 1998.

[73] X. Shan and H. Chen, Lattice Boltzmann model for simulating flows with multiple phases and components, *Physical Review E*, 47, 3, 1815–1819, 1993.

[74] J. Morris, Modeling low Reynolds number incompressible flows using smoothed particle hydrodynamics, *International Journal for Numerical Methods in Fluids*, 33, 3, 333–353, 2000.

[75] T. Young, An essay on the cohesion of fluids, *Philosophical Transactions of the Royal Society of London*, 95, 65–87, 1805.

[76] P.-S. Laplace, *Mécanique Céleste*, 4, Courcier, Paris, 1806.

[77] W. D. Harkins and H. F. Jordan, A method for determining surface tension and contact angle from the profile of a sessile drop, *Journal of the American Chemical Society*, 52, 5, 1751–1772, 1930.

[78] T. D. Blake and J. M. Haynes, Kinetics of liquid/liquid displacement, *Journal of Colloid and Interface Science*, 30, 3, 421–423, 1969.

[79] J.-F. Joanny and P.-G. de Gennes, A model for contact angle hysteresis, *Journal of Chemical Physics*, 81, 11, 5527–5530, 1984.

[80] C. W. Extrand and A. G. Shapiro, Apparent contact angles and retention of liquids on horizontal surfaces, *Journal of Colloid and Interface Science*, 170, 2, 515–521, 1995.

[81] O. Voinov, Hydrodynamics of wetting, *Fluid Dynamics*, 11, 5, 714–721, 1976.

[82] Y. Shikhmurzaev, Moving contact lines in liquid/liquid/solid systems, *Journal of Fluid Mechanics*, 334, 211–249, 1997.

[83] D. V. Nichita, R. Sander and H. Ghassemi, Dynamic receding contact angle model for multiphase flow simulations, *International Journal of Multiphase Flow*, 36, 935–947, 2010.

[84] J. Göhl, A. Mark, S. Sasic and F. Edelvik, An immersed boundary based dynamic contact angle framework for handling complex surfaces of mixed wettabilities, *International Journal of Multiphase Flow*, 109, 164–177, 2018.

[85] J. H. Snoeijer and B. Andreotti, Moving contact lines: Scales, regimes, and dynamical transitions, *Annual Review of Fluid Mechanics*, 45, 269–292, 2013.

[86] L. Huang, K. Rena, M. Lib, Tuković, P. Cardiff and G. Thomas, Fluid–structure interaction of a large ice sheet in waves, *Ocean. Eng. Ser.*, 182, 102–111, 2019.

[87] F. Danielsen, M. Sørensen, M. Olwig, V. Selvam, F. Parish, N. Burgess, T. Hiraishi, V. Karunagram, M. Rasmussen, L. Hansen et al., The asian tsunami: A protective role for coastal vegetation, *Science*, 310, 643, 2005.

[88] W. Zhou, Z. Wu and L. Mevel, Vibration-based damage detection to the composite tank filled with fluid, *Struct. Health Monit.*, 9, 433–445, 2010.

[89] M. Chella, A. Tørum and D. Myrhaug, An overview of wave impact forces on offshore wind turbine substructures, *Energy Procedia*, 20, 217–226, 2012.

[90] L. Liang, Z. Baoji, Z. Hao, T. Hailin and W. Weijie, Hydrodynamic performance optimization of marine propellers based on fluid–structure coupling, *Brodogradnja*, 74, 145–164, 2023.

[91] Z. Zhang, P. Sun, L. Pan and T. Zhao, On the propeller wake evolution using large eddy simulations and physics-informed space-time decomposition, *Brodogradnja*, 75, 75102, 2024.

[92] J. Jensen, *Load and Global Response of Ships*, Elsevier, Amsterdam, The Netherlands, 2001.

[93] A. Kwang-Jun Paik, M. Pablo, A. Carrica, B. Donghee Lee and M. Kevin, Strongly coupled fluid–structure interaction method for structural loads on surface ships, *Ocean. Eng.*, 36, 1346–1357, 2009.

[94] J. Hron and S. Turek, A monolithic fem/multigrid solver for an ale formulation of fluid–structure interaction with applications in biomechanics, *Fluid–Struct. Interact.*, 53, 146–170, 2006.

[95] J. Hron and S. Turek, A monolithic fem solver for an ale formulation of fluid–structure interaction with configuration for numerical benchmarking, *Proceedings of the European Conference on Computational Fluid Dynamics*, 5–8 September, Egmond aan Zee, The Netherlands, 2006.

[96] S. Rugonyi and K. Bathe, On finite element analysis of fluid flows fully coupled with structural interactions, *CMES*, 2, 195–212, 2001.

[97] J. Degroote, M. Hojjat, E. Stavropoulou, R. Wüchner and K. Bletzinger, Partitioned solution of an unsteady adjoint for strongly coupled fluid–structure interactions and application to parameter identification of a one-dimensional problem, *Struct. Multidiscip. Optim.*, 47, 77–94, 2013.

[98] J. Degroote, R. Haelterman, S. Annerel and J. Vierendeels, Coupling techniques for partitioned fluid–structure interaction simulations with black-box solvers, *Proceedings of the 10th MpCCI User Forum*, 17–18 February, Sankt Augustin, Germany, 2009.

[99] W. Lim, R. Xiao, T. Hong and C. Chin, Partitioned methods in computational modelling on fluid–structure interactions of concrete gravity-dam, *Comput. Informat. Sci.*, 6, 154, 2013.

[100] J. Bašić, N. Degiuli and Malenica, Insight into hydrodynamic damping of a segmented barge using numerical free-decay tests, *J. Mar. Sci. Eng.*, 11, 581, 2023.

[101] S. Seng, J. Jensen and Malenica, Global hydroelastic model for springing and whipping based on a free-surface cfd code (openfoam), *Int. J. Nav. Archit. Ocean Eng.*, 6, 1024–1040, 2014.

[102] M. Morishita, T. Ueno, K. Yabe and M. Kaneda, Enhanced prediction of global ship response using a new hybrid numerical method based on a computational fluid dynamics–structural dynamics coupled approach, *J. Marine Sci. Technol.*, 23, 1–15, 2018.

[103] Z. Tuković, A. Karač, P. Cardiff, H. Jasak and A. Ivanković, Openfoam finite volume solver for fluid-solid interaction, *Trans. Famena*, 42, 3, 1–31, 2018.

[104] E. Schillaci, F. Favre, P. Troch and A. Oliva, Numerical simulation of fluid structure interaction in free-surface flows: The wec case, *J. Phys. Conf. Ser.*, 2116, 012122, 2021.

[105] G. Fourey, G. Oger, D. Le Touzé and B. Alessandrini, Violent fluid–structure interaction simulations using a coupled sph/fem method, *IOP Conf. Ser. Mater. Sci. Eng.*, 10, 012041, 2010.

[106] Q. Yang, V. Jones and L. McCue, Free-surface flow interactions with deformable structures using an sph–fem model, *Ocean Eng.*, 55, 136–147, 2012.

[107] J. Nunez-Ramirez, J. Marongiu, M. Brun and A. Combescure, A partitioned approach for the coupling of sph and fe methods for transient nonlinear fsi problems with incompatible time-steps, *Int. J. Numer. Methods Eng.*, 109, 1391–1417, 2017.

[108] K. Wu, D. Yang and N. Wright, A coupled sph-dem model for fluid–structure interaction problems with free-surface flow and structural failure, *J. Comput. Struct.*, 177, 141–161, 2016.

[109] A. Nasar, B. Rogers, A. Revell and P. Stansby, Flexible slender body fluid interaction: Vector-based discrete element method with eulerian smoothed particle hydrodynamics, *Comput. Fluids*, 179, 563–578, 2019.

[110] O. Joseph and D. Rogers Benedict, A fluid–structure interaction model for free-surface flows and flexible structures using smoothed particle hydrodynamics on a gpu, *J. Fluids Struct.*, 104, 103312, 2021.

[111] J. Degroote, Partitioned simulation of fluid–structure interaction, *Arch. Comput. Methods Eng.*, 20, 185–238, 2013.

[112] F. Debrabandere, B. Tartinville, C. Hirsch and C. Coussement, Fluid-structure interaction using a modal approach, *J. Turbomach.*, 134, 051043, 2012.

[113] K. Sun, G. Zhang, Z. Zong, K. Djidjeli and J. Xing, Numerical analysis of violent hydroelastic problems based on a mixed mps—mode superposition method, *Ocean. Eng.*, 179, 285–297, 2019.

[114] R. CoGroth, M. Biancolini, E. Costa and U. Cella, Validation of high fidelity computational methods for aeronautical fsi analyses, *Engineering Toward Green Aircraft—CAE Tools for Sustainable Mobility*, 92, 29–70, Springer International Publishing, 2020.

[115] J. Banks, W. Henshaw, D. Schwendeman and Q. Tang, A stable partitioned fsi algorithm for rigid bodies and incompressible flow. part i: Model problem analysis, *J. Comput. Phys.*, 343, 432–468, 2017.

[116] F. Agyenim, N. Hewitt, P. Eames and M. Smyth, A review of materials, heat transfer and phase change problem formulation for latent heat thermal energy storage systems (lhtess), *Renewable and Sustainable Energy Reviews*, 14, 2, 615–628, Feb 2010.

[117] J. Jaguemont, N. Omar, J. V. Mierlo and P. V. D. Bossche, Phase-change materials (pcm) for automotive applications: A review, *Applied Thermal Engineering*, 132, 308–320, Mar 2018.

[118] A. D. Brent, V. R. Voller and K. J. Reid, Enthalpy–porosity technique for modeling convection–diffusion phase change: application to the melting of a pure metal, *Numerical Heat Transfer*, 13, 3, 297–318, 1988.

[119] L. I. Rubinstein, *The Stefan Problem*, American Mathematical Society, Providence, RI, 1971.

[120] G. Son and V. K. Dhir, Numerical simulation of film boiling near critical pressures with a level set method, *Journal of Heat Transfer*, 120, 1, 183–192, 1998.

[121] D. Juric and G. Tryggvason, Computations of boiling flows, *International Journal of Multiphase Flow*, 24, 3, 387–410, 1998.

[122] S. Tanguy, T. Ménard and A. Berlemont, A level set method for vaporizing two-phase flows, *Journal of Computational Physics*, 221, 2, 837–853, 2007.

[123] A. Arefmanesh, A. Jokar and H. Ghassemi, Meshless local petrov-galerkin simulation of buoyancy-driven fluid flow and heat transfer in a cavity with wavy side walls, *CMES-Computer Modeling in Engineering & Sciences*, 62, 2, 179–202, 2010.

[124] W. K. Liu, S. Jun and Y. F. Zhang, Reproducing kernel particle methods, *International Journal for Numerical Methods in Fluids*, 20, 8-9, 1081–1106, 1995.

[125] H. Hu and S. A. Argyropoulos, Mathematical modelling of solidification and melting: a review, Tech. rep., 1996.

[126] P. Suchde, H. Kraus, B. Bock-Marbach and J. Kuhnert, Meshfree one-fluid modeling of liquid–vapor phase transitions, *Computers and Fluids*, 273, 4 2024.

[127] O. Uyar and A. Mugan, Numerical solution of two phase solidification problem using dynamic substructuring based on adaptive error estimation, *Hittite Journal of Science and Engineering*, 2, 127–144, 2015.

[128] R. Huang, H. Wu, J. Qin and W. Li, A hybrid sph–lbm method for modeling phase change heat transfer, *International Journal of Heat and Mass Transfer*, 85, 880–896, 2015.

[129] N. Perrone and R. Kao, A general finite difference method for arbitrary meshes, *Computers & Structures*, 5, 1, 45–57, Apr 1975.

[130] T. Liszka and J. Orkisz, The finite difference method at arbitrary irregular grids and its application in applied mechanics, *Computers & Structures*, 11, 1-2, 83–95, 1980.

[131] A. I. Tolstykh and D. A. Shirobokov, On using radial basis functions in a "finite difference mode" with applications to elasticity problems, *Computational Mechanics*, 33, 1, 68–79, 2003.

[132] N. Lanson and J. P. Vila, Renormalized meshfree schemes i: Consistency, stability, and hybrid methods for conservation laws, *SIAM Journal on Numerical Analysis*, 46, 4, 1912–1934, 2008.

[133] N. Lanson and J. P. Vila, Renormalized meshfree schemes ii: Convergence for scalar conservation laws, *SIAM Journal on Numerical Analysis*, 46, 4, 1935–1964, 2008.

[134] W. Qu and H. He, A spatial–temporal gfdm with an additional condition for transient heat conduction analysis of fgms, *Applied Mathematics Letters*, 110, 106579, 2020.

[135] G. Yan, W. Lei, C. Wen and et al., Application of the meshless generalized finite difference method to inverse heat source problems, *International Journal of Heat and Mass Transfer*, 108, A, 721–729, 2017.

[136] Z.-J. Fu, Z.-C. Tang, H.-T. Zhao, P.-W. Li and T. Rabczuk, Numerical solutions of the coupled unsteady nonlinear convection–diffusion equations based on generalized finite difference method, *European Physical Journal Plus*, 134, 6, 272, 2019.

[137] X. Wang, H. Sadat and C. Prax, A new meshless approach for three dimensional fluid flow and related heat transfer problems, *International Journal of Heat and Mass Transfer*, 122, 182–194, 2018.

[138] G. Hauke and M. Lanzarote, Simulation of low-speed buoyant flows with a stabilized compressible/incompressible formulation: The full navier–stokes approach versus the boussinesq model, *Algorithms*, 15, 8, 278, 2022.

[139] J. Duintjer Tebbens and M. Tůma, Preconditioner updates for solving sequences of linear systems in matrix-free environment, *Numerical Linear Algebra with Applications*, 17, 6, 997–1019, 2010.

[140] J. Becker, A second order backward difference method with variable steps for a parabolic problem, *BIT Numerical Mathematics*, 38, 644-662, 1998.

[141] J. K. P. Suchde, Point cloud movement for fully lagrangian meshfree methods, *J. Comput. Appl. Math*, 340, 89–100, 2017.

[142] O. Bokanowski, A. Picarelli and C. Reisinger, Stability and convergence of second order backward differentiation schemes for parabolic hamilton–jacobi–bellman equations, *Numerische Mathematik*, 148, 187-222, 2021.

[143] G.-H. Cottet, Semi-lagrangian particle methods for high-dimensional vlasov–poisson systems, *Journal of Computational Physics*, 365, 362–375, 2018.

[144] A. De Boer, M. van der Schoot and H. Bijl, Mesh deformation based on radial basis function interpolation, *J. Comput. Struct.*, 85, 784–795, 2007.

[145] F. Gibou, R. P. Fedkiw, L.-T. Cheng and M. Kang, A Second-Order-Accurate Symmetric Discretization of the Poisson Equation on Irregular Domains, *Journal of Computational Physics*, 176, 1, 205–227, Feb. 2002.

[146] M. Bašić, B. Blagojević, B. Klarin, C. Peng and J. Bašić, Lagrangian split-step method for viscoelastic flows, *Polymers*, 16, 14, 2024.

[147] E. Emmrich, Convergence of the variable two-step bdf time discretisation of nonlinear evolution problems governed by a monotone potential operator, *BIT Numerical Mathematics*, 49, 297–323, 2009.

[148] R. Xu, P. K. Stansby and D. R. Laurence, Accuracy and stability in incompressible sph (isph) based on the projection method and a new approach, *Journal of Computational Physics*, 228, 18, 6703–6725, 2009.

[149] A. Khayyer, H. Gotoh and Y. Shimizu, Comparative study on accuracy and conservation properties of isph-based particle shifting techniques, *Journal of Computational Physics*, 332, 236–256, 2017.

[150] A. Khayyer, H. Gotoh and Y. Shimizu, A density-independent formulation of incompressible sph with improved pressure calculations, *Journal of Computational Physics*, 380, 245–267, 2019.

[151] M. Müller, D. Charypar and M. Gross, Particle-based fluid simulation for interactive applications, *Proceedings of the 2003 ACM SIGGRAPH/Eurographics symposium on Computer animation*, 154–159, 2003.

[152] B. Solenthaler and R. Pajarola, Predictive-corrective incompressible sph, *ACM Transactions on Graphics (TOG)*, 28, 3, 1–6, 2009.

[153] M. Macklin and M. Müller, Position based fluids, *ACM Transactions on Graphics (TOG)*, 32, 4, 104, 2013.

[154] J. Bašić, N. Degiuli, Malenica and D. Ban, Lagrangian finite-difference method for predicting green water loadings, *Ocean Engineering*, 209, 107533, 2020.

[155] I. Alduán, A. Tena and M. A. Otaduy, Dyverso: A versatile multi-phase position-based fluids solution for vfx, *Computer Graphics Forum*, 36, 32–44, 12 2017.

[156] J. Glimm, J. W. Grove, X. L. Li, W. Oh and D. H. Sharp, A Critical Analysis of Rayleigh-Taylor Growth Rates, *Journal of Computational Physics*, 169, 2, 652–677, May 2001.

[157] Monaghan, J. John and A. Rafiee, A simple sph algorithm for multi-fluid flow with high density ratios, *International Journal for Numerical Methods in Fluids*, 71, 5, 537 – 561, 2013.

[158] A. J. Chorin, Numerical solution of the navier-stokes equations, *Mathematics of Computation*, 22, 104, 745–762, 1968.

[159] G. Strang, On the construction and comparison of difference schemes, *SIAM Journal on Numerical Analysis*, 5, 3, 506–517, 1968.

[160] J. L. Guermond and A. Salgado, A splitting method for incompressible flows with variable density based on a pressure poisson equation, *Journal of Computational Physics*, 228, 2834–2846, 5 2009.

[161] M. Paneer, J. Bašić, D. Sedlar and C. Peng, Multiphase lagrangian differencing dynamics method with sharp interfaces, *Engineering Analysis with Boundary Elements*, 175, 106197, 6 2025.

[162] D. Z. C. Brackbill, J.; Kothe, A continuum method for modeling surface tension, *J. Comput. Phys.*, 100, 335–354, 1992.

[163] D. Bonn, J. Eggers, J. Indekeu, J. Meunier and E. Rolley, Wetting and spreading, *Reviews of Modern Physics*, 81, 739–805, 2009.

[164] T. D. Blake, The physics of moving wetting lines, *Journal of Colloid and Interface Science*, 299, 1–13, 2006.

[165] S. F. Kistler, Hydrodynamics of wetting, J. F. Padday, editor, *Wetting, Spreading and Adhesion*, Academic Press, 1993.

[166] T. Qian, X.-P. Wang and P. Sheng, A variational approach to moving contact line hydrodynamics, *Journal of Fluid Mechanics*, 564, 333–360, 2006.

[167] OpenFOAM Foundation, *dynamicAlphaContactAngle and dynamicContactAngle Models*, OpenFOAM, 2025, version 11. Available at https://cpp.openfoam.org/v11/dynamicContactAngle_8C_source.html (accessed October 2025).

[168] A. Esteban, J. López, J. Hernández, P. Gómez, C. Zanzi and J. Roenby, A contact line force model for the simulation of drop impacts on solid surfaces using volume of fluid methods, *Computers Fluids*, 263, 105946, 2023.

[169] V. R. Voller and C. R. Swaminathan, An enthalpy method for conduction with melting and freezing, *International Journal for Numerical Methods in Engineering*, 24, 271–284, 1987.

[170] Y. Kudoh and H. Ozoe, Numerical simulation of phase change problems by the enthalpy method, *International Journal of Heat and Mass Transfer*, 40, 15, 3659–3674, 1997.

[171] S. Molin, Particle methods for multiphase flows with phase change, *International Journal for Numerical Methods in Fluids*, 35, 45–66, 2001.

[172] M. Müller and J. Scherer, Meshless modeling of multiphase heat and mass transfer, *Computer Methods in Applied Mechanics and Engineering*, 199, 1123–1134, 2010.

[173] R. K. Sinnot, *Chemical Engineering Design*, Butterworth-Heinemann, Oxford, 4th edn., 2005.

[174] D. D. Gray and A. Giorgini, The validity of the boussinesq approximation for liquids and gases, *International Journal of Heat and Mass Transfer*, 19, 5, 545–551, 1976.

[175] H. Vogel, Temperature dependence of the viscosity of liquids, *Physikalische Zeitschrift*, 22, 645–646, 1921.

[176] W. Sutherland, The viscosity of gases and molecular force, *Philosophical Magazine*, 36, 507–531, 1893.

[177] S. Rhee, Unstructured grid based reynolds-averaged navier–stokes method for liquid tank sloshing, *J. Fluids Eng.*, 127, 572–582, 2005.

[178] C. Antoci, M. Gallati and S. Sibilla, Numerical simulation of fluid–structure interaction by sph, *J. Comput. Struct.*, 85, 879–890, 2007.

[179] M. Eswaran, U. Saha and D. Maity, Effect of baffles on a partially filled cubic tank: Numerical simulation and experimental validation, *Comput. Struct.*, 87, 198–205, 2009.

[180] S. Sankar, R. Ranganathan and S. Rakheja, Impact of dynamic fluid slosh loads on the directional response of tank vehicles, *Veh. Syst. Dyn.*, 21, 385–404, 1992.

[181] S. Nicolici and R. Bilegan, Fluid structure interaction modeling of liquid sloshing phenomena in flexible tanks, *Nucl. Eng. Des.*, 258, 51–56, 2013.

[182] S. Arora, S. Vasudevan, S. Sasic and S. Etemad, A partitioned fsi methodology for analysis of sloshing-induced loads on a fuel tank structure, *Proceedings of the 6th European Conference on Computational Mechanics (ECCM 6)*.

[183] S. Idelsohn, J. Marti, A. Souto-Iglesias and E. Onate, Interaction between an elastic structure and free-surface flows: Experimental versus numerical comparisons using the pfem, *Comput. Mech.*, 43, 125–132, 2008.

[184] C. Marcela, B. Laura, S. Mario and D. Jorge, Numerical modeling and experimental validation of free surface flow problems, *Arch. Comput. Methods Eng.*, 23, 139–169, 2016.

[185] S. Hosseinzadeh and K. Tabri, Free-fall water entry of a variable deadrise angle aluminium wedge: An experimental study, *Developments in the Analysis and Design of Marine Structures*, 9, CRC Press, 1st edn., 2021.

[186] Z. R. Kishev, Numerical simulation of violent sloshing by a cip-based method, *Journal of Marine Science and Technology*, 11, 111–122, 2006.

[187] S. H. Rhee, Unstructured Grid Based Reynolds-Averaged Navier-Stokes Method for Liquid Tank Sloshing, *Journal of Fluids Engineering*, 127, 3, 572–582, 02 2005.

[188] S. Cummins and M. Rudman, An sph projection method, *Journal of Computational Physics*, 152, 584–607, 1999.

[189] X. Hu and N. Adams, An incompressible multi-phase sph method, *Journal of Computational Physics*, 227, 278–364, 2007.

[190] H. Ozmen-Cagatay and S. Kocaman, Dam-break flow in the presence of obstacle: Experiment and cfd simulation, *Engineering Applications of Computational Fluid Mechanics*, 5, 541–552, 2011.

[191] S. Hänsch, D. Lucas, T. Höhne and E. Krepper, Application of a new concept for multi-scale interfacial structures to the dam-break case with an obstacle, *Nuclear Engineering and Design*, 279, 171–181, 2014.

[192] S. Hysing, S. Turek, D. Kuzmin, N. Parolini, E. Burman, S. Ganesan and L. Tobiska, Quantitative benchmark computations of two-dimensional bubble dynamics, *International Journal for Numerical Methods in Fluids*, 60, 1259–1288, 2009.

[193] G. Reece, B. D. Rogers, G. Fourtakas and S. Lind, Buoyancy-driven circulation and multi-component mixing using sph with a new adiabatic boundary condition, *International Journal of Heat and Mass Transfer*, 233, 125904, 2024.

[194] D. Wan, B. Patnaik and G. Wei, A new benchmark quality solution for the buoyancy-driven cavity by discrete singular convolution, *Numerical Heat Transfer, Part B: Fundamentals*, 40, 3, 199–228, 2001.

[195] A. H. Rajkotwala, A. Panda and E. A. J. F. Peters, A conservative diffuse interface model for multiphase flows with phase change, *International Journal of Multiphase Flow*, 120, 103093, 2019.

[196] G. Tomar, G. Biswas, A. Sharma and A. Agrawal, Numerical simulation of bubble growth in film boiling using a coupled level-set and volume-of-fluid method, *Physics of Fluids*, 17, 11, 112103, 2005.

Curriculum Vitae

Manigandan Paneer

Manigandan Paneer is a Product Manager and Senior CFD Engineer at Engineering Software Steyr GmbH in Austria and is completing his doctoral studies at the University of Split, Faculty of Electrical Engineering, Mechanical Engineering and Naval Architecture (FESB). He obtained a Master's degree in Aerospace Technology (2016) after completing his undergraduate studies in Aeronautical Engineering (2014). His doctoral research focuses on developing meshless numerical methods for multiphase flow simulations, including phase change and fluid–structure interaction.

His PhD-related publications in journals include: An Implicit Phase Coupled Meshless Method for Heat Transfer and Phase Change in the International Journal of Heat and Fluid Flow, 2026; Multiphase Lagrangian Differencing Dynamics Method with Sharp Interfaces, Engineering Analysis with Boundary Elements, 2025; Fluid Structure Interaction Using Modal Superposition and Lagrangian CFD, Journal of Marine Science and Engineering, 2024. Conference contributions include: Surface Tension and Contact Angle Modelling in Multiphase Lagrangian Differencing Dynamics, 12th International Conference on Fluid Flow, Heat and Mass Transfer, 2025; Elastic Behaviour of Linear Structures Using Modal Superposition and LDD, PARTICLES 2023; Automatic Meshless CFD Toolset for Slosh Dynamics, 3rd International Conference on Flight Vehicles, Aerothermodynamics and Reentry, 2025.

He has over ten years of professional experience in computational fluid dynamics within the aerospace and automotive industries. His scientific interests include multiphase flows, heat transfer, turbomachinery, advanced numerical methods, and high-performance computing.

Životopis

Manigandan Paneer

Manigandan Paneer zaposlen je kao Product Manager i viši CFD inženjer u tvrtki Engineering Software Steyr GmbH, Austrija, te pohađa doktorski studij na Sveučilištu u Splitu, Fakultetu elektrotehnike, strojarstva i brodogradnje (FESB). Diplomirao je Aeronautičko inženjerstvo 2014. godine, a 2016. godine stekao je magisterij iz područja Aerospace Technology. Njegovo doktorsko istraživanje usmjereno je na razvoj bezmrežnih numeričkih metoda za simulacije višefaznih strujanja, uključujući fazne promjene i interakciju fluida i konstrukcije.

Radovi povezani s doktorskim istraživanjem objavljeni su u časopisima: An Implicit Phase Coupled Meshless Method for Heat Transfer and Phase Change, International Journal of Heat and Fluid Flow, 2026; Multiphase Lagrangian Differencing Dynamics Method with Sharp Interfaces, Engineering Analysis with Boundary Elements, 2025; Fluid Structure Interaction Using Modal Superposition and Lagrangian CFD, Journal of Marine Science and Engineering, 2024. Konferencijski radovi uključuju: Surface Tension and Contact Angle Modelling in Multiphase Lagrangian Differencing Dynamics, 12th International Conference on Fluid Flow, Heat and Mass Transfer, 2025; Elastic Behaviour of Linear Structures Using Modal Superposition and LDD, PARTICLES 2023; Automatic Meshless CFD Toolset for Slosh Dynamics, 3rd International Conference on Flight Vehicles, Aerothermodynamics and Reentry, 2025.

Ima više od deset godina profesionalnog iskustva u području računalne dinamike fluida u zrakoplovnoj i automobilskoj industriji. Njegovi znanstveni interesi uključuju višefazna strujanja, prijenos topline, turbostrojarstvo, napredne numeričke metode i računalstvo visokih performansi.